SYSTEMATIC ANALYSIS OF WHOLE MOUSE BRAIN VASCULATURE AND INTACT HUMAN ORGANS USING MACHINE LEARNING

Mihail Ivilinov Todorov

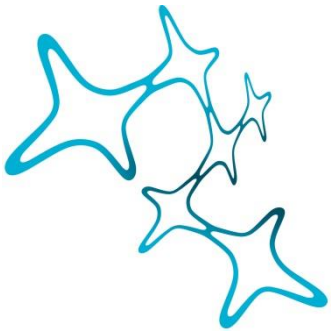

Graduate School of
Systemic Neurosciences

LMU Munich

Dissertation at the
Graduate School of Systemic Neurosciences
Ludwig-Maximilians-Universität München

August 8th, 2020

Supervisor
Dr. Ali Ertürk
Institute for Stroke and Dementia Research (ISD)
Klinikum der Universität München

First Reviewer: Dr. Ali Ertürk
Second Reviewer: Prof. Dr. med. Marco Düring

Date of Defense : November 25th, 2020

"The single most important ingredient in the recipe for success is transparency because transparency builds trust."

Denise Morrison

Table of contents

1. List of abbreviations

3D: three-dimensional

BBB: blood-brain barrier

BOLD: blood oxygen level

CD31: cluster of differentiation 31, also known as PECAM-1

CHAPS: 3-[(3-Cholamidopropyl)dimethylammonio]-1-propanesulfonate

CNN: convolutional neural network

CT: computed tomography

CW: Circle of Willis

DiI: 1,1′-dioctadecyl-3,3,3′,3′-tetramethylindocarbocyanine perchlorate

fMRI: functional magnetic resonance imaging

LSFM: laser scanning fluorescence microscope

MRA: magnetic resonance angiography

MRI: magnetic resonance imaging

NVU: neurovascular unit

PECAM-1: Platelet endothelial cell adhesion molecule, also known as CD31

PET: positron emission tomography

sCMOS: scientific Complementary metal–oxide–semiconductor

SDS: Sodium dodecyl sulfate

SHANEL: small-micelle-mediated human organ efficient clearing and labeling

SMC: smooth muscle cell

SPECT: single-photon emission computed tomography

VesSAP: Vessel Segmentation & Analysis Pipeline

2. Abstract

Optical tissue clearing methods enable the cellular and molecular investigation of complex biological specimens without sectioning. However, a reliable and scalable analysis of large imaging datasets in three dimensions (3D) remains a challenge. Adult human organs are particularly challenging to render transparent because of the accumulation of dense and sturdy molecules in decades-aged tissues. To overcome these challenges, we developed two methods: (1) SHANEL (small-micelle-mediated human organ efficient clearing and labeling), a method based on a novel tissue permeabilization approach to label and clear human organs, and (2) VesSAP (Vessel Segmentation & Analysis Pipeline), a deep learning-based framework to quantify and analyze brain vasculature.

We used SHANEL to render the intact adult human brain and other organs transparent and perform 3D histology with antibodies and dyes in centimeters-depth at the cellular resolution. Furthermore, we developed a deep learning pipeline to analyze millions of cells in cleared human brain tissues. For analyzing brain vasculature, we used VesSAP, which uses a convolutional neural network (CNN) with a transfer learning approach for segmentation, and achieves human-level accuracy. By using VesSAP, we analyzed the vascular organization in whole C57BL/6J, CD1 and BALB/c mouse brains at the micrometer scale after registering them to the Allen mouse brain atlas.

Overall, SHANEL and VesSAP are robust, unbiased, publicly available technologies to chart the cellular and molecular architecture of large intact mammalian organs, and enable scalable quantifications of the angioarchitecture of cleared mouse brains for biological insights into the vascular function of the brain.

3. Introduction

3.1. The dynamic blood vessel network of the mammalian brain

3.1.1. Angioarchitectural organization and patterns

The cerebrovascular system is responsible for the stable and controlled trafficking of oxygen, nutrients, metabolites, signaling molecules, immunity and heat in order to ensure the physiological homeostasis of the mammalian brain. Remarkably the brain lacks significant energy deposits and receives its substrates, primarily oxygen and glucose, on-demand through a specialized network of blood vessels. Moreover, because of the dynamic and regionally diverse energy requirements posed by brain activity, blood flow needs to reach the brain at the right time and place, and in sufficient amount. The brain vasculature has evolved distinctive anatomical and physiological features in order to maintain health of the extremely energy-sensitive neuronal tissue. Abnormalities of the cerebrovasculature contributes to pathology and are major cause of neuronal dysfunction, hypoxia, ischemia, and eventually cell death[1].

The anatomy of the vascular transport system defines its maximal capacity to nourish an organ. Cerebral vessels have spatial constraints in terms of tortuosity, location and anastomoses as a function of size, evolving in a complex layout of vessels approximating a globally optimal system that minimizes the costs of the construction and maintenance of the biological transport system[2]. The gross anatomy of the brain vascular tree follows the outside-in type of development of the brain resulting in three spatiotemporally typical compartments: the earliest extracerebral (pial *arteries* and *veins* in the subarachnoid space), followed by the extrinsic (*penetrating arterioles* and *ascending venules* as well as the *arterial perforators*) and finally the intrinsic dense capillary bed also known as *microvasculature*[3,4]. Brain arteries share similarities with other systemic arteries, like their endothelial lining, elastic and contractile wall, the rich autonomic and sensory ganglia innervation, and the lack of valves. Nevertheless, they differ substantially in structure and function. Cerebral arterial vessels have prominent elastic lamina with smooth muscle cells (SMC) oriented perpendicularly to the direction of blood flow as well as relatively flat bifurcation angles for efficient supply to specific regions, called arterial territories. They often form a highly collateralized network, in contrast to veins, but these anastomoses are often hypoplastic with

the potential to grow to full capacity[5,6]. This redundant blood supply has drastic effects on the vulnerability or resistance of stroke[7–10]. Blood from the heart enters the brain vasculature through the left and right internal carotid arteries and simultaneously through the unilateral basilar artery, which end ventrally at the basis of the brain in the Circle of Willis (CW). Arterial segments at the CW may easily shunt flow across adjacent territories of the middle cerebral artery, the posterior cerebral artery and the anterior cerebral artery on each hemisphere, but also the two hemispheres via the anterior communicating artery and the fusion of the bilateral posterior arteries. Despite the evolutional conservation of this arterial loop, the vascular arrangement of the CW varies in human and mice, that is, it can also be incomplete. The purpose of the CW was long considered a backup route for blood flow in case of an occlusion. Lately, Vrselja and colleagues proposed that it might also serve as a reservoir with large elastic walls to attenuate and dilute the pulsatile wave effect of the blood arriving from the heart for preventing the disruption of the delicate blood-brain barrier (BBB) from mechanical stress[11]. Next, part of the oxygenated blood enters the basal deep brain circulation or continues in the superficial pial arteries towards the cortical circulation. The -often collateralized- pial arteries branch off into orthogonal penetrating arterioles, which have thinner but still multilayered SMC and run with a continuously decreasing caliber and elastic lamina in the extension of the subarachnoid space (called perivascular space or Virchow-Robin space) until finally branching into the multitude of capillaries in the brain cortex. In the brains of gyrencephalic animals mammals also flows through the long arterial perforators to the deep subcortical regions. The deep segment of brain arterial vessels generally has discontinuous SMC layer, lacks perivascular innervation. Its basal membrane is fused with the glial membrane seamlessly transitioning into terminal capillaries. Very recently, Grubb and colleagues discovered precapillary sphincters (at the proximal branching of arterioles to downstream capillaries) encircled by contractile mural cells, which are capable of bidirectional control of the length and width of the enclosed vessel. They suggest that the location of precapillary sphincters help pressure equalization along penetrating arterioles and protect capillaries against high pressure[12]. In contrast to arteriolar SMCs, capillaries have scarce coverage of pericytes that spiral around the endothelial monolayer. Cerebral capillaries represent the deepest level in the brain vascular tree, where the absolute majority of the chemical and particle exchange occurs through the strictly controlled interface barrier, the BBB, consisting of endothelial cells, astrocyte end-feet and pericytes[13,14]. Here the endothelial cells form unique impermeable tight junctions, express unique molecular transporters, and provide selective endocytotic systems for transcytosis via membrane-bound

vesicles[15]. The only exceptions with highly permeable microvessels are the circumventricular organs, the choroid plexus and the pineal gland, which have sensory and secretory roles within the brain. Whether capillaries become arterial and venous is determined based on circulatory dynamics and functional demands. After passing through the capillaries venous blood is collected by venules to either the superficial (including the dural sinuses) or the deep cerebral veins (depending on their distance) to finally leave the brain vasculature via the bilateral jugular vein and return to the pulmonary circulation. Venules in the brain still have endothelial cells with tight junctions and tight liner sheets formed by pericytes and astrocytic end-feet. These are not present in systemic venules[16]. Recent research suggests that these venules may be involved with transcytosis across the BBB to the brain[17]. Veins of the brain have significantly less or no muscular tissue in their thin walls, and form fewer anastomoses than arteries, and they have no one-way valves to prevent blood backflow[18,19].

On top of this general layout, regional physiological differences result inhomogeneous arrangement of the cerebral vasculature in the healthy mammalian brain as a result of an adaptation to the homeostatic conditions. Densely and sparsely vascularized areas with a varying layout of large, medium and microvessels span across the brain regions[20]. Notoriously grey and white matter have different vascularization and branching patterns across mammals, namely vessels in the latter are scarce, consisting of smaller-diameter vessels that have fewer anastomoses[21]. This increases the risk of damage in the white matter in case of blood flow reduction[22]. Recently Adams and colleagues showed that the vasculature of the brain cortex follows the organization of the neuronal layers[23]. The multitude of blood vessels are arranged in a structurally heterogeneous and dynamic network (wider incorporating metabolic, myogenic and neurogenic regulation of the cerebral autoregulation system) that can adapt its structure in different situations to maintain biological homeostasis and to support tissue demands[24]. For example, the constriction or dilation of the arterioles affects the pressure of the blood in the brain, which must be maintained within narrow limits in order to avoid underperfusion and overperfusion. Vascular adaptation through plasticity is active during the entire lifespan, from ontogenesis up to the late-life and involves periendothelial cells in a complex interplay forming the neurovascular unit (NVU)[25]. The NVU consists of nearby capillaries (ca. 15 μm in the mouse and human brain[26,27]) together with its basal membrane as well as pericytes and glial cells (astroglia, microglia, oligodendroglia), and typically up to 8 “client” neurons, which enable the neurovascular coupling of neuronal activity with endothelium-dependent cerebral blood flow

through several tightly controlled, dynamic, and complex cellular interactions. Perhaps the most well-known mechanism is the transient regional perfusion increase (an increase of the vessel diameter, called the hemodynamic response) which strongly correlates with elevated neural activity. This phenomenon is now extensively used for noninvasively and indirectly probing cerebral blood volume (CBV), BBB permeability and cognitive assessments *in vivo*, using autoradiography, optical coherence tomography, ultrasonography, near-infrared spectroscopy and blood oxygenation-level dependent functional magnetic resonance imaging (fMRI). However, the uneven capillary (where the largest change in cerebral blood volume occurs) density across the brain regions poses serious challenges in the interpretation of resulting signals[28,29]. For example the baseline CBV distribution may vary over the cortical layers creating a bias of the measured signal to layers with high CBV values. Moreover, the distribution of the penetrating arteries and ascending veins does not correlate with the cortical columns of the brain consequently limiting the achievable point spread function of fMRI[30,31]. Therefore obtaining a complete quantitative map of all underlying blood vessels is necessary.

Blood supply may be constricted down to pathological levels, ranging from malnutrition up to atrophy and tissue death. Such phenomena are collapsed string vessels, which consist of empty basement membrane tubes without endothelium[32]. Chronically elevated blood pressure and traumatic brain injuries often cause damage to the brain vasculature. For example in the case of functional capillary rarefaction[33,34] through vasoconstriction, which in turn deprives the surrounding tissue of blood causing severe ischemia, even though all elements of the vascular bed are present. Morphological aberrations of existing blood vessels are known in altered hemodynamic conditions and metabolic disorders such as the highly tortuous vessels in type 2 diabetes, hypoperfusion, the spiraling in tauopathy; and aneurysms[6,35–38]. Structural rarefaction describes the decreased capillary density because of missing or permanently nonfunctional vessels, for example, as long-term consequences of hypertension, traumatic brain injuries or amyloid angiopathy. Another aspect of the postnatal vascular remodeling is angiogenesis, meaning new blood vessels are formed (linked with shear stress-dependent and oxygen tension-dependent release of angiogenic signals) from existing segments, for example, in the repair process followed by a focal ischemic stroke or cancerous pathological neovascularization[39–42]. Insufficient blood perfusion in the brain is known to be caused by vascular senescence (arrest of endothelial cell growth and decline), stiffness and reduction of arterial collaterals accompanying aging. Aging is the greatest risk factor for a premature

acceleration of neurological deficits and neurodegeneration like vascular dementia and Alzheimer's disease[3,43–47].

Based on the conservation of mass, a tight relationship is expected between blood flow rate and capillary number. With the improvement of histological instrumentation and methods, research focus has recently grown towards capillaries, which are the most abundant elements and therefore represent the largest exchange surface of the cerebrovascular network. It is generally accepted and mathematically proven that the capability of vascular trees to deliver blood flow needed to maintain an organ is linearly proportional to the number of capillaries to distribute such flow to the tissue of the organ[48]. Besides the computational modeling aspect of the vascular layout, a growing list of clinical research shows that microcirculation dysfunction may be used as an early marker of vascular-related disorders and to follow their stages[49–53], and as a sensitive proxy for classifying therapeutic healing progress[54], necessitating the complete reconstruction of the angioarchitecture for biomedical research.

3.1.2. Fundamental differences in the mouse and human brain vasculature

The most striking gross anatomical difference between the brains of mice and humans is their size. However, mice allow studying whole mammal brains in approximately 1-2 cm^3 volume with a simplified form and more primitive functions. The very first reference of a simplified form is evident from the surface of the brain: humans have folded brain cortex (called gyrencephalic) arranged in lobes in contrast to mice, which are lisencephalic. The gyrification is accounted to the vast difference in the approximate estimation of 86 billion versus the 33 million cells on average, respectively[55]. From the cross-sectional view another important difference is the proportion of the gray matter to white matter volume, namely humans have 40:60, while mice have 90:10. From a vascular perspective of view mice and humans have very similar vascularization patterns in the cortex down to the capillary level. However, the human brain has an additional distinct vascular system in the deep white matter, which becomes particularly important in the consequences of subcortical strokes, in contrast to mice[56]. Mice lack long arterial perforators, but have similar cortical blood vessel arrangement that appear similar to the ones in the human brain[57]. Another substantial difference is that mice have most often an incomplete CW, meaning that the anterior part, arising from the pair of internal carotid arteries, is connected via a unilateral hypoplastic posterior communicating artery to the posterior section supplied by the vertebral artery and consisting of the basilar and the beginning of the bilateral superior cerebellar arteries. The posterior communicating

artery might be completely missing or present on both sides based on the genetic strain leading to impaired resilience to compensate for occlusions in the nearby regions[58,59].

On a more fundamental level, there is a need to describe the structure of the vascular network of the brain: 1) quantitative datasets from complete mouse brains of widely used strains integrating angioarchitectonic patterns mapped to the anatomical brain atlas to serve as a phenotype for the healthy mammalian brain vascular network; 2) implementing optical tissue clearing on the whole human brain and revealing the 3D complexity of the spatial arrangement of the vascular networks in centimeters thick tissues.

3.2. Current methods for imaging the brain vasculature

3.2.1. Atlases and resources overview

The discovery of the closed circulatory transport system of vertebrates by Harvey in 1628 was of central importance in modern vascular biology. Documentation of the vascular anatomy, like its cellular composition (termed “endothelium”) and that arteries and veins are interconnected via (contractile) capillaries, was mainly done by drawing optical observations. Later this was extended by ink, wax and resin injections together with analog angiography image capturing. The invention of blood vessel-specific stainings, electron microscopy, (digital) computed tomography (CT, PET, SPECT, and MRA) and fluorescent microscopy revolutionized the field in the last two centuries and enabled truly volumetric representations[60]. Generally, two main strategies of characterizing the brain vascular anatomy have been adopted based on the imaging modality: the structural way, resolving continuous subsets of blood vessel network, and the probabilistic way, describing the likelihood of their occurrences. The ground setting works of Salamon and Corbaz as well as Duvernoy et al., elucidated the complex structure of the human cerebral vasculature in many regions of the brain with partial coverage of capillaries in selected areas using tedious manual labour[61,62]. Nevertheless, it is possible to convert structural information, covering the complete vascular network layout, into statistical frequency maps but not the other way around. While MRA became the state-of-the-art tool for probabilistic 3D imaging the human brain vasculature[56,63–67], capillaries remain as bulk signals due to resolution limitations. Notably these microvessels

hold far less signal, even with contrast enhancers, that prevents individually resolving them with current hardware sensitivity[67–70], which holds for rodent MRA studies too[71,72].

A sampling of major publications from mouse studies shows a growing number of attempts to resolve all vascular segments and create structural atlases of the whole cerebral vasculature using diverse microscopic[52,73–75] and CT[76,77] modalities. However these works are focusing on a single strain (either the C57BL/6 or CBA) and their imagery, from which the results are drawn, are hardly available, ranging from "available on reasonable request" to minimal "tutorial example datasets". This substantially limits the broader research community to study further and model the underlying layout of the vascular network (e.g. exploring higher organizational principles as vessel tortuosity, fractal dimension) as well as to improve the processing algorithms in order to make new discoveries using big data.

3.2.2. Volumetric imaging of the cerebrovasculature

Blood vessels run in many directions through the tissue and create a complex biological transport system, which makes traditional low-depth scanning coupled to tissue sectioning methods non-optimal for unveiling their organization. Mechanical slicing artifacts need to be carefully corrected at the reconstruction of the sections, and the very limited view of essentially two-dimensional slices contain a large number of disconnected vessel segments limiting conclusions to empirical and qualitative nature. Extrapolation from average values for "typical vessels" to network properties can lead to substantial errors[78]. Therefore, sufficient resolution volumetric imaging is required to capture the full vascular network that is currently exceeding the capabilities of *in vivo* ultrasound, MRI or optical scanners[76,79,80]. However, slice-based imaging, like confocal laser scanning, serial two-photon and electron microscopes, can undoubtedly provide extremely high-resolution ultrastructural information about the vasculature which is contributing to the anatomical, physiological and molecular systems-level understanding of the brain vasculature[20,81–84].

The brain vasculature of healthy mammals is arranged inhomogeneously. Densely and sparsely vascularized areas with a varying layout of large, medium and microvessels span across the brain regions[20]. Notoriously grey and white matter have different vascularization and branching patterns, namely vessels in the latter are scarce, consisting of smaller-diameter

vessels that have fewer anastomoses[21], which may result in a higher risk of damage in the case of infarction[22]. Recently Adams and colleagues showed that cortical cerebral vasculature follows the cytoarchitectonic organization of the neuronal layers[23]. Cerebral vessels have spatial constraints in terms of tortuosity, location and anastomoses as a function of size, evolving in a complex layout of vessels approximating a globally optimal system that minimizes the costs of the construction and maintenance of the biological transport system[2].

Up to date, various attempts were made in the last decade to acquire and resolve complete parts of the cerebrovascular network. The small size of the capillaries and the sensitivity of state-of-the-art scanners generally necessitates usage of some sort of contrast-enhancing for reliable acquisitions, like fluorescent immunostaining of vascular epitopes; casting of fluorescent gels or dyes in the vascular lumen; casting contrast enhancer in combination with corrosion of surrounding tissue. Tsai and colleagues established multi-scale correlations of neuronal and microvascular densities in the murine neocortex using two-photon fluorescent microscopy, albeit the hardware limitation of imaging maximal 2 mm depth and only in the dorsal brain surface, a limitation resulting from the curvature of the brain, the surrounding skull as well as the size and working distance of the objective[26]. An important gap of the field was filled by Xiong and colleagues using micro-optical sectioning tomography, similar to serial knife-edge scanning microscopy, for mechanically thin sectioning and then imaging whole mouse brains providing large tree-like structures and annotations of the arterial and venous vascular system in the whole mouse brain. However their method relies on manual vessel segmentation and lacks automatic registration to the common reference atlases besides using five adult mice to create a precise stereotactic atlas resource[73]. Quintana and colleagues developed an elegant method of acquiring the murine cerebrovascular network trough a luminal corrosion cast followed by tissue decalcification and maceration using microtomography to reveal sex-dependent differences[77]. However, in their work data processing limitations require manual signal thresholding of predefined volumes of interest and thus prohibits systematic whole-brain analyses and later staining of rehydrated tissue is impossible in contrast to the SHANEL method (as part of present thesis[85]). To obtain a complete picture of the angioarchitecture organization it is necessary to use 3D imaging methods for capturing the entire vascular network rather than studying data with limited resolution or space.

3.3 Optical tissue clearing for studying the angioarchitecture in the brain

3.3.1. Advantages of transparent tissue histology

Optical tissue clearing provides a solution exactly for the issues described above while being time-efficient by keeping the 3D tissue intact, thus liberating from slice alignment and stitching as well as mass staining and clearing the "slices" at once[86]. Significant evolution of fluorescent selective plane imaging microscopy equipment (such as powerful narrowband lasers, homogenous wide field micrometer-thin and stripe-free light-sheet excitation optics, long working distance and refractive index-matched objectives, sCMOS [scientific Complementary Metal-Oxide-Semiconductor] full-frame detection, motorized microscale sample moving XYZ stages) have enabled the 3D acquisition of centimeters thick intact organs, for which homogeneity of refractive indices of the samples is critical. Moreover, the field of optical tissue clearing was revived and produced a multitude of methods for interrogating complex biological tissue samples, such as the brain vasculature of mammals. The brain tissue of mammals is naturally opaque, being a highly scattering medium and absorbing light in the visible spectrum. Optical scattering occurs when light passes through materials with different optical properties and chemical composition, such as water, lipids, proteins, fibers, and mineralized tissue. Homogenizing the refractive indices of the tissue is the core concept of every optical clearing technique by either removing or oversaturating components. Optical absorption is the process of a material (like heme, melanin pigments and other biomolecules[79], converting light energy to another form of energy effectively reducing its intensity. As an optional step, these components are to be removed or quenched during the clearing process, which is commonly referred as decolorization. The continuity of the blood vessel network poses an additional difficulty in staining, imaging, and computational evaluation. Throughout the literature, all major types of tissue transparency techniques (hydrophobic, hydrophilic and hydrogel-based) have been adapted to overcome these difficulties in for labeling and reconstructing the brain vascular network, which also indicates that cerebrovascular research using optical tissue clearing is an area that continues to gain interest [74,75,87–93,93–97].

3.4. Automatized data analysis with machine learning

With the development of a diverse repertoire of tissue transparency techniques it has become relatively routine to prepare a series of experimental samples and scan them for subsequent data analysis. Modern LSFM systems enable high-throughput full-frame imaging of 3D volumes in 16-bit depth multichannel format for capturing research grade details of biological samples. Such high-resolution data sets quickly reach Teravoxel (10^{12} volumetric pixels) size[75,98] and are barely manageable by traditional processing and visualization tools on laboratory workstations. One of the most frequent tasks in *ex vivo* transparent tissue microscopy is semantic segmentation of anatomical structures from one or more grayscale channels, e.g. blood vessels in a brain, as a basis to various quantifications. In reality however imaging data is always noisy, which comes from the imperfection of the microscope (light sheet beam interference, thermal noise of the camera, chromatic or spherical aberration of all lenses and mirrors) and the tissue sample (never being perfectly transparent, thus straying light, producing shadows) to inevitably add up onto the measured signal in the scans. Also, nearly all computer displays are planar thus inspecting depth and overlapping structures in spatial data with three physical dimensions are hard-limited. These circumstances make structure delineation using manual effort a slow and tedious challenge while also particularly prone to fatigue.

Big-data algorithms and machine learning principles have relevantly contributed to the development of new brain-mapping approaches in medical image analysis, providing not only fast but also precise and unbiased quantification tools matching human accuracy[99–101]. The most important criteria are the biological validity of the segmentation results, which is ensured by the deep convolutional architecture and supervised training of a neural network with training data from as many different experts as possible. This phase is the most time consuming involving the joint work of computer science and anatomy experts. The ability of convolutional neural networks (CNN) to learn hierarchically complex patterns and their variation from experience as well as competence of many experts enables automatic and widely generalizable segmentation in comparison to hand-engineered image filters. This is extremely useful since the training of the CNN can then be extended with synthetically generated or multiple modalities and fidelities, which are significantly faster to produce and further improve the accuracy of the segmentation[102,103]. The breakthrough of CNNs occurred with the implementation onto commonly available graphic processing units, which

continuously widens the application and makes them easy-to-use for scientific purposes[104–106]. As a result, nowadays a single laboratory workstation can automatically analyze terabytes of imaging data in a couple of hours, a major speedup in the accumulation of large quantities of biomedical and clinical data, which is key for the development of reliable models to detect and predict stages of brain vascular injuries[107].

4. Aims of this thesis

Given the growing demand to statistically investigate the cerebral angiome in different brain regions and the currently available tools (optical tissue clearing, 3D light-sheet microscopy, machine learning and the detailed Allen mouse brain atlas), the motivation of present thesis is:

1. To establish a reliable pipeline for analyzing large-scale aged human organs, covering the pipeline from optical tissue clearing of fixed samples up to the accurate quantification using machine learning.

2. To set up a reliable strategy for labeling, imaging and reconstructing all segments of the blood vasculature of intact mouse brains.

3. To develop a scalable open-source software solution for accurately recognizing and statistically characterizing the brain-wide angioarchitecture of healthy commonly used laboratory mouse strains.

4. To provide an open-access database of the whole brain reconstructions and quantified morphological features mapped to the different regions defined by the latest mouse brain atlas.

5. Research articles

5.1. Machine learning analysis of whole mouse brain vasculature

Tissue clearing methods now enable the volumetric imaging of entire murine organs without sectioning. However, a reliable and scalable analysis of large imaging datasets in 3D remains a challenge. The cerebrovascular network is particularly difficult for analysis because of its 3D organization and structural continuity along with variable vascular calibers. Traditional hand-engineered image filters fail to differentiate profound changes in the illumination and vessel radius. To overcome these difficulties we developed an automatized deep learning-based framework to quantify and analyze brain vasculature, termed VesSAP. Our pipeline uses a convolutional neural network in combination with a transfer learning approach for semantic segmentation and achieves human-level accuracy. By using VesSAP, we first extracted the fundamental structure of the healthy adult cerebrovascular network of three widely used laboratory mouse strains C57BL/6J, CD1, and BALB/c at the micrometer scale. Second, after registering them to the cytoarchitectonic Allen mouse brain atlas, we established a statistical profile of the vasculature for each brain region cluster. Moreover, we demonstrate evidence of secondary intracranial collateral vascularization in CD1 mice and find reduced vascularization of the brainstem in comparison to the cerebrum. To foster reproducibility and further improvement, the code, the trained algorithm, the reconstructed raw and the segmented whole-brain scans together with the Allen brain region annotations are open source and freely available to the scientific community.

Taken together, the open-source VesSAP enables unbiased and scalable quantifications of the angioarchitecture of cleared mouse brains and yields holistic insights into the vascular function of the brain.

ARTICLES
https://doi.org/10.1038/s41592-020-0792-1

nature methods

Machine learning analysis of whole mouse brain vasculature

Mihail Ivilinov Todorov[1,2,3,10], Johannes Christian Paetzold[4,5,6,10], Oliver Schoppe[4,5], Giles Tetteh[4], Suprosanna Shit[4,5,6], Velizar Efremov[4,7], Katalin Todorov-Völgyi[2], Marco Düring[2,8], Martin Dichgans[2,8,9], Marie Piraud[4], Bjoern Menze[4,5,6,11] ✉ and Ali Ertürk[1,2,8,11] ✉

Tissue clearing methods enable the imaging of biological specimens without sectioning. However, reliable and scalable analysis of large imaging datasets in three dimensions remains a challenge. Here we developed a deep learning-based framework to quantify and analyze brain vasculature, named Vessel Segmentation & Analysis Pipeline (VesSAP). Our pipeline uses a convolutional neural network (CNN) with a transfer learning approach for segmentation and achieves human-level accuracy. By using VesSAP, we analyzed the vascular features of whole C57BL/6J, CD1 and BALB/c mouse brains at the micrometer scale after registering them to the Allen mouse brain atlas. We report evidence of secondary intracranial collateral vascularization in CD1 mice and find reduced vascularization of the brainstem in comparison to the cerebrum. Thus, VesSAP enables unbiased and scalable quantifications of the angioarchitecture of cleared mouse brains and yields biological insights into the vascular function of the brain.

Changes in cerebrovascular structures are key indicators for a large number of diseases affecting the brain. Primary angiopathies, vascular risk factors (for example, diabetes), traumatic brain injury, vascular occlusion and stroke all affect the function of the brain's vascular network[1–3]. The hallmarks of Alzheimer's disease, including tauopathy and amyloidopathy, can also lead to aberrant remodeling of blood vessels[1,4], allowing capillary rarefaction to be used as a marker for vascular damages[5]. Therefore, quantitative analysis of the entire brain vasculature is pivotal to developing a better understanding of brain function in physiological and pathological states. However, quantifying micrometer-scale changes in the cerebrovascular network of the brain has been difficult for two main reasons.

First, labeling and imaging of the complete mouse brain vasculature down to the smallest blood vessels has not yet been achieved. Magnetic resonance imaging (MRI), micro-computed tomography (micro-CT) and optical coherence tomography do not have sufficient resolution to capture capillaries in bulk tissue[6–8]. Fluorescent microscopy provides higher resolution, but can typically only be applied to tissue sections up to 200 µm in thickness[9]. Recent advances in tissue clearing could overcome this problem[10], but so far there has been no systematic description of all vessels of all sizes in an entire brain in three dimensions (3D).

The second challenge relates to the automated analysis of large 3D imaging datasets with substantial variance in signal intensity and signal-to-noise ratio (SNR) at different depths. Simple intensity- and shape-based filtering approaches such as Frangi's vesselness filters and more advanced image processing methods with local spatial adaptation cannot reliably differentiate vessels from background in whole-brain scans[11,12]. Finally, imaging of the complete vascular network of the brain at capillary resolution results in datasets of terabyte size. Established image processing methods do not scale well to terabyte-sized image volumes, as they do not generalize well to large images, and require intensive manual fine-tuning[13–15].

Here we present VesSAP (Vessel Segmentation & Analysis Pipeline), a deep learning-based method for automated analysis of the entire mouse brain vasculature, overcoming the above limitations. VesSAP encompasses three major steps: (1) staining, clearing and imaging of the mouse brain vasculature down to the capillary level with two different dyes: wheat germ agglutinin (WGA) and Evans blue (EB); (2) automatic segmentation and tracing of the whole-brain vasculature data via CNNs; and (3) extraction of vascular features for hundreds of brain regions after registration of the data to the Allen brain atlas (Fig. 1). Our deep learning-based approach for network extraction in cleared tissue is robust, despite variations in signal intensities and structures, outperforms previous filter-based methods and reaches the quality of segmentation achieved by human annotators. We applied VesSAP to the three commonly used mouse strains C57BL/6J, CD1 and BALB/c.

Results

Vascular staining, DISCO clearing and imaging. To reliably stain the entire vasculature, we used WGA and EB dyes, which can be visualized in different fluorescence channels. We injected EB dye into live mice 12 h before WGA perfusion, allowing its long-term circulation to mark vessels under physiological conditions[16], while we perfused mice with WGA during fixation. We then performed

[1]Institute for Tissue Engineering and Regenerative Medicine (iTERM), Helmholtz Zentrum München, Neuherberg, Germany. [2]Institute for Stroke and Dementia Research (ISD), Ludwig-Maximilians-Universität (LMU), Munich, Germany. [3]Graduate School of Neuroscience (GSN), Munich, Germany. [4]Department of Computer Science, Technical University of Munich (TUM), Munich, Germany. [5]Center for Translational Cancer Research of the TUM (TranslaTUM), Munich, Germany. [6]Munich School of Bioengineering, Technical University of Munich (TUM), Munich, Germany. [7]Institute of Pharmacology and Toxicology, University of Zurich (UZH), Zurich, Switzerland. [8]Munich Cluster for Systems Neurology (SyNergy), Munich, Germany. [9]German Center for Neurodegenerative Diseases (DZNE), Munich, Germany. [10]These authors contributed equally: Mihail Ivilinov Todorov, Johannes Christian Paetzold. [11]These authors jointly supervised this work: Bjoern Menze, Ali Ertürk. ✉e-mail: bjoern.menze@tum.de; erturk@helmholtz-muenchen.de

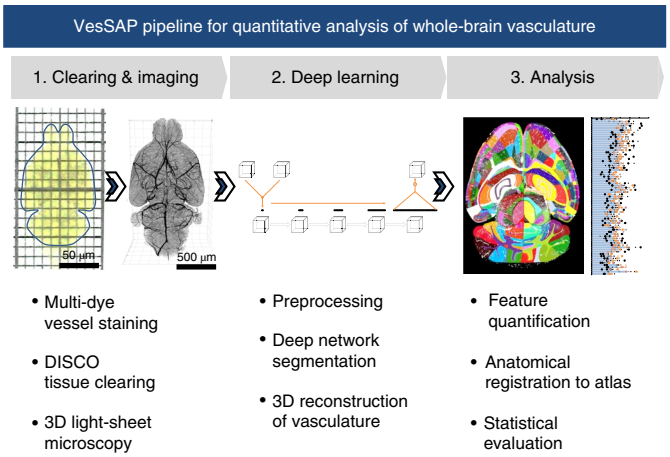

Fig. 1 | Summary of the VesSAP pipeline. The method consists of three modular steps: (1) multi-dye vessel staining and DISCO tissue clearing for high imaging quality using 3D light-sheet microscopy; (2) deep learning-based segmentation of blood vessels with 3D reconstruction; and (3) anatomical feature extraction and mapping of the entire vasculature to the Allen adult mouse brain atlas for statistical analysis.

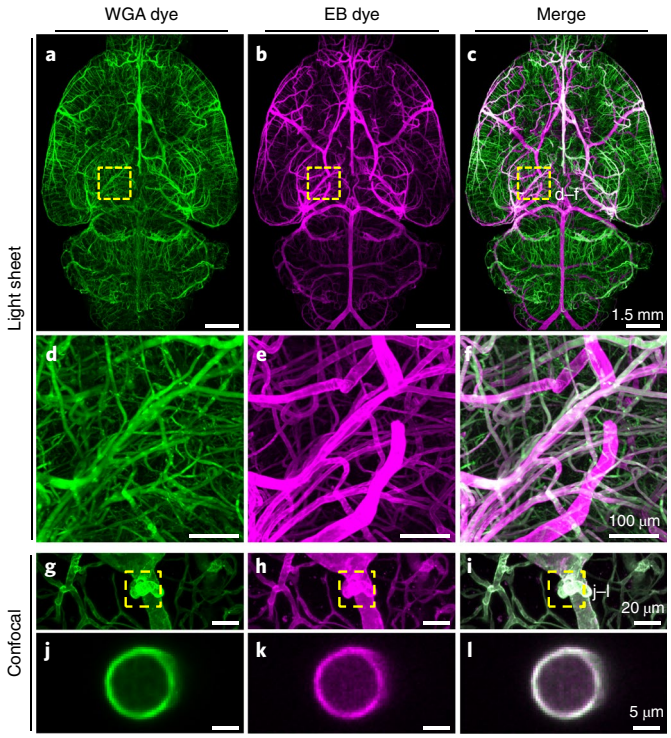

Fig. 2 | Enhancement of vascular staining using two complementary dyes. **a**–**c**, Maximum-intensity projections of automatically reconstructed tiling scans of WGA (**a**) and EB (**b**) signal in the same sample and the merged view (**c**). **d**–**f**, Magnified view of the boxed region in **c**. **g**–**l**, Confocal images of WGA- and EB-stained vessels and vascular wall (**g**–**i**, maximum-intensity projections at 112 µm; **j**–**l**, single slices of 1 µm corresponding to the boxed region in **i**). The experiment was performed on nine different mice with similar results.

3DISCO clearing[17] and light-sheet microscopy imaging of whole mouse brains (Fig. 2a–c and Supplementary Figs. 1 and 2). WGA highlighted microvessels, and EB predominantly stained major blood vessels, such as the middle cerebral artery and the circle of Willis (Fig. 2d–i and Supplementary Fig. 3). Merging the signals from the two dyes yielded more complete staining of the vasculature than relying on individual dyes alone (Fig. 2c,f and Supplementary Video 1). Staining with the two dyes was congruent in midsized vessels, with signals originating from the vessel wall layer (Fig. 2j–l and Supplementary Fig. 3a–c). When using WGA, we reached a higher SNR for microvessels than for bigger vessels. With EB, the SNR for small capillaries was lower but larger vessels reached a high SNR (Supplementary Fig. 4). Integrating the information from the two channels allowed acquisition of the entire vasculature and resulted in optimized SNR. We also compared the fluorescence signal quality of the WGA staining (targeting the complete endothelial glycocalyx lining[18]) to signal for a conventional vessel-specific antibody (anti-CD31, targeting endothelial cell–cell adhesion[19]) and found that WGA produced higher SNR for blood vessels in general (Supplementary Fig. 5).

Segmentation of volumetric images. To enable extraction of quantitative features of the vascular structure, vessels in acquired brain scans need to be segmented in 3D. Motivated by deep learning-based approaches in biomedical image data analysis[20–28], we used a five-layer CNN (Fig. 3a) to exploit the complementary signals of the two dyes to derive complete segmentation of the entire brain vasculature.

In the first step, the two input channels (WGA and EB) were concatenated. This yielded a matrix in which each voxel was characterized by two features. Then, each convolutional step integrated the information from a voxel's 3D neighborhood. We used full 3D convolutions[20] without further down- or upsampling and fewer trainable parameters than, for example, 3D U-Net and V-Net[29,30] to achieve high inference speeds. After the fourth convolution, the information from 50 features per voxel was combined with a convolutional layer with a kernel size of one and sigmoidal activation to estimate the likelihood that a given voxel represented a vessel. Subsequent binarization yielded the final segmentation. In both training and testing, the images were processed in subvolumes of $50 \times 100 \times 100$ pixels.

Deep neural networks often require large amounts of annotated data or many iterations of training. Here we circumvented this requirement with a transfer learning approach[31]. In short, we first pretrained the network on a large, synthetically generated vessel-like dataset (Supplementary Fig. 6)[32] and then refined it on a small number of manually annotated parts of real brain vessel scans. This approach reduced the training iterations on manually annotated training data.

To assess the quality of the segmentation, we compared the VesSAP CNN predictions to manually labeled ground truth and the predictions from alternative computational approaches (Table 1). We report voxel-wise segmentation metrics, namely, accuracy, F1 score[33], Jaccard coefficient and cl-F1, which weights the centerlines and volumes of the vessels (detailed in the Methods). In comparison to the ground truth, our network achieved an accuracy of 0.94 ± 0.01 and an F1 score of 0.84 ± 0.05 (for additional scores, see Table 1; all values are given as the mean $\pm$ s.d.). As controls, we implemented alternative state-of-the-art deep learning and classical methods. Our network outperformed classical Frangi filters[11] (accuracy, 0.85 ± 0.03; F1 score, 0.47 ± 0.18), as well as recent methods based on local spatial context via Markov random fields[13,34] (accuracy, 0.85 ± 0.03; F1 score, 0.48 ± 0.04). VesSAP achieved similar performance in comparison to 3D U-Net and V-Net architectures, which require substantially more trainable parameters (3D U-Net: accuracy, 0.95 ± 0.01; F1 score, 0.85 ± 0.03; V-Net: accuracy, 0.95 ± 0.02; F1 score, 0.86 ± 0.07; no statistical difference in comparison to the VesSAP CNN: two-sided t test, all $P > 0.3$). However, the VesSAP CNN substantially outperformed the other architectures in terms of speed, being ~20 and ~50 times faster in the feedforward path than

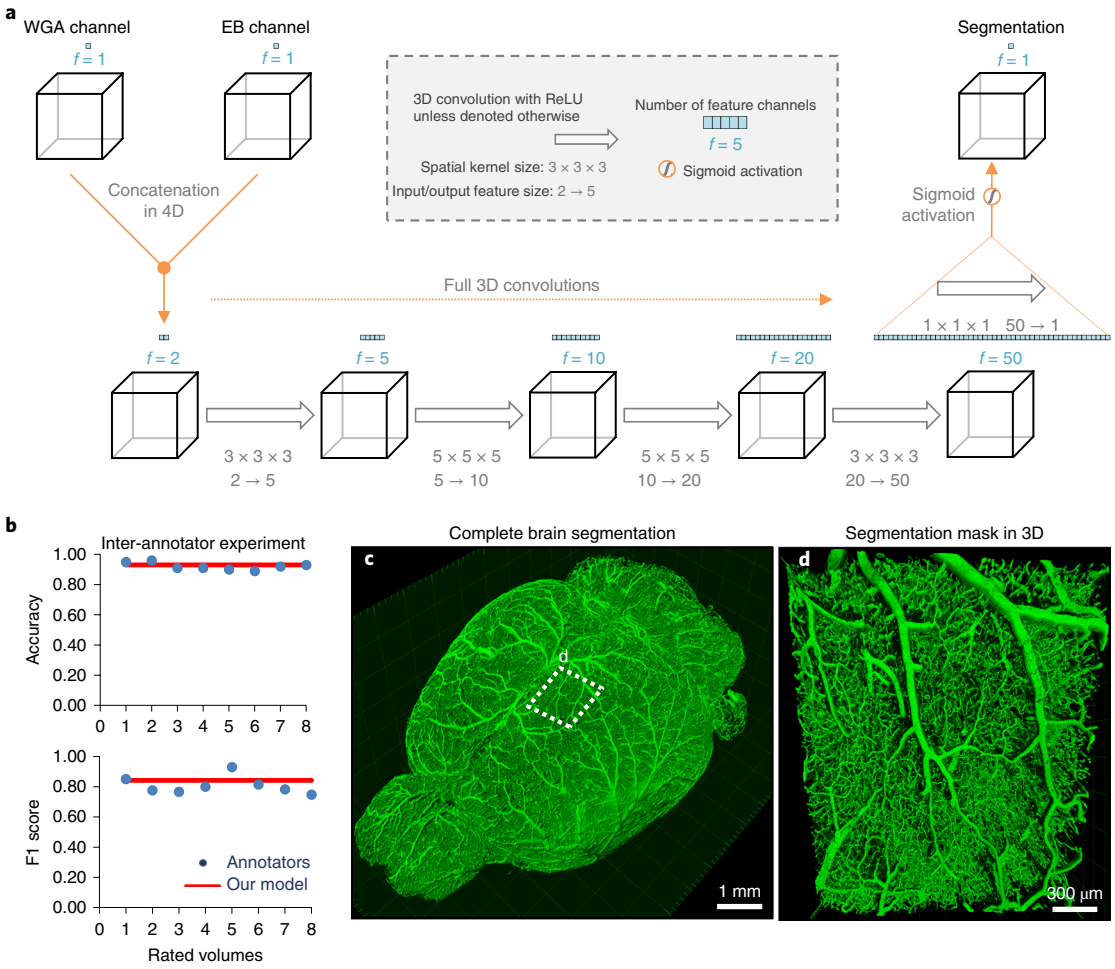

Fig. 3 | Deep learning architecture of VesSAP and performance on vessel segmentation. a, The 3D VesSAP network architecture consisting of five convolutional layers and sigmoid activation for the last layer, including the kernel size and feature size for the input/output. ReLU, rectified linear units. **b**, Accuracy and F1 score for the inter-annotator experiment (blue) as compared to VesSAP (red). **c**, 3D rendering of full brain segmentation from a CD1 mouse. **d**, 3D rendering of the small volume boxed in **c**. The experiment was performed on nine different mice with similar results.

Table 1 | Evaluation metrics of the different segmentation approaches for 75 volumes of 100 × 100 × 50 pixels

Segmentation model	cl-F1	Accuracy	F1 score	Jaccard	Parameters	Speed
VesSAP CNN	**0.93 ± 0.02***	**0.94 ± 0.01**	**0.84 ± 0.05**	**0.84 ± 0.04**	**0.0587 M***	**1.19 s***
VesSAP CNN, trained from scratch	**0.93 ± 0.02**	**0.94 ± 0.01**	**0.85 ± 0.04***	**0.85 ± 0.04**	**0.0587 M***	**1.19 s***
VesSAP CNN, synthetic training data	0.87 ± 0.02	0.90 ± 0.05	0.72 ± 0.07	0.70 ± 0.05	**0.0587 M***	**1.19 s***
3D U-Net	**0.93 ± 0.02**	**0.95 ± 0.01***	**0.85 ± 0.03***	**0.85 ± 0.03**	178.4537 M	61.22 s
V-Net	**0.94 ± 0.02***	**0.95 ± 0.02***	**0.86 ± 0.07***	**0.86 ± 0.07***	88.8556 M	26.87 s
Frangi vesselness	0.84 ± 0.03	0.85 ± 0.03	0.47 ± 0.19	-	-	117.00 s
Markov random field	0.86 ± 0.02	0.85 ± 0.03	0.48 ± 0.04	-	-	24.31 s

All values are given as the mean ± s.d. The best performing algorithms are in bold and highlighted with an asterisk; algorithms whose performance did not differ more than 2% from the best performing algorithms are in bold. The number of trainable parameters for deep learning architectures is given in millions (M).

V-Net and 3D U-Net, respectively. This is particularly important for our large datasets (hundreds of gigabytes). For example, the VesSAP CNN segmented a single brain in 4 h, whereas V-Net and 3D U-Net required 3.3 d and 8 d, respectively. The superior speed of the VesSAP CNN is due to the substantially fewer trainable parameters in its architecture (for example, our implementation of 3D U-Net had ~178 million parameters, whereas the VesSAP CNN had ~0.059 million parameters) (Table 1). Next, we compared the segmentation accuracy of our network to the accuracy of human annotations. A total of four human experts independently annotated two volumes. We found that the inter-annotator accuracy and F1 scores of the experts were comparable to those from the predicted segmentation of our network (human annotators: accuracy, 0.92 ± 0.02; F1 score, 0.81 ± 0.06; Fig. 3b). Notably, we extrapolate that human annotators

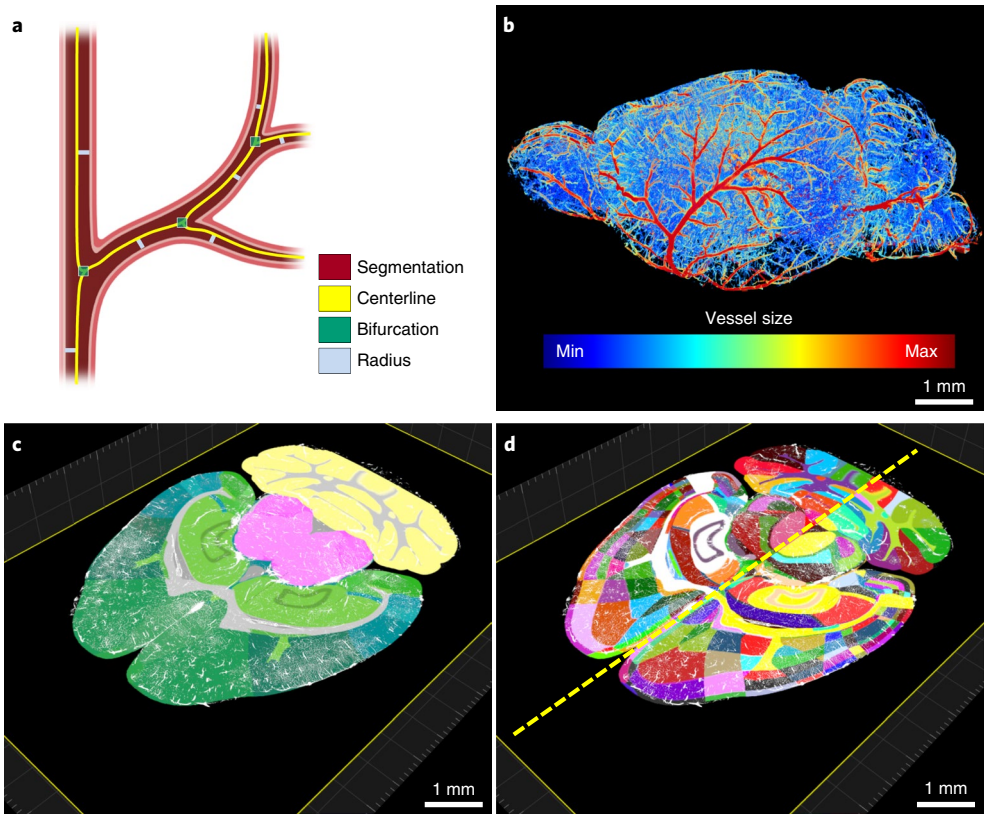

Fig. 4 | Pipeline showing the feature extraction and registration process. a, Representation of the features extracted from vessels. **b**, Radius illustration of the vasculature in a CD1 mouse brain. **c**,**d**, Vascular segmentation results overlaid on the hierarchically (**c**) and randomly (**d**) color-coded atlas to reveal all annotated regions available, including hemispheric difference (dashed line in **d**). The experiment was performed on nine different mice with similar results.

would need more than a year to process a whole brain instead of the 4 h required by our approach. Moreover, we observed differences in the human segmentations due to annotator bias. Thus, the VesSAP CNN can segment the complete brain vasculature consistently at human-level accuracy with a substantially higher speed than currently available methods, enabling high throughput for large-scale analysis.

We show an example of the vasculature from a brain segmented by VesSAP in 3D (Fig. 3c and Supplementary Videos 2 and 3). Zooming in on a smaller patch revealed that the connectivity of the vascular network was fully maintained (Fig. 3d and Supplementary Video 2). Comparing single slices of the imaging data with the predicted segmentation showed that vessels were accurately segmented regardless of absolute illumination or vessel diameter (Supplementary Fig. 7).

Feature extraction and atlas registration. Vessel lengths and radii and the number of bifurcation points are commonly used to describe the angioarchitecture[2]. Hence, we used our segmentation to quantify these features as distinct parameters to characterize the mouse brain vasculature (Fig. 4a and Supplementary Video 4). We evaluated the local vessel length (length normalized to the size of the brain region of interest), local bifurcation density (sum of the occurrences normalized to the size of the brain region of interest) and local vessel radius (average radius along the full length) of blood vessels in different brain regions.

We report the vascular features in three ways to enable comparison with various previous studies that differed in the measures used (Supplementary Fig. 8). More specifically, first, we provide the count of segmented voxels as compared to total voxels within a specific brain region (voxel space). Second, we provide the measurements by calculating the voxel size of our imaging system and accounting for the Euclidean length (microscopic space). Third, we corrected the microscopic measurements to account for tissue shrinkage caused by the clearing process (anatomical space)[35,36] (Supplementary Tables 2–10). We calculated this shrinkage rate by measuring the same mouse brain volume with MRI before clearing.

Here we use the anatomical space to report our specific biological findings, as it is closest to the physiological state. For the average blood vessel length of the whole brain, we found a value of 545.74 ± 94 mm per mm^3 (mean ± s.d.). Because our method quantifies brain regions separately, we could compare our results to the literature, which mostly reports either quantifications for specific brain regions or extrapolations to the whole brain from regional quantifications. For example, a vascular length of 922 ± 176 mm per mm^3 (mean ± s.d.) was previously reported for cortical regions (size of $508 \times 508 \times 1{,}500$ µm^3)[10]. We found a similar vessel length for the same region in the mouse cortex (C57BL/6J mice: 913 ± 110 mm per mm^3), substantiating the accuracy of our method. We performed additional comparisons to other reports (Supplementary Table 11). Moreover, we compared the measurements acquired with our algorithms to manually labeled ground truth data and found deviations of 8.21% for centerlines, 13.18% for the number of bifurcation points and 16.33% for the average radius. These deviations were substantially lower than the average deviation among human annotators (Methods).

We quantified and visualized vessel radius along the entire vascular network (Fig. 4b). After extracting vascular features for the whole brain with VesSAP, we registered the volume to the Allen brain atlas (Supplementary Videos 5 and 6). This allowed us to map the segmented vasculature and corresponding features topographically to distinct anatomical brain regions (Fig. 4c). Each anatomical

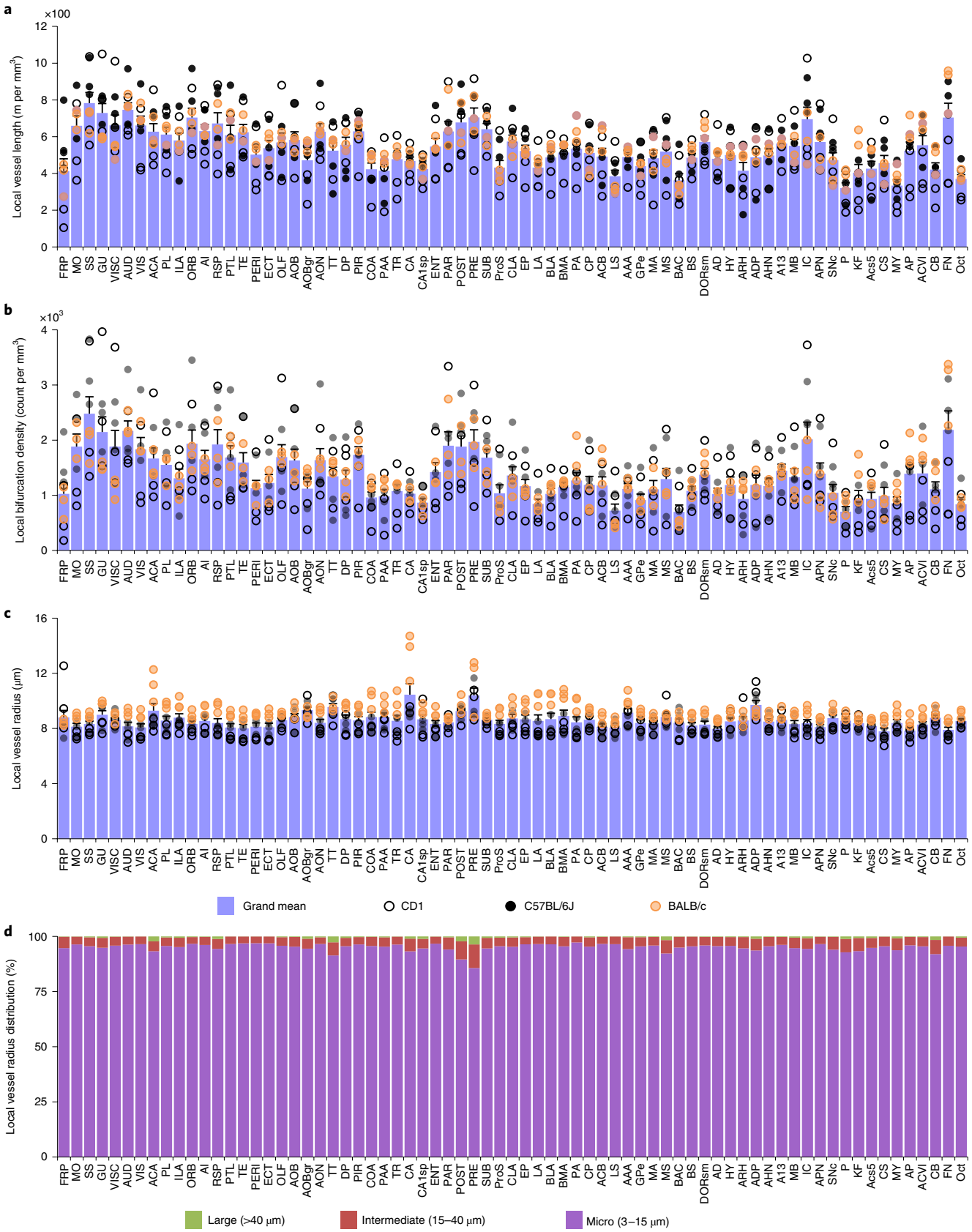

Fig. 5 | Anatomical properties of the neurovasculature in adult mouse brain mapped to the Allen brain atlas clusters. a–c, Representations of the local vessel length (**a**), density of bifurcations (**b**) and average radius (**c**) in each of the 71 main anatomical clusters of the Allen brain atlas. Open, black and orange circles denote measurements in the CD1, C57BL/6J and BALB/c strains, respectively; each circle represents a single mouse. Data are given as the mean ± s.e.m.; $n = 3$ mice per strain. **d**, Local distribution of large, intermediate and microvessels in the same anatomical clusters. Abbreviations are defined in Supplementary Table 1.

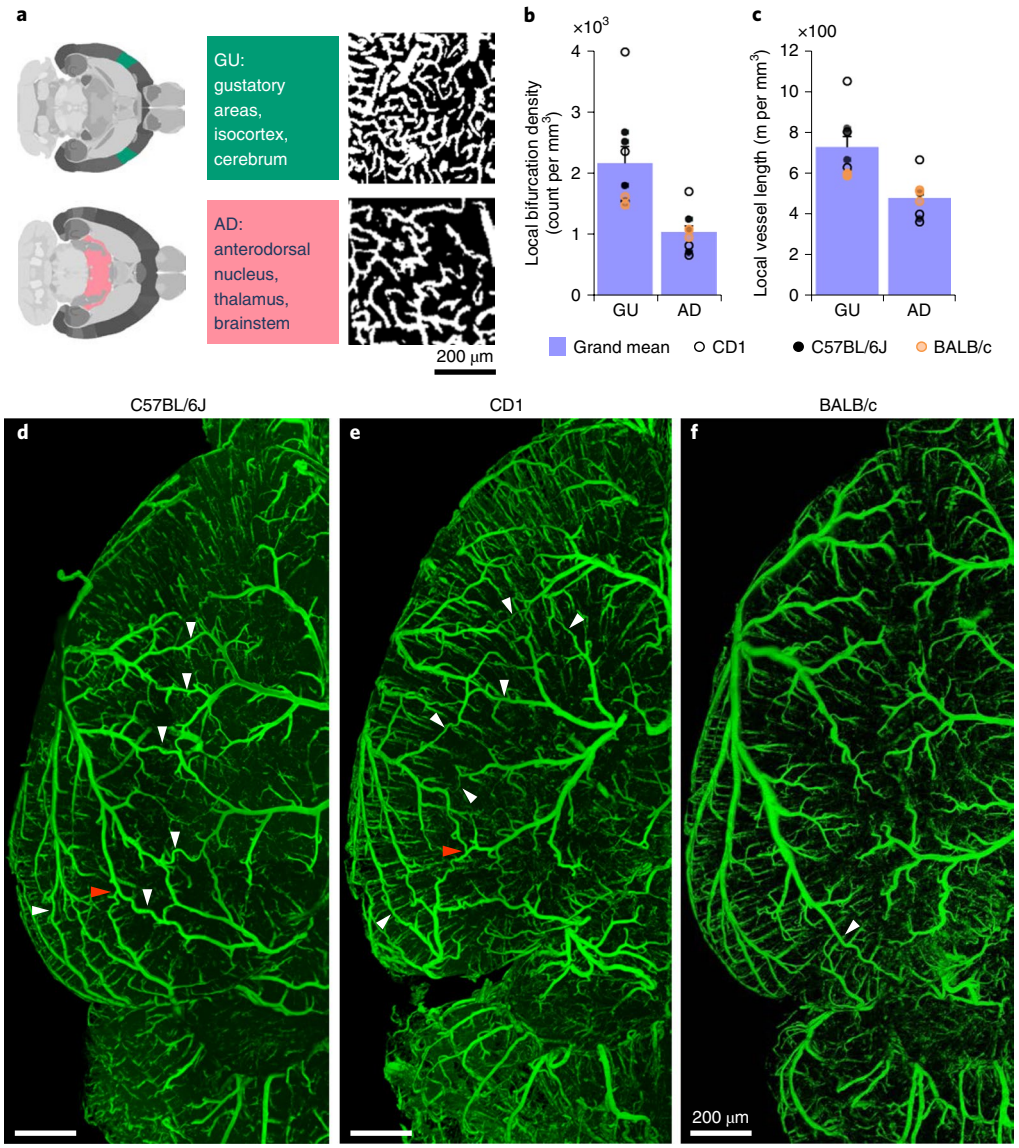

Fig. 6 | Exemplary quantitative analysis enabled by VesSAP. a, Respective locations of the anterodorsal nucleus (AD) and gustatory areas (GU) in the mouse brain (left) and maximum-intensity projections of representative volumes from segmentation of these areas ($600 \times 600 \times 33\,\mu m^3$) (right). **b**,**c**, Quantification of the bifurcation density (**b**) and local vessel length (**c**) for the anterodorsal nucleus and gustatory area clusters. CD1 mice are shown by open circles, BALB/C mice by orange circles and C57BL/6J mice by black circles. Values are the mean ± s.e.m.; $n = 3$ mice per strain. **d**–**f**, Images of the vasculature in representative C57BL/6J (**d**), CD1 (**e**) and BALB/c (**f**) mice, where white arrowheads indicate anastomoses between major arteries. Direct vascular connections between the medial cerebral artery, the anterior cerebral artery and the posterior cerebral artery are indicated by red arrowheads. The experiment was performed three times with similar results.

region could be further divided into subregions, yielding a total of 1,238 anatomical structures (619 per hemisphere) for the entire mouse brain (Fig. 4d). This allowed analysis of each denoted brain region and grouping of regions into clusters such as left versus right hemisphere, gray versus white matter, or any hierarchical cluster of the Allen brain atlas ontology. For our subsequent statistical feature analysis, we grouped the labeled structures according to the 71 main anatomical clusters of the current Allen brain atlas ontology. We thus provide the whole mouse brain vascular map with extracted vessel lengths, bifurcation points and radii down to the capillary level.

VesSAP provides a reference map of the whole brain vasculature in mice. By studying whole brain vasculature in the C57BL/6J, CD1 and BALB/c strains ($n = 3$ mice for each strain), we found that the local vessel length and local bifurcation density differed in the same brain over different regions, while they were highly correlated among different mice for the same regions (Fig. 5a,b). Furthermore, the local bifurcation density was highly correlated with the local vessel length in most brain regions (Supplementary Fig. 9), and the average vessel radius was evenly distributed in different regions of the same brain (Fig. 5c). In addition, the extracted features showed no statistical difference (by Cohen's *d*; Supplementary Table 12) for the same anatomical cluster across the strains (Supplementary Fig. 9). Finally, microvessels made up the overwhelming majority of the total vascular composition in all brain regions (Fig. 5d). We visually inspected exemplary brain regions to validate the output of VesSAP. Both VesSAP and visual inspection revealed that the gustatory areas had a higher vascular length per volume than the anterodorsal nucleus (Fig. 6a–c). Visual inspection also suggested that the number of capillaries was the primary reason for regional feature variations within the same brain.

Finally, VesSAP offered insights into the neurovascular structure of the different mouse strains in our study. There were direct intracranial vascular anastomoses in the C57BL/6J, CD1 and BALB/c strains (white arrowheads in Fig. 6d–f). The anterior cerebral artery, middle cerebral artery and posterior cerebral artery were connected at the dorsal visual cortex in CD1 mice (red arrowheads in Fig. 6d,e) unlike in the BALB/c strain[33] (Fig. 6f).

Discussion

VesSAP can generate reference maps of the adult mouse brain vasculature, which can potentially be used to model synthetic cerebrovascular networks[37]. In addition to the metrics we obtain to describe the vasculature, advanced metrics, for example, Strahler values, network connectivity and bifurcation angles, can be extracted by using the data generated by VesSAP. Furthermore, the centerlines and bifurcation points can be interpreted as the edges and nodes for building a full vascular network graph, offering a means for studying local and global properties of the cerebrovascular network in the future.

The VesSAP workflow relies on staining of blood vessels by two different dyes. WGA binds to the glycocalyx of the endothelial lining of blood vessels[38] but may miss some segments of large vessels[18]. EB is a dye with a high affinity for serum albumin[35,36,39]; thus, it remains in the large vessels after a short perfusion protocol. In addition, EB labeling is not affected by subsequent DISCO clearing.

Vessels have long and thin tubular shapes. In our images, the radii of capillaries (about 3 µm) are in the range of our voxel size. Therefore, segmentation that yields the correct diameter down to single-pixel resolution poses a challenge, as we observed a 16% deviation for the radius. This subpixel deviation did not pose a problem for segmenting the whole vasculature network and extracting features because the vascular network can be defined by its centerlines and bifurcations.

The described segmentation concept is based on a transfer learning approach, where we pretrained the CNN and refined it on a small labeled dataset of 11% of the synthetic dataset and only 0.02% of one cleared brain. We consider this to be a major advantage in comparison to training from scratch. Thus, our CNN might generalize well to different types of imaging data (such as micro-CT angiography) or other curvilinear structures (for example, neurons), as only a small labeled dataset is needed to adjust our pretrained network.

On the basis of our vascular reference map, unknown vascular properties can be discovered and biological models can be confirmed. VesSAP showed a high number of collaterals in albino CD1 mice. Such collaterals between large vessels can substantially alter the outcome of ischemic stroke lesions: blood-deprived brain regions arising from occlusion of a large vessel can be compensated by blood supply from the collateral extensions of other large vessels[33,40]. Therefore, our VesSAP method can lead to the discovery of previously unknown anatomical details that could be functionally relevant.

In conclusion, VesSAP is a scalable, modular and automated machine learning-based method to analyze complex imaging data from cleared mouse brains. We foresee that our method will accelerate the applications of tissue clearing, in particular for studies assessing brain vasculature.

Online content

Any methods, additional references, Nature Research reporting summaries, source data, extended data, supplementary information, acknowledgements, peer review information; details of author contributions and competing interests; and statements of data and code availability are available at https://doi.org/10.1038/s41592-020-0792-1.

Received: 19 April 2019; Accepted: 14 February 2020;
Published online: 11 March 2020

References

1. Bennett, R. E. et al. Tau induces blood vessel abnormalities and angiogenesis-related gene expression in P301L transgenic mice and human Alzheimer's disease. *Proc. Natl Acad. Sci. USA* **115**, E1289–E1298 (2018).
2. Obenaus, A. et al. Traumatic brain injury results in acute rarefication of the vascular network. *Sci. Rep.* **7**, 239 (2017).
3. Völgyi, K. et al. Chronic cerebral hypoperfusion induced synaptic proteome changes in the rat cerebral cortex. *Mol. Neurobiol.* **55**, 4253–4266 (2018).
4. Klohs, J. et al. Contrast-enhanced magnetic resonance microangiography reveals remodeling of the cerebral microvasculature in transgenic ArcAbeta mice. *J. Neurosci.* **32**, 1705–1713 (2012).
5. Edwards-Richards, A. et al. Capillary rarefaction: an early marker of microvascular disease in young hemodialysis patients. *Clin. Kidney J.* **7**, 569–574 (2014).
6. Calabrese, E., Badea, A., Cofer, G., Qi, Y. & Johnson, G. A. A diffusion MRI tractography connectome of the mouse brain and comparison with neuronal tracer data. *Cereb. Cortex* **25**, 4628–4637 (2015).
7. Dyer, E. L. et al. Quantifying mesoscale neuroanatomy using X-ray microtomography. *eNeuro* **4**, ENEURO.0195-17.2017 (2017).
8. Li, T., Liu, C. J. & Akkin, T. Contrast-enhanced serial optical coherence scanner with deep learning network reveals vasculature and white matter organization of mouse brain. *Neurophotonics* **6**, 035004 (2019).
9. Tsai, P. S. et al. Correlations of neuronal and microvascular densities in murine cortex revealed by direct counting and colocalization of nuclei and vessels. *J. Neurosci.* **29**, 14553–14570 (2009).
10. Lugo-Hernandez, E. et al. 3D visualization and quantification of microvessels in the whole ischemic mouse brain using solvent-based clearing and light sheet microscopy. *J. Cereb. Blood Flow Metab.* **37**, 3355–3367 (2017).
11. Frangi, A. F., Niessen, W. J., Vincken, K. L. & Viergever, M. A. in *International Conference on Medical Image Computing and Computer-Assisted Intervention* 130–137 (Springer, 1998).
12. Sato, Y. et al. Three-dimensional multi-scale line filter for segmentation and visualization of curvilinear structures in medical images. *Med. Image Anal.* **2**, 143–168 (1998).
13. Di Giovanna, A. P. et al. Whole-brain vasculature reconstruction at the single capillary level. *Sci. Rep.* **8**, 12573 (2018).
14. Xiong, B. et al. Precise cerebral vascular atlas in stereotaxic coordinates of whole mouse brain. *Front. Neuroanat.* **11**, 128 (2017).
15. Clark, T. A. et al. Artery targeted photothrombosis widens the vascular penumbra, instigates peri-infarct neovascularization and models forelimb impairments. *Sci. Rep.* **9**, 2323 (2019).
16. Yao, J., Maslov, K., Hu, S. & Wang, L. V. Evans blue dye—enhanced capillary-resolution photoacoustic microscopy in vivo. *J. Biomed. Opt.* **14**, 054049 (2009).
17. Ertürk, A. et al. Three-dimensional imaging of solvent-cleared organs using 3DISCO. *Nat. Protoc.* **7**, 1983–1995 (2012).
18. Reitsma, S. et al. Endothelial glycocalyx structure in the intact carotid artery: a two-photon laser scanning microscopy study. *J. Vasc. Res.* **48**, 297–306 (2011).
19. Schimmenti, L. A., Yan, H. C., Madri, J. A. & Albelda, S. M. Platelet endothelial cell adhesion molecule, PECAM-1, modulates cell migration. *J. Cell. Physiol.* **153**, 417–428 (1992).
20. Tetteh, G. et al. DeepVesselNet: vessel segmentation, centerline prediction, and bifurcation detection in 3-D angiographic volumes. Preprint at https://arxiv.org/abs/1803.09340 (2018).
21. Weigert, M. et al. Content-aware image restoration: pushing the limits of fluorescence microscopy. *Nat. Methods* **15**, 1090–1097 (2018).
22. Wang, H. et al. Deep learning enables cross-modality super-resolution in fluorescence microscopy. *Nat. Methods* **16**, 103–110 (2019).
23. Falk, T. et al. U-Net: deep learning for cell counting, detection, and morphometry. *Nat. Methods* **16**, 67–70 (2019).
24. Caicedo, J. C. et al. Data-analysis strategies for image-based cell profiling. *Nat. Methods* **14**, 849–863 (2017).
25. Dorkenwald, S. et al. Automated synaptic connectivity inference for volume electron microscopy. *Nat. Methods* **14**, 435–442 (2017).
26. Liu, S., Zhang, D., Song, Y., Peng, H. & Cai, W. in *Machine Learning in Medical Imaging* (eds., Wang, Q. et al.) 185–193 (Springer International Publishing, 2017).
27. Long, J., Shelhamer, E. & Darrell, T. Fully convolutional networks for semantic segmentation. in *Proceedings of the IEEE Conference on Computer Vision and Pattern Recognition* 3431–3440 (IEEE, 2015).
28. Livne, M. et al. A U-Net deep learning framework for high performance vessel segmentation in patients with cerebrovascular disease. *Front. Neurosci.* **13**, 97 (2019).
29. Çiçek, Ö., Abdulkadir, A., Lienkamp, S. S., Brox, T. & Ronneberger, O. 3D U-Net: learning dense volumetric segmentation from sparse annotation. in *Medical Image Computing and Computer-Assisted Intervention* 424–432 (2016).
30. Milletari, F., Navab, N. & Ahmadi, S.A. V-Net: fully convolutional neural networks for volumetric medical image segmentation. in *2016 Fourth International Conference on 3D Vision* 565–571 (IEEE, 2016).

31. Litjens, G. et al. A survey on deep learning in medical image analysis. *Med. Image Anal.* **42**, 60–88 (2017).
32. Schneider, M., Reichold, J., Weber, B., Szekely, G. & Hirsch, S. Tissue metabolism driven arterial tree generation. *Med. Image Anal.* **16**, 1397–1414 (2012).
33. Chalothorn, D., Clayton, J. A., Zhang, H., Pomp, D. & Faber, J. E. Collateral density, remodeling, and VEGF-A expression differ widely between mouse strains. *Physiol. Genomics* **30**, 179–191 (2007).
34. Li, S. Z. In *Computer Vision—ECCV* (ed., Eklundh, J.-O.) 361–370 (Springer, 1994).
35. Pan, C. et al. Shrinkage-mediated imaging of entire organs and organisms using uDISCO. *Nat. Methods* **13**, 859–867 (2016).
36. Cai, R. et al. Panoptic imaging of transparent mice reveals whole-body neuronal projections and skull–meninges connections. *Nat. Neurosci.* **22**, 317–327 (2019).
37. Menti, E., Bonaldi, L., Ballerini, L., Ruggeri, A. & Trucco, E. In *International Workshop on Simulation and Synthesis in Medical Imaging* 167–176 (Springer, Year).
38. Kataoka, H. et al. Fluorescent imaging of endothelial glycocalyx layer with wheat germ agglutinin using intravital microscopy. *Microsc. Res. Tech.* **79**, 31–37 (2016).
39. Steinwall, O. & Klatzo, I. Selective vulnerability of the blood–brain barrier in chemically induced lesions. *J. Neuropathol. Exp. Neurol.* **25**, 542–559 (1966).
40. Zhang, H., Prabhakar, P., Sealock, R. & Faber, J. E. Wide genetic variation in the native pial collateral circulation is a major determinant of variation in severity of stroke. *J. Cereb. Blood Flow Metab.* **30**, 923–934 (2010).

Methods

Tissue preparation. Animal experiments were conducted according to institutional guidelines (Klinikum der Universität München/Ludwig Maximilian University of Munich), after approval of the ethical review board of the government of Upper Bavaria (Regierung von Oberbayern, Munich, Germany), and in accordance with European directive 2010/63/EU for animal research. Animals were housed under a 12-h light/12-h dark cycle. For this study, we injected 150 µl (2% (vol/vol) in saline) EB dye (Sigma-Aldrich, E2129) intraperitoneally into 3-month-old male mice from the C57BL/6J, CD1 and BALB/c strains (Charles River, strain codes 027, 482 and 028, respectively; $n = 3$ mice per strain). Twelve hours after injection of EB dye, we anesthetized the animals with a combination of midazolam, medetomidine and fentanyl (administered intraperitoneally; 1 ml per 100 g body weight containing 5 mg, 0.5 mg and 0.05 mg per kg body weight, respectively) and opened their chest for transcardial perfusion. Medium with WGA (0.25 mg WGA conjugated to Alexa Fluor 594 dye (Thermo Fisher Scientific, W11262) in 150 µl PBS, pH 7.2) was supplied by peristaltic pump set to deliver the medium at a rate of 8 ml min^{-1}, along with 15 ml of 1× PBS and 15 ml of 4% paraformaldehyde. This short perfusion protocol was established on the basis of preliminary experiments, where both WGA and EB staining were partially washed out (data not shown), with the goal of delivering fixative to brain tissue via the vessels to achieve a homogenous preservation effect[41].

After perfusion, brains were extracted from the neurocranium while severing some of the segments of the circle of Willis, which is an inevitable component of most retrieval processes aside from corrosion cast techniques. Next, the samples were incubated in 3DISCO clearing solutions as described[17]. Briefly, we immersed them in a gradient of tetrahydrofuran (Sigma-Aldrich, 186562): 50%, 70%, 80% and 90% (in distilled water) followed by 100%, at 25 °C for 12 h at each concentration. At this point, we modified the protocol by incubating the samples in *tert*-butanol for 12 h at 35 °C followed by immersion in dichloromethane (Sigma-Aldrich, 270997) for 12 h at room temperature and a final incubation with refractive index-matched BABB solution (benzyl alcohol + benzyl benzoate, 1:2; Sigma-Aldrich, 24122 and W213802), for at least 24 h at room temperature until transparency was achieved. Each incubation step was carried out on a laboratory shaker.

Imaging of cleared samples with light-sheet microscopy. We used a ×4 objective lens (Olympus XLFLUOR 340) equipped with an immersion-corrected dipping cap mounted on a LaVision UltraII microscope coupled to a white-light laser module (NKT SuperK Extreme EXW-12) for imaging. Images were taken with 16-bit depth and at a nominal resolution of 1.625 µm per voxel on the *x* and *y* axes. For ×12 imaging, we used a LaVision objective (×12/0.53 NA MI PLAN with an immersion-corrected dipping cap). Brain structures were visualized by Alexa Fluor 594 (using a 580/25-nm excitation filter and a 625/30-nm emission filter) and EB fluorescent dye (using a 640/40-nm excitation filter and a 690/50-nm emission filter) in sequential order. We maximized the SNR for each dye independently to avoid saturation of differently sized vessels when only a single channel was used. We achieved this by independently optimizing the excitation power so that the strongest signal in major vessels did not exceed the dynamic range of the camera. In the *z* dimension, we took sectional images in 3-µm steps while using left- and right-sided illumination. Our measured resolution was 2.83 µm × 2.83 µm × 4.99 µm for *x*, *y* and *z*, respectively (Supplementary Fig. 2). To reduce defocus, which derives from the Gaussian shape of the beam, we used 12-step sequential shifting of the focal position of the light sheet per plane and side. The thinnest point of the light sheet was 5 µm.

Imaging of cleared samples with confocal microscopy. Additionally, the cleared specimens were imaged with an inverted laser-scanning confocal microscope (Zeiss, LSM 880) for further analysis. Before imaging, samples were mounted by placing them onto the glass surface of a 35-mm glass-bottom Petri dish (MatTek, P35G-0-14-C) and immersed in BABB. A ×40 oil-immersion objective lens was used (Zeiss, ECPlan-NeoFluar ×40/1.30 NA Oil DIC M27, WD = 0.21 mm). Images were acquired with the settings for Alexa Fluor 594 (using excitation at 561 nm and an emission range of 585–733 nm) and EB fluorescent dye (using excitation at 633 nm and an emission range of 638–755 nm) in sequential order.

Magnetic resonance imaging. We used a nanoScan PET/MR device (3 Tesla, Mediso Medical Imaging Systems) equipped with a head coil for murine heads to acquire anatomical scans in the T1 modality.

Reconstruction of the datasets from tiling volumes. We stitched the acquired volumes by using TeraStitcher's automatic global optimization function (v1.10.3). We produced volumetric intensity images of the whole brain while considering each channel separately. To improve alignment to the Allen brain atlas, we downscaled our dataset in the *xy* plane to achieve pseudouniform voxel spacing matching the *z* plane.

Deep learning network architecture. We relied on a deep 3D CNN for segmentation of our blood vessel dataset. The network's general architecture consists of five convolutional layers, four with ReLU (rectified linear units) followed by one convolutional layer with sigmoid activation (Fig. 3a). The input layer is designed to take *n* images as input. In the implemented case, the input to the first layer of the network comprised $n = 2$ images of the same brain, which had been stained differently (Fig. 3a). To specifically account for the general class imbalance (much more tissue background than vessel signal) in our dataset and the potential for high false-positive rates associated with this, we chose the generalized soft-Dice as the loss function to our network. At all levels, we used full 3D convolutional kernels (Fig. 3a).

The network's training is driven by an Adam optimizer with a learning rate of 1×10^{-5} and an exponential decay rate of 0.9 for the first moment and 0.99 for the second moment[42]. A prediction or segmentation with a trained model takes volumetric images of arbitrary size as input and outputs a probabilistic segmentation map of identical size. To deal with volumes of arbitrary size and extension, we processed them in smaller subvolumes of $100 \times 100 \times 50$ pixels in size. The algorithms were implemented by using the Tensorflow framework and KERAS[43]. They were trained and tested on two NVIDIA Quadro P5000 GPUs and on machines with 64 GB and 512 GB of RAM.

Transfer learning. Typically, supervised learning tasks in biomedical imaging are aggravated by the scarce availability of labeled training data. Our transfer learning approach aims to circumvent this problem by pretraining our models on synthetically generated data and refining them on a small set of real images[44]. Specifically, our approach pretrains the VesSAP CNN on 3D volumes of vascular image data, synthetically generated together with the corresponding training labels by using the approach of Schneider and colleagues[45]. The pretraining is carried out on a dataset of 20 volumes of $325 \times 304 \times 600$ pixels in size for 38 epochs. During pretraining, we applied a learning rate of 1×10^{-4}. Afterward, the pretrained model was fine-tuned by retraining on a real microscopic dataset consisting of 11 volumes of $500 \times 500 \times 50$ pixels in size. The image volumes were manually annotated by commissioned experts, including the expert who previously prepared the samples and operated the microscope. The labels were verified and further refined in consensus by two additional human raters. The data we used in this fine-tuning step amounted to 11% of the volume of the synthetic datasets and only 0.02% of the voxel volume of a single whole brain. For the fine-tuning step, we used a learning rate of 1×10^{-5}. The final model was obtained after training on the real dataset for six epochs. This training was substantially shorter than training from scratch, where we trained the same VesSAP CNN architecture for 72 epochs until we reached the best F1 score on the validation set. The labeled dataset consisted of 17 volumes of $500 \times 500 \times 50$ pixels from five mouse brains. Three of these brains were from the CD1 strain, and two were from the C57BL/6J strain. The volumes were chosen from regions throughout the whole brain, to represent the variability in the vascular dataset in terms of both vessel shape and illumination. To ensure independence, volumes for the training set and test/validation set were chosen from independent brains. All datasets included brains from the two strains. Our training dataset consisted of 11 volumes, the validation dataset of 3 volumes and the test dataset of 3 volumes. We cross-tested on our test and validation datasets by rotating these. The volumes were processed during training and inference in 25 small subvolumes of $100 \times 100 \times 50$ pixels.

We observed an average F1 score of 0.84 ± 0.02 (mean ± s.d.), an average accuracy of 0.94 ± 0.01 (mean ± s.d.) and an average Jaccard coefficient of 0.84 ± 0.04 (mean ± s.d.) on our test datasets (Fig. 3b). We tested the statistical significance of differences among the top three learning methods (the VesSAP CNN, V-Net and 3D U-Net) by using paired *t* tests. We found that the differences in F1 score were not statistically significant (all $P > 0.3$, rejecting the hypothesis of different distributions).

Because the F1 score, accuracy and Jaccard coefficient are all voxel-wise volumetric scores and can fall short in evaluating the connectedness of components, we developed the cl-F1 score. cl-F1 is calculated from the intersection of centerlines and vessel volumes and not from volumes only, as the traditional F1 score is[46]. To determine this score, we first calculated the intersection of the centerline of our prediction with the labeled volume and then calculated the intersection of the labeled volume's centerline with the predicted volume. Next, we treated the first intersection as recall, as it is susceptible to false negatives, and the second intersection as precision, as it is susceptible to false positives, and input this into the traditional F1 score formulation:

$$\mathrm{F1} = 2 \times \frac{\mathrm{precision} \times \mathrm{recall}}{\mathrm{precision} + \mathrm{recall}} \quad (1)$$

We report an average cl-F1 score of 0.93 ± 0.02 (mean ± s.d.) on the test set.

All scores are given as mean and s.d. Our model reached the best model selection point on the validation dataset after six epochs of training.

Comparison to 3D U-Net and V-Net. To compare our proposed architecture to different segmentation architectures, we implemented V-Net and 3D U-Net, both of which use more complex CNNs with substantially more trainable parameters, which further include down- and upsampling. While our experiments showed that 3D U-Net and V-Net reached marginally higher performance scores, the differences were not statistically significant (two-sided *t* test, $P > 0.3$). The amount

of parameters for these tools makes them 51 and 23 times slower than VesSAP during the inference stage. For segmentation of one of our large whole-brain datasets, this translated to 4 h for VesSAP versus 8 d for 3D U-Net and 3.8 d for V-Net. This difference was also prevalent in the number of trainable parameters. The VesSAP CNN had 0.058 million parameters, whereas 3D U-Net consisted of more than 178 million and V-Net of more than 88 million parameters. Furthermore, the light VesSAP CNN already reached human-level performance. We therefore consider the problem of vessel segmentation as solved by the VesSAP CNN for our data. It should be mentioned that the segmentation network is a modular building block of the overall VesSAP pipeline and can be chosen by each user according to his or her own preferences and, importantly, according to the computational power available.

Preprocessing of segmentation. Preprocessing factors into the overall success of the training and segmentation. The intensity distribution among brains and among brain regions differs substantially. To account for intensity distributions, two preprocessing strategies were applied successively.

1. High-cut filter. In this step, the intensities x above a certain threshold c are set to c; c is defined by a global percentile. Next, they were normalized by $f(x)$.

$$g(x) = \begin{cases} c, & x > c \\ x, & x \leq c \end{cases} \quad (2)$$

2. Normalization of intensities. The original intensities were normalized to a range of 0 to 1, where x was the pixel intensity and X was all intensities for the volume.

$$f(x) = \frac{x - \min(X)}{\max(X) - \min(X)} \quad (3)$$

Inter-annotator experiment for segmentation. To compare VesSAP's segmentation to human-level annotations, we implemented an inter-annotator experiment. For this experiment, we determined a gold-standard label (ground truth) for two volumes of 500×500×50 pixels from a commissioned group of three experts, including the expert who imaged our data and was therefore most familiar with the images. Next, we gave the two volumes to four other experts to label the complete vasculature. The experts spent multiple hours labeling each patch in the ImageJ and ITK-snap environment and were allowed to use their favored approaches to generate what they considered to be the most accurate labeling. Finally, we calculated the accuracy and F1 scores for the different annotators, as compared to the gold standard, and compared them to the scores for our model (Table 1).

Feature extraction. To quantify the anatomy of the mouse brain vasculature, we extracted descriptive features on the basis of our segmentation. First, we calculated the features in voxel space. Later, we registered them to the Allen brain atlas.

As features we extracted the centerlines, the bifurcation points and the radii of the segmented blood vessels. We consider these features to be independent from the elongation of the light-sheet scans and the connectedness of the vessels due to staining, imaging and/or segmentation artifacts.

Our centerline extraction was based on a 3D thinning algorithm[47]. Before extracting the centerlines, we applied two cycles of binary erosion and dilation to remove false-negative pixels within the volume of segmented vessels, as these would induce false centerlines. On the basis of the centerlines, we extracted bifurcation points. A bifurcation was the branching point on a centerline where a larger vessel split into two or more smaller vessels (Fig. 4a). In a network analysis context, bifurcations are meaningful as they represent the nodes of a vascular network[48]. Furthermore, bifurcation points have relevance in a biological context. In neurodegenerative diseases, capillaries are known to degenerate[49], thereby substantially reducing the number of bifurcation points in an affected brain region as compared to healthy brain. Next, we implemented an algorithm to detect bifurcation points. We achieved this by calculating the surrounding pixels for every point on each centerline and determined whether a point was a centerline. The radius of a blood vessel is a key feature to describe vascular networks. The radius yields information about the flow and hierarchy of the vessel network. The proposed algorithm calculates the Euclidean distance transform for every segmented pixel v to the closest background pixel b_{closest}. Next, the distance transform matrix is multiplied by the 3D centerline mask, equaling the minimum radius of the vessel around the centerline.

$$d(v, b_{\text{closest}}) = \sqrt{\sum_{1}^{3} (v_i - b_{\text{closest},i})^2} \quad (4)$$

Feature quantification. Here we describe in detail how we calculated the features between the three different spaces.

Voxel space to microscopic space. To quantify the length of our vessels in SI units instead of voxels, we calculated their Euclidean length, which depends on the direction of the connection of skeleton pixels (Supplementary Fig. 9). To calculate the Euclidean length of our centerlines, we carried out a connected component analysis, which transformed each pixel of the skeleton into an element of an undirected weighted graph, where zero weight means no connection and non-zero weights denote the Euclidean distance between two voxels (considering 26 connectivity). Thus, we obtained a large and sparse adjacency matrix. An element-wise summation of such a matrix provides the total Euclidean length of the vascular network along the extracted skeleton.

As measuring connected components is computationally very expensive, we calculated the Euclidean length of the centerlines for 12 representative volumes of 500×500×50 pixels and divided by the number of skeleton pixels. We calculated an average Euclidean length ε_{Cl} of 1.3234 ± 0.0063 voxels (mean ± s.d.) per centerline element. This corresponds to a length of 3.9701 ± 0.0188 µm (mean ± s.d.) in cleared tissue. Because the s.d. of this measurement was low, at less than 0.5% of the length, we applied this correction factor to the whole brain centerline measurements. This correction does not apply to the bifurcation points and our radius statistics, as bifurcations are independent of length and also radius extraction returns a Euclidean distance by default. Depending on the direction of the connection of skeleton pixels, the Euclidean length of a skeleton pixel is different (Supplementary Fig. 9).

Microscopic space to anatomical space. To account for tissue shrinkage (Supplementary Fig. 9), which is inherent to DISCO clearing, we carried out an experiment to measure the degree of shrinkage. Before clearing, we imaged the brains of three live BALB/c mice by MRI and calculated each brain's average volume, through precise manual segmentation by an expert. Next, we cleared three BALB/c brains, processed them with VesSAP and measured the total brain volume with atlas alignment. We report an average volume of 423.84 ± 2.04 mm³ for the live mice and 255.62 ± 6.57 mm³ for the cleared tissue. This corresponds to a total volume shrinkage of 39.69%. We applied this as a correction factor for the volumetric information (for example, for brain regions).

Similarly to previous studies, shrinkage was uniform in all three dimensions. This is important when considering shrinkage in one dimension, as needed to account for the shrinkage in centerlines and radii. The one-dimensional correction factor K_{L} then corresponds to the cube root of the volumetric correction factor K_{V}.

Accounting for these factors, we calculated the vessel length per volume (Z) in cleared (Z_{cleared}) and real (Z_{real}) tissue in equation (5), where $N_{\text{V,vox}}$ is the number of total voxels in the reference volume and $N_{\text{Cl,vox}}$ is the number of centerline voxels in the image volume:

$$Z_{\text{cleared}} = \frac{N_{\text{Cl,vox}}}{N_{\text{V,vox}}} \times \varepsilon_{\text{Cl}} \quad Z_{\text{real}} = \frac{N_{\text{Cl,vox}}}{N_{\text{V,vox}}} \times \varepsilon_{\text{Cl}} \times \frac{\kappa_{\text{L}}}{\kappa_{\text{V}}} \quad (5)$$

Similarly, we calculated the bifurcation density (B) in cleared and real tissue in equation (6), where $N_{\text{Bif,vox}}$ is the number of bifurcations in the reference volume:

$$B_{\text{cleared}} = \frac{N_{\text{Bif,vox}}}{N_{\text{V,vox}}} \quad B_{\text{real}} = \frac{N_{\text{Bif,vox}}}{N_{\text{V,vox}}} \times \frac{1}{\kappa_{\text{V}}} \quad (6)$$

Please note that the voxel spacing of 3 µm has to be taken into consideration when reporting features in SI units.

Inter-annotator experiment for features. To estimate the error in VesSAP's feature quantification, we extracted the features on a labeled test set of five volumes of 500×500×50 pixels. When comparing to the gold-standard label, we calculated errors (disagreements) of 8.21% for the centerlines, 13.18% for the number of bifurcation points and 16.33% for the average radius. To compare VesSAP's extracted features to human-level annotation, we implemented an inter-annotator experiment. For this experiment, we had four annotators label the vessels and radii in two volumes of 500×500×50 pixels by using ImageJ and ITK-snap. Finally, we calculated the agreement of the extracted features between all annotators and compared to the gold-standard labeling.

We calculated this for each of the volumes and found an average error (disagreement) of 34.62% for the radius, 25.20% for the bifurcation count and 12.55% for the centerline length.

The agreement between the VesSAP output and the gold standard was higher than the average agreement between the annotators and the gold standard. This difference underlines the quality and reproducibility of VesSAP's feature extraction.

Registration to the reference atlas. We used the average template, the annotation file and the latest ontology file (Ontology ID: 1) of the current Allen mouse brain atlas: CCFv3 201710. Then, we scaled the template and the annotation file up from 10 to 3 µm³ to match our reconstructed brain scans and multiplied the left side of the (still symmetrical) annotation file by −1 so that the labels could be later assigned to the corresponding hemispheres. Next, the average template and 3D vascular datasets were downsampled to 10% of their original size in each dimension to achieve reasonably fast alignment with the elastix toolbox[50] (v4.9.0). For the sake of the integrity of the extracted features, we aligned the template to each of the brain scans individually by using a two-step rigid and deformable registration (B-spline; optimizer, AdaptiveStochasticGradientDescent; metric, AdvancedMattesMutualInformation; grid spacing in physical units, 90; in the VesSAP repository, we host the log and parameter files for each brain scan) and applied the transformation parameters to the full-resolution annotation volume

(3-µm resolution). Subsequently, we created masks for the anatomical clusters on the basis of the current Allen brain atlas ontology.

Statistical analysis of features. Data collection and analysis were not performed with blinding to the strains. Data distribution was assumed to be normal, although this was not formally tested. All data values of the descriptive statistics are given as mean ± s.e.m. unless stated otherwise. Data were analyzed with standardized effect size indices (Cohen's *d*)[51] to investigate differences in vessel length, number of bifurcation points and radii between brain areas across the three mouse strains ($n = 3$ mice per strain). Descriptive statistics were evaluated across brain regions in the pooled ($n = 9$) dataset.

Data visualization. All volumetric datasets were rendered with Imaris, Vision4D and ITK-snap.

Reporting Summary. Further information on research design is available in the Nature Research Reporting Summary linked to this article.

Data availability

VesSAP data are publicly hosted at http://DISCOtechnologies.org/VesSAP and include original scans and registered atlas data.

Code availability

VesSAP codes are publicly hosted at http://DISCOtechnologies.org/VesSAP and include the imaging protocol, trained algorithms, training data and a reference set of features describing the vascular network in all brain regions. Additionally, the source code is hosted on GitHub (https://github.com/vessap/vessap) and on the executable platform Code Ocean (https://doi.org/10.24433/CO.1402016.v1)[52]. Implementation of external libraries is available on request.

References

41. Breckwoldt, M. O. et al. Correlated magnetic resonance imaging and ultramicroscopy (MR-UM) is a tool kit to assess the dynamics of glioma angiogenesis. *eLife* **5**, e11712 (2016).
42. Kingma, D. P. & Ba, J. Adam: a method for stochastic optimization. Preprint at https://arxiv.org/abs/1412.6980 (2017).
43. Abadi, M. et al. in *12th USENIX Symposium on Operating Systems Design and Implementation* 265–283 (2016).
44. Hoo-Chang, S. et al. Deep convolutional neural networks for computer-aided detection: CNN architectures, dataset characteristics and transfer learning. *IEEE Trans. Med. Imaging* **35**, 1285–1298 (2016).
45. Schneider, M., Hirsch, S., Weber, B., Székely, G. & Menze, B. H. Joint 3-D vessel segmentation and centerline extraction using oblique Hough forests with steerable filters. *Med. Image Anal.* **19**, 220–249 (2015).
46. Paetzold, J. C. et al. clDice—a novel connectivity-preserving loss function for vessel segmentation. in *Medical Imaging Meets NeurIPS 2019 Workshop* (2019).
47. Lee, T. C., Kashyap, R. L. & Chu, C. N. Building skeleton models via 3-D medial surface axis thinning algorithms. *Graph. Models Image Process.* **56**, 462–478 (1994).
48. Rempfler, M. et al. Reconstructing cerebrovascular networks under local physiological constraints by integer programming. *Med. Image Anal.* **25**, 86–94 (2015).
49. Marchesi, V. T. Alzheimer's dementia begins as a disease of small blood vessels, damaged by oxidative-induced inflammation and dysregulated amyloid metabolism: implications for early detection and therapy. *FASEB J.* **25**, 5–13 (2011).
50. Klein, S., Staring, M., Murphy, K., Viergever, M. A. & Pluim, J. P. Elastix: a toolbox for intensity-based medical image registration. *IEEE Trans. Med. Imaging* **29**, 196–205 (2009).
51. Cohen, J. The effect size index: *d*. *Stat. Power Anal. Behav. Sci.* **2**, 284–288 (1988).
52. Paetzold, J. C. & Tetteh, G. VesSAP: machine learning analysis of whole mouse brain vasculature. *Code Ocean* https://doi.org/10.24433/CO.1402016.v1 (2020).

Acknowledgements

This work was supported by the Vascular Dementia Research Foundation, Deutsche Forschungsgemeinschaft (DFG, German Research Foundation) under Germany's Excellence Strategy within the framework of the Munich Cluster for Systems Neurology (EXC 2145 SyNergy, ID 390857198), ERA-Net Neuron (01EW1501A to A.E.), Fritz Thyssen Stiftung (to A.E.; reference no. 10.17.1.019MN), a DFG research grant (to A.E.; reference no. ER 810/2-1), the Helmholtz ICEMED Alliance (to A.E.), the NIH (to A.E.; reference no. AG057575) and the German Federal Ministry of Education and Research via the Software Campus initiative (to O.S.). S.S. is supported by the Translational Brain Imaging Training Network (TRABIT) under the European Union's Horizon 2020 research and innovation program (grant agreement ID 765148). Furthermore, NVIDIA supported this work via the GPU Grant Program. V.E. was funded by Human Brain Project (HBP SGA 2, 785907). M.I.T. is a member of the Graduate School of Systemic Neurosciences (GSN), Ludwig Maximilian University of Munich. We thank R. Cai, C. Pan, F. Voigt, I. Ezhov, A. Sekuboyina, M. Goergens, F. Hellal, R. Malik, U. Schillinger and T. Wang for technical advice and C. Heisen for critical reading of the manuscript.

Author contributions

M.I.T. performed the tissue processing, clearing and imaging experiments. M.I.T. and K.T.-V. developed the whole-brain staining protocol. M.I.T. stitched and assembled the whole-brain scans. V.E. and J.C.P. generated the synthetic vascular training dataset. J.C.P., G.T. and O.S. developed the deep learning architecture and trained the models. J.C.P. and S.S. performed the quantitative analyses. M.I.T. annotated the data. M. Düring and M. Dichgans helped with data interpretation. B.M., M.P. and G.T. provided guidance in developing the deep learning architecture and helped with data interpretation. A.E., M.I.T., B.M. and J.C.P. wrote the manuscript. All authors edited the manuscript. A.E. initiated and led all aspects of the project.

Competing interests

The authors declare no competing interests.

Additional information

Supplementary information is available for this paper at https://doi.org/10.1038/s41592-020-0792-1.

Correspondence and requests for materials should be addressed to B.M. or A.E.

Peer review information Nina Vogt was the primary editor on this article and managed its editorial process and peer review in collaboration with the rest of the editorial team.

Reprints and permissions information is available at www.nature.com/reprints.

nature research

Corresponding author(s): Ali Ertürk, Bjoern Menze

Last updated by author(s): Feb 14, 2020

Reporting Summary

Nature Research wishes to improve the reproducibility of the work that we publish. This form provides structure for consistency and transparency in reporting. For further information on Nature Research policies, see Authors & Referees and the Editorial Policy Checklist.

Statistics

For all statistical analyses, confirm that the following items are present in the figure legend, table legend, main text, or Methods section.

n/a	Confirmed	
☐	☒	The exact sample size (*n*) for each experimental group/condition, given as a discrete number and unit of measurement
☐	☒	A statement on whether measurements were taken from distinct samples or whether the same sample was measured repeatedly
☐	☒	The statistical test(s) used AND whether they are one- or two-sided *Only common tests should be described solely by name; describe more complex techniques in the Methods section.*
☒	☐	A description of all covariates tested
☐	☒	A description of any assumptions or corrections, such as tests of normality and adjustment for multiple comparisons
☐	☒	A full description of the statistical parameters including central tendency (e.g. means) or other basic estimates (e.g. regression coefficient) AND variation (e.g. standard deviation) or associated estimates of uncertainty (e.g. confidence intervals)
☒	☐	For null hypothesis testing, the test statistic (e.g. *F*, *t*, *r*) with confidence intervals, effect sizes, degrees of freedom and *P* value noted *Give P values as exact values whenever suitable.*
☒	☐	For Bayesian analysis, information on the choice of priors and Markov chain Monte Carlo settings
☒	☐	For hierarchical and complex designs, identification of the appropriate level for tests and full reporting of outcomes
☐	☒	Estimates of effect sizes (e.g. Cohen's *d*, Pearson's *r*), indicating how they were calculated

Our web collection on statistics for biologists contains articles on many of the points above.

Software and code

Policy information about availability of computer code

Data collection	ImspectorPro [v 5.1] was used for collecting light-sheet images, Zen black [v 10.0] for confocal images and Nucline [v 3.0] for MRI data.
Data analysis	Python [v 2.7 & 3.6], MATLAB [v 9.3], elastix [v 4.9], ITK-SNAP [v 3.6], ImageJ [v 1.52p], Imaris [v 9.3] and Vision4D [v 3.1] were used. Custom codes was used in the study were used for vascular segmentation, mapping and quantification. The description of the software is available in the Method section of the manuscript. The custom codes are publicly available on http://DISCOtechnologies.org/VesSAP

For manuscripts utilizing custom algorithms or software that are central to the research but not yet described in published literature, software must be made available to editors/reviewers. We strongly encourage code deposition in a community repository (e.g. GitHub). See the Nature Research guidelines for submitting code & software for further information.

Data

Policy information about availability of data

All manuscripts must include a data availability statement. This statement should provide the following information, where applicable:

- Accession codes, unique identifiers, or web links for publicly available datasets
- A list of figures that have associated raw data
- A description of any restrictions on data availability

The data that support the findings of this study are publicly available on http://DISCOtechnologies.org/VesSAP

Field-specific reporting

Please select the one below that is the best fit for your research. If you are not sure, read the appropriate sections before making your selection.

☒ Life sciences ☐ Behavioural & social sciences ☐ Ecological, evolutionary & environmental sciences

For a reference copy of the document with all sections, see nature.com/documents/nr-reporting-summary-flat.pdf

Life sciences study design

All studies must disclose on these points even when the disclosure is negative.

Sample size	Sample sizes for this reproducibility study were determined based on the literatures in the fields. Statistics were not used to predetermine sample sizes.
Data exclusions	No animals were excluded from the study. Specific brain regions in Figure 5a-d were excluded based on visual inspection (zero vascular length), because some regions were damaged and distorted during dissection so that vessels in these regions were not annotated.
Replication	The protocols in the study were replicated successfully more than 5 times in independent experiments. Tissue-clearing, imaging, vascular segmentation, mapping and quantification procedures were performed in nine mouse brains.
Randomization	Within each strain, animals were randomly selected.
Blinding	No blinding was done because knowledge of experimental conditions were required during data collection.

Reporting for specific materials, systems and methods

We require information from authors about some types of materials, experimental systems and methods used in many studies. Here, indicate whether each material, system or method listed is relevant to your study. If you are not sure if a list item applies to your research, read the appropriate section before selecting a response.

Materials & experimental systems

n/a	Involved in the study
☒	☐ Antibodies
☒	☐ Eukaryotic cell lines
☒	☐ Palaeontology
☐	☒ Animals and other organisms
☒	☐ Human research participants
☒	☐ Clinical data

Methods

n/a	Involved in the study
☒	☐ ChIP-seq
☒	☐ Flow cytometry
☐	☒ MRI-based neuroimaging

Animals and other organisms

Policy information about studies involving animals; ARRIVE guidelines recommended for reporting animal research

Laboratory animals	This study used male mice from the C57BL/6J, CD1 and BALB/c strains at the age of 3 months.
Wild animals	The study did not involve wild animals.
Field-collected samples	This study did not involve a field-collected samples.
Ethics oversight	The experiments were done after approval of the ethical review board of the government of Upper Bavaria (Regierung von Oberbayern, Munich, Germany), and in accordance with the European directive 2010/63/EU for animal research.

Note that full information on the approval of the study protocol must also be provided in the manuscript.

Magnetic resonance imaging

Experimental design

Design type	No functional MRI (fMRI) data were acquired.
Design specifications	None.
Behavioral performance measures	None.

Acquisition

Imaging type(s)	Structural MRI.
Field strength	3T
Sequence & imaging parameters	An average of six T1 scans (3D Gradient Echo sequence with TE/TR/flip angle=5.12/14.88/10, a slice thickness = 0.2 mm and 0.1667x0.1667 mm in plane resolution) was created to get a high resolution structural image of the brain.
Area of acquisition	Whole-brain in-vivo.

Diffusion MRI ☐ Used ☒ Not used

Preprocessing

Preprocessing software	None.
Normalization	No normalization was done to ensure the precise anatomical size measurements of the tissue.
Normalization template	None.
Noise and artifact removal	None.
Volume censoring	No volume censoring was performed.

Statistical modeling & inference

Model type and settings	None.
Effect(s) tested	None.

Specify type of analysis: ☒ Whole brain ☐ ROI-based ☐ Both

Statistic type for inference (See Eklund et al. 2016)	None.
Correction	None.

Models & analysis

n/a	Involved in the study
☒	☐ Functional and/or effective connectivity
☒	☐ Graph analysis
☒	☐ Multivariate modeling or predictive analysis

nature methods

SUPPLEMENTARY INFORMATION

https://doi.org/10.1038/s41592-020-0792-1

In the format provided by the authors and unedited.

Machine learning analysis of whole mouse brain vasculature

Mihail Ivilinov Todorov[1,2,3,10], Johannes Christian Paetzold[4,5,6,10], Oliver Schoppe[4,5], Giles Tetteh[4], Suprosanna Shit[4,5,6], Velizar Efremov[4,7], Katalin Todorov-Völgyi[2], Marco Düring[2,8], Martin Dichgans[2,8,9], Marie Piraud[4], Bjoern Menze[4,5,6,11] ✉ and Ali Ertürk[1,2,8,11] ✉

[1]Institute for Tissue Engineering and Regenerative Medicine (iTERM), Helmholtz Zentrum München, Neuherberg, Germany. [2]Institute for Stroke and Dementia Research (ISD), Ludwig-Maximilians-Universität (LMU), Munich, Germany. [3]Graduate School of Neuroscience (GSN), Munich, Germany. [4]Department of Computer Science, Technical University of Munich (TUM), Munich, Germany. [5]Center for Translational Cancer Research of the TUM (TranslaTUM), Munich, Germany. [6]Munich School of Bioengineering, Technical University of Munich (TUM), Munich, Germany. [7]Institute of Pharmacology and Toxicology, University of Zurich (UZH), Zurich, Switzerland. [8]Munich Cluster for Systems Neurology (SyNergy), Munich, Germany. [9]German Center for Neurodegenerative Diseases (DZNE), Munich, Germany. [10]These authors contributed equally: Mihail Ivilinov Todorov, Johannes Christian Paetzold. [11]These authors jointly supervised this work: Bjoern Menze, Ali Ertürk. ✉e-mail: bjoern.menze@tum.de; erturk@helmholtz-muenchen.de

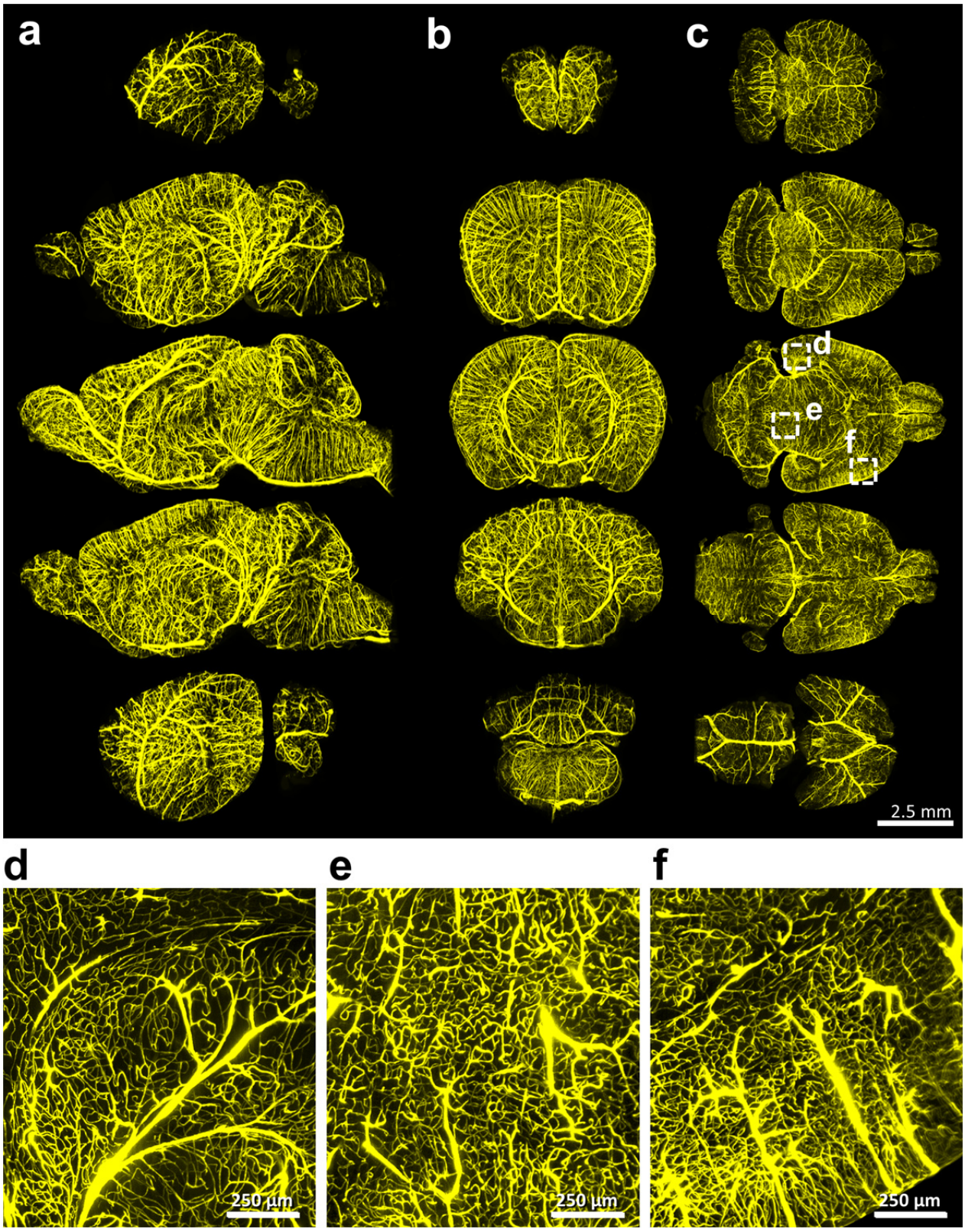

Supplementary Figure 1
Vasculature of a CD1 mouse, stained with WGA and EB.

a, Sagittal maximum intensity projections. **b,** Coronal maximum intensity projections. **c,** Axial maximum projections. **d-f**, Close-ups where capillary level staining is evident. The experiment was performed 9 times with similar results.

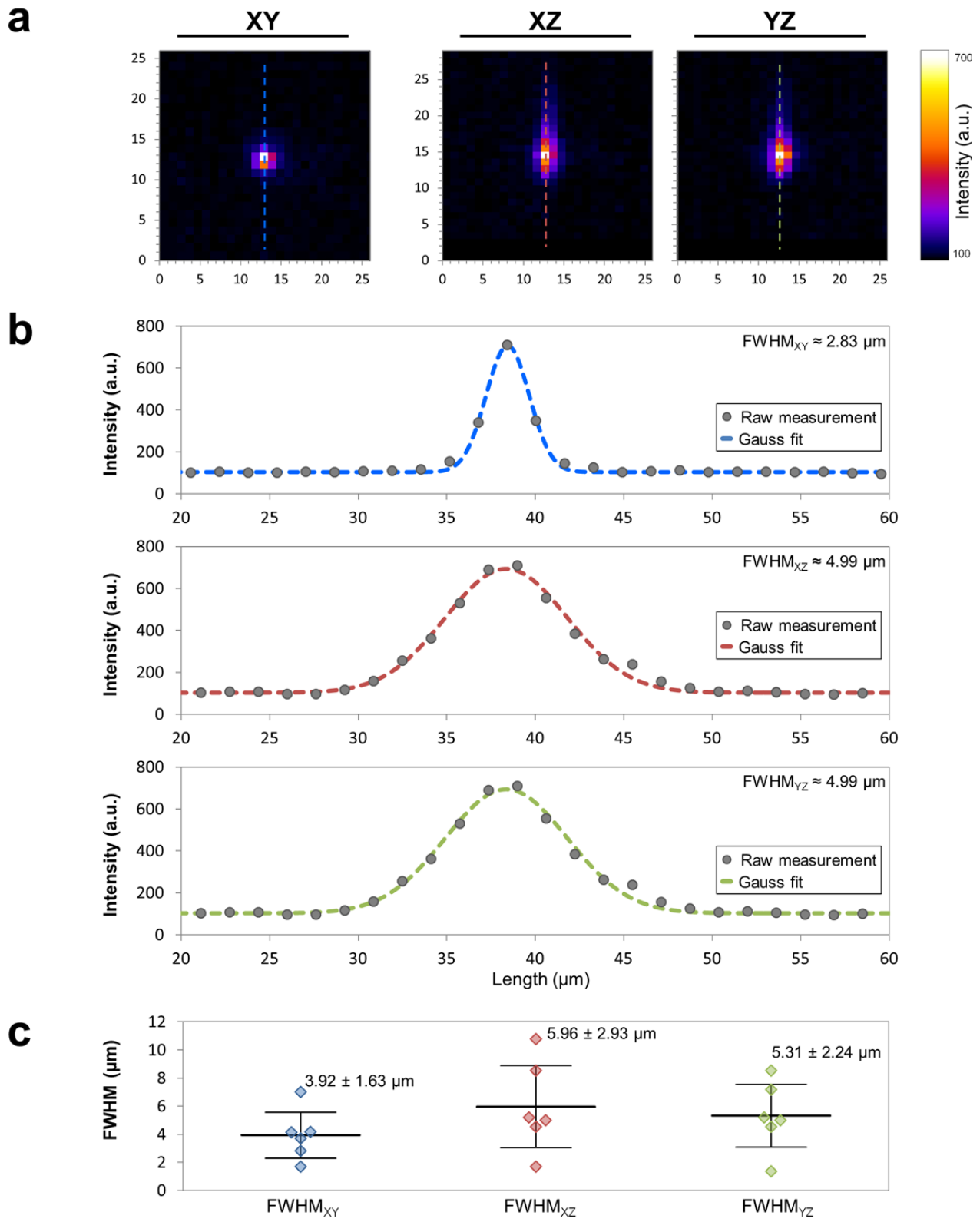

Supplementary Figure 2
Experimental measurement of the point spread function (PSF) of the LaVision light-sheet Ultramicroscope II.

a, Red fluorescent beads (diameter 0.1 µm) were embedded in 1% agarose gel and cleared using 3DISCO. The beads were then imaged in BABB medium (RI = 1.56) using 4× objective lens (Olympus XLFLUOR 340), at 580/25 nm excitation and with a 625/30 nm emission filter by sampling at 1.625 × 1.625 × 1 µm. **b,** Full width half maximum (FWHM) measure derived from the Gaussian fit to the intensity profile, along the indicated cross-sections in the center of the diffraction pattern (a) of an exemplary bead. **c,** Quantification of the PSF distribution (n = 6) derived from the Gaussian fittings. All data values are given as mean ± SEM.

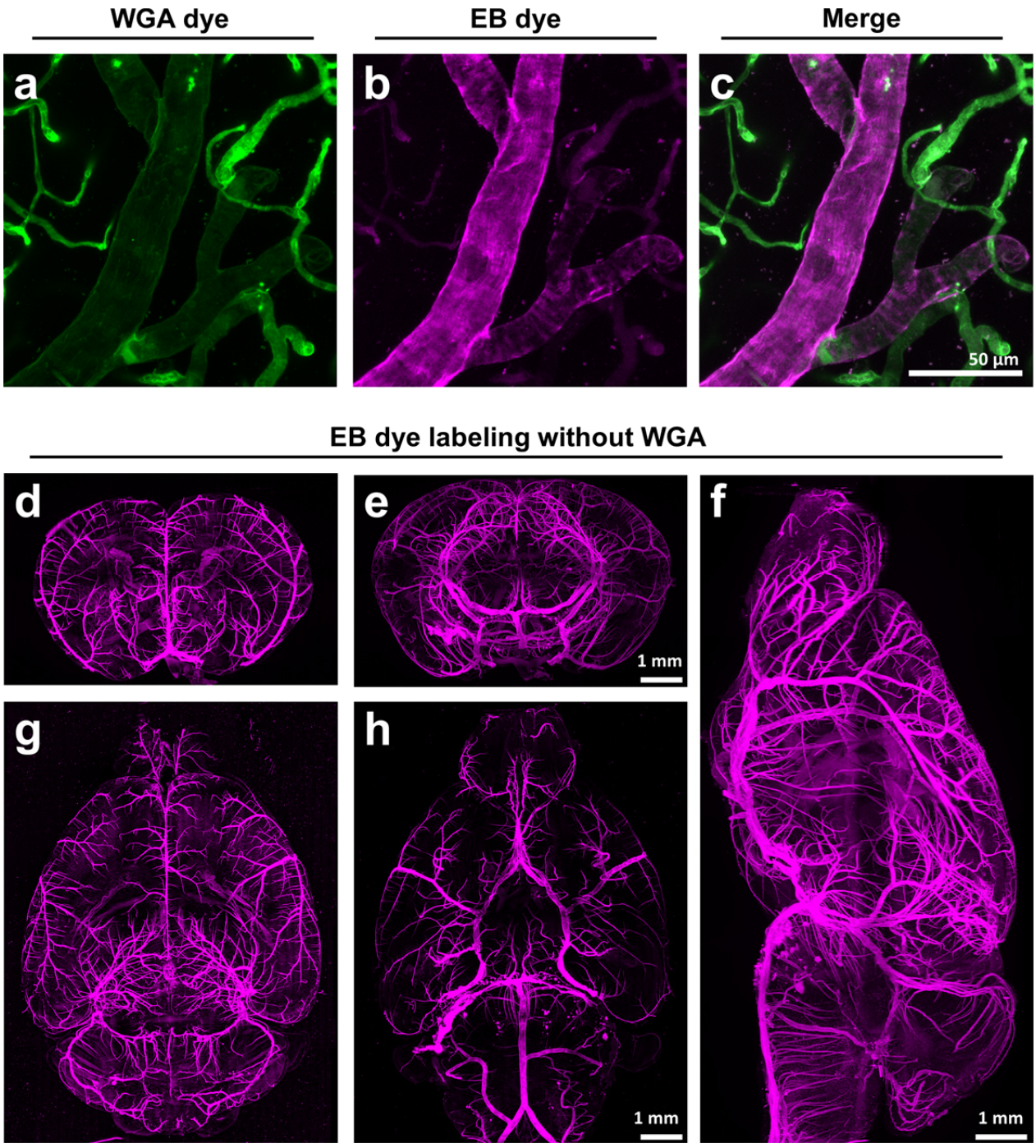

Supplementary Figure 3

Validation of complimentary staining of the neurovasculature.
a,b, Maximum intensity projection of confocal microscopy imaging of WGA and EB signal respectively. **c,** Merging of the two signals. **d-h,** Maximum intensity projections of the light-sheet microscopy imaging of a representative C57BL/6J specimen stained with EB, showing the major vascular segments in different planes. The experiment was performed 3 times with similar results.

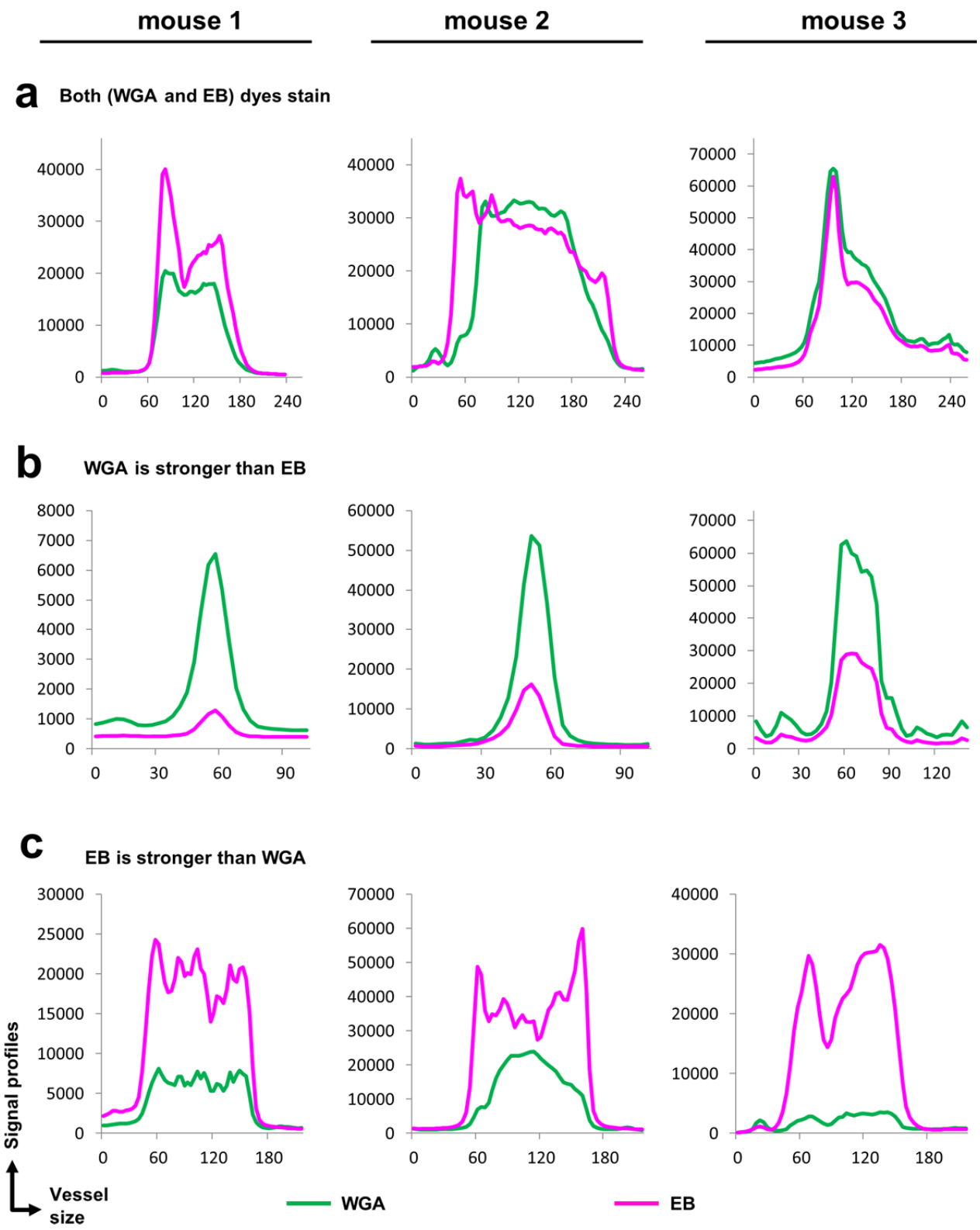

Supplementary Figure 4

Raw signal intensity distribution along line profiles across stained vessels for three animals.
Fluorescence signal profiles for WGA and EB plotted based on vessel size. Data are separated based on WGA and EB signal intensity: a) comparable WGA and EB signal intensity, b) Signal intensity is stronger for WGA than for EB, c) Signal intensity is stronger for EB than for WGA.

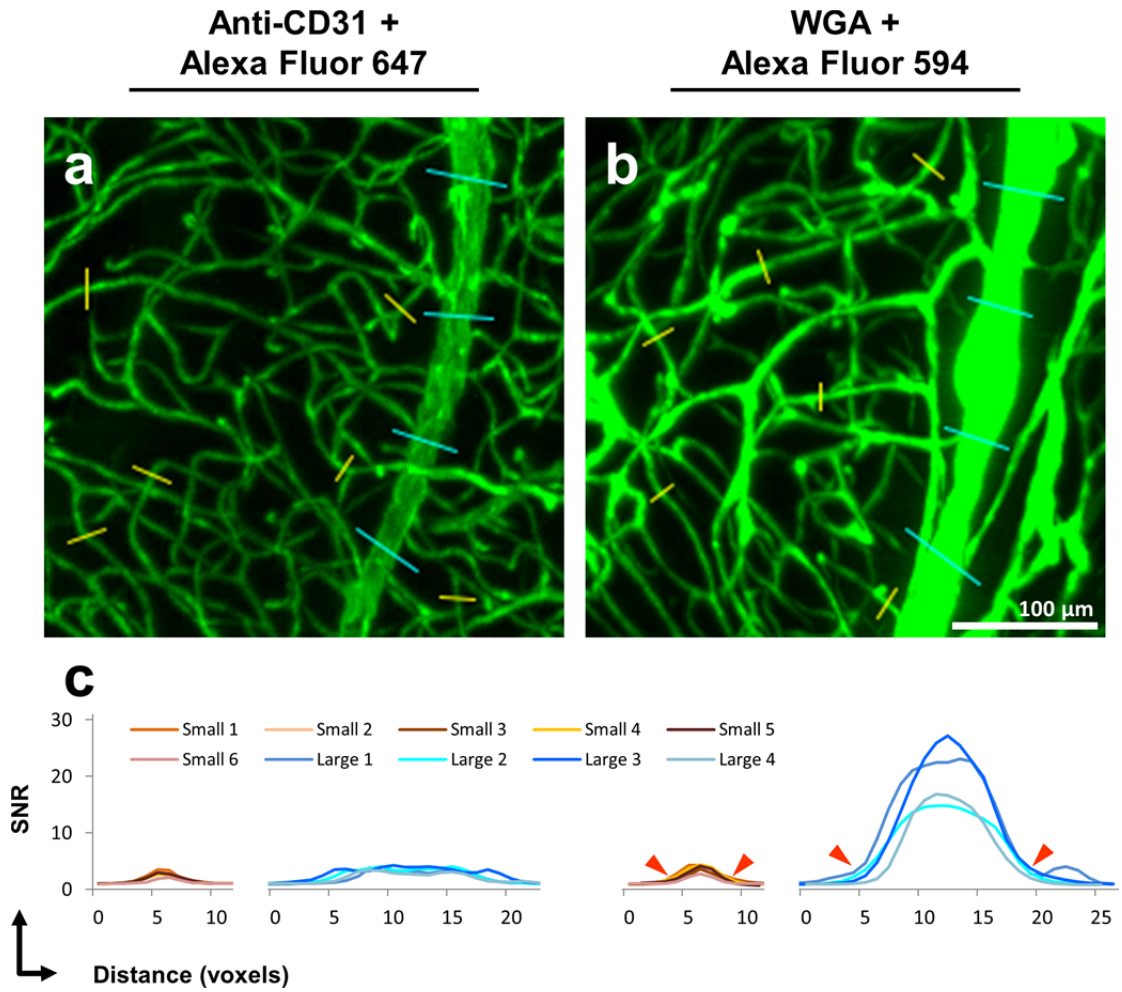

Supplementary Figure 5

Comparison of the signal strength of anti-CD31 and lectin dyes.
a-b, Axial maximum intensity projection of 150 µm thick tissue, stained as indicated. **c,** SNR quantifications on the line profiles indicated in (a) and (b) with warm and cold colored lines for small and large sized segments, respectively. The red arrowheads indicate where the signal of the vasculature gets higher. The experiments were performed on one mouse per condition.

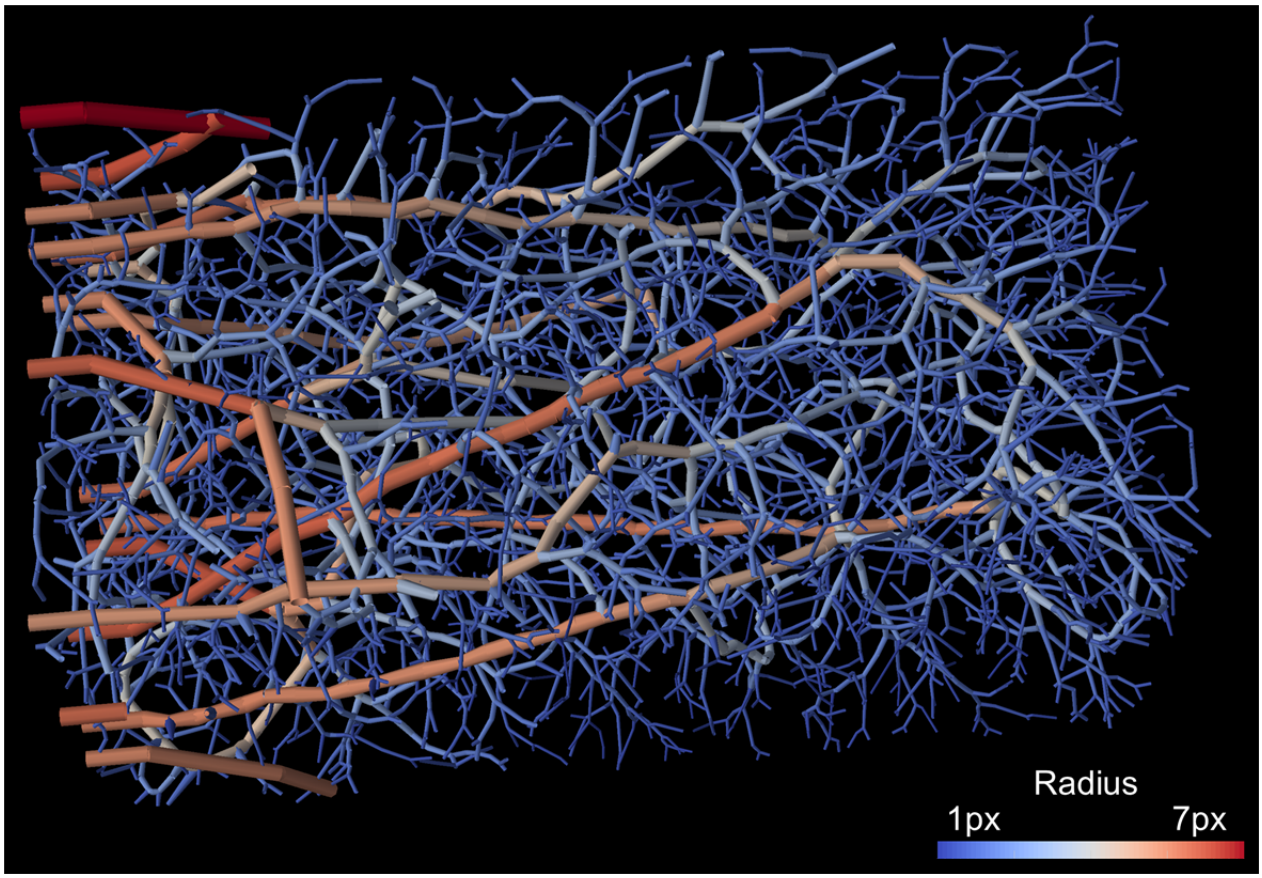

Supplementary Figure 6

Demonstration of the synthetic data used for VesSAP.
3D visualization including radius information in pixels (px) for one exemplary volume of synthetic data, which was used for pre-training our model in our transfer learning approach.

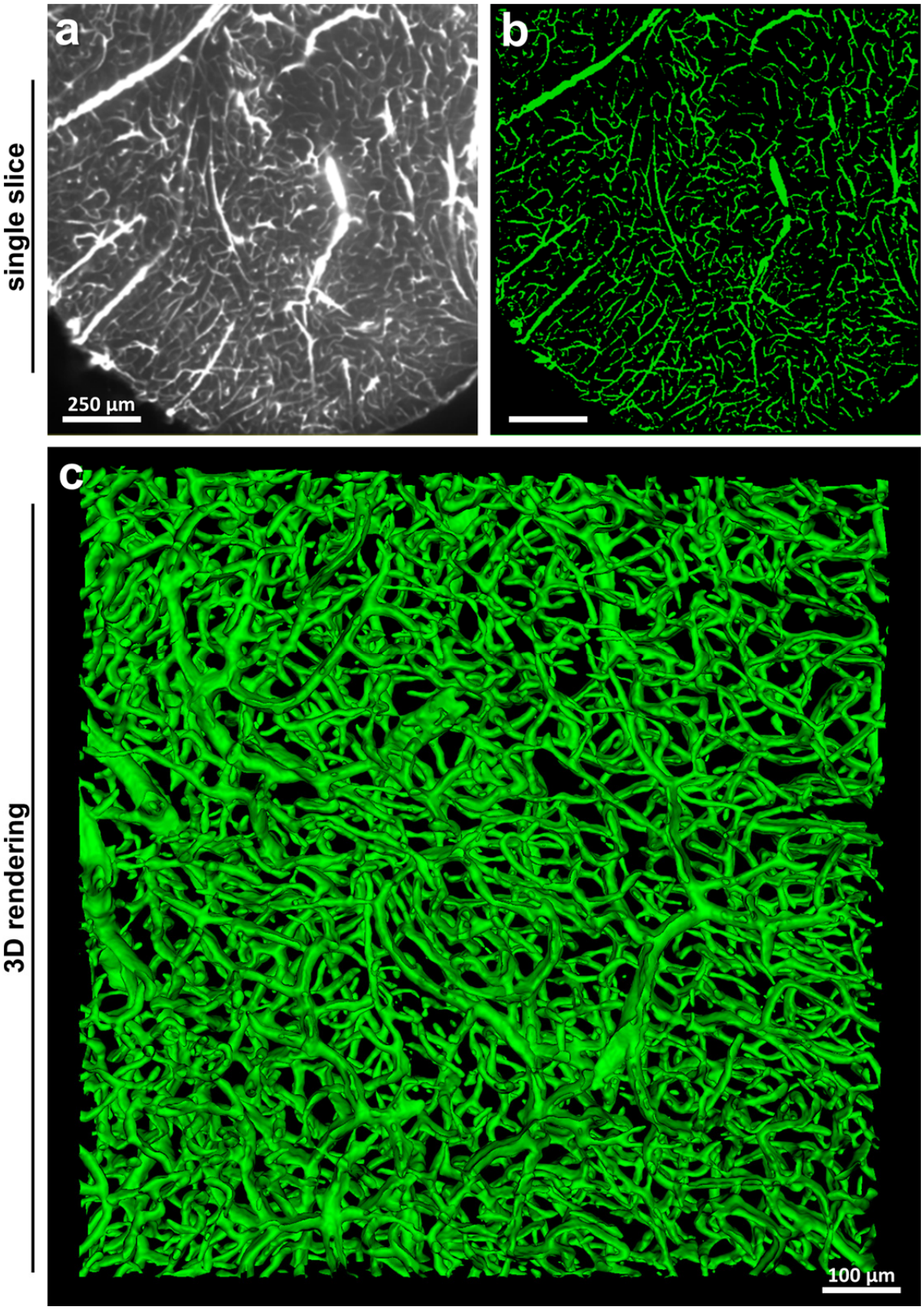

Supplementary Figure 7

Details of the segmentation quality by VesSAP.
a,b, Side by side slices of the raw WGA channel image (a) and the segmentation (b). **c,** 3D rendering of a small brain volume. The experiment was performed on 9 different mice with similar results.

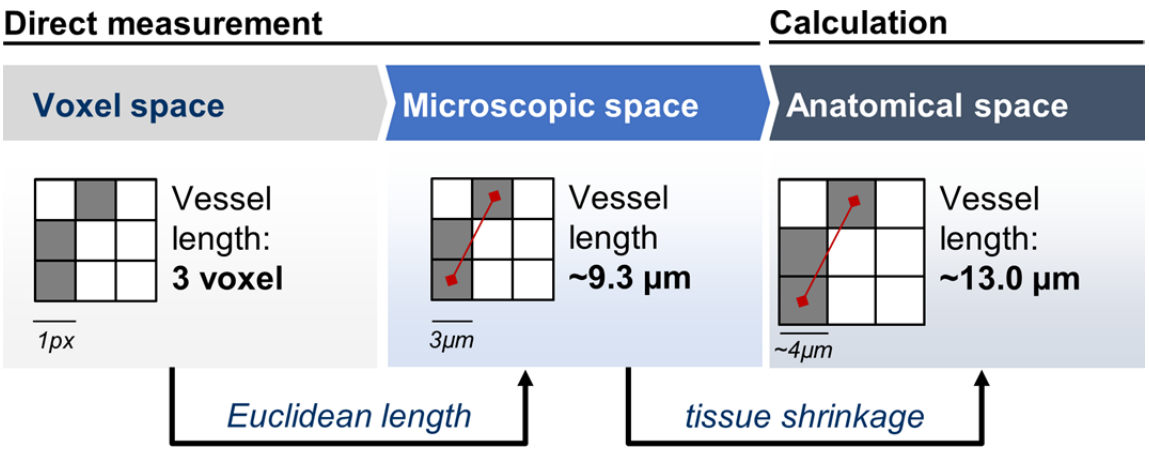

Supplementary figure 8

Three spaces of reported features.
Visualization of the three distinct spaces, in which we report the extracted features. The steps to account for the Euclidean length and the tissue shrinkage are visualized with an exemplary calculation of the vessel length of three vessel pixels in a 2D plane.

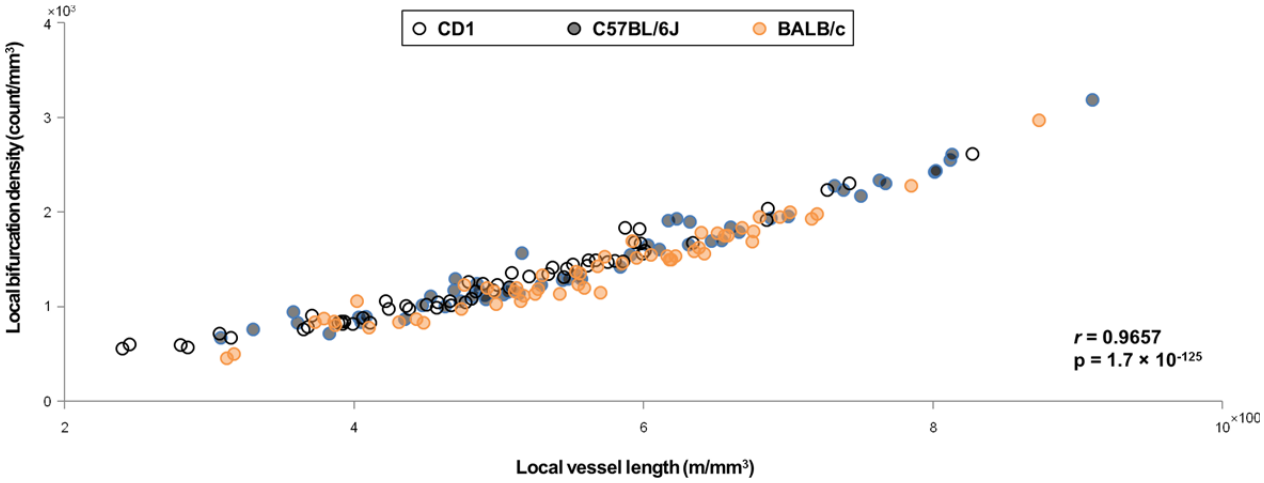

Supplementary Figure 9

Regression analysis of the neurovasculature in mouse strains.
Scatter plot of the local vessel length against the local bifurcation density (Pearson's r = 0.9657; p = 1.7 × 10^{-125}). Each point represents the mean of three animals per strain.

Cluster	All regions in the cluster	Name of cluster
FRP	FRP, FRP1, FRP2/3, FRP5, FRP6a, FRP6b	Frontal pole
MO	MO, MO1, MO2/3, MO5, MO6a, MO6b, MOp, MOp1, MOp2/3, MOp5, MOp6a, MOp6b, MOs, MOs1, MOs2/3, MOs5, MOs6a, MOs6b	Somatomotor areas
SS	SS, SS1, SS2/3, SS4, SS5, SS6a, SS6b, SSp, SSp1, SSp2/3, SSp4, SSp5, SSp6a, SSp6b, SSp-bfd, SSp-bfd1, SSp-bfd2/3, SSp-bfd4, SSp-bfd5, SSp-bfd6a, SSp-bfd6b, SSp-ll, SSp-ll1, SSp-ll2/3, SSp-ll4, SSp-ll5, SSp-ll6a, SSp-ll6b, SSp-m, SSp-m1, SSp-m2/3, SSp-m4, SSp-m5, SSp-m6a, SSp-m6b, SSp-n, SSp-n1, SSp-n2/3, SSp-n4, SSp-n5, SSp-n6a, SSp-n6b, SSp-tr, SSp-tr1, SSp-tr2/3, SSp-tr4, SSp-tr5, SSp-tr6a, SSp-tr6b, SSp-ul, SSp-ul1, SSp-ul2/3, SSp-ul4, SSp-ul5, SSp-ul6a, SSp-ul6b, SSp-un, SSp-un1, SSp-un2/3, SSp-un4, SSp-un5, SSp-un6a, SSp-un6b, SSs, SSs1, SSs2/3, SSs4, SSs5, SSs6a, SSs6b, VISrll, VISrll1, VISrll2/3, VISrll4, VISrll5, VISrll6a, VISrll6b	Somatosensory areas
GU	GU, GU1, GU2/3, GU4, GU5, GU6a, GU6b	Gustatory areas
VISC	VISC, VISC1, VISC2/3, VISC4, VISC5, VISC6a, VISC6b	Visceral area
AUD	AUD, AUDd, AUDd1, AUDd2/3, AUDd4, AUDd5, AUDd6a, AUDd6b, AUDp, AUDp1, AUDp2/3, AUDp4, AUDp5, AUDp6a, AUDp6b, AUDpo, AUDpo1, AUDpo2/3, AUDpo4, AUDpo5, AUDpo6a, AUDpo6b, AUDv, AUDv1, AUDv2/3, AUDv4, AUDv5, AUDv6a, AUDv6b, VISlla, VISlla1, VISlla2/3, VISlla4, VISlla5, VISlla6a, VISlla6b	Auditory areas
VIS	VIS, VIS1, VIS2/3, VIS4, VIS5, VIS6a, VIS6b, VISal, VISal1, VISal2/3, VISal4, VISal5, VISal6a, VISal6b, VISam, VISam1, VISam2/3, VISam4, VISam5, VISam6a, VISam6b, VISl, VISl1, VISl2/3, VISl4, VISl5, VISl6a, VISl6b, VISli, VISli1, VISli2/3, VISli4, VISli5, VISli6a, VISli6b, VISp, VISp1, VISp2/3, VISp4, VISp5, VISp6a, VISp6b, VISpl, VISpl1, VISpl2/3, VISpl4, VISpl5, VISpl6a, VISpl6b, VISpm, VISpm1, VISpm2/3, VISpm4, VISpm5, VISpm6a, VISpm6b, VISpor, VISpor1, VISpor2/3, VISpor4, VISpor5, VISpor6a, VISpor6b	Visual areas
ACA	ACA, ACA1, ACA2/3, ACA5, ACA6a, ACA6b, ACAd, ACAd1, ACAd2/3, ACAd5, ACAd6a, ACAd6b, ACAv, ACAv1, ACAv2/3, ACAv5, ACAv6a, ACAv6b	Anterior cingulate area
PL	PL, PL1, PL2, PL2/3, PL5, PL6a, PL6b	Prelimbic area
ILA	ILA, ILA1, ILA2, ILA2/3, ILA5, ILA6a, ILA6b	Infralimbic area
ORB	ORB, ORB1, ORB2/3, ORB5, ORB6a, ORB6b, ORBl, ORBl1, ORBl2/3, ORBl5, ORBl6a, ORBl6b, ORBm, ORBm1, ORBm2, ORBm2/3, ORBm5, ORBm6a, ORBm6b, ORBv, ORBvl, ORBvl1, ORBvl2/3, ORBvl5, ORBvl6a, ORBvl6b	Orbital area
AI	AI, AId, AId1, AId2/3, AId5, AId6a, AId6b, AIp, AIp1, AIp2/3, AIp5, AIp6a, AIp6b, AIv, AIv1, AIv2/3, AIv5, AIv6a, AIv6b	Agranular insular area
RSP	RSP, RSPagl, RSPagl1, RSPagl2/3, RSPagl5, RSPagl6a, RSPagl6b, RSPd, RSPd1, RSPd2/3, RSPd4, RSPd5, RSPd6a, RSPd6b, RSPv, RSPv1, RSPv2, RSPv2/3, RSPv5, RSPv6a, RSPv6b, VISm, VISm1, VISm2/3, VISm4, VISm5, VISm6a, VISm6b, VISmma, VISmma1, VISmma2/3, VISmma4, VISmma5, VISmma6a, VISmma6b, VISmmp, VISmmp1, VISmmp2/3, VISmmp4, VISmmp5, VISmmp6a, VISmmp6b	Retrosplenial area
PTL	PTLp, PTLp1, PTLp2/3, PTLp4, PTLp5, PTLp6a, PTLp6b, VISa, VISa1, VISa2/3, VISa4, VISa5, VISa6a, VISa6b, VISrl, VISrl1, VISrl2/3, VISrl4, VISrl5, VISrl6a, VISrl6b	Posterior parietal association areas

TE	TEa, TEa1, TEa2/3, TEa4, TEa5, TEa6a, TEa6b	Temporal association areas
PERI	PERI, PERI1, PERI2/3, PERI5, PERI6a, PERI6b	Perirhinal area
ECT	ECT, ECT1, ECT2/3, ECT5, ECT6a, ECT6b	Ectorhinal area
OLF	OLF, MOB, MOBipl, MOBopl	Olfactory areas
AOB	AOB, AOBgl, AOBmi	Accessory olfactory bulb
AOBgr	AOBgr, NLOT, NLOT1, NLOT1-3, NLOT2, NLOT3	AOBgr & NLOT
AON	AON, AON1, AON2, AONd, AONe, AONl, AONm, AONpv	Anterior olfactory nucleus
TT	TT, TTd, TTd1, TTd1-4, TTd2, TTd3, TTd4, TTv, TTv1, TTv1-3, TTv2, TTv3	Taenia tecta
DP	DP, DP1, DP2, DP2/3, DP5, DP6a	Dorsal peduncular area
PIR	PIR, PIR1, PIR1-3, PIR2, PIR3	Piriform area
COA	COA, COAa, COAa1, COAa2, COAa3, COAp, COApl, COApl1, COApl1-2, COApl1-3, COApl2, COApl3, COApm, COApm1, COApm1-2, COApm1-3, COApm2, COApm3	Cortical amygdalar area
PAA	PAA, PAA1, PAA1-3, PAA2, PAA3	Piriform-amygdalar area
TR	TR, TR1, TR1-3, TR2, TR3	Postpiriform transition area
CA	CA, CA1, CA1slm, CA1so, CA1sr, CA2, CA2slm, CA2so, CA2sr, CA3, CA3slm, CA3slu, CA3so, CA3sr, DG, DGcr, DGcr-mo, DGcr-po, DGcr-sg, DGlb, DGlb-mo, DGlb-po, DGlb-sg, DGmb, DGmb-mo, DGmb-po, DGmb-sg, DG-mo, DG-po, DG-sgz, FC, HIP, HPF, IG	Hippocampal formation
CA1sp	CA1sp, CA2sp, CA3sp, DG-sg	
ENT	ENT, ENTl, ENTl1, ENTl2, ENTl2/3, ENTl2a, ENTl2b, ENTl3, ENTl4, ENTl4/5, ENTl5, ENTl5/6, ENTl6a, ENTl6b, ENTm, ENTm1, ENTm2, ENTm2a, ENTm2b, ENTm3, ENTm4, ENTm5, ENTm5/6, ENTm6, ENTmv, ENTmv1, ENTmv2, ENTmv3, ENTmv4, ENTmv5/6, RHP	Retrohippocampal region
PAR	PAR, PAR1, PAR2, PAR3	Parasubiculum
POST	POST, POST1, POST2, POST3	Postsubiculum
PRE	PRE, PRE1, PRE2, PRE3	Presubiculum
SUB	SUB, SUBd, SUBd-m, SUBd-sr, SUBv, SUBv-m, SUBv-sr	Subiculum
ProS	ProS, ProSd, ProSd-m, ProSd-sr, ProSv, ProSv-m, Prosv-sr	Prosubiculum
CLA	CLA, CTXsp, 6b	Claustrum
EP	EP, EPd, EPv	Endopiriform nucleus
LA	LA	Lateral amygdalar nucleus
BLA	BLA, BLAa, BLAp, BLAv	Basolateral amygdalar nucleus
BMA	BMA, BMAa, BMAp	Basomedial amygdalar nucleus
PA	PA	Posterior amygdalar nucleus
CP	CP, CNU, STR, STRd	Caudoputamen

ACB	ACB, FS, isl, islm, LSS, OT, OT1, OT1-3, OT2, OT3, STRv	Nucleus accumbens
LS	LS, LSc, LSr, LSv, LSX, SF, SH	Lateral septal complex
AAA	AAA, BA, CEA, CEAc, CEAl, CEAm, IA, MEA, MEAad, MEAav, MEApd, MEApd-a, MEApd-b, MEApd-c, MEApv, sAMY	Anterior amygdalar area
GPe	GPe, GPi, PAL, PALd	Pallidum
MA	MA, PALv, SI	Magnocellular nucleus
MS	MS, MSC, NDB, PALm, TRS	Medial septal nucleus
BAC	BAC, BST, BSTa, BSTal, BSTam, BSTd, BSTdm, BSTfu, BSTif, BSTju, BSTmg, BSTov, BSTp, BSTpr, BSTrh, BSTse, BSTtr, BSTv, PALc	Bed nucleus of the anterior commissure
BS	BS, TH	Brain stem
DORsm	DORsm, GENd, LGd, LGd-co, LGd-ip, LGd-sh, MG, MGd, MGm, MGv, PoT, PP, SPA, SPF, SPFm, SPFp, VAL, VENT, VM, VP, VPL, VPLpc, VPM, VPMpc	Thalamus, sensory-motor cortex related
AD	AD, AM, AMd, AMv, ATN, AV, CL, CM, DORpm, EPI, Eth, GENv, IAD, IAM, IGL, ILM, IMD, IntG, LAT, LD, LGv, LGvl, LGvm, LH, LP, MD, MDc, MDl, MDm, MED, MH, MTN, PCN, PF, PIL, PIN, PO, POL, PR, PT, PVT, RE, REth, RH, RT, SGN, SMT, SubG, Xi	Anterodorsal nucleus
HY	HY	Hypothalamus
ARH	ARH, ASO, NC, PVa, PVH, PVHam, PVHap, PVHm, PVHmm, PVHmpd, PVHp, PVHpm, PVHpml, PVHpmm, PVHpv, PVi, PVZ, SO	Arcuate hypothalamic nucleus
ADP	ADP, AHA, AVP, AVPV, DMH, DMHa, DMHp, DMHv, MEPO, MPO, OV, PD, PS, PSCH, PVp, PVpo, PVR, SBPV, SCH, SFO, VLPO, VMPO	Anterodorsal preoptic nucleus
AHN	AHN, AHNa, AHNc, AHNd, AHNp, LM, MBO, MEZ, MM, MMd, MMl, MMm, MMme, MMp, MPN, MPNc, MPNl, MPNm, PH, PMd, PMv, PVHd, PVHdp, PVHf, PVHlp, PVHmpv, SUM, SUMl, SUMm, TM, TMd, TMv, VMH, VMHa, VMHc, VMHdm, VMHvl	Anterior hypothalamic nucleus
A13	A13, FF, LHA, LPO, LZ, ME,PeF, PST, PSTN, RCH, STN, TU, ZI	
MB	MB	Midbrain
IC	IC, ICc, ICd, ICe, MBsen, MEV, NB, PBG, SAG, SCO, SCop, SCs, SCsg, SCzo	Inferior colliculus
APN	APN, AT, CUN, DT, EW, III, INC, InCo, IV, LT, MA3, MBmot, MBsta, MPT, MRN, MRNm, MRNmg, MRNp, MT, ND, NOT, NPC, OP, Pa4, PAG, PN, PPT, PRC, PRT, RN, RPF, RR, SCdg, SCdw, SCig, SCig-a, SCig-b, SCig-c, SCiw, SCm, SNl, SNr, Su3, VTA, VTN	Anterior pretectal nucleus
SNc	SNc, CLI, DR, IF, IPA, IPC, IPDL, IPDM, IPI, IPL, IPN, IPR, IPRL, PPN, RAmb, RL	Substantia nigra
P	P, HB	Pons
KF	KF, NLL, NLLd, NLLh, NLLv, PB, PBl, PBlc, PBld, PBle, PBls, PBlv, PBm, PBme, PBmm, PBmv, POR, P-sen, PSV, SOC, SOCl, SOCm	Koelliker-Fuse subnucleus
Acs5	Acs5, B, DTN, I5, LTN, P5, PC5, PCG, PDTg, PG, P-mot, PRNc, PRNv, SG, SSN, SUT, TRN, V	Accessory trigeminal nucleus
CS	CS, CSl, CSm, LC, LDT, NI, PRNr, P-sat, RPO, SLC, SLD	Superior central nucleus raphe
MY	MY	Medulla

AP	AP, CN, CNlam, CNspg, CU, DCN, DCO, ECU, GR, MY-sen, NTB, NTS, NTSce, NTSco, NTSge, NTSl, NTSm, Pa5, SPVC, SPVI, SPVO, SPVOcdm, SPVOmdmd, SPVOmdmv, SPVOrdm, SPVOvl, VCO, z	Area postrema
ACVI	ACVI, ACVII, AMB, AMBd, AMBv, DMX, ECO, EV, GRN, ICB, INV, IO, IRN, ISN, LAV, LIN, LRN, LRNm, LRNp, MARN, MDRN, MDRNd, MDRNv, MV, MY-mot, NIS, NR, PARN, PAS, PGRN, PGRNd, PGRNl, PHY, PMR, PPY, PPYd, PPYs, PRP, SPIV, SUV, VI, VII, VNC, x, XII, y	Accessory facial motor nucleus
CB	CB, CBX, CBN	Cerebellum
FN	FN, IP, DN, VeCB	Fastigial nucleus
oct	oct, ab, aco, act, alv, amc, aolt, aot, apd, ar, arb, bct, bic, bsc, cbc, cbf, cbp, cbt, cc, ccb, ccg, ccr, ccs, cct, cett, cic, cing, cm, cpd, cpt, crt, csc, cst, cstc, cstu, ctb, cte, cuf, cvb, cVIIIn, das, db, dc, dcm, df, dhc, dl, dlf, drt, dscp, dtd, dtt, ec, ee, em, eps, epsc, fa, fi, fp, fpr, fr, fx, fxpo, fxprg, fxs, grf, gVIIn, hbc, hc, hht, iaf, ias, icp, IIIn, IIn, im, In, int, IVd, iVIIn, IVn, IXn, jrb, lab, lfbs, lfbst, ll, lot, lotd, lotg, mcp, mct, mfb, mfbc, mfbs, mfbse, mfbsm, mfbsma, mfbst, mfsbshy, ml, mlf, moV, mp, mtc, mtg, mtt, mtV, nst, ntt, och, onl, opt, or, pap, pc, per, php, phpd, phpl, phpm, phpv, PIS, pm, pmx, poc, ptf, pvbh, pvbt, py, pyd, rct, rrt, rst, rstl, rstm, rust, scp, scrt, sct, sctd, sctv, scwm, shp, sm, smd, snp, sop, sptV, srp, sst, st, stc, step, stf, stp, sttl, sttv, sup, supa, supd, supv, sV, svp, tb, tct, tn, tp, ts, tsp, tspc, tspd, ttp, uf, vc, vhc, VIIIn, VIIn, VIn, vlt, Vn, von, vrt, vsp, vtd, vVIIIn, XIIn, XIn, Xn	fiber tracts

Supplementary table 1

List of anatomical clusters and all the brain regions that they represent according to the current Allen adult mouse brain atlas ontology.

Cluster	BL6#1	BL6#2	BL6#3	CD1#1	CD1#2	CD1#3	BALBC #1	BALBC #2	BALBC #3
FRP	0.00490	0.00761	0.00499	0.00196	0.00405	0.00100	0.00261	0.00397	0.00428
MO	0.00713	0.00838	0.00561	0.00447	0.00743	0.00346	0.00708	0.00689	0.00606
SS	0.00831	0.00981	0.00791	0.00528	0.00987	0.00607	0.00694	0.00701	0.00589
GU	0.00782	0.00767	0.00635	0.00599	0.01000	0.00766	0.00572	0.00569	0.00560
VISC	0.00691	0.00778	0.00625	0.00496	0.00963	0.00619	0.00453	0.00520	0.00527
AUD	0.00632	0.00924	0.00637	0.00605	0.00776	0.00579	0.00725	0.00791	0.00730
VIS	0.00632	0.00845	0.00603	0.00399	0.00717	0.00412	0.00659	0.00747	0.00654
ACA	0.00700	0.00671	0.00534	0.00425	0.00814	0.00471	0.00554	0.00676	0.00533
PL	0.00727	0.00680	0.00503	0.00383	0.00704	0.00479	0.00528	0.00627	0.00614
ILA	0.00730	0.00497	0.00342	0.00495	0.00676	0.00600	0.00498	0.00601	0.00531
ORB	0.00925	0.00756	0.00613	0.00481	0.00823	0.00510	0.00591	0.00700	0.00640
AI	0.00710	0.00711	0.00546	0.00429	0.00734	0.00496	0.00624	0.00578	0.00578
RSP	0.00825	0.00794	0.00562	0.00378	0.00841	0.00478	0.00528	0.00744	0.00610
PTL	0.00401	0.00838	0.00570	0.00419	0.00687	0.00383	0.00658	0.00696	0.00557
TE	0.00474	0.00777	0.00554	0.00490	0.00758	0.00466	0.00548	0.00686	0.00604
PERI	0.00428	0.00637	0.00520	0.00296	0.00622	0.00331	0.00441	0.00507	0.00527
ECT	0.00419	0.00662	0.00514	0.00367	0.00682	0.00371	0.00449	0.00587	0.00562
OLF	0.00625	0.00360	0.00491	0.00343	0.00838	0.00526	0.00565	0.00595	0.00533
AOB	0.00745	0.00574	0.00464	0.00356	0.00744	0.00506	0.00551	0.00489	0.00565
AOBgr	0.00475	0.00345	0.00526	0.00222	0.00523	0.00375	0.00540	0.00551	0.00493
AON	0.00848	0.00529	0.00510	0.00453	0.00731	0.00493	0.00602	0.00629	0.00584
TT	0.00648	0.00275	0.00419	0.00350	0.00625	0.00533	0.00553	0.00532	0.00555
DP	0.00669	0.00395	0.00355	0.00437	0.00644	0.00643	0.00498	0.00596	0.00533
PIR	0.00690	0.00608	0.00613	0.00364	0.00699	0.00559	0.00653	0.00631	0.00578
COA	0.00353	0.00346	0.00468	0.00206	0.00494	0.00352	0.00474	0.00454	0.00480
PAA	0.00353	0.00225	0.00455	0.00183	0.00566	0.00412	0.00449	0.00481	0.00432
TR	0.00485	0.00493	0.00492	0.00248	0.00578	0.00335	0.00468	0.00477	0.00520
CA	0.00469	0.00485	0.00448	0.00340	0.00538	0.00376	0.00423	0.00501	0.00433
CA1sp	0.00447	0.00411	0.00430	0.00302	0.00478	0.00341	0.00352	0.00467	0.00414
ENT	0.00503	0.00733	0.00488	0.00351	0.00664	0.00354	0.00510	0.00575	0.00506
PAR	0.00598	0.00644	0.00524	0.00413	0.00857	0.00409	0.00602	0.00817	0.00525
POST	0.00702	0.00844	0.00744	0.00484	0.00684	0.00475	0.00592	0.00747	0.00539
PRE	0.00587	0.00785	0.00773	0.00396	0.00873	0.00583	0.00665	0.00783	0.00601
SUB	0.00646	0.00708	0.00648	0.00470	0.00723	0.00527	0.00569	0.00677	0.00524
ProS	0.00558	0.00466	0.00363	0.00340	0.00604	0.00264	0.00366	0.00399	0.00341
CLA	0.00718	0.00599	0.00533	0.00358	0.00615	0.00535	0.00533	0.00559	0.00468
EP	0.00613	0.00562	0.00495	0.00308	0.00585	0.00442	0.00488	0.00507	0.00478
LA	0.00423	0.00443	0.00379	0.00313	0.00551	0.00313	0.00395	0.00457	0.00429
BLA	0.00454	0.00460	0.00465	0.00272	0.00583	0.00391	0.00517	0.00532	0.00501
BMA	0.00483	0.00471	0.00487	0.00330	0.00561	0.00486	0.00529	0.00528	0.00530
PA	0.00511	0.00480	0.00510	0.00302	0.00536	0.00416	0.00681	0.00598	0.00547
CP	0.00634	0.00513	0.00524	0.00358	0.00642	0.00451	0.00400	0.00500	0.00368

ACB	0.00494	0.00319	0.00465	0.00263	0.00571	0.00375	0.00629	0.00608	0.00494
LS	0.00435	0.00274	0.00388	0.00313	0.00547	0.00448	0.00279	0.00316	0.00297
AAA	0.00513	0.00412	0.00453	0.00309	0.00498	0.00504	0.00519	0.00487	0.00501
GPe	0.00544	0.00394	0.00466	0.00267	0.00544	0.00330	0.00368	0.00434	0.00430
MA	0.00608	0.00373	0.00473	0.00218	0.00594	0.00421	0.00571	0.00490	0.00394
MS	0.00655	0.00345	0.00560	0.00267	0.00671	0.00519	0.00530	0.00456	0.00435
BAC	0.00532	0.00250	0.00377	0.00221	0.00475	0.00348	0.00314	0.00320	0.00273
BS	0.00479	0.00388	0.00485	0.00352	0.00556	0.00426	0.00452	0.00525	0.00503
DORsm	0.00503	0.00493	0.00517	0.00426	0.00688	0.00445	0.00564	0.00650	0.00618
AD	0.00483	0.00361	0.00481	0.00346	0.00635	0.00383	0.00442	0.00489	0.00494
HY	0.00620	0.00305	0.00465	0.00303	0.00602	0.00521	0.00519	0.00482	0.00470
ARH	0.00474	0.00167	0.00304	0.00268	0.00528	0.00358	0.00521	0.00465	0.00476
ADP	0.00623	0.00244	0.00430	0.00279	0.00616	0.00503	0.00559	0.00492	0.00441
AHN	0.00611	0.00303	0.00442	0.00300	0.00598	0.00487	0.00535	0.00511	0.00483
A13	0.00605	0.00452	0.00567	0.00391	0.00666	0.00519	0.00561	0.00533	0.00531
MB	0.00626	0.00540	0.00536	0.00401	0.00708	0.00418	0.00438	0.00575	0.00478
IC	0.00700	0.00877	0.00746	0.00511	0.00979	0.00472	0.00429	0.00697	0.00549
APN	0.00714	0.00566	0.00590	0.00465	0.00742	0.00397	0.00400	0.00570	0.00453
SNc	0.00541	0.00517	0.00500	0.00390	0.00664	0.00326	0.00318	0.00448	0.00347
P	0.00336	0.00217	0.00328	0.00179	0.00394	0.00227	0.00294	0.00374	0.00400
KF	0.00345	0.00328	0.00450	0.00192	0.00383	0.00241	0.00382	0.00528	0.00606
Acs5	0.00433	0.00243	0.00476	0.00257	0.00543	0.00313	0.00379	0.00502	0.00507
CS	0.00553	0.00381	0.00513	0.00304	0.00658	0.00324	0.00324	0.00417	0.00434
MY	0.00449	0.00248	0.00328	0.00178	0.00297	0.00214	0.00430	0.00373	0.00346
AP	0.00520	0.00541	0.00540	0.00304	0.00499	0.00260	0.00583	0.00683	0.00565
ACVI	0.00681	0.00412	0.00597	0.00303	0.00493	0.00328	0.00641	0.00683	0.00609
CB	0.00518	0.00414	0.00412	0.00202	0.00375	0.00303	0.00374	0.00493	0.00521
FN	0.00685	0.00784	0.00858	0.00330	0.00329	0.00554	0.00691	0.00913	0.00892
oct	0.00457	0.00356	0.00355	0.00243	0.00400	0.00259	0.00343	0.00403	0.00357

Supplementary table 2

Quantification of the local vascular length per volume in the C57BL/6J, CD1 and BALB/c samples in the voxel-corrected space. Units are in vx/vx3.

Cluster	BL6#1	BL6#2	BL6#3	CD1#1	CD1#2	CD1#3	BALBC #1	BALBC #2	BALBC #3
FRP	0,00064	0,00096	0,00056	0,00020	0,00053	0,00008	0,00025	0,00041	0,00051
MO	0,00107	0,00127	0,00066	0,00047	0,00107	0,00036	0,00104	0,00090	0,00075
SS	0,00138	0,00172	0,00119	0,00060	0,00170	0,00080	0,00094	0,00097	0,00071
GU	0,00119	0,00112	0,00080	0,00069	0,00178	0,00105	0,00066	0,00072	0,00066
VISC	0,00104	0,00121	0,00082	0,00055	0,00165	0,00080	0,00041	0,00057	0,00054
AUD	0,00083	0,00147	0,00080	0,00071	0,00113	0,00074	0,00097	0,00114	0,00095
VIS	0,00085	0,00131	0,00073	0,00039	0,00102	0,00044	0,00081	0,00105	0,00081
ACA	0,00100	0,00081	0,00061	0,00044	0,00128	0,00053	0,00063	0,00082	0,00061
PL	0,00104	0,00080	0,00052	0,00036	0,00097	0,00055	0,00053	0,00075	0,00074
ILA	0,00102	0,00044	0,00028	0,00049	0,00082	0,00069	0,00041	0,00061	0,00052
ORB	0,00155	0,00100	0,00073	0,00048	0,00119	0,00058	0,00065	0,00085	0,00078
AI	0,00104	0,00095	0,00061	0,00042	0,00101	0,00057	0,00075	0,00067	0,00064
RSP	0,00130	0,00116	0,00068	0,00037	0,00133	0,00055	0,00055	0,00106	0,00075
PTL	0,00049	0,00130	0,00075	0,00044	0,00093	0,00041	0,00085	0,00093	0,00068
TE	0,00053	0,00108	0,00061	0,00051	0,00109	0,00050	0,00056	0,00087	0,00067
PERI	0,00047	0,00078	0,00054	0,00024	0,00080	0,00031	0,00037	0,00053	0,00052
ECT	0,00042	0,00080	0,00053	0,00032	0,00090	0,00035	0,00039	0,00065	0,00058
OLF	0,00098	0,00048	0,00065	0,00037	0,00140	0,00067	0,00077	0,00080	0,00071
AOB	0,00115	0,00082	0,00062	0,00033	0,00115	0,00052	0,00063	0,00056	0,00078
AOBgr	0,00061	0,00034	0,00060	0,00017	0,00058	0,00038	0,00066	0,00063	0,00055
AON	0,00135	0,00057	0,00055	0,00045	0,00099	0,00055	0,00074	0,00072	0,00067
TT	0,00092	0,00025	0,00042	0,00034	0,00081	0,00064	0,00071	0,00062	0,00073
DP	0,00092	0,00033	0,00029	0,00041	0,00083	0,00077	0,00044	0,00064	0,00056
PIR	0,00103	0,00078	0,00077	0,00035	0,00098	0,00068	0,00090	0,00080	0,00069
COA	0,00040	0,00035	0,00045	0,00015	0,00055	0,00035	0,00059	0,00052	0,00051
PAA	0,00040	0,00024	0,00048	0,00012	0,00063	0,00042	0,00058	0,00057	0,00051
TR	0,00054	0,00051	0,00049	0,00018	0,00070	0,00030	0,00053	0,00054	0,00054
CA	0,00056	0,00049	0,00045	0,00030	0,00064	0,00039	0,00040	0,00051	0,00040
CA1sp	0,00053	0,00038	0,00041	0,00025	0,00052	0,00033	0,00028	0,00043	0,00036
ENT	0,00063	0,00101	0,00058	0,00034	0,00097	0,00039	0,00055	0,00072	0,00055
PAR	0,00091	0,00095	0,00071	0,00044	0,00150	0,00053	0,00078	0,00123	0,00061
POST	0,00097	0,00128	0,00101	0,00050	0,00094	0,00055	0,00072	0,00101	0,00062
PRE	0,00075	0,00112	0,00106	0,00036	0,00134	0,00071	0,00085	0,00107	0,00067
SUB	0,00089	0,00093	0,00081	0,00047	0,00106	0,00061	0,00064	0,00083	0,00054
ProS	0,00078	0,00052	0,00037	0,00036	0,00082	0,00024	0,00036	0,00041	0,00031
CLA	0,00104	0,00067	0,00056	0,00028	0,00077	0,00059	0,00054	0,00059	0,00044
EP	0,00082	0,00060	0,00050	0,00024	0,00069	0,00044	0,00047	0,00050	0,00044
LA	0,00048	0,00037	0,00032	0,00023	0,00063	0,00026	0,00032	0,00043	0,00036
BLA	0,00053	0,00042	0,00044	0,00020	0,00067	0,00035	0,00052	0,00054	0,00047
BMA	0,00057	0,00045	0,00050	0,00028	0,00065	0,00052	0,00057	0,00056	0,00054
PA	0,00063	0,00047	0,00052	0,00024	0,00063	0,00045	0,00093	0,00069	0,00057
CP	0,00090	0,00053	0,00058	0,00032	0,00081	0,00048	0,00034	0,00050	0,00032

ACB	0,00062	0,00028	0,00046	0,00021	0,00070	0,00039	0,00083	0,00072	0,00054
LS	0,00046	0,00018	0,00032	0,00024	0,00065	0,00044	0,00018	0,00022	0,00021
AAA	0,00069	0,00037	0,00044	0,00026	0,00057	0,00059	0,00058	0,00050	0,00051
GPe	0,00067	0,00033	0,00045	0,00021	0,00060	0,00029	0,00032	0,00041	0,00040
MA	0,00083	0,00031	0,00047	0,00016	0,00073	0,00044	0,00067	0,00049	0,00036
MS	0,00091	0,00028	0,00064	0,00021	0,00098	0,00063	0,00064	0,00045	0,00047
BAC	0,00065	0,00015	0,00032	0,00016	0,00052	0,00034	0,00024	0,00024	0,00020
BS	0,00057	0,00035	0,00050	0,00032	0,00067	0,00045	0,00043	0,00057	0,00051
DORsm	0,00060	0,00049	0,00056	0,00041	0,00089	0,00046	0,00062	0,00079	0,00070
AD	0,00055	0,00031	0,00048	0,00029	0,00076	0,00036	0,00042	0,00048	0,00048
HY	0,00083	0,00026	0,00049	0,00026	0,00077	0,00063	0,00056	0,00050	0,00048
ARH	0,00061	0,00013	0,00028	0,00021	0,00061	0,00037	0,00056	0,00050	0,00049
ADP	0,00087	0,00019	0,00044	0,00022	0,00083	0,00062	0,00065	0,00051	0,00046
AHN	0,00082	0,00026	0,00044	0,00024	0,00076	0,00055	0,00058	0,00054	0,00050
A13	0,00081	0,00047	0,00069	0,00040	0,00092	0,00063	0,00068	0,00064	0,00060
MB	0,00084	0,00058	0,00057	0,00037	0,00100	0,00044	0,00041	0,00064	0,00049
IC	0,00102	0,00137	0,00104	0,00053	0,00167	0,00054	0,00041	0,00090	0,00065
APN	0,00101	0,00060	0,00068	0,00045	0,00107	0,00040	0,00035	0,00062	0,00043
SNc	0,00068	0,00054	0,00051	0,00035	0,00087	0,00028	0,00025	0,00044	0,00029
P	0,00039	0,00019	0,00033	0,00014	0,00047	0,00019	0,00028	0,00040	0,00045
KF	0,00038	0,00033	0,00053	0,00015	0,00042	0,00020	0,00039	0,00062	0,00078
Acs5	0,00051	0,00018	0,00051	0,00020	0,00063	0,00029	0,00038	0,00052	0,00055
CS	0,00069	0,00032	0,00053	0,00025	0,00086	0,00026	0,00025	0,00038	0,00042
MY	0,00062	0,00026	0,00039	0,00016	0,00037	0,00022	0,00055	0,00047	0,00041
AP	0,00068	0,00064	0,00068	0,00028	0,00069	0,00025	0,00074	0,00095	0,00071
ACVI	0,00101	0,00037	0,00070	0,00025	0,00057	0,00032	0,00077	0,00091	0,00073
CB	0,00072	0,00049	0,00053	0,00017	0,00046	0,00032	0,00041	0,00065	0,00071
FN	0,00097	0,00114	0,00139	0,00029	0,00030	0,00072	0,00101	0,00151	0,00147
oct	0,00059	0,00037	0,00038	0,00020	0,00046	0,00025	0,00035	0,00043	0,00036

Supplementary table 3

Quantification of the number of bifurcation points in the C57BL/6J, CD1 and BALB/c samples in the voxel-corrected space, units are in counts/vx3.

Cluster	BL6#1	BL6#2	BL6#3	CD1#1	CD1#2	CD1#3	BALBC #1	BALBC #2	BALBC #3
FRP	2.06	2.35	2.33	3.53	2.26	2.66	2.44	2.32	2.36
MO	2.07	2.40	2.29	2.08	2.04	2.19	2.45	2.57	2.51
SS	2.14	2.47	2.38	2.12	2.17	2.25	2.47	2.59	2.50
GU	2.21	2.68	2.68	2.14	2.37	2.38	2.82	2.76	2.75
VISC	2.23	2.66	2.43	2.30	2.33	2.45	2.53	2.57	2.34
AUD	2.02	2.38	2.27	2.14	1.97	2.14	2.58	2.67	2.50
VIS	2.07	2.34	2.27	2.08	2.03	2.08	2.48	2.64	2.47
ACA	2.34	2.35	2.49	2.20	2.32	2.45	3.15	3.46	2.79
PL	2.17	2.48	2.29	2.14	2.12	2.34	2.66	2.79	2.75
ILA	2.32	2.43	2.42	2.31	2.15	2.35	2.68	2.91	2.69
ORB	2.27	2.41	2.34	2.24	2.10	2.18	2.50	2.43	2.64
AI	2.14	2.52	2.48	2.15	2.15	2.27	2.72	2.73	2.53
RSP	2.10	2.30	2.30	2.12	2.13	2.23	2.57	2.74	2.78
PTL	2.04	2.34	2.27	2.03	2.04	2.10	2.53	2.62	2.49
TE	2.04	2.41	2.27	2.04	1.98	1.99	2.49	2.63	2.42
PERI	2.13	2.42	2.33	2.02	2.07	2.03	2.54	2.57	2.51
ECT	2.13	2.38	2.28	2.03	2.02	1.99	2.55	2.65	2.47
OLF	2.29	2.44	2.47	2.26	2.20	2.48	2.54	2.59	2.52
AOB	2.15	2.70	2.58	2.16	2.46	2.44	2.64	2.78	2.45
AOBgr	2.62	2.67	2.81	2.58	2.35	2.93	2.70	2.50	2.47
AON	2.15	2.28	2.42	2.14	2.20	2.25	2.57	2.63	2.68
TT	2.86	2.53	2.86	2.54	2.31	2.92	2.91	2.67	2.61
DP	2.21	2.35	2.48	2.13	2.11	2.54	2.77	2.66	2.74
PIR	2.18	2.38	2.56	2.14	2.18	2.34	2.73	2.69	2.55
COA	2.16	2.33	2.49	2.30	2.18	2.29	3.02	2.94	2.64
PAA	2.22	2.26	2.59	2.43	2.16	2.45	2.92	2.74	2.57
TR	2.16	2.48	2.46	2.10	2.19	1.99	2.73	3.02	2.54
CA	2.56	2.49	2.65	2.57	2.24	2.70	3.93	4.14	3.22
CA1sp	2.34	2.23	2.42	2.12	2.07	2.86	2.60	2.55	2.76
ENT	2.09	2.41	2.32	2.08	2.25	2.22	2.52	2.70	2.51
PAR	2.44	2.31	2.33	2.16	2.27	2.54	2.46	2.49	2.42
POST	2.43	2.61	2.73	2.64	2.31	2.54	2.72	2.55	2.94
PRE	3.28	2.60	2.53	3.04	2.42	2.90	3.49	2.48	3.60
SUB	2.34	2.50	2.52	2.34	2.40	2.25	2.51	2.56	2.46
ProS	2.10	2.35	2.38	2.14	2.10	2.19	2.53	2.66	2.67
CLA	2.22	2.41	2.62	2.12	2.29	2.33	2.88	2.72	2.54
EP	2.17	2.42	2.56	2.12	2.20	2.28	2.85	2.78	2.60
LA	2.08	2.13	2.40	2.10	2.14	2.19	2.96	2.96	2.70
BLA	2.08	2.25	2.54	2.10	2.19	2.18	2.96	2.96	2.73
BMA	2.13	2.20	2.55	2.18	2.25	2.38	3.05	2.96	2.87
PA	2.06	2.24	2.47	2.06	2.08	2.17	2.86	2.87	2.60
CP	2.30	2.23	2.54	2.26	2.20	2.51	2.63	2.67	2.55

ACB	2.16	2.05	2.37	2.22	2.06	2.29	2.58	2.51	2.34
LS	2.05	2.13	2.44	2.15	2.29	2.15	2.34	2.49	2.38
AAA	2.30	2.27	2.51	2.60	2.31	2.63	3.03	2.75	2.79
GPe	2.19	2.07	2.46	2.18	2.22	2.43	2.58	2.65	2.52
MA	2.28	2.10	2.51	2.31	2.12	2.41	2.56	2.47	2.47
MS	2.30	2.28	2.55	2.52	2.36	2.93	2.43	2.55	2.46
BAC	2.23	2.53	2.68	2.00	2.39	2.03	2.42	2.59	2.45
BS	2.12	2.19	2.39	2.15	2.16	2.23	2.57	2.55	2.46
DORsm	2.14	2.23	2.43	2.14	2.13	2.17	2.63	2.55	2.56
AD	2.07	2.14	2.31	2.14	2.07	2.22	2.45	2.42	2.38
HY	2.22	2.11	2.48	2.23	2.23	2.60	2.59	2.66	2.48
ARH	2.17	2.29	2.50	2.28	2.29	2.88	2.45	2.61	2.29
ADP	2.52	2.82	2.94	3.21	2.43	3.00	2.56	2.64	2.50
AHN	2.27	2.23	2.58	2.25	2.20	2.49	2.50	2.60	2.44
A13	2.26	2.17	2.44	2.32	2.45	2.62	2.70	2.45	2.44
MB	2.12	2.31	2.56	2.06	2.20	2.17	2.54	2.61	2.52
IC	2.15	2.24	2.27	2.11	2.34	2.24	2.63	2.73	2.54
APN	2.14	2.28	2.40	2.03	2.19	2.13	2.48	2.48	2.40
SNc	2.31	2.53	2.63	2.26	2.22	2.29	2.60	2.75	2.60
P	2.33	2.31	2.43	2.32	2.24	2.55	2.42	2.61	2.49
KF	2.18	2.24	2.26	2.43	2.25	2.54	2.52	2.43	2.40
Acs5	2.19	2.12	2.31	2.31	2.07	2.41	2.46	2.42	2.40
CS	2.12	2.04	2.27	1.90	2.04	2.10	2.35	2.50	2.44
MY	2.20	2.16	2.36	2.17	2.28	2.29	2.59	2.74	2.50
AP	2.05	2.12	2.21	2.08	2.22	1.97	2.37	2.56	2.30
ACVI	2.30	2.12	2.35	2.27	2.22	2.12	2.50	2.66	2.46
CB	2.18	2.36	2.67	2.55	2.31	2.40	2.49	2.71	2.56
FN	2.10	2.15	2.34	2.13	2.02	2.09	2.46	2.38	2.38
oct	2.31	2.30	2.45	2.27	2.26	2.37	2.59	2.63	2.46

Supplementary table 4

Quantification of the radii in the C57BL/6J, CD1 and BALB/c samples in the voxel-corrected space, units are in vx.

Cluster	BL6#1	BL6#2	BL6#3	CD1#1	CD1#2	CD1#3	BALBC #1	BALBC #2	BALBC #3
FRP	719.81	1118.68	733.15	287.84	596.06	146.94	383.64	583.69	629.29
MO	1048.25	1232.20	825.23	656.95	1093.14	508.53	1040.80	1013.67	891.79
SS	1222.57	1441.97	1162.48	776.57	1451.00	892.96	1021.11	1031.19	866.42
GU	1149.30	1127.14	933.31	881.49	1470.88	1126.30	841.42	836.62	823.94
VISC	1016.51	1143.88	919.24	729.46	1415.35	910.67	666.37	765.01	775.18
AUD	929.26	1358.36	936.36	889.46	1141.52	851.74	1065.89	1163.60	1073.18
VIS	928.94	1242.70	886.48	586.44	1054.50	606.48	968.61	1097.99	962.29
ACA	1028.65	986.51	785.10	625.14	1197.54	693.00	814.56	994.05	783.90
PL	1069.15	1000.28	740.29	563.85	1035.32	703.89	776.62	921.60	902.68
ILA	1072.84	730.91	502.99	728.36	994.08	882.39	731.92	883.94	780.31
ORB	1359.66	1111.72	901.02	706.82	1210.53	749.79	869.66	1029.35	940.88
AI	1044.59	1045.48	802.82	630.52	1079.05	729.32	916.89	850.15	849.33
RSP	1213.69	1167.69	826.12	556.53	1236.67	703.25	776.24	1093.96	896.48
PTL	589.85	1232.58	837.70	615.78	1010.92	563.72	967.03	1023.68	818.77
TE	696.56	1142.78	814.66	720.03	1114.58	685.05	805.32	1008.26	887.77
PERI	628.88	936.89	764.54	434.56	915.32	486.02	648.91	745.63	774.86
ECT	615.54	973.08	756.32	539.22	1002.36	544.91	660.33	863.42	826.04
OLF	918.29	528.93	721.69	503.74	1232.31	773.96	831.16	874.80	784.00
AOB	1095.15	844.41	682.01	523.93	1094.73	744.21	810.80	719.11	830.29
AOBgr	698.45	506.86	772.76	326.25	769.50	551.26	793.40	809.63	725.02
AON	1246.96	777.66	750.09	665.89	1075.61	724.66	885.26	925.20	858.75
TT	952.74	404.86	616.27	514.86	919.39	783.44	812.56	782.74	815.38
DP	984.41	580.32	521.76	643.00	946.98	946.02	731.76	875.84	783.36
PIR	1014.22	893.75	902.01	535.96	1027.76	822.62	960.81	928.15	849.46
COA	519.31	508.62	688.35	302.72	726.67	517.43	697.20	668.07	705.16
PAA	519.67	331.52	669.07	268.43	832.27	605.50	660.83	707.58	635.27
TR	713.29	725.55	722.80	365.16	850.23	492.55	688.54	701.81	765.26
CA	689.09	712.58	659.15	500.22	790.85	552.59	621.69	736.13	636.36
CA1sp	657.85	604.65	632.59	443.61	703.31	500.71	517.49	686.62	608.19
ENT	739.55	1078.29	717.63	516.81	976.19	520.25	749.89	844.99	744.69
PAR	879.62	946.67	770.00	607.20	1260.23	601.76	885.30	1201.17	772.23
POST	1032.48	1241.02	1094.03	712.26	1006.41	698.99	870.70	1098.09	791.99
PRE	863.57	1153.73	1137.18	581.74	1283.05	856.64	978.21	1150.62	883.73
SUB	949.30	1041.07	953.54	690.63	1063.20	774.25	836.39	996.21	770.36
ProS	819.91	684.89	534.20	500.48	887.92	388.53	538.65	587.25	501.86
CLA	1056.38	881.31	783.01	526.75	904.03	786.12	783.96	821.79	687.97
EP	901.38	825.73	728.23	452.45	859.75	650.63	716.91	745.74	702.97
LA	622.41	651.07	557.65	460.41	810.48	459.70	580.43	671.64	631.47
BLA	667.57	675.91	683.98	399.58	857.36	575.35	760.15	782.80	736.35
BMA	709.76	692.22	715.82	485.51	824.96	714.55	777.27	776.70	779.55
PA	750.73	706.11	749.80	443.59	788.33	611.11	1001.29	879.84	804.16
CP	931.54	754.27	769.97	526.23	943.65	663.07	587.46	734.87	541.26

ACB	726.78	468.84	683.56	386.39	840.11	550.87	924.94	894.13	726.36
LS	639.18	403.36	569.81	459.94	804.94	658.75	410.96	464.19	436.64
AAA	754.54	606.42	665.74	453.88	732.46	740.79	762.91	716.18	736.72
GPe	800.59	579.02	685.23	393.02	800.25	485.55	541.33	638.24	631.98
MA	894.22	548.66	695.15	319.83	873.57	619.46	839.26	720.59	579.14
MS	963.30	506.92	823.94	393.19	987.01	762.96	779.51	670.04	639.58
BAC	782.50	367.08	554.83	325.31	698.31	511.71	461.13	470.45	401.36
BS	704.80	569.94	713.50	518.26	817.19	626.73	664.73	771.37	739.95
DORsm	739.20	724.49	759.70	625.93	1010.94	654.18	829.20	955.45	908.10
AD	710.52	530.64	707.36	509.14	933.33	562.48	650.16	718.36	726.77
HY	912.22	449.00	684.05	445.60	885.77	766.83	763.63	708.17	691.49
ARH	697.02	246.12	446.55	394.21	776.16	526.03	765.37	684.29	699.34
ADP	916.67	358.25	632.37	410.92	905.57	739.81	821.80	723.03	648.11
AHN	898.72	445.45	650.43	440.86	879.34	716.36	786.07	751.71	710.06
A13	889.18	664.83	833.02	574.50	980.00	763.20	824.92	783.77	781.41
MB	920.67	793.93	788.32	590.22	1041.19	615.08	644.43	845.51	702.16
IC	1029.18	1289.43	1096.39	751.61	1438.99	694.66	630.47	1024.37	806.88
APN	1049.56	832.80	867.45	683.94	1090.88	584.14	588.78	837.74	666.08
SNc	795.22	759.98	734.68	573.06	976.72	478.87	468.03	658.41	510.82
P	493.76	318.81	482.09	263.62	579.83	333.32	431.94	550.02	587.69
KF	507.24	482.30	661.72	282.48	563.46	354.57	561.88	776.05	891.69
Acs5	636.43	357.36	700.60	377.53	798.93	459.86	557.17	738.23	745.40
CS	812.85	560.07	754.40	447.45	967.60	476.53	476.94	612.59	637.48
MY	660.51	364.51	482.57	261.65	436.11	314.62	632.36	548.89	508.50
AP	764.94	794.94	793.32	447.33	733.75	381.68	857.35	1004.94	830.18
ACVI	1001.85	606.15	878.32	445.09	724.62	482.96	942.05	1004.80	894.96
CB	761.08	609.37	606.03	297.01	551.35	445.34	549.30	724.44	766.69
FN	1007.05	1152.18	1261.14	485.80	483.46	814.84	1016.73	1343.19	1311.83
oct	671.42	523.78	522.04	357.37	587.50	381.05	504.58	592.97	525.37

Supplementary table 5

Quantification of the local vascular length per volume in the C57BL/6J, CD1 and BALB/c samples in the microscopy space. Units are in mm/mm3.

Cluster	BL6#1	BL6#2	BL6#3	CD1#1	CD1#2	CD1#3	BALBC #1	BALBC #2	BALBC #3
FRP	23524	35671	20593	7322	19611	2991	9357	15228	19019
MO	39776	46880	24446	17511	39601	13432	38467	33505	27601
SS	50955	63539	43967	22296	62891	29549	34831	35821	26155
GU	44052	41461	29646	25455	65769	38823	24384	26636	24383
VISC	38342	44642	30287	20389	61105	29690	15299	21212	20002
AUD	30604	54404	29622	26250	41971	27252	35903	42101	35349
VIS	31402	48335	27079	14373	37617	16370	29846	38792	29951
ACA	36955	29816	22417	16131	47382	19575	23352	30328	22768
PL	38603	29477	19432	13501	35750	20427	19472	27722	27366
ILA	37816	16328	10361	17993	30320	25411	15359	22456	19290
ORB	57233	37077	27086	17922	44024	21437	23985	31380	28755
AI	38586	35276	22411	15510	37532	21014	27625	24993	23888
RSP	48191	42920	25043	13611	49439	20492	20279	39112	27817
PTL	18202	48296	27920	16219	34279	15116	31532	34435	25245
TE	19758	40058	22684	18874	40247	18696	20737	32153	24805
PERI	17292	28715	19853	8909	29664	11527	13559	19521	19375
ECT	15504	29570	19494	11924	33371	13125	14312	24089	21435
OLF	36378	17766	23892	13782	51825	24895	28538	29626	26177
AOB	42498	30535	23087	12246	42653	19413	23379	20805	28818
AOBgr	22467	12598	22046	6260	21666	14139	24596	23304	20363
AON	50084	21192	20271	16628	36730	20329	27574	26851	24663
TT	33906	9083	15401	12692	29852	23552	26186	23141	26906
DP	34126	12167	10567	15050	30600	28553	16172	23805	20569
PIR	38037	29002	28671	12779	36128	25360	33170	29812	25456
COA	14709	13070	16841	5710	20309	13039	21850	19152	18728
PAA	14677	9006	17760	4614	23225	15644	21464	21229	18715
TR	20034	18850	17977	6664	26085	11179	19672	19929	20081
CA	20639	18296	16823	11043	23758	14272	14845	18935	14943
CA1sp	19524	13929	15313	9210	19295	12350	10362	15826	13496
ENT	23338	37302	21371	12602	35910	14294	20336	26644	20433
PAR	33758	35125	26234	16274	55377	19536	28754	45529	22765
POST	35759	47237	37547	18518	34643	20191	26600	37512	22960
PRE	27593	41367	39199	13187	49737	26456	31537	39650	24860
SUB	32851	34550	29948	17240	39242	22657	23730	30609	20162
ProS	28791	19378	13664	13342	30513	8940	13334	15221	11472
CLA	38557	24851	20872	10496	28508	21857	19897	21760	16148
EP	30218	22047	18339	8850	25408	16373	17539	18654	16472
LA	17633	13708	11816	8513	23186	9707	11928	15858	13448
BLA	19702	15504	16330	7315	24692	13087	19321	19902	17472
BMA	21083	16502	18569	10279	24232	19367	20990	20558	20019
PA	23221	17257	19099	8729	23440	16623	34509	25428	20982
CP	33159	19558	21393	11784	30174	17953	12657	18690	11997

ACB	23144	10253	17072	7649	26037	14381	30581	26629	19925
LS	17041	6650	11918	9003	23904	16428	6785	8262	7815
AAA	25446	13541	16447	9484	20930	21667	21657	18400	18885
GPe	24976	12139	16739	7940	22108	10753	11803	15073	14772
MA	30875	11542	17445	5815	27084	16355	24868	18066	13439
MS	33886	10198	23886	7692	36461	23346	23606	16646	17413
BAC	24068	5733	11756	5953	19364	12447	8833	8980	7237
BS	21273	13001	18448	11699	24688	16487	15851	21019	18710
DORsm	22144	18236	20772	15104	33095	17050	23086	29349	26033
AD	20509	11571	17748	10779	28015	13326	15526	17775	17721
HY	30920	9484	18077	9572	28510	23337	20581	18623	17708
ARH	22573	4768	10441	7879	22499	13528	20835	18703	18226
ADP	32210	6960	16226	8228	30795	22818	24216	18872	16923
AHN	30442	9800	16367	9025	28260	20526	21359	20148	18619
A13	30072	17325	25442	14771	33976	23269	25072	23658	22269
MB	31271	21590	21256	13718	37148	16118	15306	23874	17994
IC	37799	50760	38351	19526	61811	19891	15307	33208	23985
APN	37315	22166	25184	16654	39738	14876	12846	23064	16041
SNc	25162	19831	18732	12978	32327	10200	9374	16264	10874
P	14324	6858	12292	5169	17488	7196	10549	14639	16594
KF	13943	12055	19606	5494	15559	7478	14543	22827	28922
Acs5	18747	6484	19025	7513	23303	10724	13977	19301	20227
CS	25654	11964	19787	9253	31869	9706	9184	14091	15509
MY	23133	9594	14425	5800	13704	8325	20281	17362	15108
AP	25007	23692	25283	10523	25399	9100	27271	35320	26199
ACVI	37345	13709	25953	9118	21117	11687	28554	33776	27172
CB	26645	18278	19501	6460	17132	12011	15181	23935	26402
FN	36062	42105	51586	10895	10967	26773	37518	55981	54320
oct	21725	13587	13891	7346	16906	9292	12936	15907	13310

Supplementary table 6

Quantification of the number of bifurcation points in the C57BL/6J, CD1 and BALB/c samples in the microscopy space, units are in counts/mm3.

Cluster	BL6#1	BL6#2	BL6#3	CD1#1	CD1#2	CD1#3	BALBC #1	BALBC #2	BALBC #3
FRP	6.17	7.04	7.00	10.60	6.79	7.98	7.33	6.95	7.09
MO	6.21	7.21	6.88	6.25	6.11	6.58	7.35	7.71	7.52
SS	6.43	7.40	7.14	6.37	6.50	6.76	7.40	7.78	7.51
GU	6.63	8.05	8.03	6.43	7.10	7.15	8.45	8.27	8.26
VISC	6.68	7.97	7.28	6.89	6.98	7.35	7.60	7.72	7.02
AUD	6.06	7.13	6.80	6.41	5.90	6.42	7.74	8.00	7.51
VIS	6.21	7.03	6.80	6.25	6.10	6.25	7.44	7.93	7.42
ACA	7.01	7.06	7.48	6.59	6.95	7.36	9.44	10.37	8.38
PL	6.52	7.44	6.87	6.41	6.35	7.01	7.99	8.38	8.24
ILA	6.95	7.28	7.26	6.93	6.45	7.05	8.05	8.73	8.08
ORB	6.81	7.24	7.01	6.71	6.31	6.55	7.51	7.30	7.92
AI	6.42	7.55	7.43	6.44	6.46	6.82	8.15	8.18	7.58
RSP	6.31	6.90	6.89	6.35	6.40	6.70	7.72	8.21	8.35
PTL	6.11	7.03	6.81	6.08	6.13	6.29	7.58	7.87	7.47
TE	6.12	7.24	6.81	6.13	5.94	5.98	7.47	7.90	7.25
PERI	6.39	7.26	6.99	6.06	6.21	6.08	7.62	7.71	7.52
ECT	6.38	7.13	6.85	6.10	6.07	5.98	7.64	7.96	7.42
OLF	6.88	7.31	7.41	6.79	6.60	7.43	7.62	7.76	7.55
AOB	6.45	8.09	7.74	6.49	7.39	7.31	7.91	8.34	7.34
AOBgr	7.87	8.01	8.44	7.75	7.05	8.80	8.11	7.49	7.42
AON	6.46	6.83	7.25	6.43	6.61	6.74	7.71	7.89	8.05
TT	8.57	7.59	8.58	7.61	6.92	8.76	8.73	8.01	7.83
DP	6.64	7.04	7.44	6.39	6.33	7.61	8.32	7.98	8.22
PIR	6.54	7.14	7.67	6.43	6.53	7.03	8.20	8.08	7.66
COA	6.48	6.99	7.47	6.90	6.53	6.86	9.06	8.81	7.93
PAA	6.67	6.77	7.76	7.28	6.47	7.36	8.76	8.23	7.72
TR	6.49	7.43	7.39	6.31	6.57	5.98	8.20	9.07	7.62
CA	7.68	7.46	7.94	7.71	6.72	8.11	11.78	12.43	9.66
CA1sp	7.02	6.69	7.25	6.37	6.22	8.57	7.80	7.65	8.29
ENT	6.26	7.24	6.95	6.24	6.74	6.67	7.55	8.11	7.53
PAR	7.32	6.92	7.00	6.48	6.81	7.61	7.39	7.46	7.26
POST	7.29	7.83	8.19	7.91	6.93	7.63	8.17	7.66	8.83
PRE	9.85	7.81	7.60	9.12	7.27	8.70	10.48	7.45	10.80
SUB	7.01	7.50	7.57	7.01	7.19	6.76	7.54	7.69	7.37
ProS	6.31	7.04	7.13	6.41	6.30	6.58	7.58	7.99	8.00
CLA	6.65	7.22	7.85	6.36	6.88	7.00	8.64	8.15	7.62
EP	6.50	7.25	7.68	6.37	6.59	6.83	8.54	8.33	7.81
LA	6.24	6.39	7.19	6.31	6.41	6.57	8.89	8.89	8.11
BLA	6.25	6.75	7.62	6.31	6.57	6.54	8.89	8.88	8.19
BMA	6.38	6.61	7.66	6.53	6.74	7.14	9.16	8.87	8.61
PA	6.18	6.72	7.42	6.18	6.25	6.50	8.57	8.62	7.79
CP	6.90	6.70	7.62	6.77	6.61	7.54	7.90	8.02	7.66

ACB	6.48	6.14	7.11	6.65	6.17	6.87	7.74	7.52	7.03
LS	6.15	6.40	7.33	6.46	6.87	6.44	7.02	7.47	7.14
AAA	6.89	6.81	7.54	7.79	6.94	7.88	9.10	8.24	8.37
GPe	6.57	6.21	7.39	6.54	6.66	7.29	7.75	7.95	7.55
MA	6.83	6.31	7.53	6.93	6.36	7.22	7.68	7.41	7.42
MS	6.90	6.83	7.66	7.57	7.07	8.80	7.28	7.65	7.38
BAC	6.69	7.60	8.04	6.00	7.16	6.09	7.27	7.78	7.34
BS	6.36	6.57	7.16	6.45	6.47	6.69	7.70	7.66	7.37
DORsm	6.42	6.68	7.30	6.43	6.40	6.52	7.90	7.64	7.67
AD	6.21	6.41	6.93	6.41	6.21	6.67	7.35	7.26	7.15
HY	6.65	6.33	7.43	6.70	6.70	7.79	7.77	7.98	7.43
ARH	6.51	6.88	7.51	6.85	6.87	8.65	7.34	7.82	6.86
ADP	7.55	8.47	8.82	9.63	7.28	8.99	7.67	7.92	7.49
AHN	6.81	6.69	7.73	6.74	6.59	7.47	7.49	7.81	7.32
A13	6.78	6.51	7.31	6.97	7.36	7.86	8.11	7.36	7.31
MB	6.37	6.92	7.68	6.17	6.60	6.51	7.62	7.82	7.56
IC	6.45	6.71	6.82	6.32	7.02	6.71	7.90	8.18	7.62
APN	6.43	6.84	7.20	6.08	6.58	6.39	7.43	7.43	7.19
SNc	6.92	7.59	7.89	6.78	6.65	6.88	7.79	8.26	7.81
P	6.99	6.92	7.30	6.96	6.72	7.65	7.27	7.83	7.46
KF	6.54	6.71	6.77	7.28	6.76	7.61	7.56	7.30	7.19
Acs5	6.58	6.37	6.94	6.92	6.21	7.24	7.38	7.26	7.21
CS	6.37	6.11	6.80	5.70	6.13	6.29	7.04	7.51	7.32
MY	6.59	6.49	7.08	6.52	6.85	6.86	7.76	8.21	7.51
AP	6.15	6.37	6.62	6.25	6.67	5.90	7.11	7.67	6.89
ACVI	6.89	6.37	7.05	6.80	6.65	6.36	7.50	7.98	7.38
CB	6.53	7.09	8.01	7.66	6.94	7.20	7.47	8.13	7.67
FN	6.30	6.44	7.01	6.40	6.05	6.27	7.37	7.13	7.14
oct	6.93	6.90	7.36	6.80	6.77	7.12	7.77	7.89	7.37

Supplementary table 7

Quantification of the radii in the C57BL/6J, CD1 and BALB/c samples in the microscopy space, units are in µm.

Cluster	BL6#1	BL6#2	BL6#3	CD1#1	CD1#2	CD1#3	BALBC #1	BALBC #2	BALBC #3
FRP	513.82	798.55	523.34	205.47	425.49	104.89	273.85	416.65	449.20
MO	748.27	879.58	589.07	468.95	780.32	363.00	742.96	723.58	636.58
SS	872.71	1029.32	829.81	554.34	1035.76	637.42	728.90	736.09	618.47
GU	820.40	804.59	666.22	629.23	1049.95	803.98	600.63	597.20	588.15
VISC	725.61	816.54	656.18	520.71	1010.32	650.06	475.67	546.08	553.35
AUD	663.33	969.64	668.40	634.92	814.85	608.00	760.86	830.61	766.07
VIS	663.10	887.08	632.79	418.62	752.73	432.92	691.42	783.77	686.91
ACA	734.28	704.20	560.42	446.24	854.84	494.68	581.45	709.58	559.57
PL	763.19	714.03	528.44	402.49	739.04	502.46	554.37	657.87	644.36
ILA	765.83	521.75	359.05	519.92	709.60	629.88	522.47	630.98	557.01
ORB	970.56	793.58	643.17	504.55	864.11	535.22	620.79	734.78	671.63
AI	745.66	746.30	573.08	450.08	770.26	520.61	654.50	606.86	606.28
RSP	866.37	833.53	589.71	397.26	882.77	502.00	554.10	780.90	639.93
PTL	421.05	879.85	597.98	439.56	721.62	402.40	690.29	730.74	584.46
TE	497.22	815.75	581.53	513.97	795.62	489.01	574.86	719.72	633.72
PERI	448.91	668.78	545.75	310.20	653.38	346.93	463.21	532.25	553.12
ECT	439.39	694.61	539.88	384.91	715.51	388.97	471.36	616.33	589.65
OLF	655.50	377.57	515.16	359.59	879.66	552.47	593.31	624.46	559.64
AOB	781.75	602.76	486.84	374.00	781.45	531.24	578.77	513.32	592.68
AOBgr	498.57	361.81	551.62	232.89	549.29	393.51	566.35	577.94	517.54
AON	890.12	555.11	535.43	475.33	767.80	517.29	631.93	660.44	613.00
TT	680.10	289.00	439.91	367.52	656.28	559.24	580.03	558.74	582.04
DP	702.70	414.25	372.45	458.99	675.98	675.29	522.35	625.20	559.19
PIR	723.98	637.98	643.88	382.58	733.64	587.21	685.85	662.54	606.37
COA	370.70	363.07	491.36	216.09	518.72	369.35	497.68	476.89	503.36
PAA	370.96	236.65	477.60	191.62	594.10	432.22	471.72	505.09	453.47
TR	509.17	517.92	515.96	260.66	606.92	351.59	491.50	500.97	546.27
CA	491.89	508.66	470.52	357.07	564.53	394.46	443.78	525.47	454.25
CA1sp	469.59	431.62	451.56	316.66	502.04	357.42	369.40	490.13	434.14
ENT	527.91	769.72	512.26	368.92	696.84	371.37	535.30	603.18	531.58
PAR	627.90	675.76	549.65	433.44	899.59	429.56	631.95	857.43	551.24
POST	737.01	885.88	780.95	508.43	718.40	498.96	621.53	783.85	565.34
PRE	616.44	823.57	811.75	415.26	915.88	611.49	698.27	821.34	630.84
SUB	677.64	743.15	680.67	492.99	758.94	552.69	597.04	711.13	549.90
ProS	585.27	488.89	381.33	357.25	633.82	277.35	384.50	419.20	358.24
CLA	754.07	629.10	558.94	376.01	645.32	561.16	559.61	586.62	491.09
EP	643.43	589.43	519.83	322.98	613.71	464.44	511.75	532.33	501.80
LA	444.29	464.75	398.06	328.65	578.55	328.14	414.32	479.44	450.76
BLA	476.53	482.49	488.25	285.23	612.01	410.70	542.62	558.78	525.62
BMA	506.65	494.13	510.97	346.57	588.88	510.07	554.84	554.43	556.47
PA	535.89	504.04	535.23	316.64	562.73	436.23	714.75	628.06	574.03
CP	664.96	538.42	549.63	375.64	673.60	473.32	419.35	524.57	386.37

ACB	518.80	334.67	487.95	275.81	599.69	393.23	660.25	638.26	518.50
LS	456.27	287.93	406.75	328.32	574.59	470.23	293.36	331.35	311.69
AAA	538.61	432.88	475.22	323.99	522.85	528.80	544.59	511.23	525.89
GPe	571.48	413.32	489.14	280.55	571.24	346.60	386.42	455.60	451.12
MA	638.32	391.65	496.22	228.30	623.58	442.19	599.09	514.38	413.41
MS	687.63	361.85	588.15	280.67	704.56	544.62	556.44	478.30	456.55
BAC	558.57	262.03	396.06	232.21	498.48	365.27	329.17	335.82	286.51
BS	503.11	406.84	509.32	369.95	583.33	447.38	474.51	550.62	528.20
DORsm	527.66	517.16	542.30	446.81	721.64	466.98	591.91	682.03	648.23
AD	507.19	378.78	504.93	363.44	666.24	401.52	464.10	512.79	518.79
HY	651.17	320.51	488.30	318.08	632.29	547.38	545.10	505.51	493.61
ARH	497.55	175.69	318.76	281.40	554.05	375.50	546.34	488.47	499.21
ADP	654.35	255.73	451.40	293.33	646.42	528.10	586.63	516.12	462.64
AHN	641.53	317.97	464.29	314.70	627.70	511.36	561.12	536.59	506.86
A13	634.72	474.57	594.64	410.09	699.55	544.80	588.85	559.48	557.79
MB	657.20	566.73	562.73	421.31	743.23	439.06	460.01	603.55	501.22
IC	734.66	920.44	782.63	536.52	1027.19	495.87	450.05	731.22	575.98
APN	749.21	594.48	619.21	488.21	778.70	416.98	420.29	598.00	475.46
SNc	567.65	542.50	524.44	409.07	697.21	341.83	334.09	469.99	364.64
P	352.46	227.58	344.13	188.18	413.90	237.93	308.33	392.62	419.51
KF	362.08	344.28	472.36	201.65	402.21	253.10	401.08	553.97	636.51
Acs5	454.30	255.09	500.11	269.49	570.30	328.26	397.73	526.97	532.09
CS	580.24	399.79	538.51	319.40	690.70	340.16	340.45	437.28	455.05
MY	471.49	260.20	344.47	186.78	311.31	224.59	451.40	391.81	362.98
AP	546.03	567.45	566.29	319.32	523.77	272.45	612.00	717.35	592.61
ACVI	715.15	432.69	626.97	317.72	517.25	344.75	672.46	717.26	638.85
CB	543.28	434.98	432.60	212.02	393.57	317.89	392.11	517.13	547.28
FN	718.86	822.46	900.24	346.78	345.11	581.66	725.77	958.80	936.42
oct	479.28	373.89	372.65	255.10	419.38	272.00	360.18	423.28	375.03

Supplementary table 8

Quantification of the local vascular length (per volume) in the C57BL/6J, CD1 and BALB/c samples in the anatomical space. Units are in mm/mm3.

Cluster	BL6#1	BL6#2	BL6#3	CD1#1	CD1#2	CD1#3	BALBC #1	BALBC #2	BALBC #3
FRP	14188	21513	12420	4416	11827	1804	5643	9184	11470
MO	23989	28273	14743	10561	23884	8101	23199	20207	16646
SS	30731	38321	26517	13447	37930	17821	21007	21604	15774
GU	26568	25005	17880	15352	39666	23414	14706	16064	14706
VISC	23124	26924	18266	12296	36853	17906	9227	12793	12063
AUD	18457	32811	17865	15831	25313	16436	21653	25391	21319
VIS	18939	29151	16331	8668	22687	9873	18000	23396	18064
ACA	22288	17982	13520	9729	28576	11806	14084	18291	13732
PL	23282	17778	11719	8143	21561	12320	11744	16719	16504
ILA	22807	9847	6249	10852	18286	15325	9263	13544	11634
ORB	34517	22361	16336	10809	26551	12929	14465	18925	17342
AI	23271	21275	13516	9354	22635	12673	16661	15073	14407
RSP	29064	25885	15103	8209	29817	12359	12230	23588	16777
PTL	10978	29128	16839	9782	20674	9116	19017	20768	15225
TE	11916	24159	13681	11383	24273	11275	12507	19391	14960
PERI	10429	17318	11973	5373	17891	6952	8177	11773	11685
ECT	9350	17833	11757	7191	20126	7916	8632	14528	12927
OLF	21940	10715	14410	8312	31256	15014	17211	17867	15787
AOB	25631	18415	13924	7386	25724	11708	14100	12548	17380
AOBgr	13550	7598	13296	3775	13067	8527	14834	14055	12281
AON	30206	12781	12226	10028	22152	12261	16630	16194	14875
TT	20449	5478	9288	7655	18004	14204	15793	13956	16227
DP	20581	7338	6373	9077	18455	17221	9754	14357	12405
PIR	22940	17491	17291	7707	21789	15295	20005	17980	15353
COA	8871	7883	10157	3444	12249	7864	13178	11551	11295
PAA	8852	5432	10711	2783	14007	9435	12945	12803	11287
TR	12082	11368	10842	4019	15732	6742	11864	12020	12111
CA	12447	11034	10146	6660	14329	8608	8953	11420	9012
CA1sp	11775	8401	9236	5555	11637	7448	6250	9545	8139
ENT	14075	22497	12889	7601	21657	8621	12264	16069	12323
PAR	20360	21184	15822	9815	33398	11782	17342	27459	13729
POST	21566	28489	22645	11168	20893	12177	16043	22624	13847
PRE	16641	24949	23641	7953	29997	15956	19020	23913	14993
SUB	19812	20837	18062	10398	23667	13664	14311	18460	12160
ProS	17364	11687	8241	8047	18403	5392	8042	9180	6919
CLA	23254	14988	12588	6330	17193	13182	12000	13124	9739
EP	18225	13296	11060	5338	15324	9875	10578	11250	9934
LA	10635	8267	7126	5134	13984	5854	7194	9564	8110
BLA	11882	9351	9849	4412	14892	7893	11652	12003	10537
BMA	12715	9952	11199	6199	14615	11681	12659	12399	12074
PA	14005	10408	11519	5265	14137	10026	20813	15336	12654
CP	19999	11795	12902	7107	18198	10827	7634	11272	7236

ACB	13958	6184	10296	4613	15703	8673	18443	16060	12017
LS	10278	4011	7188	5430	14416	9908	4092	4983	4713
AAA	15347	8166	9919	5720	12623	13067	13062	11097	11389
GPe	15063	7321	10095	4789	13333	6485	7119	9091	8909
MA	18621	6961	10521	3507	16335	9864	14998	10896	8105
MS	20437	6150	14405	4639	21990	14080	14237	10039	10502
BAC	14516	3457	7090	3590	11678	7507	5327	5416	4365
BS	12830	7841	11126	7056	14889	9943	9560	12676	11284
DORsm	13355	10998	12527	9109	19960	10283	13923	17700	15700
AD	12369	6978	10704	6501	16896	8037	9363	10720	10688
HY	18648	5720	10902	5773	17194	14075	12413	11232	10680
ARH	13614	2876	6297	4752	13569	8159	12565	11280	10992
ADP	19426	4198	9786	4962	18572	13762	14605	11382	10206
AHN	18360	5911	9871	5443	17044	12379	12882	12151	11229
A13	18137	10449	15344	8908	20491	14033	15121	14268	13430
MB	18860	13021	12820	8274	22404	9721	9231	14399	10852
IC	22796	30614	23129	11776	37278	11996	9232	20028	14466
APN	22505	13368	15188	10044	23966	8972	7747	13910	9674
SNc	15175	11960	11297	7827	19497	6152	5654	9809	6558
P	8639	4136	7413	3118	10547	4340	6362	8829	10008
KF	8409	7270	11824	3313	9383	4510	8771	13767	17443
Acs5	11307	3911	11474	4531	14054	6468	8429	11640	12199
CS	15472	7215	11933	5581	19220	5854	5539	8498	9354
MY	13952	5786	8700	3498	8265	5021	12231	10471	9112
AP	15082	14288	15248	6347	15318	5488	16447	21302	15801
ACVI	22523	8268	15652	5499	12736	7048	17221	20370	16387
CB	16070	11024	11761	3896	10333	7244	9155	14435	15923
FN	21749	25394	31112	6571	6614	16147	22627	33762	32761
oct	13102	8194	8378	4431	10196	5604	7802	9594	8028

Supplementary table 9

Quantification of the number of bifurcation points in the C57BL/6J, CD1 and BALB/c samples in the anatomical space, units are in counts/mm^3.

Cluster	BL6#1	BL6#2	BL6#3	CD1#1	CD1#2	CD1#3	BALBC #1	BALBC #2	BALBC #3
FRP	7.30	8.33	8.28	12.55	8.03	9.44	8.68	8.22	8.39
MO	7.35	8.54	8.15	7.40	7.23	7.79	8.69	9.13	8.90
SS	7.61	8.75	8.45	7.54	7.69	8.00	8.76	9.21	8.89
GU	7.85	9.52	9.50	7.61	8.40	8.46	10.00	9.78	9.77
VISC	7.90	9.43	8.62	8.15	8.26	8.69	9.00	9.14	8.31
AUD	7.18	8.44	8.05	7.59	6.99	7.60	9.17	9.47	8.88
VIS	7.35	8.32	8.04	7.40	7.22	7.39	8.81	9.39	8.78
ACA	8.29	8.35	8.86	7.79	8.23	8.71	11.18	12.27	9.92
PL	7.72	8.81	8.13	7.58	7.51	8.30	9.46	9.92	9.75
ILA	8.22	8.61	8.60	8.21	7.63	8.34	9.53	10.33	9.57
ORB	8.06	8.57	8.29	7.94	7.46	7.76	8.88	8.64	9.37
AI	7.60	8.93	8.79	7.63	7.64	8.07	9.64	9.69	8.97
RSP	7.47	8.17	8.15	7.52	7.57	7.93	9.14	9.72	9.88
PTL	7.23	8.32	8.06	7.19	7.25	7.45	8.97	9.32	8.84
TE	7.25	8.57	8.06	7.26	7.03	7.08	8.85	9.36	8.59
PERI	7.57	8.59	8.28	7.17	7.35	7.20	9.01	9.13	8.90
ECT	7.55	8.43	8.11	7.22	7.18	7.08	9.05	9.42	8.78
OLF	8.15	8.65	8.77	8.04	7.81	8.79	9.01	9.19	8.93
AOB	7.63	9.57	9.16	7.68	8.75	8.66	9.36	9.87	8.69
AOBgr	9.32	9.48	9.99	9.18	8.35	10.41	9.60	8.87	8.78
AON	7.64	8.08	8.58	7.61	7.82	7.98	9.13	9.34	9.53
TT	10.14	8.98	10.15	9.01	8.19	10.37	10.33	9.48	9.26
DP	7.86	8.33	8.80	7.57	7.49	9.01	9.85	9.44	9.73
PIR	7.74	8.45	9.08	7.61	7.73	8.32	9.70	9.57	9.07
COA	7.67	8.28	8.84	8.16	7.72	8.11	10.72	10.43	9.39
PAA	7.90	8.01	9.19	8.62	7.66	8.71	10.36	9.74	9.14
TR	7.68	8.79	8.75	7.47	7.77	7.07	9.71	10.74	9.01
CA	9.09	8.84	9.40	9.13	7.95	9.59	13.94	14.71	11.43
CA1sp	8.30	7.92	8.59	7.54	7.36	10.15	9.23	9.06	9.81
ENT	7.41	8.57	8.22	7.39	7.98	7.90	8.94	9.60	8.91
PAR	8.66	8.20	8.28	7.67	8.06	9.01	8.75	8.84	8.59
POST	8.63	9.27	9.69	9.36	8.20	9.03	9.67	9.07	10.45
PRE	11.66	9.24	9.00	10.79	8.61	10.30	12.41	8.82	12.78
SUB	8.30	8.87	8.97	8.30	8.51	8.00	8.93	9.11	8.72
ProS	7.47	8.33	8.43	7.59	7.46	7.79	8.97	9.46	9.47
CLA	7.87	8.54	9.29	7.53	8.14	8.29	10.23	9.65	9.02
EP	7.69	8.58	9.09	7.54	7.80	8.08	10.11	9.86	9.24
LA	7.39	7.57	8.51	7.47	7.58	7.78	10.52	10.52	9.60
BLA	7.40	7.98	9.02	7.47	7.77	7.75	10.52	10.51	9.70
BMA	7.56	7.83	9.07	7.73	7.97	8.45	10.84	10.50	10.19
PA	7.32	7.95	8.78	7.31	7.40	7.70	10.14	10.20	9.22
CP	8.17	7.93	9.02	8.01	7.82	8.92	9.35	9.50	9.06

ACB	7.68	7.26	8.42	7.88	7.31	8.13	9.16	8.90	8.32
LS	7.28	7.58	8.67	7.65	8.14	7.62	8.31	8.84	8.45
AAA	8.16	8.06	8.93	9.23	8.21	9.33	10.77	9.75	9.91
GPe	7.78	7.35	8.75	7.74	7.88	8.63	9.17	9.41	8.93
MA	8.08	7.47	8.91	8.21	7.53	8.55	9.09	8.77	8.79
MS	8.17	8.09	9.07	8.96	8.37	10.42	8.62	9.06	8.74
BAC	7.92	8.99	9.52	7.11	8.47	7.20	8.61	9.21	8.69
BS	7.53	7.77	8.47	7.64	7.65	7.92	9.11	9.07	8.73
DORsm	7.60	7.91	8.64	7.61	7.57	7.72	9.35	9.04	9.08
AD	7.35	7.58	8.20	7.59	7.35	7.90	8.70	8.59	8.46
HY	7.88	7.49	8.79	7.93	7.93	9.22	9.20	9.44	8.79
ARH	7.71	8.14	8.89	8.11	8.13	10.23	8.69	9.25	8.12
ADP	8.94	10.03	10.44	11.40	8.62	10.64	9.08	9.38	8.87
AHN	8.06	7.92	9.15	7.98	7.80	8.84	8.86	9.24	8.66
A13	8.02	7.71	8.65	8.25	8.71	9.31	9.60	8.72	8.66
MB	7.53	8.19	9.09	7.31	7.81	7.70	9.02	9.26	8.95
IC	7.63	7.94	8.07	7.48	8.31	7.95	9.35	9.68	9.02
APN	7.61	8.10	8.53	7.19	7.79	7.56	8.80	8.79	8.51
SNc	8.19	8.98	9.33	8.03	7.88	8.14	9.21	9.78	9.25
P	8.28	8.19	8.65	8.24	7.96	9.06	8.61	9.27	8.83
KF	7.74	7.94	8.02	8.62	8.00	9.01	8.95	8.65	8.51
Acs5	7.79	7.54	8.22	8.19	7.35	8.57	8.74	8.59	8.53
CS	7.54	7.23	8.05	6.74	7.25	7.45	8.34	8.89	8.67
MY	7.80	7.68	8.37	7.72	8.11	8.12	9.19	9.72	8.89
AP	7.28	7.54	7.83	7.40	7.90	6.98	8.42	9.08	8.16
ACVI	8.16	7.54	8.34	8.04	7.87	7.53	8.87	9.45	8.73
CB	7.73	8.40	9.49	9.07	8.21	8.52	8.85	9.62	9.08
FN	7.46	7.62	8.30	7.57	7.16	7.43	8.72	8.44	8.45
oct	8.20	8.17	8.71	8.05	8.02	8.42	9.20	9.34	8.73

Supplementary table 10

Quantification of the radii in the C57BL/6J, CD1 and BALB/c samples in the anatomical space, units are in µm.

Brain region	References	*Normalized vascular length*			Region-match	Quantified volume (µm)
		Reported (m/mm^3)	Measured by VesSAP			
			microscopic space (m/mm^3)	anatomical space (m/mm^3)		
Cortex	Lugo-Hernandez et al.*	0.92 ± 0.17	1.28 ± 0.16	0.91 ± 0.11	yes	508×508×1500
Cortex	Tsai et al. **,[1]	0.88 ± 0.17	0.87 ± 0.13	0.63 ± 0.09	yes	256×1656×700
Cortex	Di Giovanna et al. ***	0.46 - 0.47	0.67 ± 0.03	0.48 ± 0.02	yes	361×361×350
Cortex	Zhang et al. ***, α	0.44 ± 0.04	1.47 ± 0.05	1.05 ± 0.04	no	504×504×886

*: 3DISCO technique, image acquisition in low (3.2x) and in high resolution (12.6x)

**: sucrose clearing of dissected dorsal cortex pieces

***: CLARITY technique

α: This study did not exactly define the quantified cortex regions and did not indicate a numerical correction for any potential volume change due to clearing[2], which can explain the difference compared to our results.

1 Tsai, P. S. et al. Correlations of neuronal and microvascular densities in murine cortex revealed by direct counting and colocalization of nuclei and vessels. Journal of Neuroscience 29, 14553-14570 (2009).

2 Kim, J. H. et al. Optimizing tissue-clearing conditions based on analysis of the critical factors affecting tissue-clearing procedures. Scientific reports 8, 12815 (2018).

Supplementary table 11

Comparison of VesSAP measurements with those in existing literature. Each comparison is calculated from n=3 C57BL/6J animals and two ROIs per animal. Data is shown as mean ± SD.

Cluster	BL6 vs. CD1	BL6 vs. BALBC	CD1 vs. BLABC	BL6 vs. CD1	BL6 vs. BALBC	CD1 vs. BLABC	BL6 vs. CD1	BL6 vs. BALBC	CD1 vs. BLABC
Average:	Local length	Local length	Local length	Local bifurc.	Local bifurc.	Local bifurc.	Local radius	Local radius	Local radius
FRP	0.41	0.09	-0.38	0.36	0.26	-0.17	0.31	-1.30	-1.49
MO	0.39	0.07	-0.37	0.35	0.24	-0.16	0.37	-1.31	-1.59
SS	0.38	0.07	-0.36	0.34	0.24	-0.15	0.36	-1.31	-1.59
GU	0.38	0.05	-0.38	0.34	0.22	-0.17	0.36	-1.31	-1.58
VISC	0.40	0.03	-0.41	0.36	0.21	-0.20	0.34	-1.31	-1.56
AUD	0.41	0.01	-0.45	0.37	0.18	-0.24	0.34	-1.33	-1.57
VIS	0.41	0.01	-0.45	0.37	0.19	-0.24	0.34	-1.32	-1.56
ACA	0.40	0.01	-0.44	0.36	0.19	-0.22	0.33	-1.31	-1.54
PL	0.40	0.00	-0.44	0.36	0.18	-0.23	0.33	-1.30	-1.54
ILA	0.39	0.00	-0.44	0.36	0.18	-0.23	0.32	-1.29	-1.52
ORB	0.41	0.00	-0.45	0.37	0.17	-0.25	0.32	-1.27	-1.50
AI	0.40	-0.02	-0.46	0.36	0.16	-0.25	0.31	-1.27	-1.49
RSP	0.40	-0.02	-0.46	0.36	0.15	-0.25	0.30	-1.27	-1.47
PTL	0.39	-0.04	-0.46	0.35	0.13	-0.26	0.29	-1.25	-1.45
TE	0.39	-0.04	-0.46	0.34	0.14	-0.25	0.29	-1.24	-1.43
PERI	0.39	-0.03	-0.46	0.35	0.13	-0.25	0.27	-1.23	-1.42
ECT	0.38	-0.04	-0.46	0.34	0.13	-0.25	0.25	-1.22	-1.40
OLF	0.38	-0.04	-0.45	0.34	0.12	-0.26	0.24	-1.22	-1.38
AOB	0.40	-0.03	-0.47	0.36	0.13	-0.27	0.23	-1.22	-1.38
AOBgr	0.40	-0.04	-0.48	0.36	0.12	-0.28	0.23	-1.23	-1.38
AON	0.40	-0.03	-0.46	0.35	0.13	-0.26	0.23	-1.27	-1.42
TT	0.40	-0.03	-0.46	0.35	0.12	-0.26	0.22	-1.25	-1.40
DP	0.42	-0.02	-0.46	0.36	0.14	-0.26	0.22	-1.29	-1.42
PIR	0.44	-0.01	-0.48	0.38	0.14	-0.27	0.21	-1.28	-1.40
COA	0.44	-0.01	-0.48	0.38	0.14	-0.27	0.20	-1.27	-1.38
PAA	0.44	0.01	-0.47	0.38	0.16	-0.26	0.20	-1.24	-1.35
TR	0.46	0.03	-0.47	0.39	0.17	-0.25	0.20	-1.23	-1.34
CA	0.45	0.03	-0.46	0.39	0.18	-0.24	0.18	-1.21	-1.31
CA1sp	0.45	0.02	-0.46	0.39	0.18	-0.24	0.17	-1.34	-1.43
ENT	0.45	0.02	-0.46	0.39	0.17	-0.25	0.18	-1.33	-1.44
PAR	0.44	0.01	-0.46	0.38	0.16	-0.25	0.17	-1.31	-1.42
POST	0.45	0.02	-0.46	0.40	0.17	-0.26	0.17	-1.32	-1.43
PRE	0.43	0.00	-0.46	0.37	0.15	-0.26	0.17	-1.35	-1.44
SUB	0.44	-0.01	-0.47	0.38	0.14	-0.26	0.19	-1.58	-1.65
ProS	0.43	-0.03	-0.48	0.37	0.12	-0.28	0.17	-1.60	-1.65
CLA	0.43	-0.05	-0.51	0.37	0.10	-0.30	0.16	-1.58	-1.61
EP	0.42	-0.07	-0.51	0.36	0.07	-0.31	0.14	-1.58	-1.58

LA	0.41	-0.09	-0.51	0.35	0.05	-0.31	0.11	-1.57	-1.53
BLA	0.41	-0.09	-0.52	0.35	0.05	-0.32	0.11	-1.53	-1.48
BMA	0.41	-0.08	-0.51	0.35	0.06	-0.31	0.09	-1.52	-1.43
PA	0.41	-0.07	-0.50	0.36	0.07	-0.31	0.09	-1.51	-1.40
CP	0.40	-0.04	-0.47	0.35	0.10	-0.28	0.06	-1.48	-1.33
ACB	0.40	-0.08	-0.50	0.34	0.06	-0.31	0.06	-1.46	-1.31
LS	0.40	-0.04	-0.47	0.35	0.09	-0.28	0.06	-1.45	-1.29
AAA	0.43	-0.06	-0.52	0.38	0.08	-0.33	0.06	-1.46	-1.28
GPe	0.44	-0.05	-0.52	0.38	0.09	-0.32	0.09	-1.45	-1.31
MA	0.43	-0.07	-0.52	0.38	0.07	-0.33	0.10	-1.41	-1.27
MS	0.42	-0.07	-0.52	0.38	0.07	-0.33	0.10	-1.40	-1.26
BAC	0.43	-0.09	-0.55	0.40	0.06	-0.36	0.16	-1.42	-1.39
BS	0.44	-0.12	-0.59	0.41	0.03	-0.40	0.09	-1.51	-1.36
DORsm	0.45	-0.11	-0.59	0.42	0.04	-0.41	0.08	-1.46	-1.31
AD	0.47	-0.07	-0.59	0.44	0.07	-0.40	0.05	-1.41	-1.23
HY	0.49	-0.06	-0.60	0.46	0.08	-0.42	0.05	-1.40	-1.20
ARH	0.52	-0.05	-0.62	0.49	0.08	-0.44	0.07	-1.35	-1.19
ADP	0.58	0.01	-0.60	0.52	0.12	-0.43	0.12	-1.38	-1.31
AHN	0.63	0.04	-0.62	0.57	0.13	-0.45	0.23	-1.82	-1.97
A13	0.66	0.07	-0.63	0.60	0.15	-0.47	0.22	-1.87	-1.99
MB	0.70	0.07	-0.66	0.64	0.15	-0.50	0.33	-1.85	-2.19
IC	0.72	0.04	-0.71	0.66	0.12	-0.55	0.26	-1.87	-2.07
APN	0.83	-0.07	-0.89	0.79	-0.01	-0.75	0.28	-1.75	-1.98
SNc	0.89	-0.17	-1.03	0.86	-0.11	-0.90	0.20	-1.74	-1.91
P	0.94	-0.28	-1.22	0.91	-0.20	-1.07	0.08	-1.98	-1.79
KF	1.04	-0.26	-1.29	0.99	-0.19	-1.12	0.10	-2.03	-1.89
Acs5	1.05	-0.19	-1.20	1.01	-0.13	-1.06	0.26	-1.96	-2.14
CS	1.19	-0.14	-1.24	1.13	-0.11	-1.11	0.34	-1.91	-2.25
MY	1.34	-0.24	-1.53	1.29	-0.21	-1.41	0.27	-1.86	-2.21
AP	1.51	-0.25	-1.65	1.40	-0.22	-1.48	0.31	-1.64	-2.03
ACVI	1.42	-0.18	-1.49	1.37	-0.15	-1.38	0.34	-1.61	-2.08
CB	1.34	-0.08	-1.26	1.34	-0.09	-1.19	0.30	-1.35	-1.74
FN	1.31	-0.07	-1.21	1.32	-0.10	-1.18	0.65	-1.74	-2.43
oct	1.21	0.46	-1.04	1.08	0.68	-0.77	0.73	-2.34	-3.32

Supplementary table 12

Statistical estimation of the difference between the local properties of the neurovasculature in the C57BL/6J, CD1 and BALB/c samples using Cohen's *d*. Each comparison is calculated from n=3 animals per strain.

5.2. Cellular and Molecular Probing of Intact Human Organs

Optical tissue transparency would allow scalable cellular and molecular investigation of 3D tissues with complex arrangement with a primary focus on the human brain histopathology. Recent publications have already attempted the clearing and imaging of adult human organs, yet, efficient clearing and imaging of the fluorescence signal in such thick tissues have remained a challenge because of the accumulation of dense and sturdy molecules in decades-aged tissues. In order to overcome these challenges, we developed SHANEL, a comprehensive method based on a novel tissue permeabilization chemistry to optically clear and label rigid human organs. Besides, the method proved successful not only in an adult human but also in adult porcine organs. Using SHANEL, we were the first to render the entire intact adult human brain and kidney transparent, perform, and capture 3D histology with antibodies and dyes in centimeters-depth. Moreover, we revealed structural details of several large human organs including the intact human eye, human thyroid, human kidney, and transgenic pig pancreas at the cellular resolution. As a final component, we provided an automated high-throughput deep learning pipeline to analyze millions of cells in cleared human brain tissues within hours with standard lab workstations.

Altogether, SHANEL is a powerful, highly scalable, unbiased technology to chart the 3D cellular and molecular organization of large intact grown-up mammalian organs.

Resource

Cell

Cellular and Molecular Probing of Intact Human Organs

Graphical Abstract

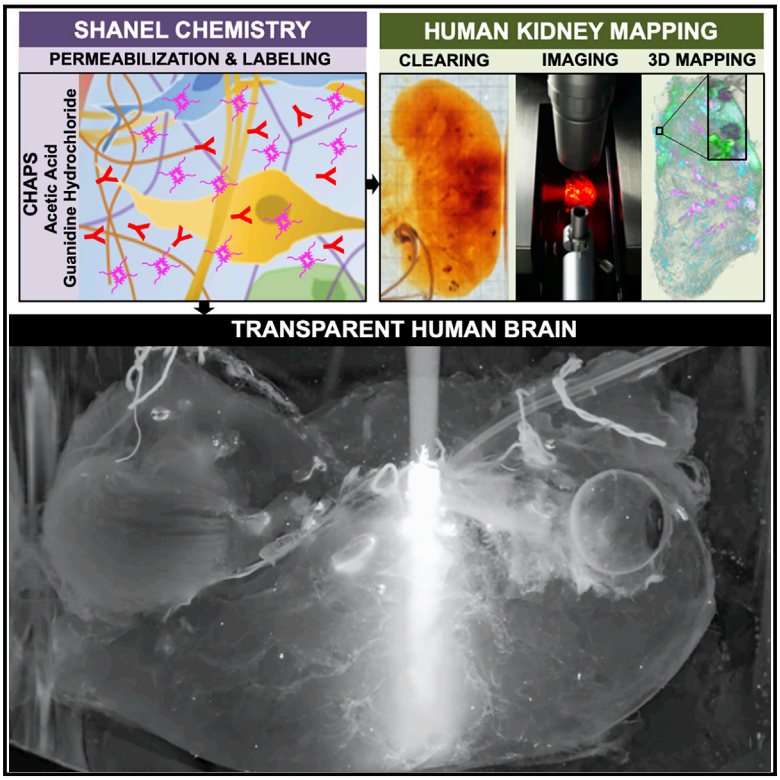

Authors

Shan Zhao, Mihail Ivilinov Todorov, Ruiyao Cai, ..., Eckhard Wolf, Ingo Bechmann, Ali Ertürk

Correspondence

erturk@helmholtz-muenchen.de

In Brief

Zhao et al. present an approach for intact human organ mapping that uses a new tissue permeabilization method to clear and deeply label whole organs followed by light-sheet microscopy imaging and a deep learning-based pipeline for 3D reconstruction and data analysis.

Highlights

- CHAPS forms smaller micelles allowing full permeabilization of aged human organs
- SHANEL enables centimeters deep molecular labeling and clearing of whole human organs
- SHANEL renders intact adult human brain and kidney transparent
- Deep learning and light-sheet microscopy with SHANEL allows human organ mapping

Zhao et al., 2020, Cell *180*, 796–812
February 20, 2020
https://doi.org/10.1016/j.cell.2020.01.030

CellPress

Cell

Resource

Cellular and Molecular Probing of Intact Human Organs

Shan Zhao,[1,2,3] Mihail Ivilinov Todorov,[1,2,4] Ruiyao Cai,[1,2] Rami Al -Maskari,[2,5,6,7] Hanno Steinke,[8] Elisabeth Kemter,[9,10,11] Hongcheng Mai,[1,2] Zhouyi Rong,[1,2] Martin Warmer,[12] Karen Stanic,[1] Oliver Schoppe,[5,6] Johannes Christian Paetzold,[5,6,7] Benno Gesierich,[2] Milagros N. Wong,[13] Tobias B. Huber,[13] Marco Duering,[2,14] Oliver Thomas Bruns,[12] Bjoern Menze,[5,6,7] Jan Lipfert,[15] Victor G. Puelles,[13,16] Eckhard Wolf,[9,10,11] Ingo Bechmann,[8] and Ali Ertürk[1,2,14,17,*]

[1]Insititute for Tissue Engineering and Regenerative Medicine (iTERM), Helmholtz Zentrum München, 85764 Neuherberg, Germany
[2]Institute for Stroke and Dementia Research (ISD), University Hospital, Ludwig Maximilian University of Munich (LMU), 81377 Munich, Germany
[3]Munich Medical Research School (MMRS), 80336 Munich, Germany
[4]Graduate School of Neuroscience (GSN), 82152 Munich, Germany
[5]Department of Computer Science, Technical University of Munich (TUM), 81675 Munich, Germany
[6]Center for Translational Cancer Research (TranslaTUM) of the TUM, 80798 Munich, Germany
[7]Graduate School of Bioengineering, Technical University of Munich (TUM), 85748 Munich, Germany
[8]Institute of Anatomy, University of Leipzig, 04109 Leipzig, Germany
[9]Institute of Molecular Animal Breeding and Biotechnology, Gene Center, Ludwig Maximilian University of Munich (LMU), 81377 Munich, Germany
[10]Center for Innovative Medical Models (CiMM), 85764 Oberschleißheim, Germany
[11]German Center for Diabetes Research (DZD), 85764 Neuherberg, Germany
[12]Helmholtz Pioneer Campus, Helmholtz Zentrum München, 85764 Neuherberg, Germany
[13]III. Department of Medicine, University Medical Center Hamburg-Eppendorf, 20246 Hamburg, Germany
[14]Munich Cluster for Systems Neurology (SyNergy), 81377 Munich, Germany
[15]Department of Physics and Center for Nanoscience, Ludwig Maximilian University of Munich (LMU), 80799 Munich, Germany
[16]Department of Nephrology, Monash Health, and Center for Inflammatory Diseases, Monash University, Melbourne VIC 3168, Australia
[17]Lead Contact
*Correspondence: erturk@helmholtz-muenchen.de
https://doi.org/10.1016/j.cell.2020.01.030

SUMMARY

Optical tissue transparency permits scalable cellular and molecular investigation of complex tissues in 3D. Adult human organs are particularly challenging to render transparent because of the accumulation of dense and sturdy molecules in decades-aged tissues. To overcome these challenges, we developed SHANEL, a method based on a new tissue permeabilization approach to clear and label stiff human organs. We used SHANEL to render the intact adult human brain and kidney transparent and perform 3D histology with antibodies and dyes in centimeters-depth. Thereby, we revealed structural details of the intact human eye, human thyroid, human kidney, and transgenic pig pancreas at the cellular resolution. Furthermore, we developed a deep learning pipeline to analyze millions of cells in cleared human brain tissues within hours with standard lab computers. Overall, SHANEL is a robust and unbiased technology to chart the cellular and molecular architecture of large intact mammalian organs.

INTRODUCTION

Structural and functional mapping of human organs is of a great interest for diverse biomedical studies. For example, mapping the human brain has been a major target of research as many countries have initiated their own "human brain mapping" projects (Reardon, 2016). Furthermore, tissue engineering efforts demand cellular maps of human organs to replicate large-scale human tissues and organs by emerging technologies including 3D-bioprinting (Kang et al., 2016; Murphy and Atala, 2014). Yet, the progress in mapping intact human organs has been limited, especially in deciphering the anatomical complexity, mainly due to a lack of scalable technologies to image human organs at the cellular level. Although magnetic resonance imaging (MRI) can provide longitudinal imaging for human organs including the brain and kidney, it lacks cellular resolution (Despotović et al., 2015; Heusch et al., 2014; Sijens et al., 2010). Therefore, tissue histology has been the major approach to study the molecular and cellular complexity of the human organs. Although routine standard histology is limited to small pieces of the human brain (typically a tissue section is ~1/10,000,000 of the whole brain volume), there have been efforts to perform histology for whole human brain mapping (Amunts et al., 2013; Ding et al., 2016). However, slicing and imaging thousands of thin sections from a whole human brain alone could require

years of labor, and subsequent reconstruction of the whole brain in 3D could be very complicated or impossible because of the numerous tissue distortions introduced by mechanical sectioning. Thus, a scalable and routine technology to enable cellular and molecular interrogation of centimeters-sized human organs could substantially reduce sectioning artifacts and also overcome complications in registering large-scale imaging data in 3D.

In the last decade, emerging optical tissue clearing methods have enabled fast 3D histology on transparent specimens avoiding major pitfalls of standard histology, especially tissue sectioning (Garvalov and Ertürk, 2017; Richardson and Lichtman, 2015). Furthermore, new deep tissue labeling methods were developed in combination with clearing methods to better phenotype whole rodent organs and human embryos (Belle et al., 2014, 2017; Cai et al., 2019; Deverman et al., 2016; Murray et al., 2015; Renier et al., 2014, 2016). Progress in optical tissue clearing first allowed the clearing of increasingly larger rodent samples (up to whole adult rodent bodies) (Jing et al., 2018; Pan et al., 2016; Tainaka et al., 2014; Yang et al., 2014). Then, the adaptation of light-sheet microscopy systems allowed the imaging of whole transparent rodent bodies (Cai et al., 2019; Kubota et al., 2017; Pan et al., 2016). However, clearing of human organs has been notoriously challenging so far, in particular for adult human brain tissue. Recent efforts with chemical screening of thousands of compounds (Tainaka et al., 2018) and application of electrical field forces (Chung et al., 2013) could achieve clearing of only small pieces of human organs. For example, it took 10 months to clear an 8 mm-thick human brain specimen (Morawski et al., 2018) and 3.5 months to clear a 5 mm-thick human striatum sample (Lai et al., 2018). Furthermore, deep-tissue antibody labeling methods developed on rodent tissues also encounter hurdles to label adult human tissue thicker than 1 mm (Park et al., 2018). We reasoned that highly myelinated content, lipidome complexity (Bozek et al., 2015), and age-related accumulation of diverse opaque and dense molecules such as lipofuscin and non-soluble collagen (Monnier et al., 1984; Moreno-García et al., 2018) impede penetration of chemicals deep into human organs, thereby blocking both clearing and labeling of centimeters-sized specimens.

Here, we introduce SHANEL (small-micelle-mediated human organ efficient clearing and labeling), a new method that is driven by detergent permeabilization chemistry allowing the penetration of labeling and clearing agents into centimeters-thick mammalian organs. Our approach enables histology using dyes and antibodies in human samples ranging from 1.5 cm thickness to whole adult human organs. We also show that the technology works on other large mammalian organs such as pig brain and pancreas, which can readily be labeled transgenically. Furthermore, we outline a deep learning-based pipeline to start accurate analysis of the large 3D dataset coming from the cleared human organs using standard lab computers. Thus, the SHANEL histology pipeline presented here can pave the way for cellular and molecular mapping of whole adult human organs for diverse applications.

RESULTS

Development of New Detergent Permeabilization Chemistry

We hypothesized that both labeling and clearing of large and sturdy human organs require a new permeabilization chemistry allowing deep tissue penetration of molecules. Ionic SDS (sodium dodecyl sulfate) and nonionic Triton X-100 are commonly used detergents for tissue clearing, and they are characterized as containing typical "head-to-tail" amphipathic regions. Their structural features lead to the formation of relatively large micelles suggesting that they can get stuck at tissue surfaces, and therefore exhibit low tissue permeabilization capacity and limit the penetration of molecules (Figures 1A–1C). We anticipated that detergents forming smaller micelles would be better candidates for deep tissue permeabilization as they could penetrate more rapidly and deeply into the tissue. We identified the zwitterionic detergent CHAPS (3-[(3-cholamidopropyl)dimethylammonio]-1-propanesulfonate), containing a rigid steroidal structure with a hydrophobic convex side, a hydrophilic concave side (bearing three hydroxyl groups), and a sulfobetaine-type polar group. CHAPS possesses atypical "facial" amphiphilicity (Lee et al., 2013). With this peculiar structure of hydrophobic and hydrophilic faces, it has higher critical micelle concentration (CMC), smaller aggregation number, and forms much smaller micelles compared to SDS and Triton X-100, which could enable its rapid permeabilization of large and sturdy tissues (Figures 1A–1C and S1A–S1C; Table S1). Indeed, CHAPS permeabilization allowed full and rapid penetration of methylene blue dye into centimeters-sized pig pancreas while SDS and Triton X-100 allowed only a limited penetration (Figures 1D–1F). Furthermore, once the micelles travel into the tissue and interact with the bilayer of lipids, the facial hydrophobic side of CHAPS reclines on the bilayer surface with a larger area rather than being embedded into the lipid as head-to-tail detergents. These different interaction behaviors of the detergents suggest that detectable fragments of SDS and Triton X-100 exist after washing while no residual of CHAPS would be left inside of the tissue (Rodi et al., 2014; White et al., 2017; Zhang et al., 2011). Thus, CHAPS could function as an efficient tissue permeabilization reagent by traveling throughout sturdy tissue and disrupting densely packed extracellular matrix ultrastructure meshes, without leaving behind residual detergent fragments after washing out.

Human organs carry residual blood clots due to several hours to days of delay until organ harvest after death. Heme in the blood causes strong autofluorescence at visible wavelengths (400–700 nm) and reduces the intensity of traveling light within the tissue, thereby impeding the full transparency of cleared organs (Tainaka et al., 2014). PFA-fixed blood was washed by detergent solutions, resulting in colorless supernatant and red pellet, indicating detergent alone was unable to remove the heme (Figure S1D). To overcome this issue, we first screened CHAPS compatible chemicals to elute the heme. In particular, we focused on effective, colorless, and cheap chemicals to facilitate scalability to large human organs (Figures 1G–1I, S1E, and S1F). Our screen showed that NMDEA (N-methyldiethanolamine) was an efficient candidate when combined

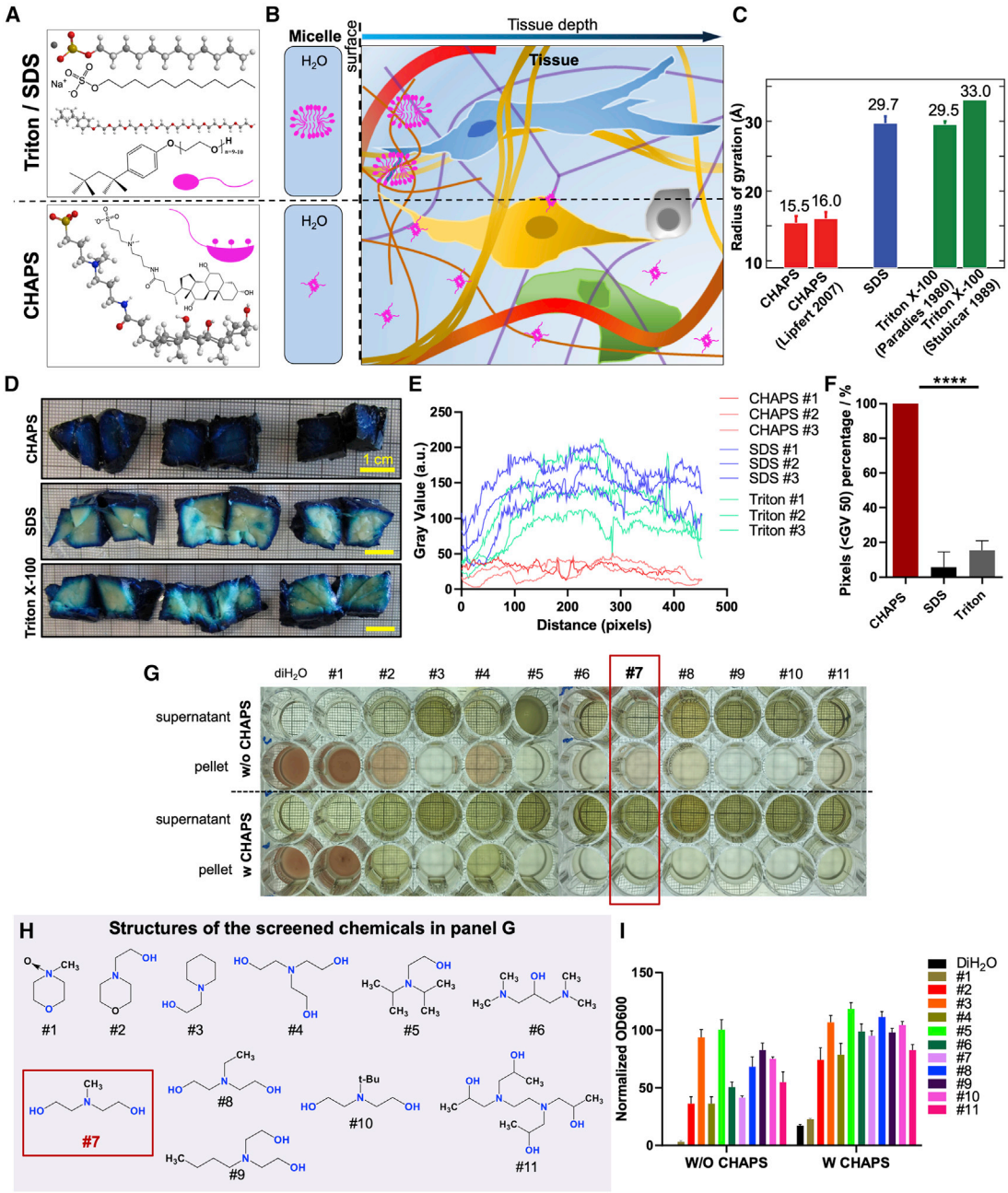

Figure 1. CHAPS-Mediated Deep Tissue Permeabilization and Blood Decolorization by Forming Small Micelle

(A) 3D molecular and structural features of SDS and Triton X-100 exhibiting typical head-to-tail amphiphilicity, whereas, CHAPS exhibiting peculiar facial amphiphilicity.

(B) Schematic diagram showing facial CHAPS could more efficiently and deeply permeabilize tissue compared to standard detergents (SDS and Triton X-100) owing to the formation of smaller micelle.

(C) Radii of gyration determined for CHAPS and SDS with their literature values (full references are in Table S1) for R_g (the size of micelle is characterized by the squared radius of gyration of the micellar core, R_g^2). Values for CHAPS and SDS represent mean and standard error from at least three independent repeats.

(D) Methylene blue dye staining of pig pancreas samples (1–1.5 cm cubes) after detergents permeabilization, showing CHAPS greatly enhanced deep tissue permeabilization for dye traveling comparing with SDS or Triton X-100.

(E) Profile plot along each sample dimension in (D).

(F) Quantification of the pixel numbers in (E) under selected threshold (gray value [GV] < 50) (n = 3). p values were calculated with a one-way ANOVA test; error bars show standard deviations.

(G and H) Screening of 11 chemicals in (H) without or with CHAPS admixtures for blood decolorization (see Table S2 for the name and CAS number of the chemicals). Good candidates show green supernatant and colorless pellet. CHAPS improves the decolorization efficiency with most tested chemicals. The structures of screened chemicals in (G) are presented in (H).

(I) Normalized OD600 of the supernatant corresponded well with the photocamera pictures in (G) (n = 3).

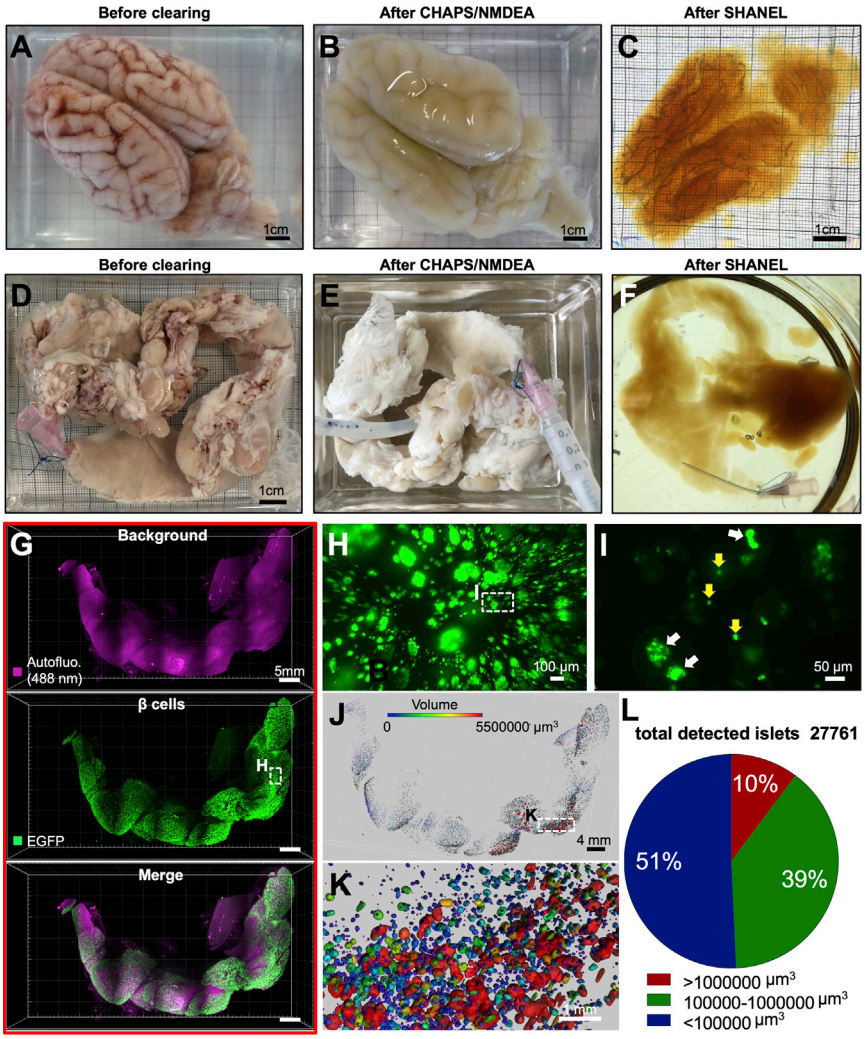

Figure 2. SHANEL Clearing of Brain and Pancreas from Adult Pigs

(A) PFA-fixed adult pig brain with retained blood.

(B) Permeabilized and decolorized pig brain by CHAPS/NMDEA.

(C) Fully transparent adult pig brain after SHANEL clearing.

(D) PFA-fixed, dissected (*INS*-EGFP transgenic pig) pancreas with retained blood.

(E) After CHAPS/NMDEA treatment, the pancreas is completely decolorized.

(F) Transparent pig pancreas after SHANEL clearing.

(G) 3D distribution of β-cell islets imaged by light-sheet microscopy after anti-EGFP nanobody boosting.

(H) High-magnification view of the region marked in (G) (middle panel).

(I) High-magnification view of the region marked in H showing β-cell islets of single cells (yellow arrows) or multiple cells (white arrows). The majority of larger islet shapes appear circular or oval. See also Video S1.

(J and K) Segmented 3D distribution of β-cells based on their volume in the islets of Langerhans. The heterogeneity of islet sizes is evident. The marked region in (J) is shown at high magnification in (K).

(L) Quantification of the total number of detected islets and categorization according to their volume.

with CHAPS, resulting in a completely colorless pellet from PFA-fixed blood (chemical 7 in Figures S1G and S1H and Table S2). In addition, NMDEA was the cheapest among the screened chemicals, reducing the cost when used in large amounts for intact human organs (Table S2). Compared to Triton X-100 and SDS that were used in prior clearing methods as detergents, CHAPS was faster and more successful in decolorizing mouse kidney, liver, heart, spleen, and brain, suggesting a better performance for large human organs (Figure S1I). Moreover, protein loss assay indicated the superior retention of endogenous biomolecules with CHAPS, assuring a more reliable molecular investigation of intact organs (Figure S1J). Thus, we anticipated that CHAPS, by forming small micelles, could completely diffuse through intact large mammalian organs and ameliorate tissue meshes, leaving behind a fully permeabilized biological tissue for cellular and molecular phenotyping.

Development of SHANEL Tissue Clearing

Next, we tested the accessibility of CHAPS permeabilized large mammalian organs using tissue clearing reagents. We chose to work with organic solvent-based clearing methods because they are fast and robust in addition to inducing tissue shrinkage (Pan et al., 2016), which helps to image larger organs with the limited sample holding capacity of light-sheet microscopy. First, we cleared the intact brain of a 2-year-old adult pig by passive immersion using standard organic solvent clearing reagents (Dodt et al., 2007; Ertürk et al., 2012). We found that a combination of ethanol for dehydration, DCM (dichloromethane) for delipidation, and BABB (benzyl alcohol + benzyl benzoate) for RI (refractive index) matching was highly effective in rendering the centimeters-thick pig brain transparent after CHAPS/NMDEA permeabilization and decolorization (all together represents the SHANEL clearing) (Figures 2A–2C; Table S3). SHANEL clearing provided rapid transparency of the ~12.0 × 7.3 × 5.0 cm size pig brain including heavily myelinated white matter, thalamus, and brainstem within 1.5 months (Figure 2C). The dimensions of the pig brain after clearing became 7.5 × 5.0 × 3.3 cm, with a shrinkage ratio of ~30% in volume. With the pretreatments of CHAPS/NMDEA, SHANEL clearing showed prominent capacity to render centimeters-sized mammal organs transparent compared with other clearing methods (Figures S2A and S2B).

Recent developments in gene editing with CRISPR/Cas9 technology have enabled the generation of large transgenic reporter mammals, expressing fluorescent proteins in the tissues of interest (Hsu et al., 2014; Kurome et al., 2017). Therefore, we applied SHANEL clearing to *INS*-EGFP transgenic pig

pancreas exhibiting porcine insulin gene (*INS*) promotor driven beta-cell-specific EGFP expression in the islets of Langerhans (Kemter et al., 2017) (Figures 2D–2F). To enhance and stabilize the EGFP signal in centimeters-sized tissue, we used anti-GFP nanobodies conjugated with bright Atto dyes (Cai et al., 2019) (Figure S2C). We demonstrated that the 3D distribution of pancreatic beta cells as single cell or groups of cells within the islets of Langerhans could be readily assessed by our new approach enabling quantification of islet volume and demonstration of islet size heterogeneity (Figures 2G–2L; Video S1).

Generation of Intact Transparent Human Brain by SHANEL Clearing

Labeling and clearing of the intact human brain would be a major step forward toward mapping its cellular content in the near future. As the human brain vascular system is an established network reaching all parts of the brain, we used it to deliver the chemical cocktails deep into the brain tissue (Figure S3A). We used the two main pairs of large arteries, the CR and CL (right and left internal carotids, respectively) and the VR and VL (right and left vertebral arteries, respectively) to circulate solutions. First, we used PBS/heparin solution to wash out the liquid blood, followed by 4% PFA/PBS solution to fix the brain. Subsequently, we carefully isolated the whole human brain with these major vessels and connected eyes (with a volume of ~1,344 cm^3 and dimensions of ~15.0 × 10.4 × 14.4 cm) from the skull. Then, we set up a pressure-driven pumping system to circulate all clearing reagents and cell nucleus labeling dye (TO-PRO-3) through the four arteries to accelerate the process (Figure 3A). By doing so, we rendered the whole adult human brain transparent for the first time. To demonstrate the full transparency, we performed the following experiments. First, we used SWIR (short-wave infrared) imaging light at 1,450 nm wavelength and visualized the text through the intact cleared human brain (Figures 3B and S3B) (Bruns et al., 2017; Carr et al., 2018). Second, we used a condensed white light from epifluorescence microscopy to illuminate the whole brain and observed that the light traveled end-to-end (Figure 3C). Third, we used MRI to visualize and quantify the proton density of uncleared and cleared human brain tissue, comparing the results to well-cleared mouse brain (Baek et al., 2019). The results showed that SHANEL clearing generated homogeneous tissue water replacements in both whole human brain and human brain slice, with the brain slice showing similar proton density values as the whole brain (Figure S3C). The difference in proton density between cleared and uncleared human samples was similar to the mouse samples (Figure S3C). The intact transparent human brain represents a 2–3 order of magnitude increase in the volume of sample that could be rendered transparent compared to prior methods (Hildebrand et al., 2018). The whole process including labeling and clearing takes ~4 months and costs ~3,200 € for one adult human brain (Table S2). The final volume of the shrunken brain was 56% of the initial volume. Next, we used light-sheet microscopy to acquire mosaic images of the intact cleared human eye with a diameter of ~3 cm. We imaged TO-PRO-3 and autofluorescence signals of the intact cleared eye and reconstructed the details of its anatomical structures including sclera, iris, and suspensory ligament in 3D (Figures 3D and 3E; Video S2). Thus, our approach provides the basis for 3D histological assessment of the whole human brain in the near future.

SHANEL Histology of Centimeters-Sized Human Organs

Because *in vivo* genetic labeling and fluorescent dye tracing are not applicable to study post-mortem human tissue, cellular and molecular interrogation of human organs requires post-mortem staining using dyes and antibodies. However, state-of-the-art antibody labeling techniques of decades-aged human samples are limited to ≤50 μm thickness in standard histology, and to a maximum of ~1 mm thickness in prior clearing methods, mainly due to the weak permeabilization of the tissue and slow diffusion of the standard antibodies (~150 kDa) (Lai et al., 2018; Murray et al., 2015; Park et al., 2018). In addition, age-related accumulation of highly autofluorescent molecules increases the background substantially in thicker tissues (Davis et al., 2014). To overcome these limitations and achieve staining of centimeters-sized human brain, we set out to develop a deep-tissue antibody labeling method. Toward this goal, we perfused an intact human brain from a 92-year-old female body donor using CHAPS/NMDEA to permeabilize and decolorize. This treatment softened the sturdy human brain and allowed its easy sectioning into 12 coronal slices (each 1.5 cm thick) using a brain slicer (Figures S3D–S3F). The permeabilized human brain slice was further slackened by delipidation using DCM/MeOH (methanol). Next, we identified acetic acid and guanidine hydrochloride as powerful reagents for loosening the ECM (extracellular matrix) for the diffusion of large molecules such as antibodies (all together represents the SHANEL histology) (Figures 4A and 4B).

We first used Methoxy-X04 (Jung et al., 2015; Klunk et al., 2002) and TO-PRO-3, which were affordable dyes in large quantities, to label Abeta plaques and cell nuclei, respectively, in an intact 16.5 × 16.5 × 1.5 cm human brain slice. After clearing, we scanned a 7.5 × 5 × 0.4 cm brain slice in ~2 days by using MAVIG upright confocal microscope that is designed to scan large slices of tissue. We detected Abeta plaque accumulation in several brain regions including CG (cingulate gyrus), PCun (precuneus), STG (superior temporal gyrus), and MTG (middle temporal gyrus) (Figures S4A–S4D; Table S3; Video S2). We also used epifluorescence microscopy to quickly screen the 1.5 cm thick half human brain slice and again readily located the regions with Methoxy-X04-labeled Abeta accumulation for subsequent high-resolution laser-scanning microscopy (Figures S4E–S4H).

Antibody labeling of tissues has been widely used to interrogate the specific cellular architecture and underlying molecular mechanisms of biological processes. Therefore, we next applied SHANEL to assess the possibility of antibody-based histology of centimeters-sized human tissues. Toward this goal, we first used Iba1 (ionized calcium binding adaptor molecule 1) antibody to immunolabel microglia (Figures 4C–4J) and PI (propidium iodide) to label cell nucleus. $Iba1^+$ microglia were identifiable throughout the 2.0 × 1.8 × 1.5 cm size human brain slice (Video S3). We also observed morphological differences: microglia cells in gray matter were mostly larger and more ramified compared to white matter (Figures 4G–4J). Next, we used

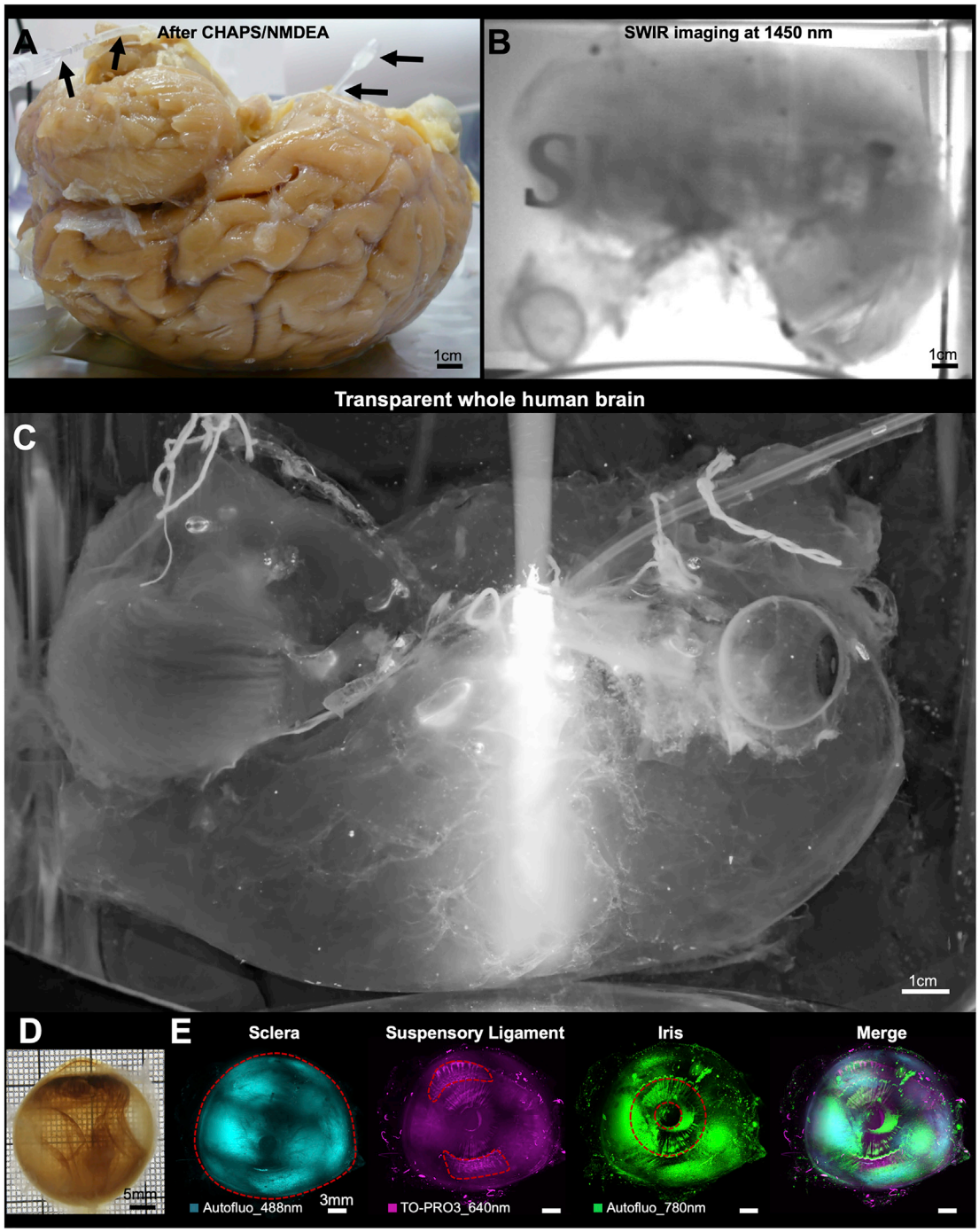

Figure 3. SHANEL Clearing of Intact Adult Human Brain

(A) A sample of permeabilized and decolorized intact adult human brain by CHAPS/NMDEA via active pumping setup (black arrows).

(B) SHANEL letters are visible, through the transparent whole human brain illuminated with 1,450 nm short-wave infrared (SWIR) light.

(C) Light of an epifluorescent microscope can travel in the brain end-to-end, demonstrating the full transparency of intact human brain, which has volume of ~1,344 cm^3 and dimensions of ~15.0 × 10.4 × 14.4 cm.

(D) Camera picture of an eye, dissected from the intact transparent human brain.

(E) 3D reconstruction from light-sheet microscopy scans of the eye showing the sclera, suspensory ligament, and iris structures.

See also Video S2.

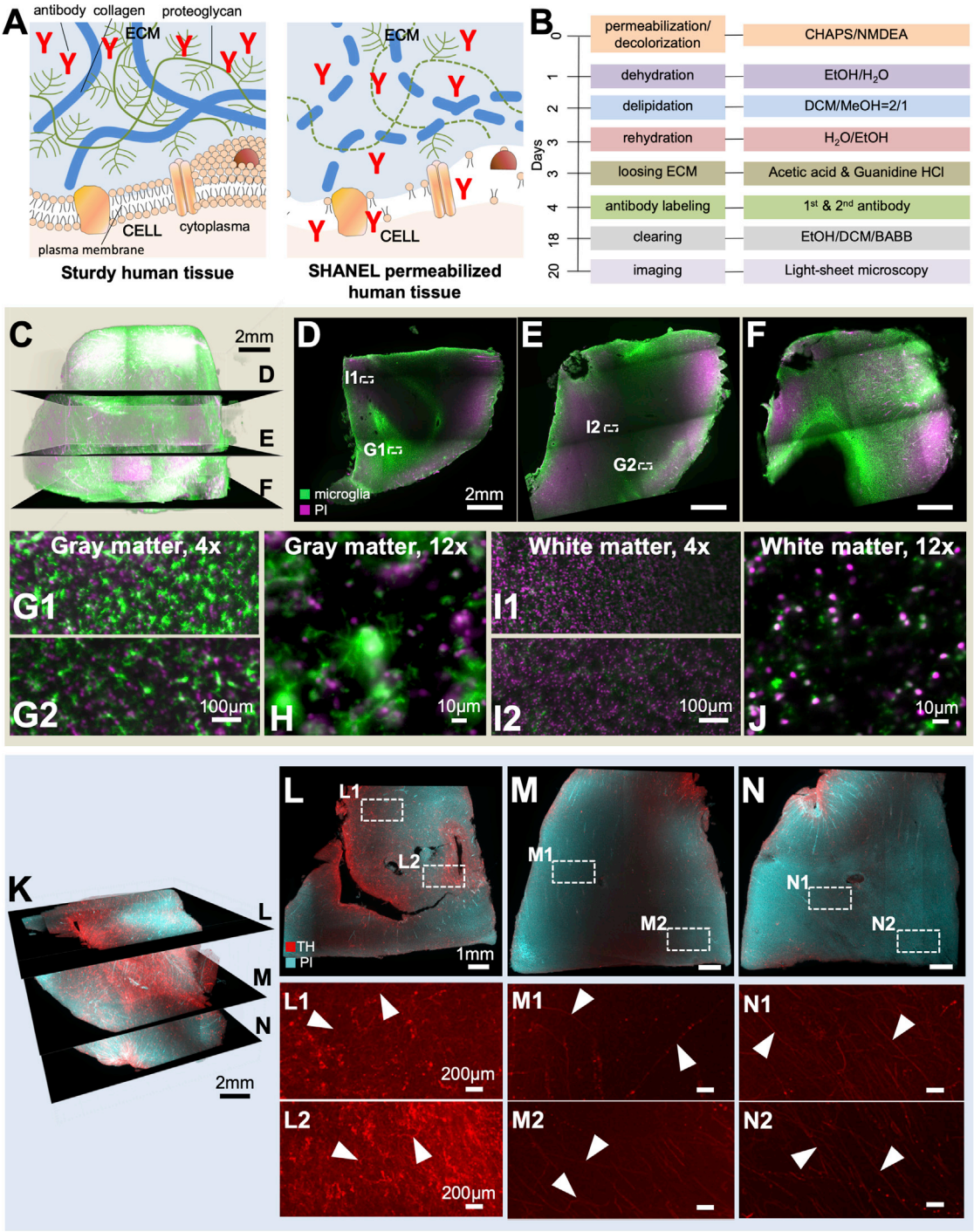

Figure 4. SHANEL Histology on Centimeters-Thick Human Tissues Imaged by Light-Sheet Microscopy

(A) SHANEL histology is further characterized by loosening extracellular matrix (ECM) and extracting lipids, which enable antibody-size molecules to fully penetrate into centimeter-thick sturdy human tissues.

(B) The step by step SHANEL histology pipeline (with durations) for deep tissue antibody labeling.

(C–F) Iba1 microglia (green) and propidium iodide (PI) (magenta) labeling of post-mortem human brain tissue with an original size of 2.0 × 1.8 × 1.5 cm (1.3 × 1.2 × 1.0 cm after shrinkage). The differences in microglia density and morphology are evident throughout the gray matter (G and H) and white matter (I and J).

(legend continued on next page)

TH (tyrosine hydroxylase) antibody to immunolabel neuronal structures along with PI labeling of the cell nucleus (Figures 4K–4N). We were able to observe specifically labeled axonal extensions throughout the 1.8 × 1.8 × 1.5 cm human brain slice (Figures 4K–4N; Video S3). These results demonstrate that SHANEL histology can successfully permeabilize the entire 1.5 cm thick sturdy human brain slices for deep tissue antibody labeling using diverse antibodies (Figure S5A). This represents a 1–2 order of magnitude enhancement in the thickness of adult human tissue that could be processed for histology compared with prior methods (Hildebrand et al., 2018). We also found that the signal was stable for several months after SHANEL histology (Figure S5B). Studying vasculature has been a valuable method to explore diverse developmental and pathological phenomena in biological tissues. Again, histological assessment of the vasculature in human tissue has been limited by the penetration of specific vascular dyes and antibodies. Here, we used Lectin dye to effectively label a human brain sample with a size of 3.0 × 1.9 × 1.5 cm (Figure S5C). In addition to specific vascular structures (Figures S5D–S5F), we could identify vasculature-related tissue abnormalities as swollen structures of vascular morphology (Figure S5F), which could be aneurysms, a prevalent vascular disorder affecting 25% of the population (Duan et al., 2018). 50% of intracranial aneurysms are <5 mm in diameter (Morita et al., 2012), which is in line with our observations. Thus, SHANEL histology allows the labeling of specific molecules, cells, and vasculature in centimeters-sized human brain samples presenting a viable tool to scale up the investigation of brain pathologies.

Next, we tested our SHANEL technology on entire human kidneys using small molecular dyes. There is a huge shortage of organ donors for hundreds of thousands of people, with a large portion (~55%) waiting for kidney transplantation (Chung et al., 2014). Overall the waiting time for donation might be several years, and the cost of transplantation can reach half a million dollars (Chung et al., 2014). Understanding the 3D structure of the human kidney would be very valuable for tissue engineering efforts aiming to generate artificial kidneys using 3D-bioprinting technologies (Murphy and Atala, 2014), which require detailed cellular and molecular knowledge on intact human kidney to be replicated. Kidneys are the major organs for blood filtration through glomeruli, whose density, size, and cellular integrity are critical for healthy organ function (Puelles and Bertram, 2015). Toward understanding the 3D cellular structures of the human kidney, we used SHANEL histology with active perfusion of TRITC-dextran and TO-PRO-3 dyes through the renal artery to label the vessels and dense cellular structure of the glomeruli in the entire kidney with a size of 11.5 × 8.2 × 3.0 cm. After labeling, we also actively pumped the clearing reagents through the kidney to overcome the age- and size-related challenges (Table S3). We achieved full transparency, revealing the primary renal artery, secondary branches of segmental arteries, and interlobar arteries (Figures 5A–5C). Using standard light-sheet microscopy, we could visualize the 3D distribution of vessels and glomeruli in the kidney cortex over large volumes (1.2 × 1.2 × 0.45 cm) and trace individual afferent arterioles and their corresponding glomeruli (Figures 5D–5F; Video S4). Through cortex profile counting, we found that the width of the cortex zone was around 2,742 ± 665 μm (mean ± SD), the diameter of glomerular caliper was 221 ± 37 μm, and afferent arteriole diameter was 71 ± 28 μm (Figure 5G).

Next, we examined whether SHANEL histology leads to tissue alterations by assessing macro- and micro-structures. The ratiometric enlargement of shrunken tissues after SHANEL histology overlaid well with their pre-cleared images suggesting an isotropic tissue shrinkage (Figure S6A). Assessing the cellular details before and after SHANEL histology, we also did not observe a notable deformation (Figure S6B). Moreover, we also rehydrated the SHANEL-treated tissues, and performed histological assessments using H&E, Nissl, and PAS (periodic acid Schiff) stainings (Puelles et al., 2019), further confirming the integrity of cellular structures upon SHANEL (Figure S6C).

3D Reconstruction of Intact Human Organs and Analysis of Big Data Using Deep Learning

To enable the imaging of intact human organs, we used a prototype light-sheet microscope with extended stage movements and a large sample accommodation chamber (size of 25 × 9 × 7 cm) (Figures 6A–6E). Using this new system, we scanned and reconstructed an intact human thyroid (7 × 5 × 3 cm) in 3D revealing the vessels and lymph nodes (Figures S7A–S7D; Table S3). We scanned an intact human kidney (11 × 6.5 × 5 cm) from a 93-year-old donor end-to-end (Figures 6F–6I). We confirmed the transparency and imaging quality by observing the perfusion/labeling-free autofluorescence signal at 780 nm channel, which was clearly visible throughout the entire scan (Video S4). Interestingly, we observed that a large segment of the kidney cortex had significantly reduced vascular structures appearing in 780 nm channel (Figures 6J and 6K; Video S4), which was also evident in dextran channel (Figure 6H). We also dissected exemplarily pieces and performed PAS staining to analyze the structural details. These experiments showed that the glomeruli structures were similar for both sides (Figure 6L). Overall, our data suggests a vascular pathology affecting a large segment of the kidney, which is typical of hypertensive related changes in older individuals that could potentially be preceding glomeruli pathology (Denic et al., 2017; Hughson et al., 2016). Thus, SHANEL technology can be a new tool to study pathologies of intact human organs at a gross scale proving valuable information to understand organ functions in health and disease.

Analyzing the large data coming from cleared tissues has remained a major obstacle. The state-of-the-art methods for

(K) Tyrosine hydroxylase (TH) (red) and propidium iodide (PI) (cyan) labeling of post-mortem human brain tissue with an original size of 1.8 × 1.8 × 1.5 cm (1.2 × 1.2 × 0.91 cm after shrinkage).

(L–N) TH+ axonal extensions in gray matter (white arrowheads in L1–L2) and white matter (white arrowheads in M1–N2) throughout the entire depth of tissue are evident. Note that cyan channel is not shown in (L1)–(N2) to emphasize the TH labeling.

See also Video S3.

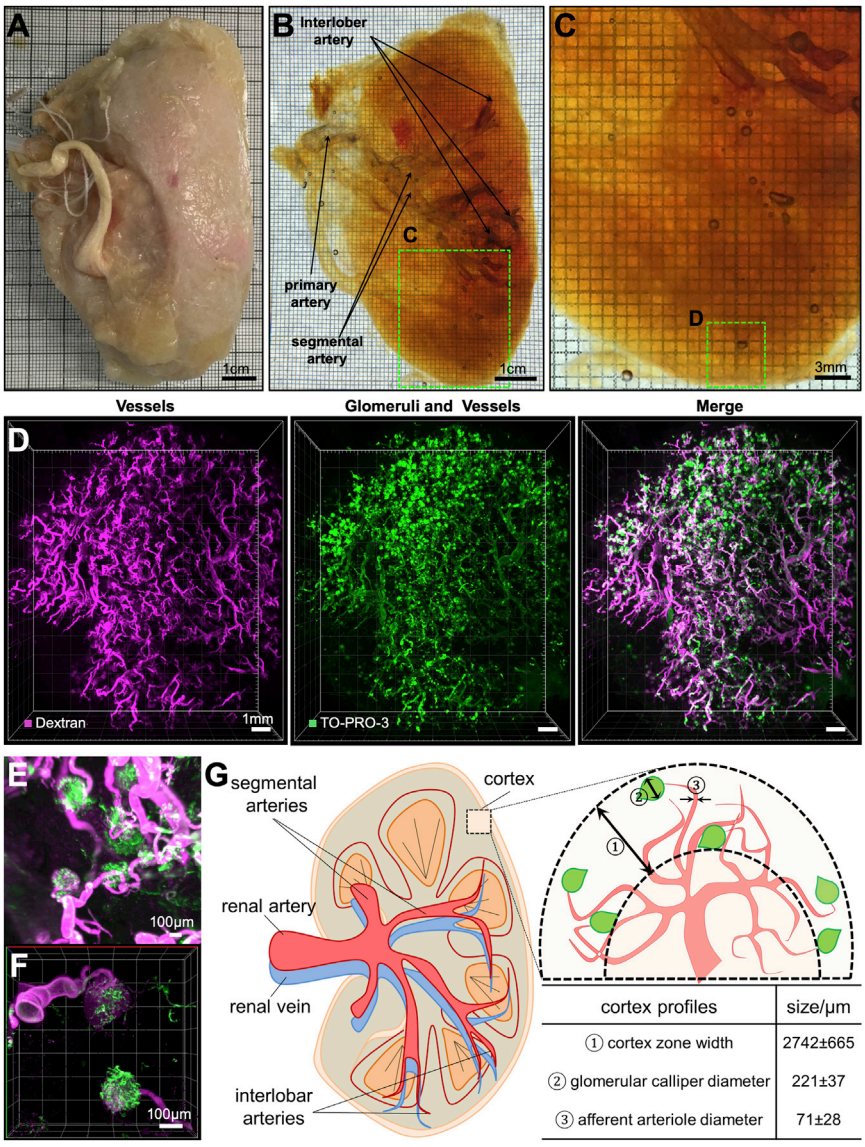

Figure 5. Cellular Investigation of Human Kidney

(A–C) A PFA-fixed adult human kidney (A) was rendered totally transparent after SHANEL clearing, revealing visible arteries (B and C). The marked region in (B) is shown at high magnification in (C).

(D) 3D reconstruction of vessels and glomeruli of the kidney cortex region marked in (C) by light-sheet microscopy.

(E and F) TRITC-dextran labels mostly the vessels (magenta), while TO-PRO-3 labels glomeruli more prominently (green). High-magnification light-sheet microscopy (E) and confocal microscopy (F) images show the structural details of afferent arteriole (magenta) and glomeruli (green).

(G) Human kidney anatomy and cortex profiles from the 3D reconstruction.

See also Video S4.

object and cell detection, for example the "3D Object Counter" tool (Bolte and Cordelières, 2006) in the Fiji software package (Schindelin et al., 2012) and Imaris software (Bitplane, 2019) rely on filter-based approaches such as brightness thresholding or watershed algorithms that cannot readily be scaled to analyzing terabytes of data. Recent deep learning approaches have proven to be superior for the analysis of large imaging data compared to prior methods both in terms of segmentation accuracy and computational power requirements (Belthangady and Royer, 2019; Kermany et al., 2018; Moen et al., 2019; Wainberg et al., 2018). To analyze large-scale data from the cleared human tissue in a scalable and unbiased manner, we adopted a deep learning approach based on CNNs (convolutional neural networks) (Tetteh et al., 2018; Todorov et al., 2019) (Figure 7A). To generalize the efforts, we chose to focus on reliable detection, segmentation, and counting millions of cells in cleared human brain tissues. Our deep learning approach consists of a CNN-based segmentation of the cells and a connected component analysis for detecting and counting of the cells. Our CNN was ~10× faster compared to the Imaris Surface Detection Tool while they had similar accuracies on the test data patches (Figures 7B and 7C). The CNN was 20× faster compared to the Fiji 3D Object Counter, which had a substantially lower performance (Figures 7B and 7C). We also tested an implementation of 3D U-Net (Çiçek et al., 2016), a common state-of-the-art CNN architecture for medical image segmentation, which performed very similar to our CNN in terms of cell detection accuracy, albeit slightly slower in processing speed (Figure 7C). Next, we applied our algorithms to 4 different large brain regions (size of ~60–145 mm^3). We could readily detect, segment, and map the 10–22 million cells in each brain region within a few hours (Figures 7D–7G), a task that is impossible to complete with the same speed and accuracy without a deep learning approach. We designed our pipeline to be able to work on any size of scan using a standard lab workstation (e.g., with Titan T1080i GPUs [graphics processing units]). Our code is freely available at Google Colab (see Data and Code Availability), where the model can be tested and applied to scientists' proprietary data in their browsers without installing any software.

DISCUSSION

Histological studies of human tissues suffer from a lack of scalable methods to label and image large human specimens. Here, we present the SHANEL method, which is derived from a new chemistry achieving thorough permeabilization of fixed

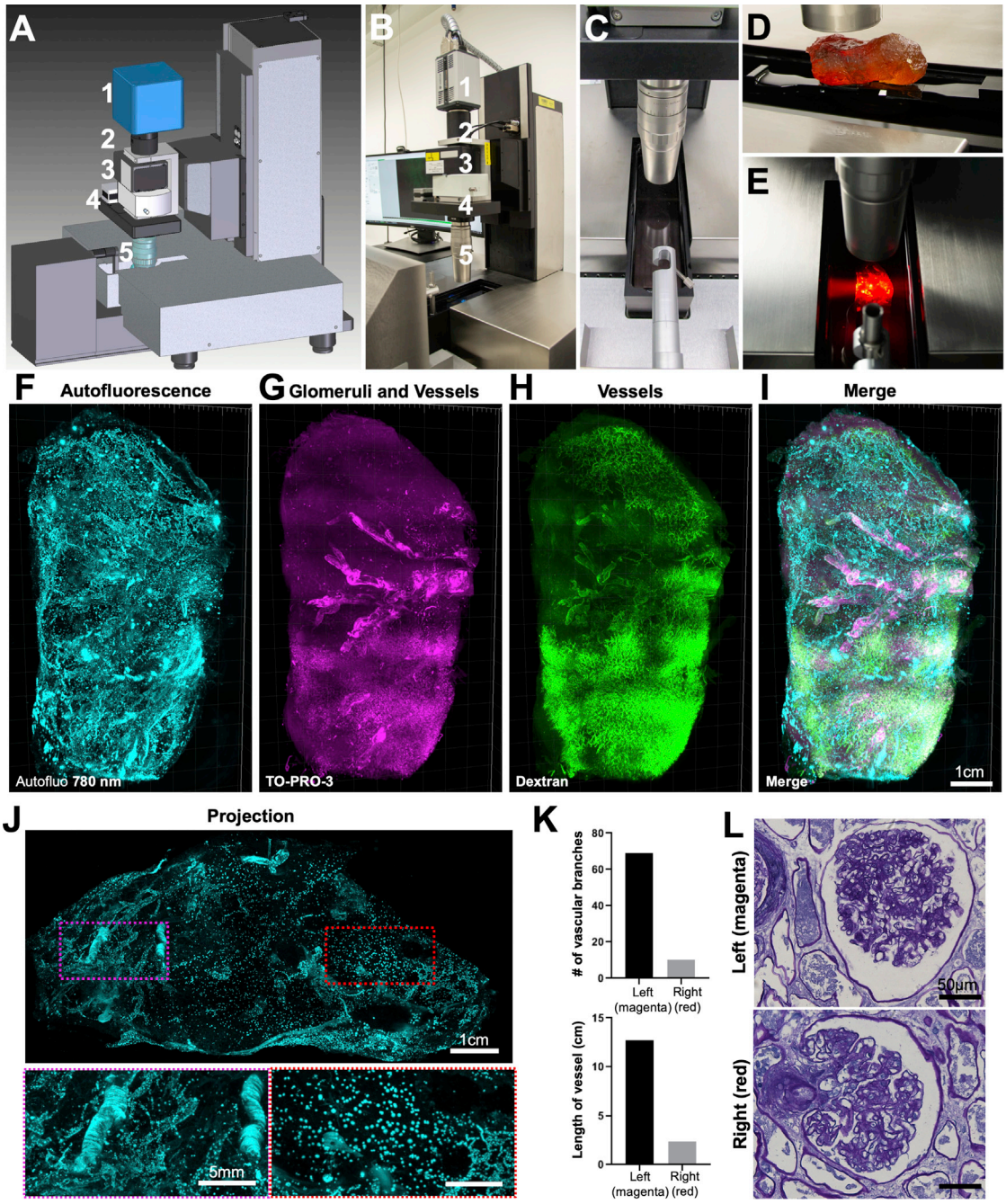

Figure 6. Whole Kidney Imaging Using Ultramicroscope Blaze with Extended Sample Holding Capacity

(A and B) Plan (A) and picture (B) of the prototype LaVision (Miltenyi) Biotec light-sheet Ultramicroscope Blaze for large samples, featuring (1) Andor sCMOS camera, (2) tube, (3) LaVision autofocusing unit for automatic focus correction at different wavelengths, (4) zoom body, and (5) 1.1× MI PLAN objective.

(C) Imaging chamber.

(D) A whole adult human kidney was mounted on the holder (note that the sample does not look transparent if not immersed in RI matching solution [BABB] as shown in the image).

(E) View of cleared whole human kidney placed in the imaging chamber with the light-sheet from the left crossing through the sample.

(F–I) 3D reconstruction of whole adult human kidney (original size of 11 × 6.5 × 5 cm) imaged by the prototype light-sheet microscope. Shown are the autofluorescence signal at 780 nm (F, cyan), the glomeruli and vessels from TO-PRO-3 labeling (G, magenta), the vessels from the dextran labeling (H, green), and the merged view of (F)–(H) in (I).

(legend continued on next page)

post-mortem human tissues. It allows full penetration of labeling molecules and clearing chemicals into centimeters-sized decades-aged human tissues such as post-mortem human brain and kidney specimens. Our method can also readily be applied to many organs in parallel, because it does not require lengthy handwork other than setting up the perfusion system and exchanging of the solutions (Table S3). Thus, this scalable method could vastly accelerate the 3D structural and molecular mapping of cells in intact human organs including the human brain.

Early efforts of adult human organ clearing started a century ago with slow progress in transparency and labeling options (Steinke and Wolff, 2001). A particular difficulty has been the age-dependent accumulation of intracellular and extracellular molecules such as lipofuscin and neuromelanin pigments. Lipofuscin is a mixture of highly oxidized cross-linked macromolecules including proteins, lipids, and sugars from different cellular metabolic processes (Moreno-García et al., 2018). Age-related accumulation of lipofuscin in the human body, in particular in the brain, correlates with senescence and sturdiness of human tissues (Moreno-García et al., 2018). Similarly, insolubility of the collagen also increases in the human body with aging, leading to hardening, browning, and autofluorescence of the tissues (Monnier et al., 1984). Due to age-related accumulation of such insoluble macromolecules in human tissues over several decades, histological examination relying on the penetration of large molecules such as antibodies deep into tissues has been very challenging. Recently developed tissue clearing methods have proven to be a promising way to achieve histological assessment of intact specimen. Although diverse clearing methods have been quite successful in rodents with the age of a few months, they have not been as effective on decades-aged human tissues. We solved this problem by developing a new method to permeabilize the sturdy human tissues, which is the prerequisite step for any tissue labeling and clearing method.

Here, we hypothesize that the micellar structures of detergents would be critical to penetrate the dense meshes of sturdy human tissues. Toward this goal, we identified CHAPS, a zwitterionic detergent having rigid steroidal structure with hydrophobic and hydrophilic faces. The ''facial'' amphiphilicity of CHAPS is responsible for the aggregation behavior and surface configuration of molecules at interface. First, CHAPS aggregates into much smaller micelles compared to standard ''head-to-tail'' detergents such as SDS and Triton X-100, facilitating its rapid penetration deep into dense human tissues. In aggregate formation, the hydrophobic faces (β-plane of steroid) are considered to contact each other, whereas the hydrophilic ones (three hydroxyl groups) remain exposed to the aqueous environment. Second, in terms of interfacial interaction, the facial amphiphiles bind to the bilayer in a unique mode that allows coverage of a larger hydrophobic area instead of being embedded into the bilayer. In this way, less facial amphiphile CHAPS is needed, and no residual CHAPS is left behind in the tissue after the treatment. Moreover, as a mild zwitterionic detergent, CHAPS exhibits better preservation of tissue endogenous biomolecules compared to SDS and Triton X-100 for cellular and molecular interrogation. Starting from this new permeabilization chemistry, we further developed our technology by loosening ECM using acetic acid and guanidine hydrochloride (Rajan et al., 2006; Yanagishita et al., 2009).

The resulting SHANEL histology method enabled diffusion of molecules as large as conventional IgG antibodies for straightforward 3D histology of centimeters-sized human organs. Thus, our approach can also tremendously help scaling up the efforts on Human Protein Atlas (HPA) by reducing the time to label and annotate across large human tissues (Sullivan et al., 2018; Vogt, 2018). Yet, SHANEL alone does not fully eliminate the tissue autofluorescence, in particular those coming from the lipofuscin in the brain tissue, without additional chemical treatments (Figures S7E–S7H). Thus, additional background signal might be observed in some of the antibody stainings. However, this autofluorescence can be used to extract more information on senescence of cells throughout different tissue layers in addition to imaging of specific dye/antibody signals in other channels. Similar to prior clearing methods using SDS and Triton, CHAPS-based SHANEL does also not preserve the lipid-base tracers such as DiI.

The SHANEL technology is also applicable to other large mammal organs. As pig is a much better model system for the human islets research compared to rodents, study of transgenic *INS*-EGFP pig pancreas in combination with SHANEL clearing can also accelerate research in metabolic disorders. We demonstrate that the 3D distribution of pancreatic beta cells as single cell or groups of cells within the islet of Langerhans can be readily imaged and quantified by our new approach demonstrating the islet size heterogeneity. Regional differences of islet size and distribution (head versus tail) in human pancreas are well known, and alterations in beta cell mass occur in diverse metabolic disorders (Chen et al., 2017). For instance, in disease conditions like type 2 diabetes, regional changes of islet distribution leading to preferentially large islets in the head region occur (Wang et al., 2013). Another interesting application would be to assess the quantity and distribution of porcine islets after intraportal xenotransplantation into the liver of non-human primate models (Kemter and Wolf, 2018; Wang et al., 2013).

The development of imaging systems with extended stages and imaging capacities would tremendously accelerate studies on phenotyping of the cellular and molecular architecture of the whole human organs. To start addressing this major need, we introduced a prototype light-sheet microscope with extended stage movement and sample holding capacity, which, in principle, could accommodate and image more than ~80% of the human organs including kidney, bladder, ovaries, testes,

(J) An orthogonal 1 mm projection of the kidney showing that vascular structures are significantly reduced at the right side (red-dashed region) compared to left side of the kidney (magenta-dashed region). See also Video S4.

(K) Quantification of vascular features between the left (magenta) and right (red) regions of the kidney.

(L) Periodic acid Schiff (PAS) images of rehydrated samples dissected from the left (magenta) and right (red) regions showing similar glomeruli structures for both sides.

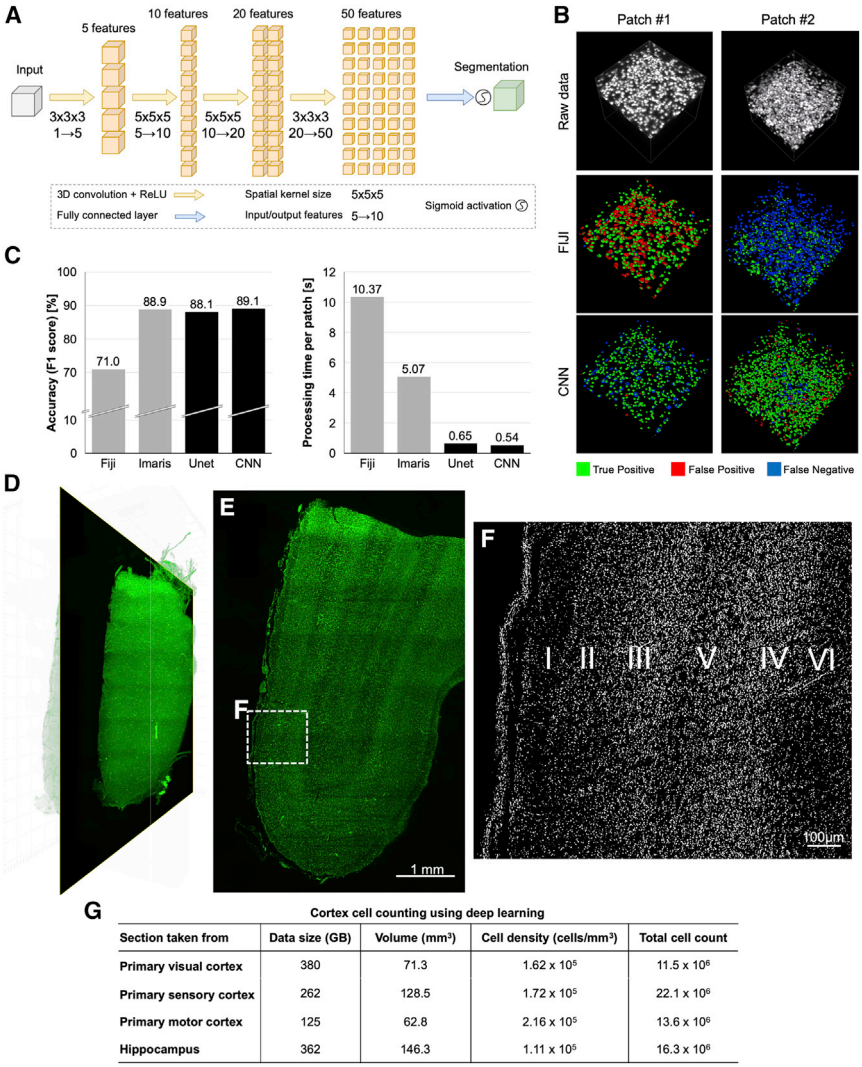

Section taken from	Data size (GB)	Volume (mm³)	Cell density (cells/mm³)	Total cell count
Primary visual cortex	380	71.3	1.62 x 10^5	11.5 x 10^6
Primary sensory cortex	262	128.5	1.72 x 10^5	22.1 x 10^6
Primary motor cortex	125	62.8	2.16 x 10^5	13.6 x 10^6
Hippocampus	362	146.3	1.11 x 10^5	16.3 x 10^6

Figure 7. Deep Learning-Based Quantification of Cleared Human Brain Tissues

(A) The architecture of our convolutional neural network (CNN).

(B) Visual comparisons of deep learning segmentation performance to alternative automated methods on two test patches, color-coded.

(C) Comparisons of deep learning (black columns) and alternative automated methods (gray columns) for cell counting accuracy (left) and processing time (right). The cell counting accuracy is quantified as the F1 score, which represents the harmonic mean of recall (cell detection rate) and precision (false positive rate). Reported processing times were measured for the task of detecting and segmenting all cells of a 3D patch (291 μm^3) on a normal workstation (32 cores, 2 GPUs).

(D) 3D reconstruction of primary visual cortex area having ~11.5 million cells.

(E) Raw orthogonal image from the middle of (D).

(F) CNN segmented image from the region marked in (E). Six layers of primary visual cortex can readily be identified in CNN segmented images (100 µm projection).

(G) The summary of cell properties from different brain regions taken from cortex and hippocampus area analyzed using our CNN.

throat, heart, thyroid, pancreas, and tongue. Imaging the entire transparent human brain on the other hand is still beyond the capacity of current microscope systems. Leading toward this possibility, Voigt et al. (2019) recently proposed the mesoSPIM (mesoscale selective plane illumination microscopy), an open-hardware microscopy platform for imaging cleared tissues several centimeters in size, which could potentially be further modified to accommodate and image the whole cleared human brain. In addition, SHANEL-induced shrinkage (e.g., 44% reduction in volume for adult human brain) and usage of light-sheet microscopes with double-sided illumination could further facilitate imaging of the large, cleared human samples. To test more imaging options, we sliced the intact adult human brain into twelve 1.5 cm-thick sections using standard slicer equipment and imaged with a mosaic upright confocal fluorescent microscopy. Still, such thick slices are much easier to handle compared to micrometer- or even millimeter-thick sections, because there is no need to embed or collect them on glass slides. Moreover, SHANEL histology allowed a thorough labeling of these 1.5 cm-thick brain slices. This allows the usage of high NA (numerical aperture) objectives such as 4× Olympus objective (NA: 0.28 and WD [working distance]: 10 mm) and 20× Zeiss clarity objective (NA: 1, WD: 5.6 mm) on defined regions of interest to reconstruct the entire 1.2–2 cm thick human tissue by scanning from both sides in such laser scanning systems. While the usage of high NA and high WD objectives enables ~1–2 µm resolution, this will also lead to large data in the order of at least hundreds of terabytes. It is noteworthy to mention that imaging samples as large as human brain will also benefit from imaging at near-infrared and SWIR wavelength having much better tissue penetration capabilities compared to the visible spectra used in the current light-sheet microscopes. In addition, imaging at longer wavelengths can provide further advantages in both reducing the tissue autofluorescence at the visible spectrum and multi-color imaging for which new probes are being developed (Cosco et al., 2017; Schnermann, 2017). Indeed, a near-infrared light-sheet microscopy has recently been presented (Wang et al., 2019). Imaging whole adult human kidney, we observed a large segment of the kidney lacked vascular structures at 780 nm autofluorescence channel. Our observations of the signal around the vessels, and at the fibrous capsule (outer membrane of the kidney) suggests that this autofluorescence signal could be coming from the collagen (Genovese et al., 2014; Jain et al., 2016; Manon-Jensen et al., 2016). Currently, we do not know the origin of this observed vascular change. Another advantage of our

approach is that, after SHANEL histology, the specimens become hard, enabling easy handling of complete organs and slices. Finally, owing to the complete dehydration and incubation in organic solvents, the tissues are preserved by SHANEL histology, allowing long-term storage for the future studies by the same investigators or in other labs.

The rapid progresses in tissue clearing methods and applications have introduced datasets of previously unseen sizes in mesoscale imaging. Even more limiting has been the lack of reliable methods to analyze these large datasets with conventional computational resources in moderately equipped biology labs. Here, we developed a deep learning-based framework using a CNN for the segmentation of millions of cells in cleared human brain tissue, which could not be completed without a deep learning approach at the same accuracy and speed. Here, we used our pipeline to detect and segment cells in diverse brain regions. Deep learning approaches could be expanded to classify the cells and analyze new structures such as vessels, nerves, and muscles—tasks that cannot be achieved easily with traditional software packages. Thanks to the adaptability of deep learning approaches, new algorithms can be trained with a small amount of training data to perform previously unknown segmentation tasks at high accuracy and speed (Belthangady and Royer, 2019; Moen et al., 2019; Todorov et al., 2019). Deep learning methods can also be parallelized on multiple GPUs (such as using cloud computing) to quickly scale up the processing speed for data size of hundreds of terabytes.

In conclusion, this work presents a new technology to permeabilize centimeters-sized aged human tissues for molecular and cellular phenotyping. This method allows deep tissue labeling and clearing of human specimens as large as the intact human kidney and brain. Thus, in combination with light-sheet microscopy systems having extended sample scanning capacity and deep learning-based algorithms, SHANEL histology can be a key technology to map intact human organs in the near future, which would accelerate our understanding of physiological and pathological conditions governing human life.

STAR★METHODS

Detailed methods are provided in the online version of this paper and include the following:

SUPPLEMENTAL INFORMATION

Supplemental Information can be found online at https://doi.org/10.1016/j.cell.2020.01.030.

ACKNOWLEDGMENTS

We thank Oliver Thorn-Seshold for the critical comments on the manuscript and David Eliezer and Sebastian Doniach for support in the initial stages of this project. We thank Lavision BioTec for producing the protoype Utramicrscope light-sheet microscope. We thank Alireza Ghasemigharagoz for RMSE analysis and Melanie Shaper for technical assistance. We thank Doris Kaltenecker for discussion about the name of the technology. The authors are grateful to the patients and their families, who made brain donation possible. This work was supported by the Vascular Dementia Research Foundation, Deutsche Forschungsgemeinschaft (DFG, German Research Foundation) under Germany's Excellence Strategy within the framework of the Munich Cluster for Systems Neurology (EXC 2145 SyNergy, ID 390857198), ERA-Net Neuron (01EW1501A to A.E.), Fritz Thyssen Stiftung (10.17.1.019MN to A.E.), DFG (ER 810/2-1 to A.E., BR 5355/2-1 to O.T.B., CRC/1192 to T.B.H. and V.G.P., TRR127 to E.W. and E.K., and SFB 1052 to I.B.), German Center of Diabetes Research (DZD) (82DZD00802 to E.W.), NIH (to A.E.), Helmholtz ICEMED Alliance (to A.E. and I.B.), National Health and Medical Research Council of Australia (NHMRC), the Humboldt Foundation, and BMBF eMed Consortia Fibromap (to V.G.P.), NVDIA GPU grant program, and Software Campus grant (to O.S.). The procurement of the MRI scanners was supported

by the DFG within the framework of SyNergy (EXC 2145 SyNergy, ID 390857198) and (DFG, INST 409/193-1 FUGG).

AUTHOR CONTRIBUTIONS

S.Z. developed the protocols and performed organs processing, labeling, clearing, imaging, and data analysis. M.I.T. and R.C. contributed to optimize the protocol, organs processing, imaging, and data analysis. R.A.-M., O.S., J.C.P., and B.M. developed the deep learning architecture and quantitative analyses. H.S. and I.B. perfused and dissected the human organs. E.K. and E.W. generated the *INS*-EGFP transgenic pig line. E.K. perfused and dissected pig pancreas. S.Z., R.C., H.M., and Z.R. annotated the ground truth data. M.W. and O.T.B. designed and performed SWIR images. M.D. and B.G. performed the MRI images and analysis. J.L. performed the SAXS experiment and data analysis. K.S., V.G.P., M.N.W., and T.B.H. contributed to confocal, tissue recycling, and histology analyses. S.Z. and A.E. wrote the manuscript. All authors edited the manuscript. A.E. initiated and led all aspects of the project.

DECLARATION OF INTERESTS

A.E. has filed a patent on SHANEL technologies described in this study.

Received: May 22, 2019
Revised: December 4, 2019
Accepted: January 22, 2020
Published: February 13, 2020

SUPPORTING CITATIONS

The following references appear in the Supplemental Information: Corrin and Harkins (1947); le Maire et al. (2000); Mandal et al. (1988); Paradies (1980); Stubičar and Petres (1981); Stubičar et al. (1989).

REFERENCES

Amunts, K., Lepage, C., Borgeat, L., Mohlberg, H., Dickscheid, T., Rousseau, M.E., Bludau, S., Bazin, P.L., Lewis, L.B., Oros-Peusquens, A.M., et al. (2013). BigBrain: an ultrahigh-resolution 3D human brain model. Science *340*, 1472–1475.

Annunziato, M.E., Patel, U.S., Ranade, M., and Palumbo, P.S. (1993). p-maleimidophenyl isocyanate: a novel heterobifunctional linker for hydroxyl to thiol coupling. Bioconjug. Chem. *4*, 212–218.

Baek, K., Jung, S., Lee, J., Min, E., Jung, W., and Cho, H. (2019). Quantitative assessment of regional variation in tissue clearing efficiency using optical coherence tomography (OCT) and magnetic resonance imaging (MRI): A feasibility study. Sci. Rep. *9*, 2923.

Belle, M., Godefroy, D., Dominici, C., Heitz-Marchaland, C., Zelina, P., Hellal, F., Bradke, F., and Chédotal, A. (2014). A simple method for 3D analysis of immunolabeled axonal tracts in a transparent nervous system. Cell Rep. *9*, 1191–1201.

Belle, M., Godefroy, D., Couly, G., Malone, S.A., Collier, F., Giacobini, P., and Chedotal, A. (2017). Tridimensional Visualization and Analysis of Early Human Development. Cell *169*, 161–173.

Belthangady, C., and Royer, L.A. (2019). Applications, promises, and pitfalls of deep learning for fluorescence image reconstruction. Nat. Methods *16*, 1215–1225.

Bitplane. (2019). Imaris Microscopy Image Analysis (Oxford Instruments Group).

Bolte, S., and Cordelières, F.P. (2006). A guided tour into subcellular colocalization analysis in light microscopy. J. Microsc. *224*, 213–232.

Bozek, K., Wei, Y., Yan, Z., Liu, X., Xiong, J., Sugimoto, M., Tomita, M., Pääbo, S., Sherwood, C.C., Hof, P.R., et al. (2015). Organization and evolution of brain lipidome revealed by large-scale analysis of human, chimpanzee, macaque, and mouse tissues. Neuron *85*, 695–702.

Brett, M., Hanke, M., Cipollini, B., Côté, M.-A., Markiewicz, C., Gerhard, S., Larson, E., Lee, G.R., Halchenko, Y., and Kastman, E. (2016). nibabel: 2.1.0 (Zenodo).

Brett, M., Markiewicz, C.J., Hanke, M., Côté, M.-A., Cipollini, B., McCarthy, P., Cheng, C.P., Halchenko, Y.O., Cottaar, M., Ghosh, S., et al. (2020). nipy/nibabel: 3.0.1 (Zenodo) https://doi.org/10.5281/zenodo.3628482.

Bruns, O.T., Bischof, T.S., Harris, D.K., Franke, D., Shi, Y., Riedemann, L., Bartelt, A., Jaworski, F.B., Carr, J.A., and Rowlands, C.J. (2017). Next-generation in vivo optical imaging with short-wave infrared quantum dots. Nat. Biomed. Eng. *1*, 0056.

Cai, R., Pan, C., Ghasemigharagoz, A., Todorov, M.I., Forstera, B., Zhao, S., Bhatia, H.S., Parra-Damas, A., Mrowka, L., Theodorou, D., et al. (2019). Panoptic imaging of transparent mice reveals whole-body neuronal projections and skull-meninges connections. Nat. Neurosci. *22*, 317–327.

Carr, J.A., Aellen, M., Franke, D., So, P.T.C., Bruns, O.T., and Bawendi, M.G. (2018). Absorption by water increases fluorescence image contrast of biological tissue in the shortwave infrared. Proc. Natl. Acad. Sci. USA *115*, 9080–9085.

Carrim, Z.I., Chohan, A.W., and Devlin, H.C. (2006). Iris damage and acute pigment dispersion following photo-epilation. Eye (Lond.) *20*, 1486–1488.

Chen, C., Cohrs, C.M., Stertmann, J., Bozsak, R., and Speier, S. (2017). Human beta cell mass and function in diabetes: Recent advances in knowledge and technologies to understand disease pathogenesis. Mol. Metab. *6*, 943–957.

Chung, K., Wallace, J., Kim, S.Y., Kalyanasundaram, S., Andalman, A.S., Davidson, T.J., Mirzabekov, J.J., Zalocusky, K.A., Mattis, J., Denisin, A.K., et al. (2013). Structural and molecular interrogation of intact biological systems. Nature *497*, 332–337.

Chung, R., Howard, K., Craig, J.C., Chapman, J.R., Turner, R., and Wong, G. (2014). Economic evaluations in kidney transplantation: frequency, characteristics, and quality-a systematic review. Transplantation *97*, 1027–1033.

Çiçek, Ö., Abdulkadir, A., Lienkamp, S.S., Brox, T., and Ronneberger, O. (2016). 3D U-Net: learning dense volumetric segmentation from sparse annotation. arXiv, arXiv:1606.06650. https://arxiv.org/abs/1606.06650.

Clarke, S. (1981). The hydrophobic effect: Formation of micelles and biological membranes, 2nd edition (Tanford, Charles). J. Chem. Educ. *58*, A246.

Corrin, M.L., and Harkins, W.D. (1947). The effect of salts on the critical concentration for the formation of micelles in colloidal electrolytes. J. Am. Chem. Soc. *69*, 683–688.

Cosco, E.D., Caram, J.R., Bruns, O.T., Franke, D., Day, R.A., Farr, E.P., Bawendi, M.G., and Sletten, E.M. (2017). Flavylium Polymethine Fluorophores for Near- and Shortwave Infrared Imaging. Angew. Chem. Int. Engl. *56*, 13126–13129.

Davis, A.S., Richter, A., Becker, S., Moyer, J.E., Sandouk, A., Skinner, J., and Taubenberger, J.K. (2014). Characterizing and Diminishing Autofluorescence in Formalin-fixed Paraffin-embedded Human Respiratory Tissue. J. Histochem. Cytochem. *62*, 405–423.

De Maria, A., Wilmarth, P.A., David, L.L., and Bassnett, S. (2017). Proteomic Analysis of the Bovine and Human Ciliary Zonule. Invest. Ophthalmol. Vis. Sci. *58*, 573–585.

Denic, A., Mathew, J., Lerman, L.O., Lieske, J.C., Larson, J.J., Alexander, M.P., Poggio, E., Glassock, R.J., and Rule, A.D. (2017). Single-Nephron Glomerular Filtration Rate in Healthy Adults. N. Engl. J. Med. *376*, 2349–2357.

Despotović, I., Goossens, B., and Philips, W. (2015). MRI segmentation of the human brain: challenges, methods, and applications. Comput. Math. Methods Med. *2015*, 450341.

Deverman, B.E., Pravdo, P.L., Simpson, B.P., Kumar, S.R., Chan, K.Y., Banerjee, A., Wu, W.L., Yang, B., Huber, N., Pasca, S.P., and Gradinaru, V. (2016). Cre-dependent selection yields AAV variants for widespread gene transfer to the adult brain. Nat. Biotechnol. *34*, 204–209.

Ding, S.L., Royall, J.J., Sunkin, S.M., Ng, L., Facer, B.A., Lesnar, P., Guillozet-Bongaarts, A., McMurray, B., Szafer, A., Dolbeare, T.A., et al. (2016).

Comprehensive cellular-resolution atlas of the adult human brain. J. Comp. Neurol. *524*, 3127–3481.

Dodt, H.U., Leischner, U., Schierloh, A., Jährling, N., Mauch, C.P., Deininger, K., Deussing, J.M., Eder, M., Zieglgänsberger, W., and Becker, K. (2007). Ultramicroscopy: three-dimensional visualization of neuronal networks in the whole mouse brain. Nat. Methods *4*, 331–336.

Duan, Z., Li, Y., Guan, S., Ma, C., Han, Y., Ren, X., Wei, L., Li, W., Lou, J., and Yang, Z. (2018). Morphological parameters and anatomical locations associated with rupture status of small intracranial aneurysms. Sci. Rep. *8*, 6440.

Ertürk, A., Becker, K., Jährling, N., Mauch, C.P., Hojer, C.D., Egen, J.G., Hellal, F., Bradke, F., Sheng, M., and Dodt, H.U. (2012). Three-dimensional imaging of solvent-cleared organs using 3DISCO. Nat. Protoc. *7*, 1983–1995.

Garvalov, B.K., and Ertürk, A. (2017). Seeing whole-tumour heterogeneity. Nat. Biomed. Eng. *1*, 772–774.

Genovese, F., Manresa, A.A., Leeming, D.J., Karsdal, M.A., and Boor, P. (2014). The extracellular matrix in the kidney: a source of novel non-invasive biomarkers of kidney fibrosis? Fibrogenesis Tissue Repair *7*, 4.

Guinier, A. (1939). La diffraction des rayons X aux très petits angles: application à l'étude de phénomènes ultramicroscopiques. Ann Physiol. *11*, 161–237.

Hammouda, B. (2013). Temperature Effect on the Nanostructure of SDS Micelles in Water. J. Res. Natl. Inst. Stand. Technol. *118*, 151–167.

Heusch, P., Wittsack, H.J., Blondin, D., Ljimani, A., Nguyen-Quang, M., Martirosian, P., Zenginli, H., Bilk, P., Kröpil, P., Heusner, T.A., et al. (2014). Functional evaluation of transplanted kidneys using arterial spin labeling MRI. J. Magn. Reson. Imaging *40*, 84–89.

Hildebrand, S., Schueth, A., Herrler, A., Galuske, R., and Roebroeck, A. (2018). Scalable cytoarchitectonic characterization of large intact human neocortex samples. bioRxiv. https://doi.org/10.1101/274985.

Hsu, P.D., Lander, E.S., and Zhang, F. (2014). Development and applications of CRISPR-Cas9 for genome engineering. Cell *157*, 1262–1278.

Hughson, M.D., Hoy, W.E., Mott, S.A., Puelles, V.G., Bertram, J.F., Winkler, C.L., and Kopp, J.B. (2016). *APOL1* Risk Alleles are Associated with More Severe Arteriosclerosis in Renal Resistance Vessels with Aging and Hypertension. Kidney Int. Rep. *1*, 10–23.

Jain, M., Robinson, B.D., Aggarwal, A., Shevchuk, M.M., Scherr, D.S., and Mukherjee, S. (2016). Multiphoton microscopy for rapid histopathological evaluation of kidney tumours. BJU Int. *118*, 118–126.

Jing, D., Zhang, S., Luo, W., Gao, X., Men, Y., Ma, C., Liu, X., Yi, Y., Bugde, A., Zhou, B.O., et al. (2018). Tissue clearing of both hard and soft tissue organs with the PEGASOS method. Cell Res. *28*, 803–818.

Jung, C.K., Keppler, K., Steinbach, S., Blazquez-Llorca, L., and Herms, J. (2015). Fibrillar amyloid plaque formation precedes microglial activation. PLoS ONE *10*, e0119768.

Kang, H.W., Lee, S.J., Ko, I.K., Kengla, C., Yoo, J.J., and Atala, A. (2016). A 3D bioprinting system to produce human-scale tissue constructs with structural integrity. Nat. Biotechnol. *34*, 312–319.

Kemter, E., and Wolf, E. (2018). Recent progress in porcine islet isolation, culture and engraftment strategies for xenotransplantation. Curr. Opin. Organ Transplant. *23*, 633–641.

Kemter, E., Cohrs, C.M., Schäfer, M., Schuster, M., Steinmeyer, K., Wolf-van Buerck, L., Wolf, A., Wuensch, A., Kurome, M., Kessler, B., et al. (2017). INS-eGFP transgenic pigs: a novel reporter system for studying maturation, growth and vascularisation of neonatal islet-like cell clusters. Diabetologia *60*, 1152–1156.

Kermany, D.S., Goldbaum, M., Cai, W., Valentim, C.C.S., Liang, H., Baxter, S.L., McKeown, A., Yang, G., Wu, X., Yan, F., et al. (2018). Identifying Medical Diagnoses and Treatable Diseases by Image-Based Deep Learning. Cell *172*, 1122–1131.

Kingma, D.P., and Ba, J. (2014). Adam: A method for stochastic optimization. arXiv, arXiv:14126980. https://arxiv.org/abs/1412.6980.

Klunk, W.E., Bacskai, B.J., Mathis, C.A., Kajdasz, S.T., McLellan, M.E., Frosch, M.P., Debnath, M.L., Holt, D.P., Wang, Y., and Hyman, B.T. (2002). Imaging Abeta plaques in living transgenic mice with multiphoton microscopy and methoxy-X04, a systemically administered Congo red derivative. J. Neuropathol. Exp. Neurol. *61*, 797–805.

Kubota, S.I., Takahashi, K., Nishida, J., Morishita, Y., Ehata, S., Tainaka, K., Miyazono, K., and Ueda, H.R. (2017). Whole-Body Profiling of Cancer Metastasis with Single-Cell Resolution. Cell Rep. *20*, 236–250.

Kurome, M., Leuchs, S., Kessler, B., Kemter, E., Jemiller, E.M., Foerster, B., Klymiuk, N., Zakhartchenko, V., and Wolf, E. (2017). Direct introduction of gene constructs into the pronucleus-like structure of cloned embryos: a new strategy for the generation of genetically modified pigs. Transgenic Res. *26*, 309–318.

Lai, H.M., Liu, A.K.L., Ng, H.H.M., Goldfinger, M.H., Chau, T.W., DeFelice, J., Tilley, B.S., Wong, W.M., Wu, W., and Gentleman, S.M. (2018). Next generation histology methods for three-dimensional imaging of fresh and archival human brain tissues. Nat. Commun. *9*, 1066.

le Maire, M., Champeil, P., and Moller, J.V. (2000). Interaction of membrane proteins and lipids with solubilizing detergents. Biochim. Biophys. Acta *1508*, 86–111.

Lee, S.C., Bennett, B.C., Hong, W.X., Fu, Y., Baker, K.A., Marcoux, J., Robinson, C.V., Ward, A.B., Halpert, J.R., Stevens, R.C., et al. (2013). Steroid-based facial amphiphiles for stabilization and crystallization of membrane proteins. Proc. Natl. Acad. Sci. USA *110*, E1203–E1211.

Lipfert, J., and Doniach, S. (2007). Small-angle X-ray scattering from RNA, proteins, and protein complexes. Annu. Rev. Biophys. Biomol. Struct. *36*, 307–327.

Lipfert, J., Millett, I.S., Seifert, S., and Doniach, S. (2006). Sample holder for small-angle x-ray scattering static and flow cell measurements. Rev. Sci. Instrum. *77*, 046108.

Lipfert, J., Columbus, L., Chu, V.B., Lesley, S.A., and Doniach, S. (2007). Size and shape of detergent micelles determined by small-angle X-ray scattering. J. Phys. Chem. B *111*, 12427–12438.

Mandal, A.B., Nair, B.U., and Ramaswamy, D. (1988). Determination of the critical micelle concentration of surfactants and the partition coefficient of an electrochemical probe by using cyclic voltammetry. Langmuir *4*, 736–739.

Manon-Jensen, T., Kjeld, N.G., and Karsdal, M.A. (2016). Collagen-mediated hemostasis. J. Thromb. Haemost. *14*, 438–448.

McCulloch, C. (1954). The zonule of Zinn: its origin, course, and insertion, and its relation to neighboring structures. Trans. Am. Ophthalmol. Soc. *52*, 525–585.

McKinney, W. (2010). Data structures for statistical computing in python. In Proceedings of the 9th Python in Science Conference (SciPy 2010), pp. 51–56.

Moen, E., Bannon, D., Kudo, T., Graf, W., Covert, M., and Van Valen, D. (2019). Deep learning for cellular image analysis. Nat. Methods *16*, 1233–1246.

Monnier, V.M., Kohn, R.R., and Cerami, A. (1984). Accelerated age-related browning of human collagen in diabetes mellitus. Proc. Natl. Acad. Sci. USA *81*, 583–587.

Morawski, M., Kirilina, E., Scherf, N., Jäger, C., Reimann, K., Trampel, R., Gavriilidis, F., Geyer, S., Biedermann, B., Arendt, T., and Weiskopf, N. (2018). Developing 3D microscopy with CLARITY on human brain tissue: Towards a tool for informing and validating MRI-based histology. Neuroimage *182*, 417–428.

Moreno-García, A., Kun, A., Calero, O., Medina, M., and Calero, M. (2018). An Overview of the Role of Lipofuscin in Age-Related Neurodegeneration. Front. Neurosci. *12*, 464.

Morita, A., Kirino, T., Hashi, K., Aoki, N., Fukuhara, S., Hashimoto, N., Nakayama, T., Sakai, M., Teramoto, A., Tominari, S., and Yoshimoto, T.; UCAS Japan Investigators (2012). The natural course of unruptured cerebral aneurysms in a Japanese cohort. N. Engl. J. Med. *366*, 2474–2482.

Moschovakis, A.K., and Highstein, S.M. (1994). The anatomy and physiology of primate neurons that control rapid eye movements. Annu. Rev. Neurosci. *17*, 465–488.

Murphy, S.V., and Atala, A. (2014). 3D bioprinting of tissues and organs. Nat. Biotechnol. *32*, 773–785.

Murray, E., Cho, J.H., Goodwin, D., Ku, T., Swaney, J., Kim, S.Y., Choi, H., Park, Y.G., Park, J.Y., Hubbert, A., et al. (2015). Simple, Scalable Proteomic Imaging for High-Dimensional Profiling of Intact Systems. Cell *163*, 1500–1514.

Oliver, R.C., Lipfert, J., Fox, D.A., Lo, R.H., Doniach, S., and Columbus, L. (2013). Dependence of micelle size and shape on detergent alkyl chain length and head group. PLoS ONE *8*, e62488.

Oliver, R.C., Lipfert, J., Fox, D.A., Lo, R.H., Kim, J.J., Doniach, S., and Columbus, L. (2014). Tuning micelle dimensions and properties with binary surfactant mixtures. Langmuir *30*, 13353–13361.

Pan, C., Cai, R., Quacquarelli, F.P., Ghasemigharagoz, A., Lourbopoulos, A., Matryba, P., Plesnila, N., Dichgans, M., Hellal, F., and Ertürk, A. (2016). Shrinkage-mediated imaging of entire organs and organisms using uDISCO. Nat. Methods *13*, 859–867.

Paradies, H.H. (1980). Shape and size of a nonionic surfactant micelle. Triton X-100 in aqueous solution. J. Phys. Chem. *84*, 599–607.

Park, Y.-G., Sohn, C.H., Chen, R., McCue, M., Yun, D.H., Drummond, G.T., Ku, T., Evans, N.B., Oak, H.C., Trieu, W., et al. (2018). Protection of tissue physicochemical properties using polyfunctional crosslinkers. Nat. Biotechnol. *37*, 73.

Paszke, A., Gross, S., Massa, F., Lerer, A., Bradbury, J., Chanan, G., Killeen, T., Lin, Z., Gimelshein, N., Antiga, L., et al. (2019). PyTorch: An imperative style, high-performance deep learning library. Adv. Neural Inf. Process. Syst., 8024–8035.

Puelles, V.G., and Bertram, J.F. (2015). Counting glomeruli and podocytes: rationale and methodologies. Curr. Opin. Nephrol. Hypertens. *24*, 224–230.

Puelles, V.G., Fleck, D., Ortz, L., Papadouri, S., Strieder, T., Böhner, A.M.C., van der Wolde, J.W., Vogt, M., Saritas, T., Kuppe, C., et al. (2019). Novel 3D analysis using optical tissue clearing documents the evolution of murine rapidly progressive glomerulonephritis. Kidney Int. *96*, 505–516.

Rajan, N., Habermehl, J., Coté, M.F., Doillon, C.J., and Mantovani, D. (2006). Preparation of ready-to-use, storable and reconstituted type I collagen from rat tail tendon for tissue engineering applications. Nat. Protoc. *1*, 2753–2758.

Reardon, S. (2016). Worldwide brain-mapping project sparks excitement - and concern. Nature *537*, 597.

Renier, N., Wu, Z., Simon, D.J., Yang, J., Ariel, P., and Tessier-Lavigne, M. (2014). iDISCO: a simple, rapid method to immunolabel large tissue samples for volume imaging. Cell *159*, 896–910.

Renier, N., Adams, E.L., Kirst, C., Wu, Z., Azevedo, R., Kohl, J., Autry, A.E., Kadiri, L., Umadevi Venkataraju, K., Zhou, Y., et al. (2016). Mapping of Brain Activity by Automated Volume Analysis of Immediate Early Genes. Cell *165*, 1789–1802.

Richardson, D.S., and Lichtman, J.W. (2015). Clarifying Tissue Clearing. Cell *162*, 246–257.

Rodi, P.M., Bocco Gianello, M.D., Corregido, M.C., and Gennaro, A.M. (2014). Comparative study of the interaction of CHAPS and Triton X-100 with the erythrocyte membrane. Biochim. Biophys. Acta *1838*, 859–866.

Ronneberger, O., Fischer, P., and Brox, T. (2015). U-Net: convolutional networks for biomedical image segmentation. In Proceedings of the International Conference on Medical Image Computing and Computer-Assisted Intervention (MICCAI 2015), *9351*, N. Navab, J. Hornegger, W. Wells, and A. Frangi, eds., pp. 234–241, (Springer). https://doi.org/10.1007/978-3-319.

Schindelin, J., Arganda-Carreras, I., Frise, E., Kaynig, V., Longair, M., Pietzsch, T., Preibisch, S., Rueden, C., Saalfeld, S., Schmid, B., et al. (2012). Fiji: an open-source platform for biological-image analysis. Nat. Methods *9*, 676–682.

Schneider, C.A., Rasband, W.S., and Eliceiri, K.W. (2012). NIH Image to ImageJ: 25 years of image analysis. Nat. Methods *9*, 671–675.

Schnermann, M.J. (2017). Chemical biology: Organic dyes for deep bioimaging. Nature *551*, 176–177.

Shen, G., Anand, M.F., and Levicky, R. (2004). X-ray photoelectron spectroscopy and infrared spectroscopy study of maleimide-activated supports for immobilization of oligodeoxyribonucleotides. Nucleic Acids Res. *32*, 5973–5980.

Sijens, P.E., Edens, M.A., Bakker, S.J., and Stolk, R.P. (2010). MRI-determined fat content of human liver, pancreas and kidney. World J. Gastroenterol. *16*, 1993–1998.

Steinke, H., and Wolff, W. (2001). A modified Spalteholz technique with preservation of the histology. Ann. Anat. *183*, 91–95.

Stubičar, N., and Petres, J. (1981). Micelle Formation by Tritons in Aqueous Solutions. Croat. Chem. Acta *54*, 255–266.

Stubičar, N., Matejaš, J., Zipper, P., and Wilfing, R. (1989). Size, shape and internal structure of Triton X-100 micelles determined by light and small-angle X-ray scattering techniques. In Surfactants in Solution (Springer), pp. 181–195.

Sullivan, D.P., Winsnes, C.F., Åkesson, L., Hjelmare, M., Wiking, M., Schutten, R., Campbell, L., Leifsson, H., Rhodes, S., Nordgren, A., et al. (2018). Deep learning is combined with massive-scale citizen science to improve large-scale image classification. Nat. Biotechnol. *36*, 820–828.

Svergun, D.I., and Koch, M.H.J. (2003). Small-angle scattering studies of biological macromolecules in solution. Rep. Prog. Phys. *66*, 1735–1782.

Tainaka, K., Kubota, S.I., Suyama, T.Q., Susaki, E.A., Perrin, D., Ukai-Tadenuma, M., Ukai, H., and Ueda, H.R. (2014). Whole-body imaging with single-cell resolution by tissue decolorization. Cell *159*, 911–924.

Tainaka, K., Murakami, T.C., Susaki, E.A., Shimizu, C., Saito, R., Takahashi, K., Hayashi-Takagi, A., Sekiya, H., Arima, Y., Nojima, S., et al. (2018). Chemical Landscape for Tissue Clearing Based on Hydrophilic Reagents. Cell Rep. *24*, 2196–2210.

Tetteh, G., Efremov, V., Forkert, N.D., Schneider, M., Kirschke, J., Weber, B., Zimmer, C., Piraud, M., and Menze, B.H. (2018). Deepvesselnet: Vessel segmentation, centerline prediction, and bifurcation detection in 3-d angiographic volumes. arXiv, arXiv:180309340.

Todorov, M.I., Paetzold, J.C., Schoppe, O., Tetteh, G., Efremov, V., Voelgyi, K., Duering, M., Dichgans, M., Piraud, M., and Menze, B. (2019). Automated analysis of whole brain vasculature using machine learning. bioRxiv. https://doi.org/10.1101/613257.

Van Der Walt, S., Colbert, S.C., and Varoquaux, G. (2011). The NumPy array: a structure for efficient numerical computation. Comput. Sci. Eng. *13*, 22.

Virtanen, P., Gommers, R., Oliphant, T.E., Haberland, M., Reddy, T., Cournapeau, D., Burovski, E., Peterson, P., Weckesser, W., Bright, J., et al. (2020). SciPy 1.0: fundamental algorithms for scientific computing in Python. Nat. Methods. https://doi.org/10.1038/s41592-019-0686-2.

Vogt, N. (2018). Raising the game in image classification. Nat. Methods *15*, 759.

Voigt, F.F., Kirschenbaum, D., Platonova, E., Pagès, S., Campbell, R.A., Kästli, R., Schaettin, M., Egolf, L., Van Der Bourg, A., Bethge, P., and Haenraets, K. (2019). The mesoSPIM initiative: open-source light-sheet mesoscopes for imaging in cleared tissue. bioRxiv. https://doi.org/10.1101/577122.

Wainberg, M., Merico, D., Delong, A., and Frey, B.J. (2018). Deep learning in biomedicine. Nat. Biotechnol. *36*, 829–838.

Wang, X., Misawa, R., Zielinski, M.C., Cowen, P., Jo, J., Periwal, V., Ricordi, C., Khan, A., Szust, J., Shen, J., et al. (2013). Regional differences in islet distribution in the human pancreas–preferential beta-cell loss in the head region in patients with type 2 diabetes. PLoS ONE *8*, e67454.

Wang, F., Wan, H., Ma, Z., Zhong, Y., Sun, Q., Tian, Y., Qu, L., Du, H., Zhang, M., Li, L., et al. (2019). Light-sheet microscopy in the near-infrared II window. Nat. Methods *16*, 545–552.

White, L.J., Taylor, A.J., Faulk, D.M., Keane, T.J., Saldin, L.T., Reing, J.E., Swinehart, I.T., Turner, N.J., Ratner, B.D., and Badylak, S.F. (2017). The impact of detergents on the tissue decellularization process: A ToF-SIMS study. Acta Biomater. *50*, 207–219.

Yanagishita, M., Podyma-Inoue, K.A., and Yokoyama, M. (2009). Extraction and separation of proteoglycans. Glycoconj. J. *26*, 953–959.

Yang, B., Treweek, J.B., Kulkarni, R.P., Deverman, B.E., Chen, C.K., Lubeck, E., Shah, S., Cai, L., and Gradinaru, V. (2014). Single-cell phenotyping within transparent intact tissue through whole-body clearing. Cell *158*, 945–958.

Yushkevich, P.A., Gao, Y., and Gerig, G. (2016). ITK-SNAP: An interactive tool for semi-automatic segmentation of multi-modality biomedical images. In 38th Annual International Conference of the IEEE Engineering in Medicine and Biology Society (EMBC) (IEEE) Orlando, FL, pp. 3342–3345.

Zhang, Q., Tao, H., and Hong, W.X. (2011). New amphiphiles for membrane protein structural biology. Methods *55*, 318–323.

Zhao, H.L., Zhang, C.P., Zhu, H., Jiang, Y.F., and Fu, X.B. (2017). Autofluorescence of collagen fibres in scar. Skin Res. Technol. *23*, 588–592.

STAR★METHODS

KEY RESOURCES TABLE

REAGENT or RESOURCE	SOURCE	IDENTIFIER
Antibodies		
Rabbit Anti-Iba1	Wako	Cat.# 019-19741; RRID: AB_839504
Rabbit Anti-Tyrosine Hydroxylase	abcam	Cat.# ab112; RRID: AB_297804
Alexa 647-conjugated secondary antibody	Thermo Fisher	Cat.# A-21245; RRID: AB_2535813
Mouse Anti-MBP	Atlas antibodies	Cat.# AMAb91064; RRID: AB_2665784
Rabbit Anti-Laminin	Sigma	Cat.# L9393; RRID: AB_477163
Rabbit Anti-Neuropeptide Y	abcam	Cat.# Ab30914; RRID: AB_1566510
Rabbit Anti-GFAP	Dako	Cat.# Z033401-2; RRID: AB_10013382
Alexa 647 goat anti-rabbit secondary antibody	Life Technology	Cat.# A31852; RRID: AB_162553
Chemicals, Peptides, and Recombinant Proteins		
Phosphate Buffer Saline containing Heparin	Ratiopharm	Cat.# N68542.03
4% paraformaldehyde (PFA)	Morphisto	Cat.# 11762.05000
CHAPS	Roth	Cat.# 1479.4
Triton X-100	PanReac Applichem	Cat.# A4975,1000
SDS	PanReac Applichem	Cat.# A2572,0250
Methylene blue	Sigma	Cat.# M9140
N-Methyldiethanolamine	Sigma	Cat.# 471828
Ethanol	Merck	Cat.# 10098535000
Benzyl benzoate	Sigma	Cat.# W213802
Benzyl alcohol	Sigma	Cat.# 24122
Dichloromethane	Roth	Cat.# KK47.1
Methyl-β –cyclodextrin	Sigma	Cat.# 332615
Trans-1-acetyl-4-hydroxy-l-proline	Sigma	Cat.# 441562
Atto647N-conjugated anti-GFP nanobooster	Chromotek	Cat.# gba647n-100; RRID: AB_2629215; Batch No. 60920001SAT2
TO-PRO-3	Thermo Fisher	Cat.# T3605
Methoxy X-04	Tocris	Cat.# 4920
NaOH	Roth	Cat.# 6771.1
Acetic acid	Roth	Cat.# T179.1
Guanidine hydrochloride	Roth	Cat.# 6069.3
Sodium acetate	Sigma	Cat.# S2889
DMSO	Roth	Cat.# A994.2
Propidium iodide	Thermo Fisher	Cat.# P3566
Gill's hematoxylin	Sigma	Cat.# GHS3
Eosin	Roth	Cat.# 7089.1
Cresyl violet	Sigma	Cat.# C5042
Copper sulfate	Roth	Cat.# CP86.1
Ammonium chloride	Roth	Cat.# P726.1
DyLight 649-lectin	Vector	Cat.# DL-1178
Goat serum	GIBCO	Cat.# 16210072
Bovine Serum Albumin	Sigma	Cat.# A7906
Critical Commercial Assays		
Bio-Rad DC protein assay kit	Bio-Rad	Cat.# 5000116
PAS staining system	Sigma	Cat.# 395B

(*Continued on next page*)

Continued

REAGENT or RESOURCE	SOURCE	IDENTIFIER
Deposited Data		
Raw data and data labels for SHANEL	This paper	http://discotechnologies.org/SHANEL/
Experimental Models: Organisms/Strains		
CD-1 IGS	Charles River	Cat.# 022
Software and Algorithms		
ImageJ	Schneider et al., 2012	https://imagej.nih.gov/ij/
AxioZoom EMS3 software	Carl Zeiss AG	https://www.zeiss.com/microscopy/int/products/stereo-zoom-microscopes/axio-zoom-v16.html#downloads
ImSpector	Aberrior/LaVision	https://www.lavisionbiotec.com/
Photoshop CS6	Adobe	https://www.adobe.com/products/photoshop.html
Imaris	Bitplane	https://imaris.oxinst.com/
Vision4D	Arivis	https://www.arivis.com/de/imaging-science/arivis-vision4d
SciPy package for Python	Virtanen et al., 2020	https://www.scipy.org
Python Anaconda distribution	Anaconda	https://www.anaconda.com/distribution/
PyTorch deep learning framework for Python	Paszke et al., 2019	https://pytorch.org/
Cuda	NVIDIA	https://developer.nvidia.com/cuda-downloads
NiBabel	Brett et al., 2020	https://nipy.org/nibabel
Connected-components-3d	Seung Lab	https://github.com/seung-lab/connected-components-3d
SHANEL algorithm	This paper	https://github.com/erturklab/shanel-network
CuDNN	NVIDIA	https://developer.nvidia.com/cuda-downloads
Other		
Online demonstration of the SHANEL algorithm	This paper	https://colab.research.google.com/drive/1Lpfo6AoHGfpzHvHiD7pnH6DuW9VQxFgq
Resource website for SHANEL	This paper	http://discotechnologies.org/SHANEL/

LEAD CONTACT AND MATERIALS AVAILABILITY

Further information and requests for resources and reagents should be directed to and will be fulfilled by the Lead Contact, Ali Ertürk (erturk@helmholtz-muenchen.de). The clearing protocols as well as cleared samples, algorithms and data on SHANEL are freely available from the Lead contact and shared at http://discotechnologies.org/SHANEL/.

EXPERIMENTAL MODEL AND SUBJECT DETAILS

Mouse samples

CD-1 IGS (Charles River, stain code: 022) mice were used for blood collection, organs screening and protein loss assay. The animals were housed under a 12/12 hours light/dark cycle. The animal experiments were conducted according to institutional guidelines: Klinikum der Universität München / Ludwig Maximilian University of Munich and after approval of the Ethical Review Board of the Government of Upper Bavaria (Regierung von Oberbayern, Munich, Germany) and in accordance with the European directive 2010/63/EU for animal research. All data are reported according to the ARRIVE criteria. Animals were randomly selected related to age and gender. Mice were deeply anesthetized using a combination of medetomidine, midazolam and fentanyl (MMF; 5 mg, 0.5 mg and 0.05 mg per kg body mass for mice; intraperitoneal). As soon as the animals did not show any pedal reflex, the chest of the animal was opened and exposed. The blood was extracted intracardially from the left ventricle. The animals were sacrificed afterward. Then the blood was mixed with 2 times volume of 4% paraformaldehyde (PFA, pH 7.4; Morphisto, 11762.05000) in 0.01 M PBS (pH 7.4; Morphisto, 11762.01000) and incubated for 24 h at 4°C. Animals for protein loss assay were intracardially perfused with heparinized 0.01 M PBS (10 U ml^{-1} of heparin, Ratiopharm; ~110 mmHg pressure using a Leica Perfusion One system) for 5–10 min at room temperature until the blood was washed out, followed by 4% PFA for 10–20 min. The brains were dissected and post-fixed in 4% PFA for 1 d at 4°C and later washed with 0.01 M PBS for 10 min 3 times at room temperature.

Pig samples

An intact pig brain was bought from a local slaughterhouse and selected randomly relate to gender, then fixed for 10 days immersing it in 4% PFA at 4°C. Housing, breeding and animal experiments of *INS*-EGFP transgenic pigs were done at the Institute of Molecular Animal Breeding and Biotechnology at LMU Munich according to the approval of the Ethical Review Board of the Government of Upper Bavaria (Regierung von Oberbayern, Munich, Germany) and in accordance with the European directive 2010/63/EU for animal research. All data are reported according to the ARRIVE criteria. *INS*-EGFP transgenic pigs have a beta-cell specific EGFP reporter gene expression driven by the porcine insulin (*INS*) promoter (Kemter et al., 2017). Pancreas of an exsanguinated 5.5 month-old *INS*-EGFP transgenic male pig of a German landrace background was dissected, its pancreatic ducts were cannulated and 20 mL of ice-cold 4% PFA was slowly injected into the ducts.

Human samples

Intact human brains were taken from different human body donors with no known neuropathological diseases. All donors gave their informed and written consent to explore their cadavers for research and educational purposes, when still alive and well. The signed consents are kept at the Anatomy Institute, University of Leipzig, Germany. Institutional approval was obtained in accordance to the Saxonian Death and Funeral Act of 1994. The signed body donor consents are available on request.

The brains of a 92 years-old female and a 48 years-old male of the body donation program of the Institute of Anatomy, University of Leipzig were fixed *in situ* by whole head perfusion via carotid and vertebral arteries under a pressure of below 1 bar. The head was first perfused with 5 L heparinized 0.01 M PBS (10 U ml^{-1} of heparin, Ratiopharm), followed by 3 L 4% PFA in 0.01 M PBS for 2-3 h. The veins were finally closed to maintain the PFA to the brain. Then the brains were recovered by calvarian dissection and preserved at least 1-2 weeks for post-fixation submersed in the 4% PFA solution. The thyroid was dissected and post-fixed by 200 mL PFA for 3 days. The kidneys of a 93 years-old female donor were dissected from the body. The blood was flushed with 200 mL of heparinized PBS in a PBS bath for 1 hr and perfused with 400 mL of PFA immersed in PFA solution. The kidneys were preserved at least 1-2 weeks for post-fixation submersed in the 4% PFA solution at 4°C.

METHOD DETAILS

Small-angle X-ray scattering measurements

We used small-angle X-ray scattering to determine the size, shape and aggregation number of CHAPS and SDS micelles. Experimental data were collected at beam line 12ID at the Advanced Photon Source (APS) using procedures as previously described (Lipfert et al., 2007; Oliver et al., 2013, 2014). In brief, measurements were carried out with a custom-made sample cell and holder (Lipfert et al., 2006), at a temperature of 25°C and an X-ray energy of 12 keV, with a sample-to-detector distance of 1.8 m. We defined the magnitude of momentum transfer as $q = 4\pi / \lambda \cdot sin(\theta)$, where 2θ is the total scattering angle and $\lambda = 1$ Å the X-ray wavelength. The useable q-range in our measurements was 0.02 $Å^{-1} < q < 0.275$ $Å^{-1}$. Scattering angles were calibrated using a silver behenate standard sample. Data read out, normalization, and circular averaging were performed using custom routines at beam line 12ID, APS. SDS and CHAPS were measured in PBS buffer for 10 exposures of 0.1 s. Matching buffer profiles were subtracted for background correction. Subsequent exposures were compared to verify the absence of radiation damage. Horse heart cytochrome *c* at 8 mg/ml was used as a molecular mass standard.

Small-angle X-ray scattering data analysis

Radii of gyration R_g and forward scattering intensities *I(0)* were determined from Guinier analysis (Guinier, 1939; Lipfert and Doniach, 2007; Svergun and Koch, 2003) of the low q region of scattering profiles, i.e., from a fit of the logarithm of the scattering intensity versus q^2 for small q (Figures S1A and S1B). The fitted radii of gyration are in excellent agreement with previously reported values, as far as available (Figure 1C). In addition, the full scattering profiles were fitted with one- and two-component ellipsoid models (Lipfert et al., 2007) (Figure S1C). We found that the CHAPS data were well described by a prolate one-component ellipsoid model with long axis of ≈30 Å and short axis ≈12 Å. In contrast, the SDS data require a two-component ellipsoid model for a convincing fit, similar to other 'head-to-tail' detergents (Lipfert et al., 2007), and were well described by a oblate two-component ellipsoid model with an inner core (representing the region occupied by the hydrophobic tail groups) with small axis ≈15 Å and long axis ≈25 Å (in good agreement with results from neutron scattering) (Hammouda, 2013), surrounded by a shell (representing the head groups) of thickness ≈3.5 Å.

Aggregation numbers for CHAPS and SDS micelles were determined using two independent approaches (Lipfert et al., 2007). One approach was to use the fitted geometric models to compute the volumes of the micelle (in the case of CHAPS) or of the hydrophobic core (in the case of SDS) and to compute the aggregation number by dividing the total volume by the volume of the monomer (for CHAPS, see Table S1) or the hydrophobic core volume by the volume of the alkyl tail (determined from the Tanford formula (Clarke, 1981), 350.2 $Å^3$ for SDS). We note that the approach of using the micelle volume to determine the aggregation number uses the entire scattering profile in the model fit, but is independent of the scale of the scattering intensity, since only the shape of the scattering pattern is fit. An alternative and independent approach to determining the aggregation number is to determine the forward scattering intensity *I(0)* from Guinier analysis and to compute the aggregation number from the equation (Lipfert et al., 2007):

$$N = I(0)/I_{mon}(0) = I(0) \Big/ \left[K \times (C - CMC) \times (r_{det} - r_{sol})^2 \times V_{mon}^2\right]$$

Here K is a proportionality constant that was determined from measurements of horse heart cytochrome c as a scattering standard, C is the detergent concentration, CMC the critical micelle concentration, ρ_{det} the electron density of the detergent, ρ_{sol} = 0.34 e/Å^3 the electron density of the solvent, and V_{mon} the detergent monomer volume. Values for CMC, ρ_{det} and V_{mon} are given in Table S1. The approach of using $I(0)$ to determine the aggregation number only uses the very low q information in the scattering pattern and is independent of any model assumptions about the size or shape of the micelles. Aggregation numbers determined by the independent approaches are in good agreement.

Comparison of permeabilization capacity of different detergents on pig pancreas using methylene blue dye staining

1-2 cm pig pancreas cubic samples were incubated with the following detergents: 10% w/v CHAPS (Roth, 1479.4), 10% w/v Triton X-100 (PanReac Applichem, A4975,1000) or 200 mM SDS (PanReac Applichem, A2572,0250) for 2 days at 37°C. After PBS wash, the samples were incubated with 50 mL of 0.05% methylene blue dye (Sigma, M9140) in plastic tubes (Falcon) at 37°C overnight. After PBS wash, the samples were cut into half to evaluate the staining efficiency of the inner tissue. The camera pictures of the samples were analyzed by ImageJ for profile plot along the center of the cut samples, and we quantified the pixels under threshold gray value.

Screening of affordable and scalable chemicals for blood decolorization

PFA-fixed mouse blood was thoroughly vortexed with either only 25% w/v screened chemicals (Sigma, for the catalog codes, see Table S2) or only detergents (10% w/v CHAPS, 10% w/v Triton X-100 or 200 mM SDS), or the mixture of detergents and 25% w/v chemicals, and then immediately centrifuged at 15000 rpm for 5 min at room temperature. Supernatants were transferred into multi-well plates (Corning, CLS3527) and pellets were dissolved in diH_2O and also transferred into the paired wells. Camera images were immediately captured. In accordance with our hypothesis that electron-rich nitrogen donor and polarizable hydrogen of chemicals tend to bind with the iron of heme as double-action multidentate ligands, then eluting the heme from the blood, all of the tested chemicals would partly decolorize the red heme. These effects were improved with the addition of detergents. 100 μL supernatant solution from each well was transferred to a 96-well black microplate (Corning, CLS3925) and the visible spectra were recorded using a microplate reader (Fluostar Omega, BMG Labtech). The OD600 values were measured with the Omega analysis software. Considering the practical prices and availability of reagents to process large samples such as the human brain, we optimized the concentration of CHAPS with N-Methyldiethanolamine (chemical 7, Sigma, 471828) for later experiments (Tainaka et al., 2014).

Permeabilization and decolorization of mouse organs containing remaining blood

Mouse organs were dissected and post-fixed with 4% PFA/PBS from deeply anesthetized animals intended to be euthanized. The blood-rich organs were washed with PBS for 3 h x 3 times and put into a multi-well plate and camera pictures images were taken. Then the organs were incubated with the following mixtures: 10% w/v CHAPS and 25% w/v N-Methyldiethanolamine, 10% w/v Triton X-100 and 25% w/v N-Methyldiethanolamine, 200 mM SDS and 25% w/v N-Methyldiethanolamine at 37°C on a shaking rocker (IKA, 2D digital). The solutions were refreshed when the color changed to green until colorless. Then the grouped samples were washed with PBS 3 times for 3 h at room temperature and imaged again with a camera.

Protein loss assay

PFA-fixed adult mouse (3-4 months) brains were cut into 1-mm-thick sections using a vibratome (Leica, VT1200S) (Chung et al., 2013; Murray et al., 2015). All sections were weighted and randomly grouped, then placed in 5 mL solutions as follow: distilled water, 2.5% w/v CHAPS, 5% w/v CHAPS, 10% w/v CHAPS, 200 mM SDS or 10% w/v Triton X-100. The samples were incubated for 2 weeks at 37°C on a shaking rocker. The respective solutions and quantity of protein loss from the tissue which diffused into the solutions were measured using Bio-Rad *DC* protein assay kit (Bio-Rad, 5000116). Total protein in the mouse brain was estimated at 10% (wt). For each group, the standard solution was prepared in the same buffer as the sample.

Pig brain clearing with passive SHANEL

PFA-fixed pig brain samples were washed with PBS at room temperature in a 500 mL glass beaker and incubated with 10% w/v CHAPS and 25% w/v N-Methyldiethanolamine solution at 37°C on a shaking rocker. The incubation time for a single whole brain was 10 days, with the solution refreshed once at day 5. After the PBS washing performed at room temperature, the samples were shaken with a series of Ethanol (Merck, 10098535000)/DiH_2O solutions (50%, 70%, 100%, 100% v/v) at room temperature, followed by a DCM (Roth, KK47.1) incubation and in the end they were immersed into the BABB (benzyl benzoate:benzyl alcohol = 2:1, Sigma, W213802, 24122) solution until complete transparency. The incubation time depended on the sample size: for whole brains, 4 days for each step were needed.

Active SHANEL clearing of pig pancreas

Pancreas from a 5.5-months old *INS*-EGFP transgenic pig was dissected without the tail part, a G 20 venous catheter was inserted into the pancreatic duct and sewed on. 4% PFA was injected to fix the tissue, followed by post-fixation for 3 days at 4°C. Then the

sample was placed into the active pumping system consisting of a peristaltic pump (ISMATEC, REGLO Digital MS-4/8 ISM 834), chemical-resistant PTFE tubing (VWR, 228-0735) and a glass chamber (Omnilab, 5163279). After PBS washing, 200 mL solution of 5% w/v CHAPS and 12.5% w/v N-Methyldiethanolamine was circulated through the pancreas for 8 days in total, refreshing the solution with fresh one every 2 days. After 2 times of PBS washing for 3 hours, the sample was pretreated with 200 mL of permeabilization solution containing 1.5% goat serum (GIBCO, 16210072), 0.5% Triton X-100, 0.5 mM of methyl-β –cyclodextrin (Sigma, 332615), 0.2% trans-1-acetyl-4-hydroxy-l-proline (Sigma, 441562) and 0.05% sodium azide (Sigma, 71290) in PBS for half day at room temperature. Subsequently, the perfusion proceeded further, through connection of a 0.20 μm syringe filter (Sartorius, 16532) to the intake-ending of the tube to prevent accumulation of dye aggregates in the sample. At the same time, an infrared lamp (Beuer, IL21) was used to heat up the solution to 26–28°C. With this setting, the pancreas was perfused for 13 days with 250 mL of the same permeabilization solution containing 30 μL of Atto647N-conjugated anti-GFP nanobooster (Chromotek, gba647n-100, 60920001SAT2). After that, the pancreas was washed out by perfusing with a washing solution (1.5% goat serum, 0.5% Triton X-100, 0.05% of sodium azide in PBS) for 6 h 3 times at room temperature and PBS for 3 h at room temperature. The clearing was started with a series of 250 mL of Ethanol(EtOH)/DiH_2O solutions (50%, 70%, 100%, 100% v/v) pumping for 6 hours at each step. Then the pancreas was passively incubated with DCM for 1 day, proceeded by incubation into BABB solution until complete transparency in around 2 weeks.

Other clearing methods

Centimeters-sized pig pancreas, human brain and human kidney samples were cleared by 1) SHANEL without CHAPS/NMEDA pretreatment, 2) 3DISCO, 3) uDISCO, 4) vDISCO, 5) iDISCO+, 6) PACT (Passive CLARITY) and 7) MASH (RIMS = WGO/CA) protocols. 1) Samples were incubated in 50%, 70%, 100%, 100% v/v Ethanol/DiH_2O solutions at room temperature for 4h each step, followed by overnight DCM and then BABB incubation. 2) Samples were incubated in 50%, 70%, 80%, 100%, 100% v/v THF(Roth, CP82.1)/DiH_2O solutions at room temperature for 4h each step, followed by overnight DCM and then dibenzyl ether (DBE, Sigma, 33630) incubation. 3) Samples were incubated in 30%, 50%, 70%, 80%, 90%, 96%, 100% v/v tert-butanol(Roth, AE16.3)/DiH_2O solutions at room temperature for 4h each step, following DCM overnight and in the end BABB. 4) Samples were incubated in permeabilization solution (1.5% goat serum, 0.5% Triton X-100, 0.5 mM methyl-β -cyclodextrin, 0.2% trans-1-acetyl-4-hydroxy-l-proline and 0.05% sodium azide in PBS) at 37°C for 1 day, then washed with washing solution (1.5% goat serum, 0.5% Triton X-100, 0.05% sodium azide in PBS) and PBS for 4 hours each. Next, the samples were treated with 50%, 70%, 80%, 100%, 100% v/v THF/DiH_2O solutions at room temperature for 4 hours each step, followed by overnight DCM and then BABB incubation. 5) We were following the latest protocol updates from https://idisco.info. Samples were incubated in 20%, 40%, 60%, 80%, 100%, 100% v/v methanol (Roth, 4627.6)/DiH_2O solutions at room temperature for 4h each step and, after chilling at 4°C, the samples were shaken in 66%DCM/33%methanol. Then, after two washing in 100% methanol, the samples were chilled at 4°C and bleached with 5% H_2O_2 in methanol overnight. Next, samples were rehydrated with methanol/DiH_2O 80%, 60%, 40%, 20%, PBS at room temperature for 4 hours each step. Then, the samples were permeabilized with 20% DMSO and 2.3% w/v glycine solution overnight at room temperature. Last, the samples were cleared with 20%, 40%, 60%, 80%, 100%, 100% v/v methanol/DiH_2O solution for 4 hours each step, 66% DCM/33% methanol overnight, DCM 4h and DBE. 6) The samples were incubated at 4°C for 2 days in the hydrogel monomer solution of 4% acrylamide in PBS supplemented with 0.25% photoinitiator 2,2′-Azobis[2-(2-imidazolin-2-yl)propane]dihydrochloride (a.k.a VA-044, Wako Chemicals, 011-19365). Samples were degassed and incubated at 37°C for 6 hours to initiate the tissue-hydrogel hybridization. After removing the excess of hydrogel on the surface, the matrices were delipidated with 8% SDS in PBS for 5 days with shaking. Last, the samples were transferred to the RIMS media (Forty grams of Sigma D2158 (Histodenz) in 30 mL of 0.02 M PBS with 0.1% tween-20 and 0.01% sodium azide, pH to 7.5 with NaOH—which results in a final concentration of 88% Histodenz w/v). 7) MASH protocol was modified iDISCO+ protocol with another RIMS solution (WGO/CA: 72% methyl salicylate also known as wintergreen oil (WGO, Sigma-Aldrich, 84332) and 28% trans-Cinnamaldehyde (CA, Sigma-Aldrich, C80687).

0.5 cm thick *INS*-EGFP transgenic pig pancreas slices were incubated with 10% w/v CHAPS and 25% w/v N-Methyldiethanolamine solution at 37°C overnight. Half of the samples were dehydrated with EtOH/DiH_2O solutions: 50%, 70%, 100%, 100% v/v for 2 hours at each step and delipidated with DCM, then immersed into BABB solution until transparency. The other half of the samples were incubated with the permeabilization solution (1.5% goat serum, 0.5% Triton X-100, 0.5 mM methyl-β -cyclodextrin, 0.2% trans-1-acetyl-4-hydroxy-l-proline and 0.05% sodium azide in PBS) at 37°C for 5 hours, then with 10 mL of the same permeabilization solution containing 20 μL of Atto647N-conjugated anti-GFP nanobooster (Chromotek, gba647n-100) for 4 days. After that, the pancreas samples were washed with the washing solution (1.5% goat serum, 0.5% Triton X-100, 0.05% of sodium azide in PBS) for 1 hour 3 times at room temperature and then with PBS for 1 hour at room temperature. The clearing was started with a series of incubation in EtOH/DiH_2O solutions (50%, 70%, 100%, 100% v/v) for 2 hours for each step. Then, the samples were passively incubated with DCM for 1 hour, and finally treated with the BABB solution until complete transparency. The fluorescent signal was imaged with epifluorescence microscopy at designed time point.

Active SHANEL clearing of intact human brain

The four main arteries of the PFA-fixed intact human brain were connected to the ISMATEC peristaltic pump through a chemical-resistant PTFE tubing in a glass chamber. 5 L of 10% w/v CHAPS and 25% w/v N-Methyldiethanolamine solution was pumped continuously into arteries keeping the pressure at 180-230 mmHg (50-60 rpm). One channel from the pump, made by a single refer-

ence tube, was set for circulation of the solution through the artery into the brain vasculature system: one ending of the tube was connected to the tip which inserted into the artery tubing, and the other ending was immersed in the solution chamber where the brain was placed. The perfusion tip pumped appropriate solution into the artery, and the other ending collected the solution inside of the glass chamber to recirculate the solution, pumping it back into the brain. At the same time, the solution was also stirred using a blender (IKA, RCT B S000) and heated to 37-39°C. With this setting, the human brain was perfused for one month with the solution refreshed once at day 15. Then the solution was changed to PBS for washing for 2 days. Using the same setting without heating, the human brain was labeled with TO-PRO-3 (Thermo Fisher, T3605) in 2 L PBS (1:2000 dilution) for 1 month at room temperature. After labeling the clearing was performed by perfusing with 5 L of the following series of EtOH/DiH_2O solutions: 50%, 70%, 100%, 100% v/v for one week for each step, followed by perfusion of 5 L of DCM for another week to delipidate, in the end the sample was perfused with 5 L of BABB solution until complete transparency. When the brain was getting transparent, the BABB was refreshed and the brain was stored in this solution at room temperature without further circulation or stirring.

After transparency of intact human brain, we dissected one of the eyes for 3D reconstruction using light-sheet microscopy. According to the specific signals from different channels, we identified following structures of the eye. Sclera, also known as the white of the eye, is the opaque, fibrous outer layer of the human eye containing mainly collagen and elastic fibers. Collagen and elastic fibers normally have strong autofluorescence at a wide spectra- more strongly at 488 nm and emission 540nm (Zhao et al., 2017). Iris is a thin, circular structure in the eye. Eye color is defined by the iris. The iris consists of two layers: pigmented fibrovascular layer and pigmented epithelial layer, which were visible at 640 nm and 780 nm. The 780 nm autofluorescence could come from the collagen and/or pigments as suggested (Carrim et al., 2006; Moschovakis and Highstein, 1994). Suspensory ligaments of the lens also refer to the zonule of zinn, which is mainly a collection of zonular fibers (De Maria et al., 2017; McCulloch, 1954). This eye was from a donor with blue eyes, therefore the amount of melanin present was already low. Overall, we don't have any evidence that SHANEL removes the melanin/neuromelanin pigments.

1.5 cm-thick human brain slices preparation

PFA-fixed intact human brain was actively pumped with 5 L 10% w/v CHAPS and 25% w/v N- Methyldiethanolamine solution for one month with solution refreshed once at day 15. Then the solution was changed to PBS for active washing for 2 days. The intact human brain was cooled in PBS at 4°C overnight, then directly cut into 1.5 cm-thick slices in coronal plane using a Rotation Cutting Slicer (Rotation Schneidemaschine, Biodur, Heidelberg, Germany). The total 12 slices were serially labeled and stored in 70% EtOH at 4°C.

Passive histology of a 1.5 cm-thick intact human brain slice

A 1.5 cm-thick intact human brain slice (Number 7, see Figure S3) was randomly chosen and passively incubated with 400 mL TO-PRO-3 (1:2000 dilution) in PBS at room temperature for 1 week. Then the solution was changed to 400 mL with 100 μM of Methoxy X-04 (Tocris, 4920) in 40% EtOH (pH = 10 adjusted by NaOH (Roth, 6771.1)) and the sample was incubated for another week. After labeling, the slice was washed with PBS for 1 day. The clearing started with dehydration using a series of 1 L of EtOH/DiH_2O solutions (50%, 70%, 100%, 100% v/v) and followed by delipidation using 1 L DCM. Each step lasted 1 day. Then the samples were incubated in 1 L BABB solution at room temperature until completely transparency in around 2 weeks.

Passive SHANEL antibody histology of 1.5 cm-thick human brain samples

1.5 cm-thick human brain slices (Number 4 and 6, see Figure S3) were randomly chosen and dehydrated with a series of 1 L EtOH/DiH_2O (50%, 70%, 100%, 100% v/v), then delipidated with 2 L DCM/MeOH (2:1 v/v), then rehydrated with a series of 1 L EtOH/DiH_2O (100%, 70%, 50%, 0% v/v) at room temperature. After incubating with 1 L 0.5 M acetic acid (Roth, T179.1) in DiH_2O, this solution was changed to a mixture of 4 M guanidine hydrochloride (Roth, 6069.3), 0.05 M sodium acetate (Sigma, S2889) and 2% Triton X-100 in PBS, pH = 6.0, at room temperature to loosen the extra cellular matrix. The incubation time for each of all above mentioned solutions was 1 day. Next, the slices were shortly incubated with 10% w/v CHAPS and 25% w/v N-Methyldiethanolamine solution for 4 hours and washed with PBS for 1 day. The intact slices were stored in the blocking buffer (0.2% Triton X-100/10% DMSO (Roth, A994.2)/10% goat serum/PBS) at 4°C. Regions of interest (including hippocampus, primary motor cortex, primary sensory cortex, and primary visual cortex, 2-4 cm x 2-4 cm x 1.5 cm) were cut and incubated with the same blocking buffer at 37°C for 1 day. Then the samples were incubated with rabbit antibody anti-Iba1 (1:1000, Wako, 019-19741) or rabbit antibody anti-TH (1:250, abcam, ab112) in the antibody incubation buffer (3% goat serum/3% DMSO/0.2% Tween-20/10mg·L^{-1}Heparin/PBS) for 1 week at 37°C. After the primary antibody incubation, samples were washed with the washing buffer (0.2%Tween-20/10mg·L^{-1}Heparin/PBS) for 1 day refreshing 3 times and then incubated with Alexa 647-conjugated secondary antibodies (1:500, Thermo Fisher, A-21245) in the antibody incubation buffer for 1 week at 37°C. Other samples were incubated with DyLight 649-lectin (1:500, Vector, DL-1178) in the antibody incubation buffer for 1 week at 37°C. After washing with PBS, propidium iodide (1:100, Thermo Fisher, P3566) or TO-PRO-3 dye was added in PBS for 3 days at 37°C for cell nuclei staining. After labeling, the samples were dehydrated with a series of solutions of EtOH/DiH_2O (50%, 70%, 100%, 100% v/v) and delipidated with the DCM solution for 4 hours each solution followed by BABB incubation at room temperature until the sample transparency was reached in 2-3 days.

To test other SHANEL-compatible antibodies, we cut 1 mm thick brain slices pretreated with SHANEL histology using the vibratome, and we stained them with the following primary antibodies: mouse antibody anti-MBP (myelin basic protein) (1:250, atlas antibodies, AMAb91064), rabbit antibody anti-Laminin (1:100, Sigma, L9393), rabbit antibody anti-Neuropeptide Y (1:300, abcam, ab30914), then the incubation was performed with the respective secondary antibodies (1:500, Thermo Fisher, A-21245) for overnight. After washing with PBS, propidium iodide (1:100) was added in PBS for cell nuclei staining for 1 hour. The samples were dehydrated with a series of solutions of EtOH/DiH_2O (50%, 70%, 100%, 100% v/v) and delipidated with DCM solution for 1 hour each solution. BABB solution replaced the DCM solution and the samples were incubated in BABB at room temperature until complete transparency.

To evaluate the macroscopic and microscopic deformation after SHANEL clearing, we used 1 mm thick human brain slices. The gross shape of the samples was imaged by the Zeiss AxioZoom EMS3/SyCoP3 epifluorescence stereomicroscope before and after SHANEL clearing. For the evaluation of the deformation at the microscopic level, samples were labeled to highlight cellular structures: in particular microglia and astrocytes in the samples were stained using the primary rabbit antibody anti-Iba1 (1:1000, Wako, 019-19741), and the primary rabbit antibody anti-GFAP (1:1000, Dako, Z033401-2) respectively, followed by the secondary antibody Alexa 647 goat anti-rabbit (1:500, Life Technology, A31852) using the SHANEL histology protocol (see previous sections). Subsequently, same regions before and after clearing of the labeled slices were imaged with the Zeiss confocal microscope LSM 880 coupled with a 25x water-immersion long working distance objective (Leica, 0.95 NA, WD = 2.5 mm) mounted on a custom mounting thread. The mounting of the slices for the imaging session was done by putting the individual samples on the glass surface of 35 mm glass-bottom Petri dishes (MatTek, P35G-0-14-C) for both epifluorescence and confocal microscopy. Closing or sealing of the Petri dish was not needed. These confocal scans were later used for the calculation of the root mean square error (see next section).

A second experiment to demonstrate the preservation of cellular and tissue morphology after SHANEL was performed as follows: SHANEL histology cleared human brain and kidney pieces were rehydrated with DCM, EtOH/diH_2O (100%, 70%, 50%) and PBS. These rehydrated samples together with PFA-fixed samples were cut into 20 μm thin slices using a cryostat (Cryostar NX70, Thermo Fisher) for standard hematoxylin and eosin (H&E), Nissl, Periodic Acid Schiff (PAS) staining to qualitatively assess the cellular and extracellular matrix structures with and without SHANEL histology clearing. Hematoxylin-eosin staining was carried out as follows: cryosections were passed through 2 diH2O steps before incubating in Gill's hematoxylin solution (Sigma-Aldrich, GHS3) for 90 s followed by washing under running tap water. Subsequently, cryosections were passed through a battery of increasing concentration of ethanol (50%, 70%, 80% v/v, 2 min each) and then incubated in eosin solution 1% (Roth, 7089.1) for 3 min, followed by 3 quick washes in 96% ethanol and dehydration for 2 times 5 min each in absolute ethanol and Roti-Histol 100% (Roth, 6640.2). Cryosections were then mounted in hydrophobic mounting medium (Sigma-Aldrich, Eukitt 03989) and let dry until imaging. For Nissl staining, cryosections were incubated for 2 min in 70% ethanol prior to incubation in cresyl violet solution 0.5% (Sigma-Aldrich, C5042) for 15 minutes. Following that, slides were quickly washed in distillated water twice and then passed quickly through increasing concentrations of ethanol (70%, 96%, 100% v/v), followed by incubation for 2 min in 100% isopropanol and final dehydration in 100% Roti-Histol twice for 5 minutes. Slides were mounted as described previously. Periodic acid shift staining was performed using PAS staining system (Sigma-Aldrich, 395B) according to manufacturer's instructions. In brief, hydrated cryosections were incubated for 5 minutes in periodic acid solution and then rinsed several times in diH_2O, followed by incubation in Schiff's reagent for 15 min. After washing under running tap water, slides were counterstained in Gill's Hematoxylin for 90 s and subsequently dehydrated and mounted as stated earlier. Image acquisition was performed with an AXIO Imager.M2 microscope (Zeiss) couple with AXIOCam MRc camera (Zeiss) and a EC Pan-NEOFLUAR 40x/0,75(NA) M27 WD:0.71 mm dry objective (Zeiss, 420360-9900).

Copper sulfate treatment in SHANEL to eliminate tissue autofluorescence

1 mm thick human brain slices were cut using the vibratome after SHANEL histology pretreatment. Slices were cleared and imaged with light-sheet microscopy in different wavelengths for autofluorescence. Then, the slices were rehydrated with a series of solutions: 5 mL EtOH/DiH_2O (100%, 70%, 50%, 0% v/v) into water, 1 hour each step, and incubated with 10 mM copper sulfate ($CuSO_4$, Roth, CP86.1) and 50 mM ammonium chloride (Roth, P726.1) pH = 5.0 solution for 1 hour at room temperature. After washing with PBS, the slices were cleared again and imaged with light-sheet microscopy at the same wavelengths used before to check the grade of autofluorescence elimination after the copper sulfate treatment. The images were then analyzed by ImageJ for profile plots and signal intensity. We also processed slices labeled with DyLight 649-lectin and propidium iodide with the same autofluorescence-elimination procedure to check that copper sulfate treatment did not affect the fluorescence signal from the staining while eliminating the autofluorescence from the tissue.

Passive SHANEL histology of intact human thyroid

A thyroid from an 80 years-old female donor was dissected and post-fixed with PFA for 3 days. After PBS wash for 4 hours at room temperature, the thyroid was incubated at 37°C in 200 mL of a 10% w/v CHAPS and 25% w/v N-Methyldiethanolamine solution for 5 days refreshing once at day 3. Then the dehydration of the sample was done with a series of solutions: 200 mL EtOH/DiH_2O (50%, 70%, 100%, 100% v/v), half day each solution, followed by delipidation with 200 mL DCM/MeOH (2:1 v/v) for 2 days in a sealed glass container, and rehydrating with a series of solutions: 200 mL EtOH/DiH_2O (100%, 70%, 50%, 0% v/v) half day each solution.

The ECM was loosened with 0.5 M acetic acid in PBS for 1 day and a mixture of 4 M guanidine hydrochloride, 0.05 M sodium acetate and 2% Triton X-100 in PBS, pH = 6.0, for 1 day. After PBS wash, 100 mL of TO-PRO-3 dye (1:1000) was used to label the sample for 10 days. The clearing was started incubating the sample in a series solutions consisting of 200 mL of EtOH/DiH_2O solutions (50%, 70%, 100%, 100% v/v), shaking for half day each step, followed by 200 mL of DCM for 5 hours, then proceeded with 200 mL BABB solution until complete transparency reached in 3-5 days.

Active SHANEL histology study of intact human kidney

The PFA-fixed intact kidneys were pumped through primary artery with 36 mL of the mixture of 25 mg/ml tetramethylrhodamine isothiocyabate-dextran, 2 mM *p*-maleimidophenyl isocyanate (PMPI) and 5 mM DL-dithiothreitol (DTT) in PBS (Annunziato et al., 1993; Shen et al., 2004). Then the kidneys were sealed inside a plastic bag and incubated in 37°C overnight. After dextran labeling, we set up the perfusion system with an ismatec peristaltic pump and PTFE tubing at room temperature as the human brain. The first step consisted of the washing with 2 L PBS for one day twice. The second step was the decolorization and permeabilization steps performed with 2 L of the 10% w/v CHAPS and 25% w/v N-Methyldiethanolamine solution for one week. The third step was the dehydration step with a series of solutions: 2 L of EtOH/DiH_2O (50%, 70%, 100% v/v), 4 days with each solution. The fourth step was the delipidation step with 4 L DCM/MeOH (2:1 v/v) for 4 days, by sealing the glass container. The fifth step was the rehydration with a series of solutions: 2 L EtOH/DiH_2O (100%, 70%, 50%, 0% v/v), 4 days with each solution. The sixth step consisted of the loosening of the ECM with 0.5 M acetic acid for 4 days and mixture of 4 M guanidine hydrochloride, 0.05 M sodium acetate and 2% Triton X-100 in PBS pH = 6.0, for 4 days. The seventh step was again PBS washing for one day twice. Next, 1 L of TO-PRO-3 dye (1:2000) in PBS was continuously pumped for 2 weeks, then washed with PBS for one day twice. The clearing was started with a series solutions consisting of 2 L of EtOH/DiH_2O solutions (50%, 70%, 100%, 100% v/v) pumping for 2 days for each solution, followed by 2 L of DCM for 3 days, then proceeded with 2 L BABB solution until complete transparency.

To examine the whole kidney pathology, we used tissue recycling reported in details in Puelles et al. (2019). Briefly, the concept is based on reversing the main clearing steps. Thus, after SHANEL, BABB-immersed tissues were gently placed in sequential washes of 100% ethanol, 30 minutes each, 3-5 times (depending on tissue size). Next, sequential washes in PBS were performed, 30 minutes each, 5 times to get rid of residual BABB. Then, conventional paraffin embedding and slicing (5 μm thick) was carried out, thereby allowing subsequent PAS staining as previously described.

To quantify the vessel structures in normal and reduced areas, 8 mm projection (200-1200 slices) of 780nm autofluorescence signal of whole kidney was evaluated by counting the vessel branches and length in same size areas using ImageJ.

Safety recommendations of handling chemicals

According to the open chemistry database from National Institute of Health (NIH) through PubMed, we summarized the safety recommendations of handling SHANEL chemicals. CHAPS is not a hazard substance. It will cause skin and eye irritation and may cause respiratory irritation. NMDEA will cause eye irritation. EtOH is highly flammable liquid. DCM will cause skin, eye and nose irritation, and in case of inhalation, it could cause anesthetic effects, nausea and drunkenness. Benzyl benzoate is harmful if swallowed, and cause skin and eye irritation. Benzyl alcohol is harmful is swallowed and inhaled. However, it meets Safer Choice Criteria for its functional ingredient-class. According to the American Food and Drug Administration (FDA), both benzyl alcohol and benzyl benzoate can be used in minimum quantity as food additive or cosmetic ingredient for human use and consumption. Storing SHANEL chemicals must follow dispositions for hazardous, inflammable, explosive and toxic substances. In particular, handling must be performed in fume hoods, while wearing safety goggles, nitrile gloves (preferably double layer) and lab coats.

SWIR imaging

The cleared human brain was placed in a rectangular glass jar filled with BABB. The jar was positioned between a 1450nm LED light source (Thorlabs, M1450L3) and a cooled InGaAs camera (Allied Vision, G-032 cool TEC2) equipped with a 35mm objective lens (Navitar, SWIR-35). Homogeneous illumination of the sample was established with the help of an engineered diffuser (Thorlabs, ED1-S50) after the collimated LED and plastic diffuser foils at the illuminated side of the glass jar. Two aligned laser printed transparencies with the "SHANEL" lettering were placed between the diffuser foils and the glass wall. Images were taken at 40ms exposure time in high gain mode (gain 1).

An overhead projector (A+K lux) with a 250W halogen light bulb was used for transmissive illumination of the cleared and uncleared 1.5 cm thick human brain slices. Samples were imaged in glass dishes containing BABB and DCM for the cleared and uncleared samples, respectively. SWIR images where taken with a cooled InGaAs camera (Allied Vision, G-032 cool TEC2) together with a 35mm objective lens (Navitar, SWIR-35) equipped with a 1450/50nm bandpass (Edmund optics 85-901) mounted in front of the objective, 54μs exposure time, gain 0. Visible light images where taken with a silicon industry camera (IDS UI3370CP-NIR) together with a 35mm objective lens (Spacecom VHF 35-MP SWIR), 800μs exposure time.

Proton density MRI imaging

Quantitative MRI experiments were conducted to determine the chemical constitution of uncleared and cleared brain samples as assessed by proton density imaging. Uncleared samples in PBS or cleared samples in BABB were separately encapsulated in Eppendorf tubes (mouse brains) or sealed plastic bags (human brains), which in turn were put in a lager container with 1.5% agarose

gel as reference. For all samples, we used a T2-weighted multi-echo spin echo sequence for relaxometry. For animal samples, images were acquired on a Mediso NanoScan 3T (Mediso Medical Imaging Systems, Budapest, Hungary) with repetition time 3850 ms, delta-echo-time 15 ms, 12 echos, field-of-view 16 mm x 16 mm, matrix 96 × 96 and slice thickness 1 mm. For human samples, images were acquired on a Siemens Magnetom Prisma (Siemens Healthineers, Erlangen, Germany) with repetition time 1000 ms, delta-echo-time 15 ms, 15 echos, field-of-view 256 mm x 256 mm, matrix 320 × 320 and slice thickness 1 mm. In order to determine proton density signal (S0), a logarithmic curve was fit to the signal decay measured along the multiple echoes, using MATLAB. S0 was then extrapolated as the fitted T2 signal amplitude at TE = 0 ms. The resulting S0 was normalized to S0 in the 1.5% agarose gel for comparison across the samples.

Light-sheet microscopy imaging

Single plane illuminated (light-sheet) image stacks were acquired using the light-sheet microscopes: Ultramicroscope II featuring the following filter sets: ex 470/40 nm, em 535/50 nm; ex 545/25 nm, em 605/70 nm; ex 580/25 nm, em 625/30 nm; ex 640/40 nm, em 690/50 nm; ex 780 nm, em 845/55 nm; and a prototype Ultramicroscope featuring the following filter sets: ex 470 nm, em 525/50 nm; ex 561 nm, em 595/40 nm; ex 640 nm, em 680/30 nm; ex 785 nm, em 845/55 nm (LaVision BioTec). Samples (detailed information in Table S3) were imaged with a 1x Olympus air objective (Olympus MV PLAPO 1x/0.25 NA [WD = 65mm]) coupled to an Olympus MVX10 zoom body, which provided zoom-out and -in ranging from 0.63x up to 6.3x. Alternatively, the samples were scanned with a dipping 1.1x objective (LaVision BioTec MI PLAN 1.1x/0.1 NA [WD = 17 mm]) coupled with an Olympus revolving zoom body unit (U-TVCAC) on the prototype Ultramicroscope. After low magnification imaging of whole organs, samples were imaged using high magnification objectives (Olympus XLFLUOR 4x corrected/0.28 NA [WD = 10 mm], LaVision BioTec MI PLAN 12x/0.53 NA [WD = 10 mm]) coupled to an Olympus revolving zoom body unit (U-TVCAC) kept at 1x. Tile scans with 20% or 30% overlap along the longitudinal x axis and y axis were obtained using a z-step of 3 μm, 5 μm or 8 μm. Exposure time was 90-120 ms, laser power was adjusted depending on the intensity of the fluorescent signal (in order to avoid saturation of the signal) and the light-sheet width was kept at 80% of maximum. The LaVision light-sheet microscope has ∼4 μm lateral and ∼6.5 μm axial resolutions (1x objective).

Laser-scanning confocal microscopy imaging

We used different kinds of confocal microscopes: the Zeiss LSM 880 confocal microscope was used for method characterization experiments and the imaging of regions of interest from the samples (1 mm thick, 5-10 mm long) already imaged with light-sheet microscopy. In particular, areas of interest from the human brain and the human kidney, were dissected and imaged with this inverted laser-scanning Zeiss confocal microscope using Zen 2 software (v.10.0.4.910; Carl Zeiss AG). Before imaging, samples were mounted by placing them onto the glass surface of 35 mm MatTek glass-bottom Petri dishes while adding a few drops of BABB to make sure that the imaging region was immersed in BABB (Cai et al., 2019). The imaging was done using a 40x oil-immersion objective (Zeiss, ECPlan-NeoFluar × 40/1.30 oil DIC M27, 1.3 NA [WD = 0.21 mm]) and a 25x objective (Leica, 0.95 NA [WD = 2.5 mm]) mounted on a custom thread.

The second confocal microscope is the upright confocal microscope RSG4 from MAVIG. This microscope was used to image a 7.5 × 5 x 1.5 cm brain section, which was cut from the human slice number 7 previously labeled and cleared. The imaging was performed using Caliber I.D. RS-G4 research software. The working dimensions of the stage of this latter microscope were 46 × 40 × 66 cm. The images were acquired with the UPLFLN 10x objective (OLYMPUS 0.3 NA [WD = 10mm]). Tile scans were obtained along the longitudinal y axis. Laser power was adjusted depending on the intensity of the fluorescent signal (in order to avoid saturation of the signal).

Epifluorescence stereomicroscopy imaging

Epifluorescence stereomicroscope was performed to image a cleared 1.5 cm thick whole human brain slice and 1 mm think small sections of human brain slices. The whole brain slice was put in a glass chamber while the small sections in the MatTek glass bottom dishes. The microscope was a Zeiss AxioZoom EMS3/SyCoP3 fluorescence stereomicroscopy coupled with a 1x long working distance air objective (Plan Z 1x, 0.25 NA, WD = 56 mm). The magnification was set as 32x and for the whole brain slice the imaging areas were selected manually to cover half of the slice. The images were taken with 405 nm filters and files were exported as tiff images.

QUANTIFICATION AND STATISTICAL ANALYSIS

Image processing

Processing, data analysis, 3D rendering and video generation for the imaging data were done on an HP workstation Z840, with 8 core Xeon processor, 196 GB RAM, and Nvidia Quadro k5000 graphics card and HP workstation Z840 dual Xeon 256 GB DDR4 RAM, nVidia Quadro M5000 8GB graphic card. We used Imaris (v.9.1, Bitplane), Arivis, Photoshop (Adobe, CC2018) and Fiji for 3D and 2D image visualization. 16-bit grayscale TIFF images for each channel were separately acquired by the light-sheet microscope software ImSpector (v.5.295, LaVision BioTec). Tile scans were stitched by Fiji's stitching plugin49. Stitched images (Figures 2G–2I, 3D, 3E, 4C–4N, 5D, 5E, 6F–6J, 7D, 7E, S4B–S4H, S5B–S5F, and S7B–S7D) were saved in TIFF format and optionally

compressed in LZW format to enable fast processing. To merge the neighboring stacks, alignment was done by manually selecting 3 anatomic landmarks from the overlapping regions. The stitching was performed sequentially with the Scope Fusion module of the Vision4D (v.2.12.6 × 64, Arivis) software. Landmarks were mainly chosen from the cellular structures or vessel structures on the basis of visual inspection of the anatomical features. Please note that the apparent borders (dimmer lines) typically appear at the stitching lines of the mesoscale light-sheet imaging due to overlapping scan of the same region, which can reduce the signal intensity of borders (e.g., Figures S4K–S4N). In addition, some blocks might appear brighter or darker in mesoscale imaging due to 1) long distance travel of light-sheets from left and right, which cannot be equal all the time at different points, 2) a blockage of one of the light-sheets (e.g., Figure 7E) and 3) lack of imaging data at certain positions (e.g., Figure S4E). However, such artifacts does not impede 3D-visualzation. After finishing the 3D reconstructions, the data visualization was done with Imaris in both volumetric and maximum-intensity projection color mapping. Epifluorescence stereomicroscopy images were saved as series TIFF images. The images were stitched manually in Photoshop by overlapping regions from landmarks.

Tissue deformation analysis using RMSE calculation

The grade of the deformation of the tissue caused by SHANEL was assessed visually on the microscopy images and by using the calculation of the Root Mean Square Error (RMSE) that evaluated the morphological deformation of the tissue structures at single-cell level. We applied the same calculation method on 2 different cell types: microglia expressing Iba1 and astrocytes expressing GFAP. To do so, first we imaged the same cells with the Zeiss LSM 880 confocal microscope (see confocal microscopy imaging section) in the samples before and after SHANEL clearing (n = 3 tissue slices per each cell type), then we selected the images (maximum intensity projections) of at least 4 individual cells per each experimental replicate before and after SHANEL clearing, to compare the after-clearing cellular morphology to the corresponding one before the clearing. All the selected images were preprocessed in Fiji using background subtraction (radius 30) and median filtering (radius 2) functions in order to remove artifacts and ease the registration process. Then in the same software, images were scaled up by a factor of 2. Since the clearing process shrinks the samples, we performed a similarity registration to approximately scale the cells from after-clearing samples to match the size of the same cells before-clearing. In this way the RMSE will be calculated on scale-matched images and since the shrinkage effect will not be then considered after the scale matching, the result will be an indication of the grade of the isotropicity of the shrinkage and of the deformation that SHANEL might cause. The similarity transformation was performed using linear stack alignment with SIFT plugin.

Next, we calculated the deformation of the structures of each cell after-clearing over the structures of the same cell before-clearing. To do so, we used a non-rigid Bspline registration, from the Fiji plugin ''bUnwarpJ'' to align the two cell images with the following parameters: registration mode→ accurate, initial deformation → coarse and saving the transformation. To achieve better results, a couple of cellular structures were manually selected as landmarks. We could then visualize this registration as a deformation space or a deformation field, the latter indicated how much each pixel was transformed (how big the error) to match the destination image. The single spot where the deformation field showed minimal value was chosen as center of the cell for the subsequent analysis, therefore its coordinates were taken. To calculate the deformation, we converted the Bspline transformation to raw transformation using ''bUnwarpJ'': in this step the RMSE was calculated for each pixel. However, in order to calculate this change in morphology (considering RMSE) only for the pixels representing the cells, in Fiji we created a binary image that separated cells from the background by using the ''convert to mask'' function. Afterward the skeleton image of the cell representing the gross morphology of the cell was created in python using the skeletonize function from the skimage library. We masked the deformation image with the skeleton image giving as output the deformation image of the skeleton. In the end, we calculated the grade of deformation in term of RMSE considering sequential distances away from the previously selected cell center: the radial profile for the deformation was calculated step by step at defined increasing distances from the cell center. We binned the pixels based on their distances from the cell center and calculated the average and the standard deviation of the RMSE of the all pixels falling inside each distance range. These results were then aggregated for the total analysis taking into account all cells considered per each replicate, then the averaged result of the 3 replicates and their standard deviations were displayed together as radial profiles shown in the Figure S6. The analysis procedure from the skeletonization step could be automatized using a scripting language such as Python or MATLAB.

3D volume and iso-surface rendering and quantification of pig pancreas islets

Insulin positive β-cell volumes were quantified by 3D iso-surfacing using the Imaris software. In the software islet volumes were segmented using the 'absolute threshold' thresholding option and the intensity threshold was set manually for most of the pancreas with the filter of 'number of voxels Img = 1'. Statistical data parameters (Overall, Area, Center of Homogeneous Mass, Ellipsoid Axis A, Ellipsoid AxisB, Ellipsoid Axis C, Ellipsoid Axis Length A, Ellipsoid Axis Length B, Ellipsoid Axis Length C, Ellipticity (oblate), Ellipticity (prolate), Number of Voxels, Position, Sphericity and Volume) were exported from Imaris into an Office Excel (14.0.6023.1000, Microsoft, 2010)) spread sheet (*.xls). Statistical analysis of the islet volumes was performed using GraphPad Prism8.

Cell detection and image analysis

General data processing

Data processing after image stitching was performed using Python as well as various libraries such as SciPy (Virtanen et al., 2020), Numpy (Van Der Walt et al., 2011), Pandas (McKinney, 2010) and Nibabel (Brett et al., 2016). Deep learning algorithms were implemented in PyTorch (Paszke et al., 2019). To enable memory efficient and parallel patch-wise processing, the obtained 3D scans were subdivided into neighboring patches of $(100\ \text{px})^3$ (around 4MB file size uncompressed). Patches overlapped 5% in all directions (corresponding to 15% volumetric overlap) to ensure no cell would be divided at a patch boundary. Subsequent re-concatenation rules out double counting of any cells.

Selection of data

In total four different sections of the human brain have been selected for our deep learning pipeline. One section was chosen from the human hippocampus and three sections from the cortex region, namely the areas of the cortex connected to visual, motor and sensory tasks. These scans were acquired with a 12x objective using light-sheet microscope. The x-y-resolution of this scan is 0.54 μm × 0.54 μm and the z-step is 5μm. In total, 278656 patches from the human brain scan were processed.

Data annotation

In order to have a meaningful sample of our complete dataset, representative patches from 12 locations were selected for data annotation. We chose 6 locations from the hippocampus section and 2 locations from each of the three cortex sections. In each location, 8 neighboring patches were sampled for a total of 96 patches. The ground truth annotation was performed by four human experts in this field. These annotations were used for training our deep learning models as well as evaluating and comparing the performance of each method (see below for details). Every cell in a patch has been annotated by marking the core region of the cell in *ITKSnap* (Yushkevich et al., 2016). Afterward, an independent expert reviewed each patch individually to make sure that the annotation was consistent. This revision resulted in the manual refinement of 24 patches until the result was deemed correct.

Non-deep learning approaches to cell counting

Approach 1: FIJI

Fiji is an image processing package for scientific image analysis on the basis of Image-J (Schindelin et al., 2012). To segment and count single cells the function "3D Objects Counter" (Bolte and Cordelières, 2006) was used. This method requires manually setting a threshold for segmentation of a given patch. Automated segmentation for a very large number of patches thus requires of determining one single threshold that will then be used for all patches. For this, we optimized the threshold for all 96 patches individually. The final segmentation mask and cell counting were computed using the average threshold as the threshold value. As the optimal threshold for the entire dataset may differ from the optimal threshold we determined for the 96 patches we annotated for performance assessment, the reported cell counting performance for Fiji may be seen as an upper bound.

Approach 2: Imaris

Imaris is a microscopy image analysis software from Bitplane (2019). All patches have been converted to the Imaris file format. The function "Surfaces" with the following parameters was applied to all patches: "Shortest distance," "Background Subtraction (local contrast)," "Split touching objects" enabled. This function segments the cells of a patch into vector-based surfaces, which are then converted into a pixel-based image of connected components. In contrast to Fiji, this method requires to set two, not one parameter. Again, they were optimized for all 96 patches individually. The final processing was then performed using the average values for each parameter. Just like for Fiji, the reported cell counting performance may be seen as an upper bound. While Imaris also provides an automatic method to determine these parameters, this fully automatic mode failed to yield meaningful results.

Deep learning model 1: Our CNN

Architecture

We designed a 5-layer deep neural network as depicted in Figure 7A. This neural network consists of four convolutional layers with the respective 3D kernel sizes of 3x3x3, 5x5x5, 5x5x5, 3x3x3 and a fully connected layer. Every convolution is followed by a rectifying linear unit (ReLU) and increases the feature channel size from one to a maximum of 50 feature channels. The final fully connected layer reduces the 50 feature channels to one channel. A sigmoid activation function is applied to yield a probability distribution for the presence of a cell in a given voxel. Subsequent threshold at a probability of 50% finally turns the output into a binary mask. This network architecture is similar to the published "Deep Vessel Net" (Tetteh et al., 2018; Todorov et al., 2019)

Hyperparameters

The network is trained for 200 epochs (no data augmentation). The initial learning rate for the training is set to 0.0001. A learning rate scheduler based on the validation performance is used with the patience of 15 epochs and the reduction factor of 0.5. Batch size for training is set to 32. We used the Adam (Kingma and Ba, 2014) optimizer with $\beta_1 = 0.9$, $\beta_2 = 0.999$, $\varepsilon = 1e\text{-}8$.

Training procedure

Each model was trained on 80 of the 96 patches available (the remaining 16 were set aside for testing). Those 80 patches are then further split down into 16 patches for validation of the model and adjusting the learning rate scheduler and 64 patches for training the network. Afterward, the model with the lowest loss of the validation set is chosen for the final prediction on the corresponding test set. The loss function used to calculate the gradients is the Dice loss defined by

$$L_{Dice} = 1 - \frac{\varepsilon + \sum_{n=1} \widehat{y}_n y_n}{\varepsilon + \sum_{n=1} \widehat{y}_n + \sum_{n=1} y_n}$$

with $\widehat{y}$ being the prediction, y the ground truth and $\varepsilon = 1$ to ensure numerical stability.

Postprocessing

In order to distinguish between single cells of the resulting binary mask, a connected component analysis is performed. All connected components smaller than 50% of the median cell size of the dataset (here: ca. 76 voxels) are automatically removed from the prediction. Such cases may occur, for instance, for partially visible cells at the boundary of the patch, and can be safely removed due to the overlap of patches (see General data processing). All remaining connected components which are smaller than two standard deviations of the median cell size are counted as one cell, all bigger connected components are counted as the size of the component divided by the median cell size. This approach was verified by human labeling and analysis of connected components of the ground truth dataset.

Deep learning model 2: 3D UNet

To compare our approach with a more commonly used "standard" model for segmentation of biomedical images, we implemented a 3 layer version of 3D UNet (Çiçek et al., 2016; Ronneberger et al., 2015) with 3 down-sampling and pooling layers and 3 up-sampling layers. We trained it with the almost same hyper parameters and training schedule as for the first deep learning model. The only difference in the hyper parameter set for the initial learning rate is 0.001 and the reduction factor of the learning rate scheduler is set to 0.1.

Performance comparison of models

K-fold cross validation for deep learning models

Model training and evaluation are based on a k-fold cross-validation with k = 6. Our annotated dataset is thus split into two mutually exclusive datasets with 16 of the 96 patches for testing. The exhaustive rotation throughout the dataset leads to a real test performance for our deep learning models on all 96 patches. Importantly, this ensures that the model performance is evaluated based on its prediction on completely unseen data.

Cell counting performance (F1 Score)

To assess the quality of a model's predicted segmentation of individual cells in the scan, we use the F1 score. This is a commonly used metric to assess the quality for any detection task. It quantifies the performance in percent, taking into account the share of detected cells (recall) and the false positive rate (quantified as precision). Here, a detected cell or true positive (TP) is a cell for which the predicted binary mask overlaps with the ground truth. Similarly, a false positive (FP) is a predicted cell which does not exist in the ground truth. Cells in the ground truth which are missed by the model, as in there do not exist overlapping prediction cells, are counted as false negatives (FN). Precision is defined as the fraction of correct detected cells among all detected cells:

$$Precision = \frac{TP}{TP + FP}$$

Recall is defined as the amount of total detected cells of all existing cells:

$$Recall = \frac{TP}{TP + FN}$$

The F1 score is then calculated as following:

$$F1 = 2 * \frac{Precision * Recall}{Precision + Recall}$$

Processing speed

The comparison of processing speed measures the actual prediction speed of all models in a like-for-like setting. All tests were performed on the same hardware with 32 Intel Xeon E5-2620 v4 at 32x 3GHz processors, 252 GB of RAM and two Nvidia Titan V GPUs. To enables a fair and direct comparison, all data was already loaded into the RAM memory of the computer. The speed measurement comprises the segmentation of multiple patches and the connected component analysis for all 4 methods. Final speeds for each method were then averaged over the number of patches. Please note that the patch-wise processing ensures linear scaling of processing times.

DATA AND CODE AVAILABILITY

A fully functional online demo of our CNN segmentation and cell counting is available at Google Colab: https://colab.research.google.com/drive/1Lpfo6AoHGfpzHvHiD7pnH6DuW9VQxFgq. The complete source code for training the network as well as segmenting cells is available online at our github repository: https://github.com/erturklab/shanel-network.

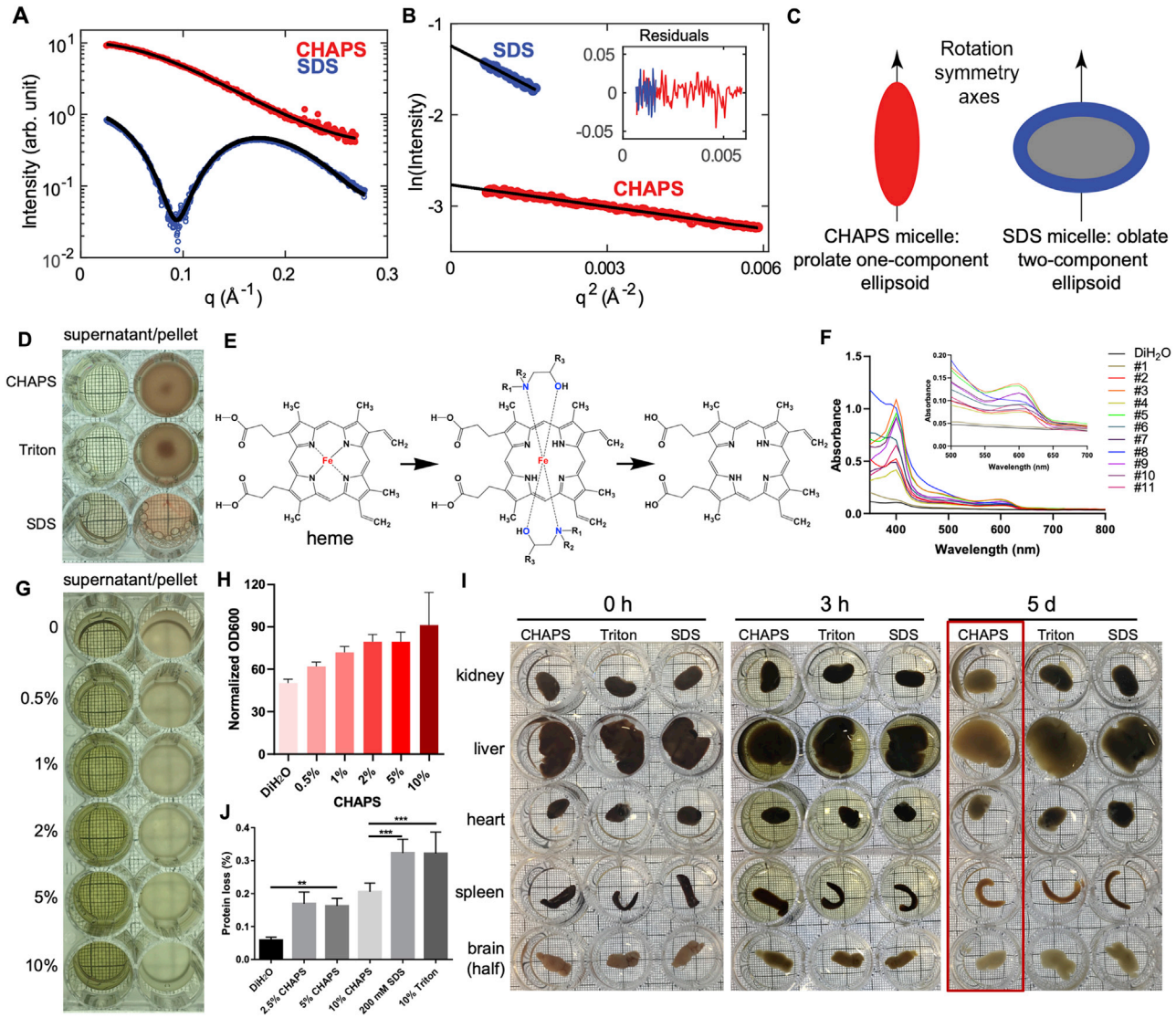

Figure S1. CHAPS Micelle Characterization for Blood Decolorization, Related to Figure 1

(A) Small-angle X-ray scattering profiles of CHAPS (red) and SDS (blue) micelles in PBS buffer. Fits of ellipsoid to the data are shown in black models (see Methods for details).

(B) Guinier analysis of the scattering profiles from panel (A). The black lines indicate linear fits to $ln(I)$ versus q^2; the steeper slope for SDS corresponds to a larger radius of gyration R_g. The fitting ranges were chosen such that the largest q-values included in the fit, q_{max}, satify the condition $q_{max} \cdot R_g < 1.2$. The inset shows the residual of the fit, confirming good linearity of the data in the Guinier region.

(C) Schematics of the geometrical models fit the CHAPS and SDS scattering data, shown to relative scale.

(D) Detergents including CHAPS, Triton X-100 and SDS cannot decolorize PFA-fixed blood, showing colorless supernatant and red pellet solution.

(E) Schematic of hypothesized mechanism how chemicals interact with the iron of heme for an efficient decolorization.

(F) Absorbance at visible spectra of the supernatant from 11 screened chemicals. Inset in F: the magnification of the Q-band (500-700 nm) region showing the new peak of 600 nm can be used as quantitative index for the decolorization efficiency.

(G) Optimization of CHAPS concentration combined with 25% w/v N-Methyldiethanolamine (chemical 7) for blood decolorization.

(H) Normalized OD600 quantifications of different CHAPS concentration (n = 3) in G.

(I) After incubation with mixtures of 25% w/v N-Methyldiethanolamine and detergent of 10% w/v CHAPS or 10% w/v Triton X-100 or 200 mM SDS, CHAPS mixture shows superior permeabilization to remove the heme from blood-retaining mouse organs (red rectangle).

(J) Protein loss assay indicating the superior retention of endogenous proteins after CHAPS treatment compared to other detergents (*P value*s were calculated using one-way ANOVA test; error bars show standard deviations).

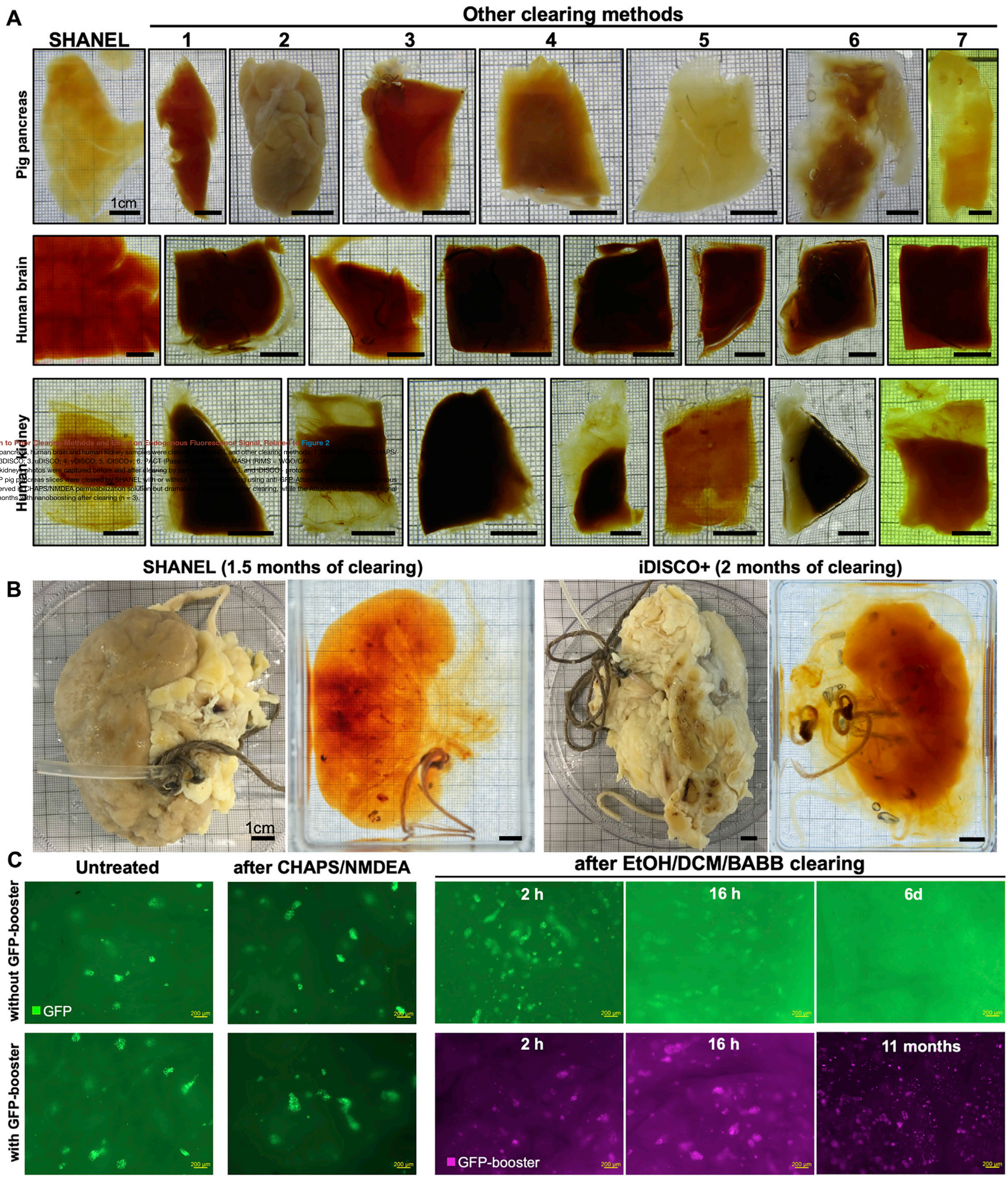

Figure S2. Comparison to Prior Clearing Methods and Effect on Endogenous Fluorescence Signal, Related to Figure 2

(A) Centimeters-sized pig pancreas, human brain and human kidney samples were cleared by SHANEL and other clearing methods: 1. SHANEL without CHAPS/NMDEA pretreatment; 2. 3DISCO; 3. uDISCO; 4. vDISCO; 5. iDISCO+; 6. PACT (Passive CLARITY); 7. MASH (RIMS = WGO/CA).

(B) A pair of adult human kidneys photos were captured before and after clearing by perfusion of SHANEL and iDISCO+ protocols.

(C) 0.5 cm thick *INS*-EGFP pig pancreas slices were cleared by SHANEL with or without GFP nanoboosting using anti-GFP-Atto647n nanobody. Endogenous GFP signal was well preserved in CHAPS/NMDEA permeabilization solution but dramatically decreased after clearing, while the Atto647n fluorescence signal was preserved up to 11 months with nanoboosting after clearing (n = 3).

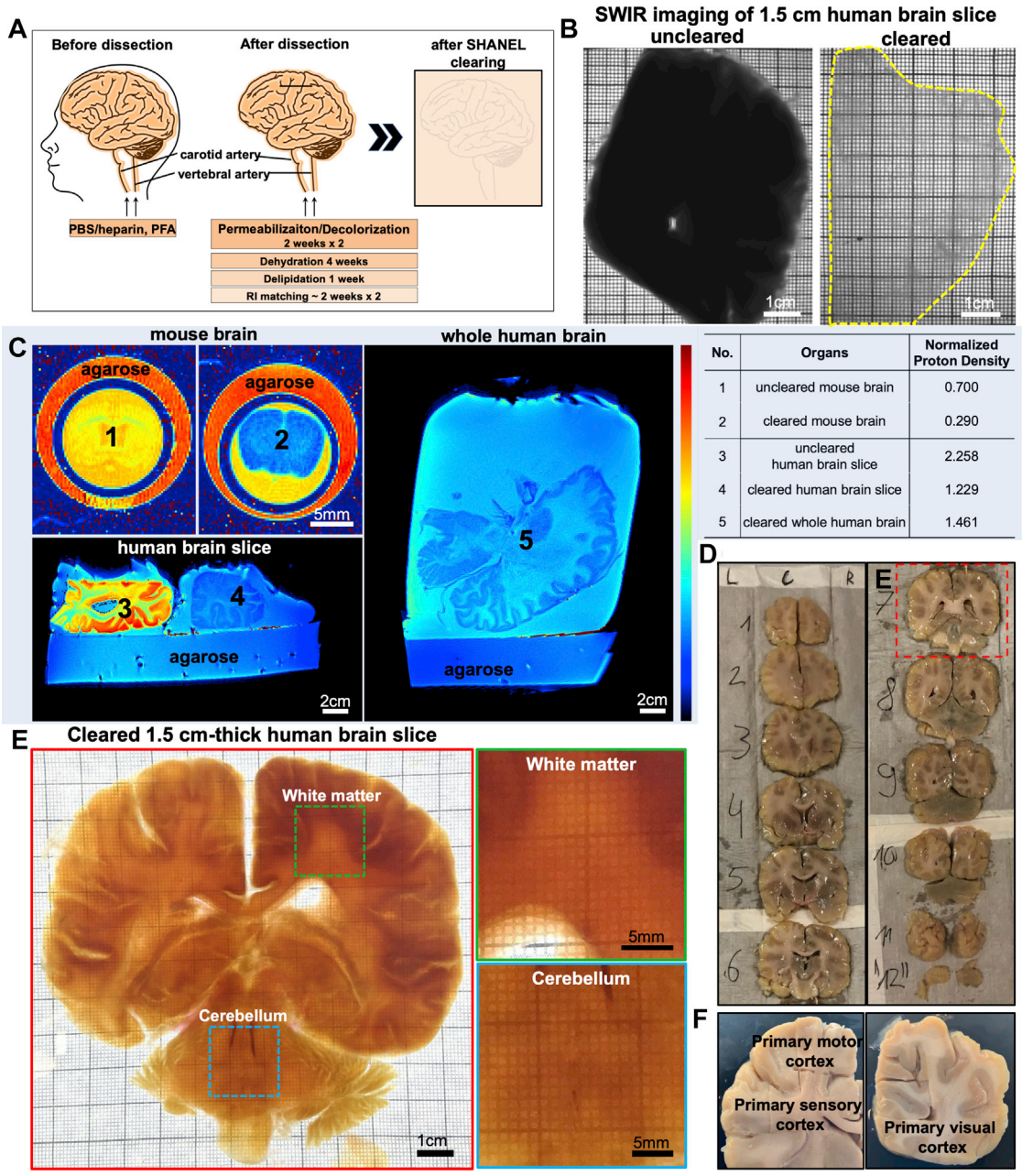

Figure S3. SHANEL Clearing of Intact Adult Human Brain and Human Brain Slices, Related to Figures 3 and 4

(A) Active perfusion pipeline is used to accelerate whole human brain SHANEL clearing.

(B) Short-wave infrared (SWIR) imaging at 1450 nm of uncleared (left) and cleared (right) 1.5 cm thick human brain slice. The underneath printed grids are visible through the cleared sample.

(C) Color-coded maps of proton density by MRI demonstrated homogeneous replacement of tissue water in the human brain slice and whole human brain similar to in the mouse brain. The difference in normalized proton density (1.5% agarose as reference) between uncleared and cleared samples was comparable for mouse and human samples (see table). Please note that color code and values are not directly comparable between the mouse and human samples because of different measurement setups (e.g., scanner hardware and sequences).

(D) 12 slices with 1.5 cm thickness from an intact adult human brain after CHAPS/NMDEA treatment.

(E) Photo of the slice (#7) after SHANEL clearing showing the full transparency. The colored rectangles from heavily myelinated white matter and cerebellum are shown in higher magnification on the right hand side.

(F) Some cortex areas were cut for further staining as listed in Figure 7G.

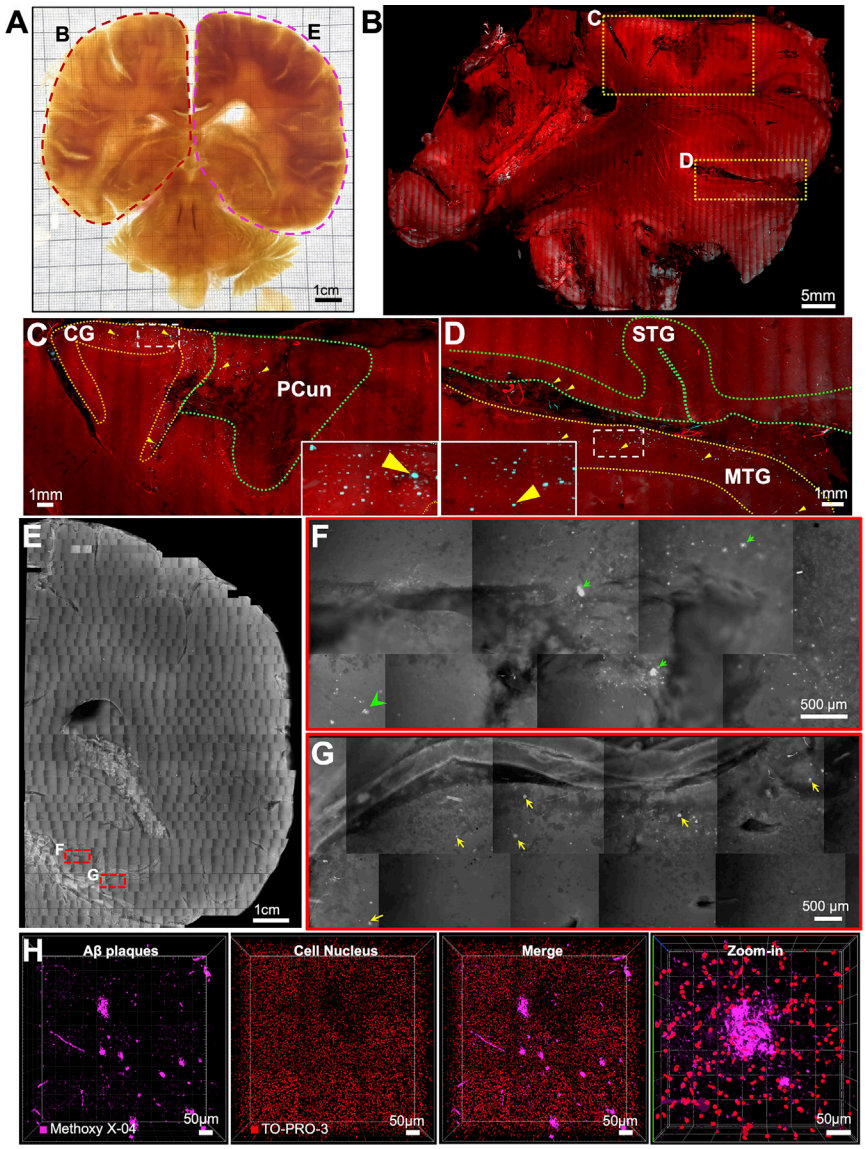

Figure S4. Imaging Centimeters-Sized Human Brain Slice with an Upright Confocal and with an Epifluorescence Microscope, Related to Figures 3 and 4

(A) We imaged large parts of the example slice (#7) using an upright confocal microscope (left side, red dashed region) and with an epifluorescence microscope (right side, purple dashed region).

(B-D) 3D reconstruction of upright confocal images of the left side of the brain slice in (A) showing the TO-PRO-3 labeled cell nuclei (red) and Methoxy-X04 labeled Abeta plaques (cyan). Zoom-in images indicating plaque accumulation regions (arrowheads in C and D) including cingulate gyrus (CG), precuneus (PCun), superior temporal gyrus (STG) and middle temporal gyrus (MTG).

(E-G) Stitched epifluorescent data of the right side of the brain slice in (A) showing Aβ plaques accumulating in the parahippocampal gyrus (PHG, green arrows) and fusiform gyrus (FuG, yellow arrows).

(H) Tiled 3D images from an inverted confocal microscope showing Aβ plaques (magenta) and surrounding cell nuclei (red) from the cortex.

See also Video S2.

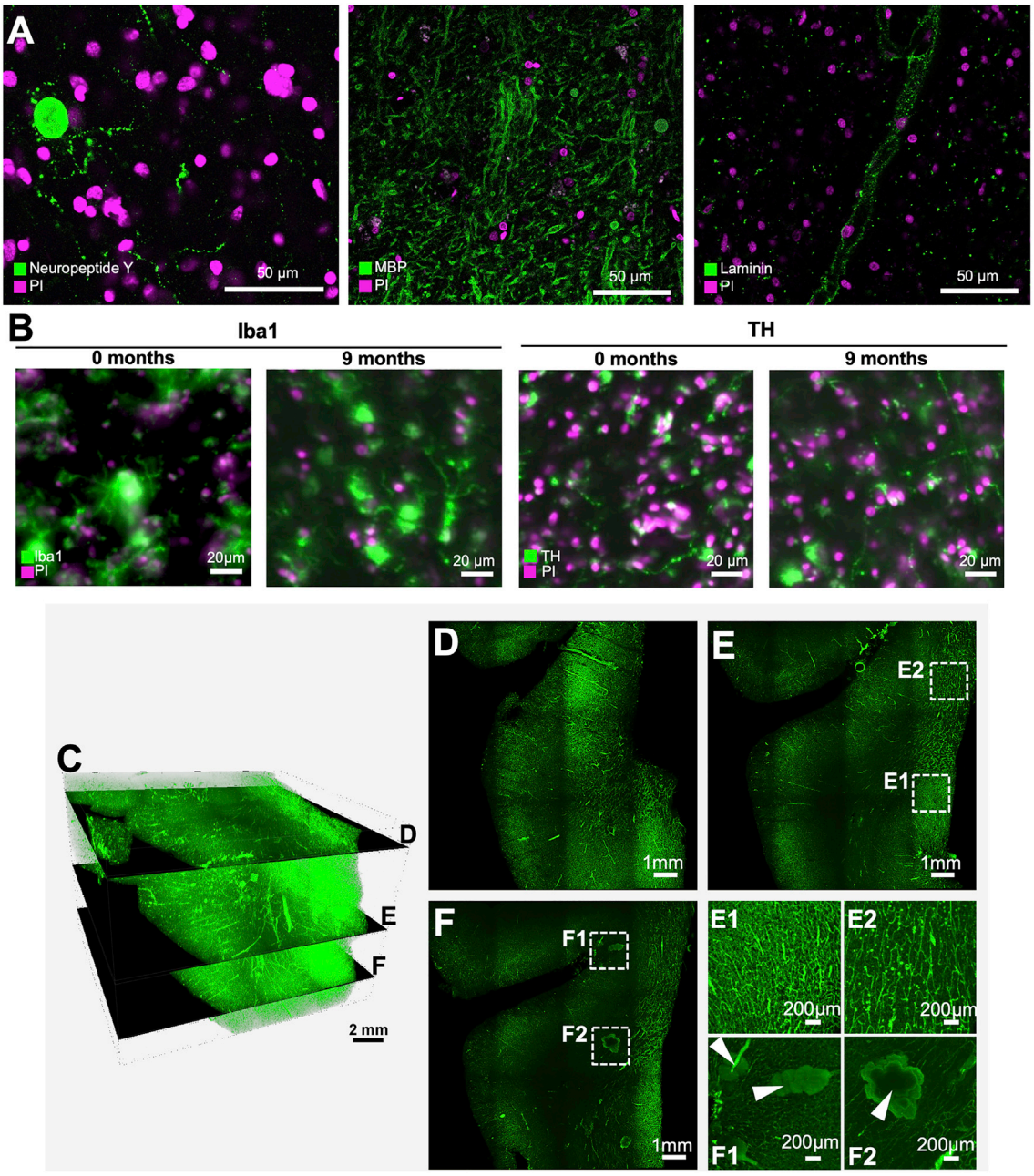

Figure S5. SHANEL Histology of Different Cellular Structures, Related to Figure 4

(A) Human brain slices immunostained with anti-Neuropeptide Y, anti-MBP (myelin basic protein), anti-laminin antibodies and with PI to visualize different cellular structures after SHANEL histology.

(B) Light-sheet images of an antibody-labeled 1.5 cm thick human brain slice showing good preservation of fluorescence signals after 9 months of SHANEL clearing.

(C-F) Lectin labeling of a post-mortem human brain tissue with a size of 3.0 × 1.9 × 1.5 cm. The lectin labeling throughout the entire depth of the centimeters-sized human brain tissue is evident. For example, alteration of regional density of vasculature (compare E1 to E2) and tissue abnormalities (potentially aneurysms) are evident e.g., swollen structures pointed by arrowheads in F1 and F2.

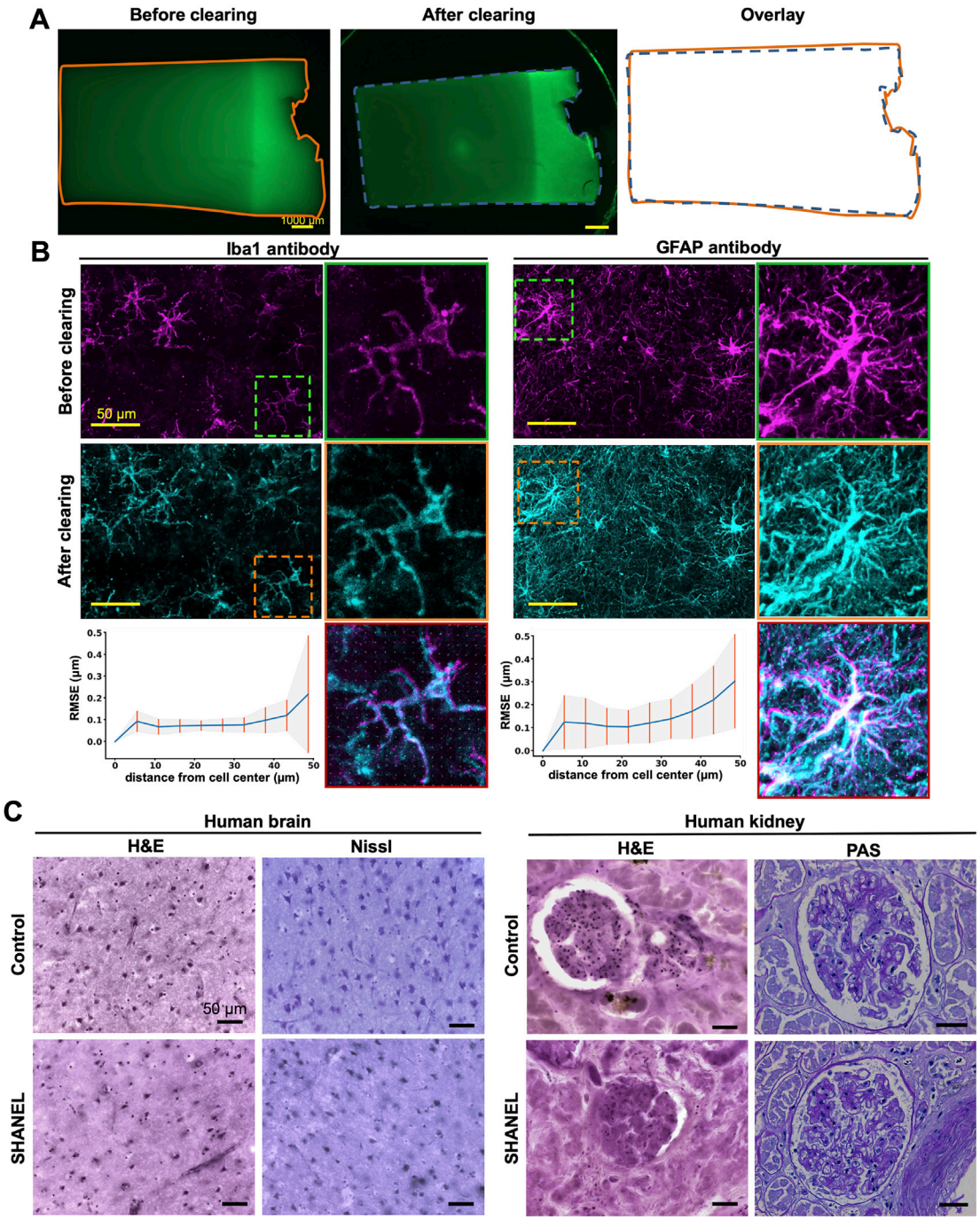

Figure S6. SHANEL Histology Preserves the Morphology of the Tissue and Cellular Structures, Related to Figure 4

(A–B) Macroscopic (A) and microscopic (B) assessments of tissue integrity after SHANEL clearing of 1 mm thick human brain slices immunolabeled for Iba1 and GFAP, then imaged with a stereo-fluorescence microscope (A) and a confocal microscope (B). The preservation of tissue proportions (A) and cellular shape (B) (as calculated by RMSE) after SHANEL treatment (slice n = 3). Please note that there are more cells visible after clearing as expected with the enhanced imaging depth.

(C) Hematoxylin & eosin (H&E), Nissl and Periodic Acid Schiff (PAS) stainings of human brain and kidney without (control) and with SHANEL treatment. Preserved structures after SHANEL histology (similar to controls) are evident.

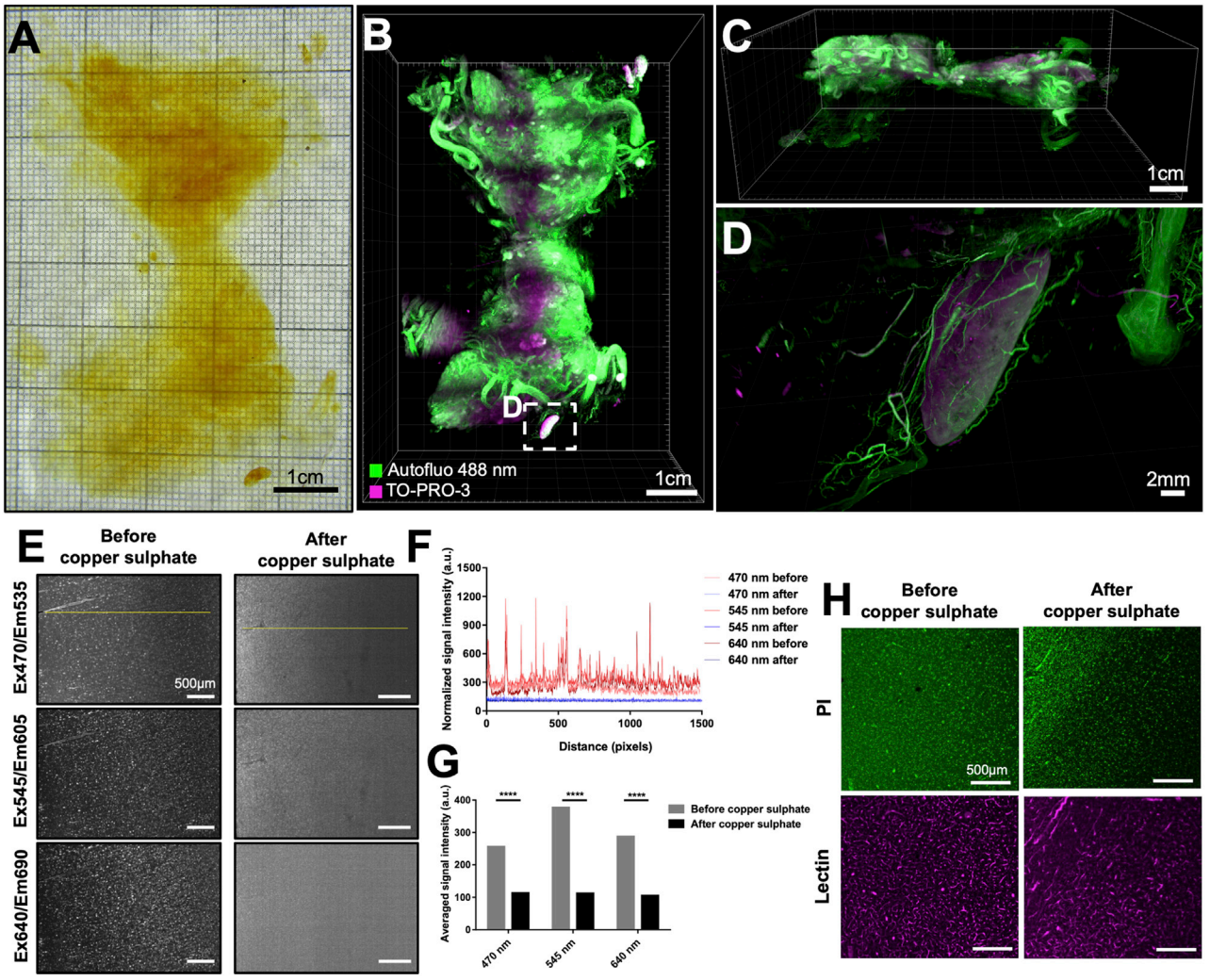

Figure S7. SHANEL on Whole Human Thyroid and Autofluorescence Reduction of SHANEL Samples by Copper Sulfate Treatment, Related to Figure 6

(A) SHANEL cleared intact human thyroid (original size of 7 × 5 x 3 cm) showing full transparency.

(B, C) 3D reconstruction of the thyroid imaged with the new light-sheet system.

(D) Zoomed-in view of lymph node with surrounding vessels.

(E) Autofluorescence of SHANEL cleared human brain sample imaged by light-sheet microscopy before and after copper sulfate ($CuSO_4$) treatment.

(F) Plots of autofluorescence signal intensity profiles along the yellow lines in E.

(G) Averaged autofluorescence signal intensity before and after copper sulfate treatment. P values were calculated using unpaired *t* test; error bars show standard deviations.

(H) Fluorescent dye signals (PI labeled cell nuclei, lectin labeled vessels) are preserved after copper sulfate treatment.

Cell, Volume *180*

Supplemental Information

Cellular and Molecular Probing of Intact Human Organs

Shan Zhao, Mihail Ivilinov Todorov, Ruiyao Cai, Rami AI -Maskari, Hanno Steinke, Elisabeth Kemter, Hongcheng Mai, Zhouyi Rong, Martin Warmer, Karen Stanic, Oliver Schoppe, Johannes Christian Paetzold, Benno Gesierich, Milagros N. Wong, Tobias B. Huber, Marco Duering, Oliver Thomas Bruns, Bjoern Menze, Jan Lipfert, Victor G. Puelles, Eckhard Wolf, Ingo Bechmann, and Ali Ertürk

Table S1. Physical/chemical/geometrical properties of detergent micelles related to Figure 1 and Small-angle X-ray scattering measurements

Detergent	CHAPS	SDS	Triton X-100
CMC[a] (mM)	8 [Corrin et al., 1947]	1-8 [Corrin et al., 1947; le et al., 2000]	0.3 [Mandal et al., 1988]
Aggregation number	10 [Corrin et al., 1947] 11-12 [from I(0)][b] 15-17 [from model][b]	80-90 [from I(0)][b] 90-100 [from model][b]	80 [Stubicar et al., 1989] 142 [Stubicar et al., 1981] 75-165[c]
Monomer mass (Da)	615	288	628 [Stubicar et al., 1981]
Micelle molecular mass[d] (kDa)	≈ 7	≈ 26	≈ 63
Radius of gyration (Å)	16.0 ± 1.0 [Lipfert et al., 2007] 15.5 ± 1.0	29.7 ± 1.0	≈ 33 [Stubicar et al., 1989] 29.5 ± 0.2 [Paradies et al., 1980]
Monomer volume[e] V_{mon} (Å^3)	830.3	414.2	
Electron density[f] ρ_{det} (e/Å^3)	0.405	0.377	
Micelle shape	Prolate ellipsoid; Long axis: 30-32 Å Short axis: 10-11 Å	Oblate two-component ellipsoid; Long axis core: 23-25 Å Short axis core: 15-16 Å Outer shell: 2-4 Å	

[a]Critical micelle concentration. The CMC for ionic detergents such as SDS depends on ionic strength of the solution (Corrin et al., 1947). For 150 mM monovalent salt, corresponding to the ionic strength of PBS buffer and the approximate physiological ionic strength the CMC for SDS is 1.5 mM. [b]Aggregation numbers determined from SAXS analysis. Two independent estimates were obtained by i) analyzing the forward scattering intensity I(0) and ii) fitting the shape of the scattering patterns with a geometrical model (see Methods). [c]Anatrace catalogue (2014). [d]Computed from the monomer mass and the estimated aggregation number. [e]Monomer volumes were computed were calculated from the monomer mass and the published specific densities (le et al., 2000). [f]Electron densities were computed from the atomic composition and the monomer volume.

Table S2. Costs and scalability of chemicals for labeling and clearing of human organs related to Figure 1 and 3

No.	CAS No.	Name	Structure	Catalog No.	Package kg or L	€ kg or L	Color
1	7529-22-8	4-Methylmorpholine N-oxide		224286	0.1	1670	-
2	622-40-2	4-(2-Hydroxyethyl)morpholine		H28203	0.25	133	+
3	3040-44-6	1-(2-Hydroxyethyl)piperidine		116068	0.5	630	+
4	102-71-6	Triethanolamine	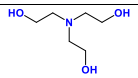	90279	2.5	72	-
5	96-80-0	2-(Diisopropylamino)ethanol	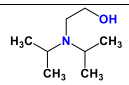	471488	0.5	125	+
6	5966-51-8	1,3-Bis(dimethylamino)-2-propanol	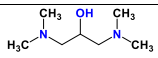	B42985	0.01	16300	+
7[a]	105-59-9	N-Methyldiethanolamine	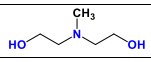	471828	18	30	-
8	139-87-7	N-Ethyldiethanolamine	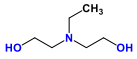	112062	0.005	4740	+
9	102-79-4	N-Butyldiethanolamine	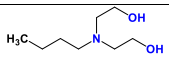	471240	2	46	-
10	2160-93-2	N-tert-Butyldiethanolamine	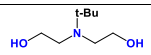	455709	0.25	290	+
11	102-60-3	Quadrol	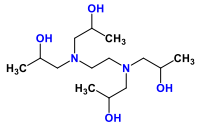	122262	1	71	-

-: colorless; +: color. [a]red highlights the chemical used in SHANEL

Chemicals for clearing human brain	Cost €, Kg^{-1} or L^{-1}	Amount, g or L	€
CHAPS	149	1000	1490
N-Methyldiethanolamine	30	10	300
EtOH	38	16	608
DCM	25	5	125
BABB	20	10	200
TO-PRO-3	483	1 vial	483
Total	∑ 3206 €		

Organs / Antibody	adult whole human brain	1.5cm-thick human brain slice	adult whole human kidney	adult whole human thyroid
delivery method	circulation	passive	circulation	passive
antibody working concentration (μg/ml)	0.2-2	0.2-2	0.2-2	0.2-2
volume of working solution (L)	2	0.4	0.5	0.1
total antibody (μg)	400-4000	80-800	100-1000	20-200

As an example, to label the whole human brain with rabbit antibody anti-Iba1 (catlog # Wako 019-19741, dilation 1:000, $315/50μg/vial), the total price would be: 2L x 0.5 μg/ml / 50 μg x $315 = $6300 (20 vials)

Table S3 Timeline of organs labeling & clearing, and imaging specifications related to Figure 2, 3, 4, 5, 6 and 7

Organs / Clearing	adult pig brain	*INS*-EGFP pig pancreas	adult whole human brain	1.5cm-thick human brain slice
Permeabilization/ Decolorization (CHAPS/NMDEA)	5 days x 2	2 days x 4	14 days x 2	14 days x 2
small molecular dye Labeling	-	Anti-GFP nanobooster 14 days	TO-PRO-3 28 days	TO-PRO-3: 7 days Methoxy X-04: 7 days
Dehydration (50%,70%,100%,100% EtOH/diH_2O)	4 days x 4	6 h x 4	7 days x 4	1 day x 4
Delipidation (DCM)	4 days	1 day	7 days	1 day
RI matching (BABB)	7-10 days	7-10 days	14 days x 2	5-7 days
Total time	37-40 days	31-34 days	119 days	52-54 days

Organs / SHANEL histology	1.5cm-thick human brain slice	adult whole human kidney	adult whole human thyroid
Permeabilization/Decolorization (CHAPS/NMDEA)	14 days x 2 (whole brain)	7 days	2.5 days x 2
Dehydration (50%,70%,100%,100% EtOH/diH_2O)	1 day x 4 (whole slice)	4 days x 4	0.5 days x 4
Delipidation (DCM/MeOH=2:1)	1 day (whole slice)	4 days	2 days
Rehydration (100%,70%,50%,0% EtOH/diH_2O)	1 day x 4 (whole slice)	4 days x 4	0.5 days x 4
Loosing ECM (acetic acid & guanidine HCl)	1 day x 2 (whole slice)	4 days x 2	1 day x 2
Antibody Labeling	14-15 days (interested cortex)	TO-PRO-3 14 days	TO-PRO-3 10 days
Dehydration (50%,70%,100%,100% EtOH/diH_2O)	4h x 4	2 days x 4	0.5 days x 4
Delipidation (DCM)	4h	3 days	5h
RI matching(BABB)	1-2 days	7-10 days	3-5 days
Total time	46-47 days	73-76 days	29-31 days

HAPS/NMEDA: 10% w/v 3-[(3-cholamidopropyl)dimethylammonio]-1-propanesulfonate and 25% w/v N-methyldiethanolamine in diH_2O. BABB: benzyl alcohol + benzyl benzoate (1:2) in volume. DCM: dichloromethane.

FIGURES		SYSTEM					PARAMETERS			IMAGE SIZE	DATA SIZE
			Magnification	NA	RI	WD	Image pixel size	z-step	type		
Figures											
2	G-I	protype UM	1.1x corr.	0.1	1.56	17 mm	6.5 x 6.5 µm	8 µm	3D reconstruction	3.6 x 5.5 x 1.7 cm	486 GB
3	E	protype UM	1.1x corr.	0.1	1.56	17 mm	6.5 x 6.5 µm	6 µm	3D reconstruction	2.8 x 2.8 x 2.2 cm	309 GB
4	C-F	UM II	4x corr.	0.28	1.56	10 mm	1.625 x 1.625 µm	5 µm	3D reconstruction	1.36 x 1.26 x 1.26 cm	886 GB
	K-N	UM II	4x corr.	0.28	1.56	10 mm	1.625 x 1.625 µm	3 µm	3D reconstruction	1.24 x 1.1 x 0.9 cm	899 GB
5	D-E	UM II	4x corr.	0.28	1.56	10 mm	1.625 x 1.625 µm	3 µm	3D reconstruction	1.2 x 1.2 x 0.45 cm	368 GB
	F	LSM880	Zeiss 20x	0.8	1.56	0.55 mm	0.69 x 0.69 µm	1 µm	3D reconstruction	0.7 x 0.7 x 0.2 mm	403 GB
6	F-G	protype UM	1x air	0.25	1.56	65 mm	10.3 x 10.3 µm	8 µm	3D reconstruction	7.5 x 3.3 x 3.7 cm	1.87 TB
Sup. Figures											
S4	H	LSM880	Zeiss 40x	1.3	1.56	0.22 mm	0.21 x 0.21 µm	1 µm	3D reconstruction	0.6 x 0.6 x 0.2 mm	3.83GB
S5	C-F	UM II	4x corr.	0.28	1.56	10 mm	1.625 x 1.625 µm	3 µm	3D reconstruction	1.22 x 1.1 x 0.87 cm	486 GB
S7	A-C	protype UM	1.1x corr.	0.1	1.56	17 mm	6.5 x 6.5 µm	8 µm	3D reconstruction	7 x 4.7 x 2.7 cm	1.18 TB

Legend of abbreviations

Imaging Systems

UM II	LaVision BioTec - UltraMicroscope II
prototype UM	LaVision BioTec - prototype UltraMicroscope
LSM880	Zeiss confocal LSM880 with Airyscan
NA	Numberical aperture
RI	Refractive Index
WD	Working distance

Objectives

1x	Olympus MV PLAPO
LVBT 1.1x	1.1x NA 0.1 MI PLAN
4x corr.	Olympus XLFLUOR4x corrected
Ziess 20x	Zeiss Clr Plan-Apochromat 20x/0.8 M27
Ziess 40x	Zeiss ECPlan-NeoFluar 40x/1.30 Oil DIC M27

6. Discussion

6.1 Pipeline for statistically analyzing large-scale human organs

Optical tissue clearing and volumetric imaging methods facilitate 3D holistic cellular and molecular examination of complex intact organs. However, conventional organic solvent-based optical tissue clearing is incompatible with living tissue. The majority of samples are available post-mortem fixed in formalin for many days or years. From a methodological point of view, decades-aged brain tissue accumulates neuropigments, lipofuscin and collagen, which increase stiffness and light scattering of the brain tissue limiting the penetration of clearing and labeling reagents and consecutively hinders histological examination. The large amount of white matter is another major challenge to render human brain samples transparent with recent tissue clearing techniques[108]. Next, the sheer size of the adult human brain makes it exceptionally slowly penetrable to traditional immunohistochemistry stainings. Therefore only small blocks were demonstrated in the literature[109–113]. The high-resolution imaging give rise to Teravoxel-sized datasets, that reach beyond the justified efforts for manual or even traditional image filtering based data processing techniques. Towards this goal, we established the SHANEL pipeline, which provides an end-to-end solution from the tissue clearing step up to the artificial intelligence mediated statistical quantification of intact human organs and other large mammalian tissues.

The basis of SHANEL is the novel application of the CHAPS (3-[(3-Cholamidopropyl)dimethylammonio]-1-propanesulfonate) detergent for tissue permeabilization, which has the advantages over previously described attempts with Triton X-100 or SDS. The zwitterionic, rigid steroidal amphiphilic structure of CHAPS and the substantially small micelle size efficiently makes the intracellular and extracellular space of the mammalian tissue passable for the subsequent chemicals as optical clearing reagents and staining molecules. Moreover, it is compatible with passive incubation and with active, pressure-driven delivery such as the peristaltic pump-aided perfusion of the adult human kidney and brain. Therefore it can be applied on a wide scale of very large mammalian tissues, like the adult pig brain and pancreas, without elaborate laboratory equipment. We found that the micelles of CHAPS are better in preserving non-lipidic biomolecules and can be completely washed out, which is in direct contrast to the traditional SDS and Triton X-100.

As a result, we achieved diffusion of immunohistochemistry labels, such as IgG (ca. 150 kDa) and lectin (ca. 71 kDa, from Lycopersicon esculentum), into centimeters-deep adult human organs, which are traditionally considered as significantly difficult due to their relatively large size. The pipeline proved practical for application to a diverse series of intact very large mammal organs, among which: adult pig brain and pancreas, adult human kidney, and thyroid[85]. Because the skull of adults is too thick for imaging through, we removed it while leaving the dura mater and the eyes intact with the intention to preserve the anterior cerebral circulatory network uninterrupted. Using the vasculature as a natural liquid transport system, we successfully cleared the intact brain of an adult human for the very first time, allowing visible and infrared light to travel through its whole thickness. Although the use of organic solvents, introduces moderate isotropic shrinkage of the tissue, cellular imaging of the transparent adult human brain *in toto* is beyond the capabilities of modern microscopes. In fact, it proved critical for the imaging of an entire human kidney and porcine pancreas. Nevertheless, we achieved unprecedented microscopic imaging of large intact blocks of adult human brain tissue, e.g. thick coronal slices of up to $7.5 \times 5 \times 1.5$ (56.25 cm^3 in total) centimeters by using state-of-the-art high-throughput prototypes of fluorescent light sheet and upright confocal microscopes.

Finally, we faced continuous volumetric imagery of many terabytes. We showed that scale-invariant human-level precise deep learning data analysis effectively rules out traditional hand-engineered algorithms and manual segmentation. These CNN algorithms run even on common research workstations, they are expandable to analyze various anatomical structures, like vessels, cells soma, and processes, and we openly provide their source code and documentation to the scientific community on our repository.

6.2 Complementary stains for brain-wide reconstruction of blood vessels

The mammalian cerebrovascular network constitutes a strategically located exchange surface and a continuous barrier at the interface between blood and brain parenchyma. Indeed, this stringent continuity makes staining and reconstruction of blood vessels a serious challenge. Moreover, deep tissue fluorescent imaging mainly requires a high signal to background and minimal emission signal disturbances. In this regard synthetic, exogenous vascular dyes

provide a higher fluorescent signal, more bleaching resistance, narrow excitation and emission spectra and broader applicability (in wild type animals) over genetically expressed reporter proteins. Traditional fluorescent histology approaches rely on identifying a single universal marker of the brain vasculature, such as CD31, CD34 and the von Willebrand factor that are targeted with immunolabels, the spectrum of lectins binding the carbohydrate parts of the luminal glycocalyx, or the crosslinkable lipophilic carbocyanine DiI dye derivative that embeds into the cell membranes. Alternative attempts were made to label the microenvironment of blood vessels, e.g. Collagen type IV in the basal membrane or Aquaporin-4. However, all these markers fulfill distinct zone and time-dependent biological roles[84,114,115]. Therefore their functional abundance is strictly limited to specific subtypes of vascular beds and is not optimally suited for comprehensively capturing the brain vasculature in its entirety. Anti-CD31 immunolabeling is one of the gold standards for marking vascular endothelium[90]. However, it is targeting the intercellular junctions but not the majority of the luminal surface resulting in a dimmer signal. Simultaneously large-diameter vessels expose a large luminal endothelial surface, which disperses the probes resulting in fluorescent signal below the maximum correctable by extensive computational algorithms. The work of Kirst and colleagues[75] shows that differential immunostaining can be combined for labeling specific subsets of the murine cerebral vasculature hemispheres. In contrast the VesSAP approach provides simpler single-pass vessel segmentation. Towards this, we developed a dual dye circulation method in combination with a minimal fixation-perfusion protocol to keep as much blood with dyes in the vasculature as possible. The blood is used to hold the dyes which -presumably- get tangled between the crosslinked protein net and effectively marks all vessels which are perfused at the time of the experiment. In this case string vessels or complete vasospasms are not visible.

Uniform staining of thick samples may require repeated protocol and probe optimization. Thus the costs for the specific labels to stain a whole organ may considerably limit the widespread usage in research laboratories. Evans blue (EB, also known as T-1824 and Direct Blue 53) is an organic bis-azo dye with a very high affinity to blood serum albumin that has over a century-long history as a natural dye and diagnostic agent since 1914. Besides using the dye for viability assays, more importantly, it gained popularity for the ability to highlight the degraded integrity of the BBB by labeling albumin extravasation. Biomedical research found that intravenously or intraperitoneally administered albumin-bound EB remains stable in the blood circulation, distributes throughout the entire body and has a far-red fluorescent

emission spectrum centered at 680 nm. These biophysical properties make EB particularly suited for fluorescent imaging in deep tissue. Interestingly, despite being cost-effective, EB is rarely seen in slice-based histological studies, presumably because it is washed out either at the fixative perfusion step or at the subsequent rinsing steps.

In the VesSAP study we were motivated to establish the usability of EB in organic solvent optical tissue clearing in combination with the wheat germ agglutinin conjugated to the Alexa Fluor 594 dye for cost-effective and consistent labeling strategy, and an end-to-end framework for quantitative atlasing of the brain vasculature in whole adult mouse brains. In doing so, we proved that EB and WGA provide partially overlapping but complementary highlighting of the brain blood vessel walls down to the capillary level, with preference to large and mid-sized vessels and microvessels. More importantly, the two neighboring fluorescent emission bands (centered at 594 and 680 nm) allow independent signal fine-tuning that aids high contrast acquisition of typically dim microvessels and extremely bright large vessels. From a physiological point of view we showed that EB could be used as long term vascular dye up to twelve hours, potentially allowing prolonged BBB integrity-related experiments, in contrast to concurrent intravenous labels. Furthermore, we showed that mild fixative perfusion, which likely leaves blood residues in the blood vessels, is not detrimental for the acquisition and downstream analysis of the angioarchitecture in its entirety. In doing so we were able to reconstruct the brain-wide structural description of the brain vascular geometry establishing correspondences of vessel length, number of bifurcations and average caliber at the single capillary level in three widely used major mouse strains, C57BL/6J, CD1 and BALB/c.

Additionally, we reported the vascular features in three ways to enable comparison with various previous studies that differ in the measures used. First, we provided the count of segmented voxels per the total voxels within a specific brain atlas region (voxel space). Second, we listed our data for the voxel size of our imaging system and the 3D geometry (microscopic space). Third, we corrected the microscopic measurements to account for tissue shrinkage caused by the optical tissue clearing (anatomical space)[116,117]. We determined tissue shrinkage rate by measuring the same mouse brain volume with MRI before clearing. In the following we use the anatomical space to report our specific biological findings, as it is closest to the physiological state. With the registration to the Allen mouse brain atlas, we could compare our results to the literature, which mostly reports either quantifications for

specific brain regions or extrapolations to the whole brain from regional quantifications. For example, Lugo-Hernandez et al. reported that the vascular length of some cortical regions of interest to be 922 ± 176 mm per mm³ (mean ± s.d.)[118]. We found a similar vessel length for the same region (C57BL/6J mice: 913 ± 110 mm per mm³). Di Giovanna et al. measured the vascular length to be between 460 and 470 mm per mm³, which is very close to our results (480 ± 20 mm per mm³) for the same region of interest[74]. These similarities show that our method is reliably processing and quantifying vessels of the mouse brain but also that the vascular density varies across the different regions. Kirst et al. showed that the density of bifurcation of the brain vasculature strongly correlated with the vessel length density in different brain regions[75], which is in accordance to our results. Notably, Tsai et al. reported an average vascular length 880 ± 170 mm per mm³ for sucrose-cleared slabs of mouse brain tissue[26], which is very similar to our results (870 ± 130 mm per mm³) but in the microscopic space. The latter example underlines the importance of the atlas-based brain-wide analysis instead of regions of interest and also to report any corrections used on the measurements.

6.3 Deep learning-based quantification of the brain vasculature

A fundamental common challenge originates in most 3D histological studies from the need to visualize and track the location of specific entities, such as neurons, glia, or vasculature. Combining this with quantifiable measurements is useful for obtaining automated analyses. Quantifying large-scale vessel and cell staining using automated segmentation reduces the workload, especially when combined with deep learning tools. Specifically, CNN image segmentation in combination with supervised transfer learning is dramatically accelerating digital 3D histology by leveraging rapid human-level accurate recognition models. The architecture of a CNN can vary depending on the types and number of layers included, which in turn depend on the particular application or data. However, we showed that CNNs with similar architecture could reliably perform diverse image quantification tasks, such as cell body from a single fluorescent channel and vasculature detection from complementary fluorescent stainings, as in the SHANEL and VesSAP methods without human intervention. In both cases, the key similarities of the CNNs are the five fully convolutional layer structure with four ReLU (rectified linear units) coupled to the one sigmoid activation layer in the end, which ensures structure delineation with high precision. This lightweight architecture results

in superior performance in terms of accuracy and speed in automatically segmenting Teravoxel sized volumetric data from transparent human and mouse brain tissue less than one day even on single conventional computer workstations, which can speed up approximating the variability of natural vascular patterns to better understand homogeneity of transport, spatial distribution of hemodynamic properties and biomass allocation to the vascular wall or blood during development, or during evolution of circulatory systems.

6.4 Open access release of the reconstructed datasets and software

To facilitate research in this area, we uploaded the trained VesSAP models to public web services where researchers can easily run the segmentation, and even the retraining, on their data samples without installing the complete runtime environments (links and details are in the SHANEL and VesSAP publications). Moreover, we openly host the source code, the trained models, and the training datasets for further collaborative development. Finally, the VesSAP data repository is, to our best knowledge, the only publicly accessible source, where researchers can access the reconstructed imaging volumes along with their segmentation and regional mapping for healthy whole-brain vascular models of three common mouse strains. These maps of the brain vasculature can contribute in understanding the limitations on the achievable point spread function of fMRI and the complex fMRI transients on top of the time-varying amount of excitatory and inhibitory neuronal information.

6.5 Current limitations and future considerations of biomedical research

This thesis showed that *ex vivo* organs, particularly the brain, can be perceived as large post mortem samples in a broader sense. Such tissues are the long-established gold standard in the histopathological diagnosis of diseases but are not suited for longitudinal monitoring because of the inherent invasiveness. However, histological samples - as in this case organ-scale biological systems - provide a substantial benefit for standardized, exhaustingly detailed atlasing of anatomical and molecular patterns without the general ethical and physiological limitations associated with in vivo experimentation, e.g. biochemical incompatibility with

clearing and or staining reagents, motion artifacts, behavioral variances. Particularly, optical clearing and labeling methods provide powerful tools for extensive spatial imaging of the large spectrum of histologically stained structural and biochemical features of tissues.

An inherent consequence of all current tissue clearing methods is the change of the tissue volume - either increasing with hyperhydration (benefiting expansion microscopy) or decreasing due to delipidation and dehydration and demineralization, etc. - and is therefore highly tissue composition-dependent, e.g. bones shrink less than brain tissue in 3DISCO clearing. Notably, the latter is encapsulated in the neurocranium. In our experience, the undissected brain shrinks non-linearly by most often detaching from the leptomeninges except the medulla and the olfactory bulbs, which skews the tissue and is undesirable. Altogether, we chose to extract the brain tissue and showed their volumetric shrinkage using MRI and light-sheet registration in the VesSAP study. However, we are well aware of the disrupted leptomeningeal and direct intracranial vascular connections that are missing due to this process. However, this points out a need for the future development of tissue clearing and acquisition techniques in order to preserve the native volume of the biological samples.

Soon an expansion of studies is expected to arise on diverse large mammal samples using optical tissue clearing, based on improved RI-mixing concepts[119]. Narrowly, the tissue preparation protocols, as in delipidation, decolorization, deliberate autofluorescence quenching of adult mammal brains remain to be optimized, while upgraded large-aperture, long working distance optics are developed. The datasets will quickly grow into the Petabytes range necessitating the development of even faster informatics. More importantly, we believe that these aspects will enable truly integrated molecular, ultrastructural and spatiotemporal connectivity maps for systems-level functional insights into the human brain during health and disease.

7. Conclusion

To understand the transport system of the brain vasculature requires integration of hemodynamic (blood flow), morphological (e.g., diameter, length, volume, etc.), and topological (e.g., connectivity patterns) information of the vasculature and any potential structure-function relations thereof. Taken together, this thesis presents the building blocks for the ultimate goal of mapping the morphological and topological organization of the vasculature throughout the human and mouse brain.

Over the past three years multiple independent approaches were demonstrated in order to reconstruct the whole brain vasculature of laboratory mice[73–75,77,120], which highlights the significant need of obtaining the maps of the blood vessels across the brain. Moreover, we showed that the very same mouse can be subjected to neuroimaging and subsequently analyzed with VesSAP to reveal its quantitative 3D angioarchitecture using artificial intelligence.

The VesSAP data repository is freely accessible to encourage scientists to use it for upstream experimentation, computational research and mathematical modeling for a wide array of different applications. It is also intended as an anatomical brain vascular framework, compatible with the Allen Mouse Common Coordinate Framework, to facilitate the translation of the large body of genetic, molecular, functional, neuroimaging and ultrastructural findings for an interdisciplinary brain research.

8. References

1. Iadecola, C. Neurovascular regulation in the normal brain and in Alzheimer's disease. *Nat. Rev. Neurosci.* **5**, 347–360 (2004).
2. LaBarbera, M. Principles of design of fluid transport systems in zoology. *Science* **249**, 992–1000 (1990).
3. Marín-Padilla, M. & Knopman, D. S. Developmental Aspects of the Intracerebral Microvasculature and Perivascular Spaces: Insights into Brain Response to Late-Life Diseases. *J. Neuropathol. Exp. Neurol.* **70**, 1060–1069 (2011).
4. Mastorakos, P. & McGavern, D. The anatomy and immunology of vasculature in the central nervous system. *Sci. Immunol.* **4**, (2019).
5. Lehman, R. M., Owens, G. K., Kassell, N. F. & Hongo, K. Mechanism of enlargement of major cerebral collateral arteries in rabbits. *Stroke* **22**, 499–504 (1991).
6. Völgyi, K. *et al.* Chronic Cerebral Hypoperfusion Induced Synaptic Proteome Changes in the rat Cerebral Cortex. *Mol. Neurobiol.* **55**, 4253–4266 (2018).
7. Majid, A. *et al.* Differences in Vulnerability to Permanent Focal Cerebral Ischemia Among 3 Common Mouse Strains. *Stroke* **31**, 2707–2714 (2000).
8. Zhang, H., Prabhakar, P., Sealock, R. & Faber, J. E. Wide Genetic Variation in the Native Pial Collateral Circulation is a Major Determinant of Variation in Severity of Stroke. *J. Cereb. Blood Flow Metab.* **30**, 923–934 (2010).
9. Schulte-Herbrüggen, O., Klehmet, J., Quarcoo, D., Meisel, C. & Meisel, A. Mouse Strains Differ in Their Susceptibility to Poststroke Infections. *Neuroimmunomodulation* **13**, 13–18 (2006).
10. Liu, J. *et al.* Vascular remodeling after ischemic stroke: Mechanisms and therapeutic potentials. *Prog. Neurobiol.* **115**, 138–156 (2014).
11. Vrselja, Z., Brkic, H., Mrdenovic, S., Radic, R. & Curic, G. Function of circle of Willis. *J. Cereb. Blood Flow Metab.* **34**, 578–584 (2014).
12. Grubb, S. *et al.* Precapillary sphincters maintain perfusion in the cerebral cortex. *Nat. Commun.* **11**, 395 (2020).
13. Ballabh, P., Braun, A. & Nedergaard, M. The blood-brain barrier: an overview: structure, regulation, and clinical implications. *Neurobiol. Dis.* **16**, 1–13 (2004).
14. Iadecola, C. The Neurovascular Unit Coming of Age: A Journey through Neurovascular Coupling in Health and Disease. *Neuron* **96**, 17–42 (2017).
15. Zhao, Z., Nelson, A. R., Betsholtz, C. & Zlokovic, B. V. Establishment and Dysfunction of the Blood-Brain Barrier. *Cell* **163**, 1064–1078 (2015).
16. Arima, Y. *et al.* Regulation of immune cell infiltration into the CNS by regional neural inputs explained by the gate theory. *Mediators Inflamm.* **2013**, 898165 (2013).
17. Kucharz, K. *et al.* Post-capillary venules is the locus for transcytosis of therapeutic nanoparticles to the brain. *bioRxiv* 2020.06.05.133819 (2020) doi:10.1101/2020.06.05.133819.

18. Kiliç, T. & Akakin, A. Anatomy of cerebral veins and sinuses. *Front. Neurol. Neurosci.* **23**, 4–15 (2008).

19. Hill, R. A. *et al.* Regional blood flow in the normal and ischemic brain is controlled by arteriolar smooth muscle cell contractility and not by capillary pericytes. *Neuron* **87**, 95–110 (2015).

20. Cavaglia, M. *et al.* Regional variation in brain capillary density and vascular response to ischemia. *Brain Res.* **910**, 81–93 (2001).

21. Nonaka, H. *et al.* The microvasculature of the cerebral white matter: arteries of the subcortical white matter. *J. Neuropathol. Exp. Neurol.* **62**, 154–161 (2003).

22. De Reuck, J. The human periventricular arterial blood supply and the anatomy of cerebral infarctions. *Eur. Neurol.* **5**, 321–334 (1971).

23. Adams, D. L., Piserchia, V., Economides, J. R. & Horton, J. C. Vascular supply of the cerebral cortex is specialized for cell layers but not columns. *Cereb. Cortex* **25**, 3673–3681 (2015).

24. Hirsch, S., Reichold, J., Schneider, M., Székely, G. & Weber, B. Topology and Hemodynamics of the Cortical Cerebrovascular System: *J. Cereb. Blood Flow Metab.* (2012) doi:10/f3zxx6.

25. Wang, D.-B., Blocher, N. C., Spence, M. E., Rovainen, C. M. & Woolsey, T. A. Development and Remodeling of Cerebral Blood Vessels and Their Flow in Postnatal Mice Observed with in vivo Videomicroscopy. *J. Cereb. Blood Flow Metab.* **12**, 935–946 (1992).

26. Tsai, P. S. *et al.* Correlations of Neuronal and Microvascular Densities in Murine Cortex Revealed by Direct Counting and Colocalization of Nuclei and Vessels. *J. Neurosci.* **29**, 14553–14570 (2009).

27. Schlageter, K. E., Molnar, P., Lapin, G. D. & Groothuis, D. R. Microvessel Organization and Structure in Experimental Brain Tumors: Microvessel Populations with Distinctive Structural and Functional Properties. *Microvasc. Res.* **58**, 312–328 (1999).

28. Uludağ, K. & Blinder, P. Linking brain vascular physiology to hemodynamic response in ultra-high field MRI. *NeuroImage* **168**, 279–295 (2018).

29. Schmid, F., Barrett, M. J. P., Jenny, P. & Weber, B. Vascular density and distribution in neocortex. *NeuroImage* **197**, 792–805 (2019).

30. Harel, N., Lin, J., Moeller, S., Ugurbil, K. & Yacoub, E. Combined imaging-histological study of cortical laminar specificity of fMRI signals. *NeuroImage* **29**, 879–887 (2006).

31. Zhao, F., Wang, P., Hendrich, K., Ugurbil, K. & Kim, S.-G. Cortical layer-dependent BOLD and CBV responses measured by spin-echo and gradient-echo fMRI: insights into hemodynamic regulation. *NeuroImage* **30**, 1149–1160 (2006).

32. Brown, W. R. A Review of String Vessels or Collapsed, Empty Basement Membrane Tubes. *J. Alzheimers Dis.* **21**, 725–739 (2010).

33. Cheng, C., Diamond, J. J. & Falkner, B. Functional Capillary Rarefaction in Mild Blood Pressure Elevation. *Clin. Transl. Sci.* **1**, 75–79 (2008).

34. Obenaus, A. *et al.* Traumatic brain injury results in acute rarefication of the vascular network. *Sci. Rep.* **7**, 239 (2017).

35. Sho, E. *et al.* Arterial enlargement, tortuosity, and intimal thickening in response to sequential exposure to high and low wall shear stress. *J. Vasc. Surg.* **39**, 601–612 (2004).

36. Humphrey, J. D., Eberth, J. F., Dye, W. W. & Gleason, R. L. Fundamental role of axial stress in compensatory adaptations by arteries. *J. Biomech.* **42**, 1–8 (2009).

37. Li, W. *et al.* Adaptive Cerebral Neovascularization in a Model of Type 2 Diabetes: Relevance to Focal Cerebral Ischemia. *Diabetes* **59**, 228–235 (2010).

38. Bennett, R. E. *et al.* Tau induces blood vessel abnormalities and angiogenesis-related gene expression in P301L transgenic mice and human Alzheimer's disease. *Proc. Natl. Acad. Sci.* **115**, E1289–E1298 (2018).

39. Djonov, V. G., Kurz, H. & Burri, P. H. Optimality in the developing vascular system: Branching remodeling by means of intussusception as an efficient adaptation mechanism. *Dev. Dyn.* **224**, 391–402 (2002).

40. Peng, J., Zhang, L., Drysdale, L. & Fong, G.-H. The transcription factor EPAS-1/hypoxia-inducible factor 2alpha plays an important role in vascular remodeling. *Proc. Natl. Acad. Sci.* **97**, 8386–8391 (2000).

41. Zhang, H., Rzechorzek, W., Aghajanian, A. & Faber, J. E. Hypoxia induces de novo formation of cerebral collaterals and lessens the severity of ischemic stroke. *J. Cereb. Blood Flow Metab.* 0271678X2092410 (2020) doi:10/ggzk9m.

42. Zhu, J., Merkle, C., Bernucci, M., Chong, S. & Srinivasan, V. Can OCT Angiography Be Made a Quantitative Blood Measurement Tool? *Appl. Sci.* **7**, 687 (2017).

43. Peters, R. Ageing and the brain. *Postgrad. Med. J.* **82**, 84–88 (2006).

44. Brown, W. R. & Thore, C. R. Review: Cerebral microvascular pathology in ageing and neurodegeneration: Cerebral microvascular pathology. *Neuropathol. Appl. Neurobiol.* **37**, 56–74 (2011).

45. Steppan, J. *et al.* Commonly used mouse strains have distinct vascular properties. *Hypertens. Res.* 1–7 (2020) doi:10/ggzk9p.

46. Engelhardt, E. & Grinberg, L. T. Alzheimer and vascular brain diseases: Focal and diffuse subforms. *Dement. Neuropsychol.* **9**, 306–310 (2015).

47. Zhang, H., Jin, B. & Faber, J. E. Mouse models of Alzheimer's disease cause rarefaction of pial collaterals and increased severity of ischemic stroke. *Angiogenesis* **22**, 263–279 (2019).

48. Razavi, M. S., Shirani, E. & Kassab, G. S. Scaling Laws of Flow Rate, Vessel Blood Volume, Lengths, and Transit Times With Number of Capillaries. *Front. Physiol.* **9**, 581 (2018).

49. Malpass, K. Retinal changes predict subsequent vascular events in ischemic stroke. *Nat. Rev. Neurol.* **7**, 538–538 (2011).

50. Nation, D. A. *et al.* Blood–brain barrier breakdown is an early biomarker of human cognitive dysfunction. *Nat. Med.* **25**, 270–276 (2019).

51. Abularrage, C. J. *et al.* Evaluation of the microcirculation in vascular disease. *J. Vasc. Surg.* **42**, 574–581 (2005).

52. Zhang, X. *et al.* High-resolution mapping of brain vasculature and its impairment in the hippocampus of Alzheimer's disease mice. *Natl. Sci. Rev.* **6**, 1223–1238 (2019).

53. Ali, Z. *et al.* Intussusceptive Vascular Remodeling Precedes Pathological Neovascularization. *Arterioscler. Thromb. Vasc. Biol.* **39**, 1402–1418 (2019).

54. Weller, R. O., Boche, D. & Nicoll, J. A. R. Microvasculature changes and cerebral amyloid angiopathy in Alzheimer's disease and their potential impact on therapy. *Acta Neuropathol. (Berl.)* **118**, 87 (2009).

55. Herculano-Houzel, S., Catania, K., Manger, P. R. & Kaas, J. H. Mammalian Brains Are Made of These: A Dataset of the Numbers and Densities of Neuronal and Nonneuronal Cells in the Brain of Glires, Primates, Scandentia, Eulipotyphlans, Afrotherians and Artiodactyls, and Their Relationship with Body Mass. *Brain. Behav. Evol.* **86**, 145–163 (2015).

56. Krafft, P. R. *et al.* Etiology of stroke and choice of models. *Int. J. Stroke* **7**, 398–406 (2012).

57. Shih, A. Y. *et al.* The smallest stroke: occlusion of one penetrating vessel leads to infarction and a cognitive deficit. *Nat. Neurosci.* **16**, 55–63 (2013).

58. Barone, F. C., Knudsen, D. J., Nelson, A. H., Feuerstein, G. Z. & Willette, R. N. Mouse Strain Differences in Susceptibility to Cerebral Ischemia are Related to Cerebral Vascular Anatomy. *J. Cereb. Blood Flow Metab.* **13**, 683–692 (1993).

59. Qian, B., Rudy, R. F., Cai, T. & Du, R. Cerebral Artery Diameter in Inbred Mice Varies as a Function of Strain. *Front. Neuroanat.* **12**, 10 (2018).

60. Hwa, C. & Aird, W. C. The history of the capillary wall: doctors, discoveries, and debates. *Am. J. Physiol.-Heart Circ. Physiol.* **293**, H2667–H2679 (2007).

61. Salamon, G. & Corbaz, J. M. *Atlas of arteries of the human brain*. (Sandoz, 1971).

62. Duvernoy, H. M., Delon, S. & Vannson, J. L. Cortical blood vessels of the human brain. *Brain Res. Bull.* **7**, 519–579 (1981).

63. Forkert, N. D. *et al.* A statistical cerebroarterial atlas derived from 700 MRA datasets. *Methods Inf. Med.* **52**, 467–474 (2013).

64. Viviani, R. A digital atlas of middle to large brain vessels and their relation to cortical and subcortical structures. *Front. Neuroanat.* **10**, 12 (2016).

65. Dunås, T. *et al.* A stereotactic probabilistic atlas for the major cerebral arteries. *Neuroinformatics* **15**, 101–110 (2017).

66. Nowinski, W. L. *et al.* Three-dimensional reference and stereotactic atlas of human cerebrovasculature from 7 Tesla. *Neuroimage* **55**, 986–998 (2011).

67. Mouches, P. & Forkert, N. D. A statistical atlas of cerebral arteries generated using multi-center MRA datasets from healthy subjects. *Sci. Data* **6**, 1–8 (2019).

68. Bernier, M., Cunnane, S. C. & Whittingstall, K. The morphology of the human cerebrovascular system. *Hum. Brain Mapp.* **39**, 4962–4975 (2018).

69. Huck, J. *et al.* High resolution atlas of the venous brain vasculature from 7 T quantitative susceptibility maps. *Brain Struct. Funct.* **224**, 2467–2485 (2019).

70. Kim, E., Zhang, J., Hong, K., Benoit, N. E. & Pathak, A. P. Vascular phenotyping of brain tumors using magnetic resonance microscopy (μMRI). *J. Cereb. Blood Flow Metab.* **31**, 1623–1636 (2011).

71. Dorr, A., Sled, J. G. & Kabani, N. Three-dimensional cerebral vasculature of the CBA mouse brain: a magnetic resonance imaging and micro computed tomography study. *Neuroimage* **35**, 1409–1423 (2007).

72. MungSoo, K., SeokHa, J., Lee, D. & HyungJoon, C. MRI Visualization of Whole Brain Macro-and Microvascular Remodeling in a Rat Model of Ischemic Stroke: A Pilot Study. *Sci. Rep. Nat. Publ. Group* **10**, (2020).

73. Xiong, B. *et al.* Precise cerebral vascular atlas in stereotaxic coordinates of whole mouse brain. *Front. Neuroanat.* **11**, 128 (2017).

74. Di Giovanna, A. P. *et al.* Whole-brain vasculature reconstruction at the single capillary level. *Sci. Rep.* **8**, 1–11 (2018).

75. Kirst, C. *et al.* Mapping the Fine-Scale Organization and Plasticity of the Brain Vasculature. *Cell* **180**, 780-795.e25 (2020).

76. Ghanavati, S., Lisa, X. Y., Lerch, J. P. & Sled, J. G. A perfusion procedure for imaging of the mouse cerebral vasculature by X-ray micro-CT. *J. Neurosci. Methods* **221**, 70–77 (2014).

77. Quintana, D. D. *et al.* The cerebral angiome: High resolution MicroCT imaging of the whole brain cerebrovasculature in female and male mice. *NeuroImage* **202**, 116109 (2019).

78. Pries, A. R., Secomb, T. W. & Gaehtgens, P. Structure and hemodynamics of microvascular networks: heterogeneity and correlations. *Am. J. Physiol.-Heart Circ. Physiol.* **269**, H1713–H1722 (1995).

79. Upputuri, P. K. & Pramanik, M. Recent advances in photoacoustic contrast agents for in vivo imaging. *Wiley Interdiscip. Rev. Nanomed. Nanobiotechnol.* e1618 (2020) doi:10/ggzmcp.

80. Dolezyczek, H. *et al.* In vivo brain imaging with multimodal optical coherence microscopy in a mouse model of thromboembolic photochemical stroke. *Neurophotonics* **7**, 015002 (2020).

81. Amato, S. P., Pan, F., Schwartz, J. & Ragan, T. M. Whole brain imaging with serial two-photon tomography. *Front. Neuroanat.* **10**, 31 (2016).

82. Meyer, E. P., Ulmann-Schuler, A., Staufenbiel, M. & Krucker, T. Altered morphology and 3D architecture of brain vasculature in a mouse model for Alzheimer's disease. *Proc. Natl. Acad. Sci.* **105**, 3587–3592 (2008).

83. Schnell, S., Wu, C. & Ansari, S. A. 4D MRI flow examinations in cerebral and extracerebral vessels. Ready for clinical routine? *Curr. Opin. Neurol.* **29**, 419 (2016).

84. Vanlandewijck, M. *et al.* A molecular atlas of cell types and zonation in the brain vasculature. *Nature* **554**, 475 (2018).

85. Zhao, S. *et al.* Cellular and Molecular Probing of Intact Human Organs. *Cell* **180**, 796-812.e19 (2020).

86. Garvalov, B. K. & Ertürk, A. Seeing whole-tumour heterogeneity. *Nat. Biomed. Eng.* **1**, 772–774 (2017).

87. Moy, A. J., Wiersma, M. P. & Choi, B. Optical Histology: A Method to Visualize Microvasculature in Thick Tissue Sections of Mouse Brain. *PLoS ONE* **8**, (2013).

88. Takase, Y., Tadokoro, R. & Takahashi, Y. Low cost labeling with highlighter ink efficiently visualizes developing blood vessels in avian and mouse embryos. *Dev. Growth Differ.* **55**, 792–801 (2013).

89. Ertürk, A., Lafkas, D. & Chalouni, C. Imaging cleared intact biological systems at a cellular level by 3DISCO. *J. Vis. Exp. JoVE* (2014) doi:10/ggz9dg.

90. Lugo-Hernandez, E. *et al.* 3D visualization and quantification of microvessels in the whole ischemic mouse brain using solvent-based clearing and light sheet microscopy. *J. Cereb. Blood Flow Metab. Off. J. Int. Soc. Cereb. Blood Flow Metab.* **37**, 3355–3367 (2017).

91. Steinman, J., Koletar, M. M., Stefanovic, B. & Sled, J. G. 3D morphological analysis of the mouse cerebral vasculature: Comparison of in vivo and ex vivo methods. *PloS One* **12**, e0186676 (2017).

92. Qi, Y. *et al.* FDISCO: Advanced solvent-based clearing method for imaging whole organs. *Sci. Adv.* **5**, eaau8355 (2019).

93. Salehi, A. *et al.* A Novel Technique for Visualizing and Analyzing the Cerebral Vasculature in Rodents. *Transl. Stroke Res.* (2018) doi:10/ggz9f9.

94. Khoradmehr, A., Mazaheri, F., Anvari, M. & Tamadon, A. A Simple Technique for Three-Dimensional Imaging and Segmentation of Brain Vasculature Using Fast Free-of-Acrylamide Clearing Tissue in Murine. *Cell J. Yakhteh* **21**, 49–56 (2019).

95. Miyawaki, T. *et al.* Visualization and molecular characterization of whole-brain vascular networks with capillary resolution. *Nat. Commun.* **11**, 1104 (2020).

96. Henriksen, B. L. E., Jensen, K. H. R. & Berg, R. W. Vasculature-staining with lipophilic dyes in tissue-cleared brains assessed by deep learning. *bioRxiv* 2020.05.16.099705 (2020) doi:10/ggz9dj.

97. Richardson, A. *et al.* Use of high-refractive index hydrogels and tissue clearing for large biological sample imaging. *bioRxiv* 2020.01.22.905695 (2020) doi:10/ggz9hn.

98. Murakami, T. C. *et al.* A three-dimensional single-cell-resolution whole-brain atlas using CUBIC-X expansion microscopy and tissue clearing. *Nat. Neurosci.* **21**, 625–637 (2018).

99. Alber, M. *et al.* Integrating machine learning and multiscale modeling-perspectives, challenges, and opportunities in the biological, biomedical, and behavioral sciences. *NPJ Digit. Med.* **2**, 115 (2019).

100. Zeng, N., Zuo, S., Zheng, G., Ou, Y. & Tong, T. Editorial: Artificial Intelligence for Medical Image Analysis of Neuroimaging Data. *Front. Neurosci.* **14**, (2020).

101. Pan, C. *et al.* Deep Learning Reveals Cancer Metastasis and Therapeutic Antibody Targeting in the Entire Body. *Cell* **179**, 1661-1676.e19 (2019).

102. Yang, Q., Zhang, Y., Dai, W. & Pan, S. J. *Transfer Learning*. (Cambridge University Press, 2020). doi:10.1017/9781139061773.

103. Paetzold, J. C. *et al.* Transfer learning from synthetic data reduces need for labels to segment brain vasculature and neural pathways in 3D. in (2019).

104. Schaumberg, A. J. *et al.* Interpretable multimodal deep learning for real-time pan-tissue pan-disease pathology search on social media. *Mod. Pathol. Off. J. U. S. Can. Acad. Pathol. Inc* (2020) doi:10/ggzmfv.

105. Ekins, S. *et al.* Exploiting machine learning for end-to-end drug discovery and development. *Nat. Mater.* **18**, 435–441 (2019).

106. Lopatkin, A. J. & Collins, J. J. Predictive biology: modelling, understanding and harnessing microbial complexity. *Nat. Rev. Microbiol.* (2020) doi:10/ggzm2n.

107. Zheng, W. & Ghersi-Egea, J.-F. Brain Barrier Systems Play No Small Roles in Toxicant-induced Brain Disorders. *Toxicol. Sci. Off. J. Soc. Toxicol.* **175**, 147–148 (2020).

108. Ueda, H. R. *et al.* Whole-Brain Profiling of Cells and Circuits in Mammals by Tissue Clearing and Light-Sheet Microscopy. *Neuron* **106**, 369–387 (2020).

109. Harrison, C. H. *et al.* A novel method to visualise the three-dimensional organisation of the human cerebral cortical vasculature. *J. Anat.* **232**, 1025–1030 (2018).

110. Tainaka, K. *et al.* Chemical Landscape for Tissue Clearing Based on Hydrophilic Reagents. *Cell Rep.* **24**, 2196-2210.e9 (2018).

111. Chung, K. *et al.* Structural and molecular interrogation of intact biological systems. *Nature* **497**, 332–337 (2013).

112. Morawski, M. *et al.* Developing 3D microscopy with CLARITY on human brain tissue: Towards a tool for informing and validating MRI-based histology. *NeuroImage* **182**, 417–428 (2018).

113. Ku, T. *et al.* Elasticizing tissues for reversible shape transformation and accelerated molecular labeling. *Nat. Methods* **17**, 609–613 (2020).

114. Zhao, L. *et al.* Zonation-dependent single-endothelial cell transcriptomic changes in the aged brain. *bioRxiv* 800318 (2019) doi:10/ggz9jr.

115. Kalucka, J. *et al.* Single-Cell Transcriptome Atlas of Murine Endothelial Cells. *Cell* **180**, 764-779.e20 (2020).

116. Pan, C. *et al.* Shrinkage-mediated imaging of entire organs and organisms using uDISCO. *Nat. Methods* **13**, 859–867 (2016).

117. Cai, R. *et al.* Panoptic imaging of transparent mice reveals whole-body neuronal projections and skull-meninges connections. *Nat. Neurosci.* **22**, 317–327 (2019).

118. Lugo-Hernandez, E. *et al.* 3D visualization and quantification of microvessels in the whole ischemic mouse brain using solvent-based clearing and light sheet microscopy. *J. Cereb. Blood Flow Metab.* **37**, 3355–3367 (2017).

119. Ueda, H. R. *et al.* Whole-Brain Profiling of Cells and Circuits in Mammals by Tissue Clearing and Light-Sheet Microscopy. *Neuron* **106**, 369–387 (2020).

120. Todorov, M. I. *et al.* Machine learning analysis of whole mouse brain vasculature. *Nat. Methods* **17**, 442–449 (2020).

9. Publication list

9.1. First authorship

- **Todorov, Mihail Ivilinov**, Johannes Christian Paetzold, Oliver Schoppe, Giles Tetteh, Suprosanna Shit, Velizar Efremov, Katalin Todorov-Völgyi, et al. 2020. "Machine Learning Analysis of Whole Mouse Brain Vasculature." Nature Methods 17 (4): 442–49. https://doi.org/10/ggxkpz.

9.2. Co-authorship

- Zhao, Shan, **Mihail Ivilinov Todorov**, Ruiyao Cai, Rami Ai -Maskari, Hanno Steinke, Elisabeth Kemter, Hongcheng Mai, et al. 2020. "Cellular and Molecular Probing of Intact Human Organs." Cell 180 (4): 796-812.e19. https://doi.org/10/dmnn.

- Pan, Chenchen, Oliver Schoppe, Arnaldo Parra-Damas, Ruiyao Cai, **Mihail Ivilinov Todorov**, Gabor Gondi, Bettina von Neubeck, et al. 2019. "Deep Learning Reveals Cancer Metastasis and Therapeutic Antibody Targeting in the Entire Body." Cell 179 (7): 1661-1676.e19. https://doi.org/10/ggzmfp.

- Cai, Ruiyao, Chenchen Pan, Alireza Ghasemigharagoz, **Mihail Ivilinov Todorov**, Benjamin Förstera, Shan Zhao, Harsharan S. Bhatia, et al. 2019. "Panoptic Imaging of Transparent Mice Reveals Whole-Body Neuronal Projections and Skull-Meninges Connections." Nature Neuroscience 22 (2): 317–27. https://doi.org/10/gfttgr.

- Völgyi, Katalin, Péter Gulyássy, **Mihail Ivilinov Todorov**, Gina Puska, Kata Badics, Dávid Hlatky, Katalin Adrienna Kékesi, et al. 2018. "Chronic Cerebral Hypoperfusion Induced Synaptic Proteome Changes in the Rat Cerebral Cortex." Molecular Neurobiology 55 (5): 4253–66. https://doi.org/10/ggzk6t.

- Simor, Attila, Balázs András Györffy, Péter Gulyássy, Katalin Völgyi, Vilmos Tóth, **Mihail Ivilinov Todorov**, Viktor Kis, et al. 2017. "The Short- and Long-Term Proteomic Effects of Sleep Deprivation on the Cortical and Thalamic Synapses." Molecular and Cellular Neurosciences 79: 64–80. https://doi.org/10/f9xmbk.

10. Acknowledgements

I wish to express my sincere appreciation to my supervisor, Dr. Ali Ertürk, whose knowledge and advices into the subject matter steered me through this research. His support, guidance and overall insights in this field have made this an inspiring experience for me.

Additionally, I would like to sincerely thank the members of my Thesis Advisory Committee, Dr. Ali Ertürk, PD Dr. Marco Düring, Prof. Dr. Bjoern Menze and Prof. Dr. Martin Dichgans. They are not only supervisors giving me advices about my experiments and career, but also mentors and collaborators deeply involved in the projects. The meetings and conversations were vital in inspiring me to think outside the box, from multiple perspectives to form a comprehensive and objective critique.

Next, I am grateful to Dr. Farida Hellal, Dr. med. vet. Manuela Schneider and Dr. med. vet. Ulrike Schillinger for their enthusiasm for the project, for their support, encouragement, and patience.

I would like to thank the following people, without whom I would not have been able to complete this research, and without whom I would not have made it through this thesis. I would like to express my gratitude to the active members and alumni of the Acute Brain Injury research group, the Image-Based Biomedical Modeling group, and the Institute of Anatomy in Leipzig. I also wish to thank the Graduate School of Systemic Neurosciences and the Munich Cluster for Systems Neurology for creating the soil for great collaborations, and for letting me be part of this incredible research network.

My biggest thanks to my family for all the support and great love through this research, the culmination of years of distance learning. Special thanks to my wife Katalin, my wise and patient advisor who continuously supported me with my stresses for the past years of study!

11. Affidavit / Eidesstattliche Versicherung

Hiermit versichere ich an Eides statt, dass ich die vorliegende Dissertation „SYSTEMATIC ANALYSIS OF WHOLE MOUSE BRAIN VASCULATURE AND INTACT HUMAN ORGANS USING MACHINE LEARNING“ selbstständig angefertigt habe, mich außer der angegebenen keiner weiteren Hilfsmittel bedient und alle Erkenntnisse, die aus dem Schrifttum ganz oder annähernd übernommen sind, als solche kenntlich gemacht und nach ihrer Herkunft unter Bezeichnung der Fundstelle einzeln nachgewiesen habe.

I hereby confirm that the dissertation “SYSTEMATIC ANALYSIS OF WHOLE MOUSE BRAIN VASCULATURE AND INTACT HUMAN ORGANS USING MACHINE LEARNING” is the result of my own work and that I have only used sources or materials listed and specified in the dissertation.

Munich, 2020/08/04

_____

Mihail Ivilinov Todorov

12. Declaration of authors' contributions

Authors contributed to the Research Articles as follows:

1. M.I. Todorov*, J.C. Paetzold*, O. Schoppe, G. Tetteh, S. Shit, V. Efremov, K. Todorov-Völgyi, M. Düring, M. Dichgans, M. Piraud, B. Menze & A. Ertürk. * equally contributed. **Machine learning analysis of whole mouse brain vasculature. M.I.T.** performed the tissue processing, clearing and imaging experiments. **M.I.T.** and K.T.-V. developed the whole-brain staining protocol. **M.I.T.** stitched and assembled the whole-brain scans. V.E. and J.C.P. generated the synthetic vascular training dataset. J.C.P., G.T. and O.S. developed the deep learning architecture and trained the models. J.C.P. and S.S. performed the quantitative analyses. **M.I.T.** annotated the data. M. Düring and M. Dichgans helped with data interpretation. B.M., M.P. and G.T. provided guidance in developing the deep learning architecture and helped with data interpretation. A.E., **M.I.T.**, B.M. and J.C.P. wrote the manuscript. All authors edited the manuscript. A.E. initiated and led all aspects of the project.

2. S. Zhao, M.I. Todorov, R.Cai, R.AI-Maskari, H. Steinke, E. Kemter, H. Mai, Z. Rong, M. Warmer, K. Stanic, O. Schoppe, J.C. Paetzold, B. Gesierich, M.N.Wong, T.B.Huber, M.Düring, O.T. Bruns, B. Menze, A. Ertürk. **Cellular and Molecular Probing of Intact Human Organs.** S.Z. developed the protocols and performed organs processing, labeling, clearing, imaging, and data analysis. M.I.T. and R.C. contributed to optimize the protocol, organs processing, imaging, and data analysis. R.A.-M., O.S., J.C.P., and B.M. developed the deep learning architecture and quantitative analyses. H.S. and I.B. perfused and dissected the human organs. E.K. and E.W. generated the INS-EGFP transgenic pig line. E.K. perfused and dissected pig pancreas. S.Z., R.C., H.M., and Z.R. annotated the ground truth data. M.W. and O.T.B. designed and performed SWIR images. M.D. and B.G. performed the MRI images and analysis. J.L. performed the SAXS experiment and data analysis. K.S., V.G.P., M.N.W., and T.B.H. contributed to confocal, tissue recycling, and histology analyses. S.Z. and A.E. wrote the manuscript. All authors edited the manuscript. A.E. initiated and led all aspects of the project.

Herewith, I confirm the contributions to the manuscripts.

Munich, 2020/06/08

Mihail Ivilinov Todorov	Dr. Ali Ertürk (supervisor)
Johannes Christian Paetzold (shared first author for Research Article 1)	Shan Zhao (first author for Research Article 2)